

# MAGNETIC TRACKING FOR MEDICAL APPLICATIONS

by

**Rubing Jin**

**A Dissertation**

*Submitted to the Faculty of Purdue University*

*In Partial Fulfillment of the Requirements for the degree of*

**Doctor of Philosophy**



School of Electrical and Computer Engineering

West Lafayette, Indiana

May 2022

**THE PURDUE UNIVERSITY GRADUATE SCHOOL**  
**STATEMENT OF COMMITTEE APPROVAL**

**Dr. Byunghoo Jung, Chair**

School of Electrical and Computer Engineering

**Dr. Kaushik Roy**

School of Electrical and Computer Engineering

**Dr. Dimitrios Peroulis**

School of Electrical and Computer Engineering

**Dr. Babak Ziaie**

School of Electrical and Computer Engineering

**Approved by:**

Dr. Dimitrios Peroulis

*This thesis is dedicated to my parents.*

## **ACKNOWLEDGMENTS**

I wish to express my sincere gratitude to my major professor, Dr. Byunghoo Jung, for his direction and friendship. Without his kind instructions, this work would not have been accomplished.

Special thanks are extended to the other members of my dissertation committee, Dr. Dimitrios Peroulis, Dr. Kaushik Roy, and Dr. Babak Ziaie, for their support and guidance.

I would like to thank my fellow graduate students Bong Chan Kim, Chamika Liyanagedera, Suchitra Ramesh, Weeseong Seo, Ravi Abhishek Shankar, Youngtae Shin, Mohit Singh, and many others for all those interesting and beneficial discussions.

Finally, I wish to thank my parents, Zhen Wu and Di Jin, for their love, support, and encouragement.



# TABLE OF CONTENTS

LIST OF TABLES .....	8
LIST OF FIGURES .....	10
ABSTRACT .....	17
1. INTRODUCTION .....	19
1.1 Motivation .....	19
1.2 Objective .....	22
1.3 Magnetic Positioning System .....	26
2. LITERATURE REVIEW .....	28
2.1 Tracking Systems .....	28
2.2 Electromagnetic Positioning System Models .....	28
2.2.1 Medical Applications .....	28
2.2.2 Dipole Based Model .....	32
2.2.3 Tracking the Transmitter .....	33
2.2.4 Tracking the Receiver .....	34
2.3 Optimization Methods for Position Calculation .....	37
2.3.1 Optimization Methods .....	37
2.3.2 Other Optimization Methods .....	41
2.4 Electromagnetic Tracking Sensors .....	44
3. TRACKING SYSTEM DESCRIPTION AND HARDWARE DESIGN .....	47
3.1 System Description .....	47
3.2 Transmitter Analysis .....	48
3.2.1 Transmitter Magnetic Field Model Selection .....	48
3.2.2 Transmitter Coil Introduction .....	52
3.2.3 Transmitter Core .....	56
3.2.4 Transmitter Coil Design .....	57
3.2.5 Heat Considerations .....	63
3.2.6 Transmitter Coil Winding .....	65
3.2.7 Transmitter Coil Specifications .....	66
3.2.8 Transmitter Driver Design .....	69

Transmitter Driver (H-Bridge) Simulation and Evaluation .....	70
Transmitter Driving Circuit (Op-Amp Based Driver) and Coil Connection .....	80
3.2.9 AC Input Signal Generation and Feedback .....	82
3.2.10 Transmitter Integration into System Level.....	93
3.3 Sensing Coil Analysis .....	94
3.3.1 Selection of Sensing Coils .....	95
3.3.2 Connection of Sensing Coils to Microcontroller .....	97
3.3.3 Sensing Coil Resistor Noise Analysis .....	98
3.3.4 Analog Front End (Amplifiers) .....	101
Op-Amp Noise .....	102
3.3.5 Analog Front End Integration .....	108
3.3.6 Sensitivity .....	115
3.3.7 Sensing Coil Test.....	119
3.3.8 Sensing Coils Configuration.....	123
4. MAGNETIC POSITIONING FIRMWARE .....	125
4.1 Firmware Optimization .....	125
4.2 Positioning Algorithm.....	127
4.2.1 Algorithm 1: Position Solver .....	128
4.2.2 Algorithm 2: Position Search.....	134
4.3 Kalman Filter .....	139
4.4 Optimal Detection .....	141
4.5 Algorithm Convergence Speed .....	143
4.6 Computational Cost .....	145
4.7 Link Budget Analysis .....	151
4.8 Algorithm Divergence Correction .....	152
5. SYSTEM INTEGRATION AND CALIBRATION.....	161
5.1 Hardware Integration .....	161
5.2 Potential Electrical System Integration in Medical Environment.....	162
5.3 Mechanical Integration .....	163
5.4 System Calibration.....	167
5.4.1 Gain.....	169

Analog Front End (AFE) Gain Stage Mismatch .....	169
Coil Gain Mismatch .....	170
Magnitude.....	172
Phase.....	172
5.4.2 Orientation .....	172
5.4.3 Mutual Coupling.....	173
6. SYSTEM SETUP AND TESTING .....	177
6.1 Prototype System Setup .....	177
6.2 Test Results .....	180
6.2.1 Static Tests .....	182
6.2.2 Dynamic Tests .....	189
6.3 Repeatability .....	199
6.4 System Comparison .....	201
6.5 System Cost Estimation .....	204
7. SUMMARY AND FUTURE WORK .....	205
7.1 Conclusions.....	205
7.2 Future Work .....	206
7.2.1 Additional Sensing Coils and Layout Optimization .....	206
7.2.2 Commercialization and Medical Device Classification .....	207
7.2.3 6DOF Tracking.....	207
7.2.4 Multi-Catheter Support.....	207
REFERENCES .....	209
VITA .....	219
PUBLICATION .....	220

## LIST OF TABLES

Table 1.2.1. French catheter scale.....	24
Table 3.2.1. Comparison of commercially available coils.....	52
Table 3.2.2. $R_{ac}/R_{dc}$ for each layer. ....	62
Table 3.2.3. Hand calculated B-field and voltage estimations of the transmitter coil.....	63
Table 3.2.4. Comparison of designed coils (no external connections). ....	67
Table 3.2.5. Comparison of designed coils (with twisted pair wire). ....	68
Table 3.2.6. RMS current and power of coil at 32kHz for various operating voltages. ....	75
Table 3.2.7. RMS current and power of final version transmitter coil 32kHz. ....	77
Table 3.2.8. Comparison of simulated and measured harmonic tones. ....	79
Table 3.3.1. Comparison of triaxial sensing coils.....	96
Table 3.3.2. 3DCC10 triaxial sensing coil specifications. ....	97
Table 3.3.3. Triaxial sensing coil specifications with PCB and SMA connector attached.....	98
Table 3.3.4. Simulated frequency domain magnitudes of 1 <sup>st</sup> , 2 <sup>nd</sup> , and 3 <sup>rd</sup> harmonics with unit in dBv (a) and unit in dBm (b). ....	107
Table 3.3.5. Null noise measurement with transmitter coil as reference. ....	112
Table 3.3.6. Null noise measurement with Ch4 probe as reference. ....	112
Table 3.3.7. Voltage level and measured frequency domain magnitudes of 1 <sup>st</sup> , 2 <sup>nd</sup> , and 3 <sup>rd</sup> harmonics.....	114
Table 3.3.8. Measured frequency domain magnitudes for first three harmonic tones.....	114
Table 3.3.9. Rx1: Fundamental tone and harmonic magnitudes.....	120
Table 3.3.10. Rx2: Fundamental tone and harmonic magnitudes.....	120
Table 4.6.1. Computation cost for optimal detection and mismatch. ....	148
Table 4.6.2. Computation cost for position algorithm. ....	149
Table 4.6.3. Computation cost for Kalman filter. ....	150
Table 4.6.4. Total computation cost in clock cycles for one iteration (position estimation).....	150
Table 4.6.5. Computation time for one position update. ....	151
Table 6.1.1. Tracking position tests. ....	179
Table 6.2.1. Position error of static position tests.....	188

Table 6.2.2. Orientation error of static position tests.....	188
Table 6.2.3. Dynamic position tests: jitter (mm). ....	198
Table 6.2.4. Dynamic orientation tests: jitter (deg). ....	198
Table 6.3.1. Offsets in position test results.....	199
Table 6.3.2. Comparison of mean and standard deviation of position errors. ....	200
Table 6.3.3. Comparison of mean and standard deviation of orientation errors.....	200
Table 6.4.1. System comparison. ....	203
Table 6.5.1. System cost breakdown. ....	204

## LIST OF FIGURES

Figure 1.1.1. EKG showing irregular beating of the heart.....	19
Figure 1.1.2. Treatment of bradycardia with a pacemaker. ....	20
Figure 1.1.3. Catheter ablation.....	20
Figure 1.1.4. Contrast agents may cause damage to kidney. ....	22
Figure 1.2.1. Heart surgery. ....	23
Figure 1.2.2. Catheter used in heart surgery. ....	23
Figure 1.2.3. Diameters of heart arteries and veins. ....	25
Figure 1.2.4. Diagnostic mapping catheter tip with platinum band EKG sensors.....	25
Figure 1.2.5. Angiography for heart mapping. ....	26
Figure 2.2.1. Two types of medical tracking systems: tracking receiver (Rx) inside a patient (left) and tracking transmitter (Tx) inside a patient (right).....	29
Figure 2.2.2. NDI Aurora sensing coils. ....	30
Figure 2.2.3. Tracking the transmitter (fixed receiver).....	33
Figure 2.2.4. Tracking the receiver (fixed transmitter).....	35
Figure 2.2.5. Type 1 tracking receiver system overview.....	37
Figure 2.3.1. Search path to an optimal solution. ....	41
Figure 2.3.2. Objective function showing position errors, optimal position at $(x, y) = (0\text{cm}, 0\text{cm})$ . .....	41
Figure 2.3.3. A system for tongue tracking. ....	42
Figure 2.3.4. Simplex method to find optimal solution. ....	42
Figure 2.3.5. Algorithm for Nelder-Mead simplex method.....	43
Figure 2.3.6. Algorithm for particle swarm optimization. ....	44
Figure 2.4.1. Ascension sensing coils.....	45
Figure 2.4.2. Magnetically tracked sensors. ....	45
Figure 2.4.3. Magnetically tracked 6DOF sensors. ....	46
Figure 3.1.1. Catheter tracking system illustration. ....	48
Figure 3.2.1. Simulated B-field at $x = 0.5\text{cm}$ , $y = 1\text{cm}$ , $z$ varying between 1 and 15cm. ....	50
Figure 3.2.2. Errors at $x = 0.5\text{cm}$ , $y = 1\text{cm}$ , $z$ varying between 1 and 15cm.....	50

Figure 3.2.3. Simulated B-field at $x = 1\text{cm}$ , $y = 2\text{cm}$ , $z$ varying between 1 and 15cm. ....	51
Figure 3.2.4. Errors at $x = 1\text{cm}$ , $y = 2\text{cm}$ , $z$ varying between 1 and 15cm.....	51
Figure 3.2.5. Commercially available coils tested.....	53
Figure 3.2.6. Core saturation waveform behavior. ....	54
Figure 3.2.7. Oscilloscope output of EPCOS B82450A*E coil: clock signal for transmitter driver (blue) and transmitter coil inductor voltage waveform (magenta). ....	54
Figure 3.2.8. Catheter tip. ....	55
Figure 3.2.9. Different plastic cores for transmitter coil.....	56
Figure 3.2.10. Plastic core for the proposed transmitter coil. ....	56
Figure 3.2.11. Current density in a 1.32mm diameter wire. ....	58
Figure 3.2.12. Resistance of wire in relation to AWG.....	58
Figure 3.2.13. Skin and proximity effects on coils. ....	59
Figure 3.2.14. Multi-layer coil shapes. ....	59
Figure 3.2.15. Geometry of a long coil.....	60
Figure 3.2.16. Ratio of AC to DC resistance by the number of layers. ....	62
Figure 3.2.17. Fluid bulk flow in relation to cross-sectional area and average velocity. ....	64
Figure 3.2.18. Simulated temperature compared to IEC temperature limit (left) and simulated magnetic radiation (SAR) compared to IEC magnetic radiation limit (right). ....	65
Figure 3.2.19. Coil winding apparatus.....	66
Figure 3.2.20. Coil being wound (left), coil winding completed (middle), version 1 transmitter coil (right). ....	66
Figure 3.2.21. Transmitter coil version 2 (left) and final version (right).....	67
Figure 3.2.22. 30AWG twisted pair wire version 2.....	68
Figure 3.2.23. Transmitter coil (final version) attached to catheter tip. ....	68
Figure 3.2.24. Possible transmitter system with an H-bridge driver. ....	70
Figure 3.2.25. Break before make allows for shorting prevention. ....	71
Figure 3.2.26. H-bridge driver design with voltage sensing feedback circuit. ....	72
Figure 3.2.27. Hypothetical frequency domain curve of noise sources (gray) relative to transmitter coil inductor current (red). ....	73
Figure 3.2.28. Flicker noise waveform pattern relative to white noise.....	73
Figure 3.2.29. Transmitter driver LC loop (final version coil).....	74

Figure 3.2.30. Simulation results: blue line: voltage across inductor and green line: current through inductor. ....	75
Figure 3.2.31. Frequency domain simulation results of current across inductor. ....	76
Figure 3.2.32. PCB for H-bridge transmitter driver. ....	76
Figure 3.2.33. Measured voltage across the transmitter coil. ....	77
Figure 3.2.34. Frequency domain plot of voltage across the transmitter coil. ....	78
Figure 3.2.35. Frequency domain plot of voltage at LC node and mixing frequencies for 1 <sup>st</sup> and 2 <sup>nd</sup> order harmonics. ....	80
Figure 3.2.36. Transmitter system diagram. ....	81
Figure 3.2.37. Block diagram of the transmitter system. ....	82
Figure 3.2.38. Comparison of STM32F4 PWM (blue) and DAC (red). ....	83
Figure 3.2.39. Phase and amplitude-controlled DAC with Tx driver. ....	84
Figure 3.2.40. Simulation schematic of parallel LC (left) and series LC (right). ....	86
Figure 3.2.41. Simulation Bode plot of transmitter inductor current for parallel LC I(L1) and series LC I(L2) driver circuits. ....	86
Figure 3.2.42. Simulation transient plot of op-amp and inductor currents for parallel LC (I(V1) and I(L1)) and series LC (I(V2) and I(L2)) driver circuits. ....	87
Figure 3.2.43. Schematic of op-amp based transmitter driver with sensing circuit (left) and LTSPICE simulation (right). ....	88
Figure 3.2.44. Time domain simulation results of op-amp based transmitter driver. ....	89
Figure 3.2.45. Frequency domain simulation results of op-amp based transmitter driver. ....	90
Figure 3.2.46. Time domain voltage of DAC signal (upper) and inductor voltage (lower). ....	91
Figure 3.2.47. Fast Fourier transform (FFT) of DAC signal (upper) and inductor voltage (lower). ....	91
Figure 3.2.48. Transmitting coil RMS voltage over time. ....	92
Figure 3.2.49. Block diagram of complete system. ....	93
Figure 3.2.50. Transmitter driver with feedback sensing circuit (left), battery and coil twisted pair wire connected to transmitter driver (right). ....	94
Figure 3.3.1. 3DCC10 triaxial sensing coil (left) and PCB sensing LC circuit (right). ....	97
Figure 3.3.2. Sensing coil resistor noise ( $v_{n,R}$ ) in relation to measured signal ( $v_{emf}$ ). ....	99
Figure 3.3.3. Signal (red) and noise (blue) over distance. ....	100
Figure 3.3.4. Effect of Q on resistor and amplifier noise. ....	100



Figure 3.3.5. Block diagram of amplifier transfer function showing input referred noise having same magnitude whether it is inside or outside the feedback loop.....	102
Figure 3.3.6. Two possible gain stage designs.....	103
Figure 3.3.7. Two-stage amplifier.....	104
Figure 3.3.8. Frequency sweep simulation. ....	105
Figure 3.3.9. Simulation for DC offset shift. ....	105
Figure 3.3.10. Fourier analysis simulation closed loop amplification of stage 1 (V(vout1)) and stage 1+2 (V(vout2)).....	106
Figure 3.3.11. IP2 and IP3 plots of 1 <sup>st</sup> stage amplifier. ....	108
Figure 3.3.12. Analog front end.....	109
Figure 3.3.13. Block diagram of analog front end. ....	110
Figure 3.3.14. Voltage level at different distances, with emphasis on critical SNR. ....	111
Figure 3.3.15. Oscilloscope null noise measurement test. ....	112
Figure 3.3.16. Measured voltage by distance between Tx and Rx. ....	113
Figure 3.3.17. Measured voltage by distance between Tx and Rx in terms of separate harmonic tones. ....	113
Figure 3.3.18. IP2 and IP3 plots of the 1 <sup>st</sup> stage amplifier (left) and 2 <sup>nd</sup> stage amplifier (right). ....	115
Figure 3.3.19. Position algorithm error when SNR = 40 dB (no filter applied). ....	116
Figure 3.3.20. Frequency response of receiving $x$ , $y$ , $z$ coils measured at 20 cm in $x$ distance from Tx to Rx (upper) and 40 cm in $x$ distance (lower). ....	117
Figure 3.3.21. Measured vs. simulated magnetic field strength. ....	118
Figure 3.3.22. Rx <sub>1</sub> measured voltage values at different $x$ distances.....	121
Figure 3.3.23. Rx <sub>2</sub> measured voltage values at different $x$ distances.....	121
Figure 3.3.24. Rx <sub>1</sub> measured voltage values at different positions.....	122
Figure 3.3.25. Rx <sub>2</sub> measured voltage values at different positions.....	123
Figure 3.3.26. Two 3DCC10 sensing coil setup. ....	124
Figure 4.1.1. ADC data sample for position calculation.....	126
Figure 4.1.2. Timing of microcontroller computations.....	127
Figure 4.2.1. Tracking system overview.....	128
Figure 4.2.2. Tracking the transmitter with two fixed receivers.....	130
Figure 4.2.3. Orientation angles.....	132

Figure 4.2.4. Simulated position and orientation errors. ....	133
Figure 4.2.5. Transmitter as reference frame and two receivers on iso-power surface. ....	135
Figure 4.2.6. Block diagram for position search algorithm. ....	138
Figure 4.3.1. Kalman filter algorithm flow. ....	140
Figure 4.4.1. Optimal detection. ....	142
Figure 4.5.1. Number of iterations to converge in position algorithm. ....	144
Figure 4.6.1. Computational cost – the execution time per time step. ....	145
Figure 4.6.2. Visual Big O meaning. ....	146
Figure 4.6.3. Comparing factors. ....	146
Figure 4.7.1. Forward link budget calculation. ....	152
Figure 4.8.1. Flat objective function in search algorithm. ....	153
Figure 4.8.2. Four triaxial receiver layout. ....	154
Figure 4.8.3. Location of positions tested. ....	155
Figure 4.8.4. Simulated determinant for text positions for two different Rx pairs (groups). Rx group 1: (0, 0, -0.5) and (23, 23, -0.5); Rx group 2: (0, 23, -0.5) and (23, 0, -0.5). ....	155
Figure 4.8.5. Simulated determinant for text positions for two different Rx pairs (groups). Rx group 1: (0, 0, -0.5) and (23, 23, -0.5); Rx group 2: (0, 23, -0.5) and (23, 0, -0.5) at Z=20cm. ....	156
Figure 4.8.6. <b>p</b> -vector shift shown by dashed lines. ....	157
Figure 4.8.7. The effects of <b>p</b> -vector correction on X position. ....	158
Figure 4.8.8. The effects of <b>p</b> -vector correction on Y position. ....	159
Figure 4.8.9. The effects of <b>p</b> -vector correction on Z position. ....	159
Figure 5.1.1. Tracking system diagram. ....	162
Figure 5.2.1. Electrical system integration (with planned future connection). ....	163
Figure 5.3.1. Transmitter coil with twisted pair wire wrapped on catheter. ....	164
Figure 5.3.2. Catheter installed in medical robot, with patient mannequin. ....	164
Figure 5.3.3. Reference sensing coils placed underneath patient table. ....	165
Figure 5.3.4. Real-time tracking of catheter. ....	166
Figure 5.3.5. Graphical user interface for the position/orientation of catheter tip 2D (left) and 3D heart (right). ....	166
Figure 5.3.6. Point-cloud GUI representation of catheter tip and camera pointed at the tip. ....	167
Figure 5.4.1. XYZ test station for calibration. ....	168

Figure 5.4.2. Tx and two Rx locations with the midpoint of the two Rx as reference. ....	169
Figure 5.4.3. Mismatch test bench. ....	171
Figure 5.4.4. Rx <sub>1</sub> induced field measurement. ....	175
Figure 5.4.5. Rx <sub>2</sub> induced field measurement. ....	176
Figure 6.1.1. Test bench. ....	177
Figure 6.1.2. XYZ test station used for the test. ....	178
Figure 6.1.3. Coordinate frame. ....	179
Figure 6.1.4. Position tracking area: test area shown by 3D red box. ....	180
Figure 6.2.1. Voltage measured in receiver and transmitting coils. ....	181
Figure 6.2.2. 0-degree azimuth orientation position result. ....	182
Figure 6.2.3. -30-degree azimuth orientation position result. ....	183
Figure 6.2.4. -60-degree azimuth orientation position result. ....	183
Figure 6.2.5. -90-degree azimuth orientation position result. ....	184
Figure 6.2.6. -120-degree azimuth orientation position result. ....	184
Figure 6.2.7. -150-degree azimuth orientation position result. ....	185
Figure 6.2.8. -180-degree azimuth orientation position result. ....	185
Figure 6.2.9. $z = 10\text{cm}$ orientation angle varying result. ....	186
Figure 6.2.10. $z = 15\text{cm}$ orientation angle varying result. ....	186
Figure 6.2.11. $z = 20\text{cm}$ orientation angle varying result. ....	187
Figure 6.2.12. $z = 25\text{cm}$ orientation angle varying result. ....	187
Figure 6.2.13. Determinant for azimuth angle: -90 degrees. ....	189
Figure 6.2.14. Determinant for azimuth angle: 0 degrees. ....	189
Figure 6.2.15. Dynamic test: position change (a). ....	191
Figure 6.2.16. Dynamic test: position change (b). ....	191
Figure 6.2.17. Dynamic test: position change (c). ....	192
Figure 6.2.18. Dynamic test: position change (d). ....	192
Figure 6.2.19. Dynamic test: position change (e). ....	193
Figure 6.2.20. Dynamic test: position change (f). ....	193
Figure 6.2.21. Dynamic test: orientation change (a). ....	194

Figure 6.2.22. Dynamic test: orientation change (b). .....	195
Figure 6.2.23. Dynamic test: orientation change (c).....	196
Figure 6.2.24. Dynamic test: orientation change (d). .....	197
Figure 6.3.1. Trial 1 (left) and Trial 2 (right) position test results.....	200
Figure 6.3.2. Trial 1 (left) and Trial 2 (right) orientation test results. ....	201

## ABSTRACT

This thesis explores the implementation of an electromagnetic positioning system to track medical instruments used in minimally invasive surgeries. The end application is for catheter cardiac ablation. Cardiac ablation is a low-risk procedure that can correct arrhythmia. In the procedure, a diagnostic mapping catheter is inserted into the heart to identify locations causing incorrect heartbeat, and an ablation catheter applies radiofrequency (RF) thermal energy, which burns tissue that emits abnormal heart rhythm. Current techniques which determine the mapping catheter's tip position while a patient is undergoing heart surgery are usually invasive, often inaccurate, and require some forms of imaging.

Most existing electromagnetic (EM) tracking systems track a tiny sensing coil on the catheter tip by placing planar magnetic transmitters in reference locations around a patient. However, the tracking speed of these systems is extremely limited apart from deficiency in positioning accuracy due to poor sensitivity of the small sensor. In this study, we develop a unique real-time tracking system which can track the position and orientation of a medical catheter tip inside a human heart. A configuration of a small transmitting coil on the catheter tip with multiple larger receiving coils placed at reference locations is investigated.

We propose a novel tracking system based on a single uniaxial transmitter (1.5 mm diameter) placed on a medical catheter tip and two triaxial receivers placed in reference locations. The electromagnetic field generated by the uniaxial transmitter is controlled by an operational amplifier LC tank driver with a unique active feedback sensing system in the form of a digital phased lock loop (DPLL), which generates a low noise low distortion AC signal for the LC circuit. Such control is vital because the small transmitting coil has a relatively large DC resistance, resulting in copious amounts of heat. This unique transmitter driver active feedback system is optimized to ensure a stable magnetic field transmitted with minimal noise and distortion.

Precise and efficient calibration and compensation techniques are developed for the proposed system. The calibration techniques include mutual coupling correction, which rectifies one of the main limitations of a triaxial coil-based implementation. In addition, a novel divergence mitigation method for the position algorithm is developed in the form of a software-based reference sensing coil distance offset. This is advantageous compared to a hardware-based solution, which involves adding more coils to the system, in turn, leading to decreased tracking speed and

higher risk of interference among coils. Because of its simplicity, the proposed EM tracking system also has the advantage of supporting a wide dynamic range, multiple catheters, and can be applied to other medical systems in need of real-time positioning.

This EM tracking system is demonstrated on a test bench in a research lab and in a pre-clinical environment with a 3D-printed heart inside a phantom. The tested system features a fast update rate of 200 Hz and an average position error of 1.6 mm, which indicates that the proposed system can successfully track a catheter RF tip with millimeter precision.

This dissertation presents the proposed EM tracking system. First, the motivation of this research and a review of existing tracking methodologies used in the medical field are presented. Then, the hardware design of individual modules and magnetic positioning firmware are described, which is followed by discussions of full system integration and calibration, as well as system test results. A summary, highlighting novelties of the tracking system, and discussion of future research directions are included in the final chapter.

# 1. INTRODUCTION

## 1.1 Motivation

Cardiovascular diseases are the leading cause of death globally, accounting for 30% of all deaths [1]. One of the more common cardiovascular diseases is arrhythmia, irregular beating of the heart, as depicted in Figure 1.1.1 below.

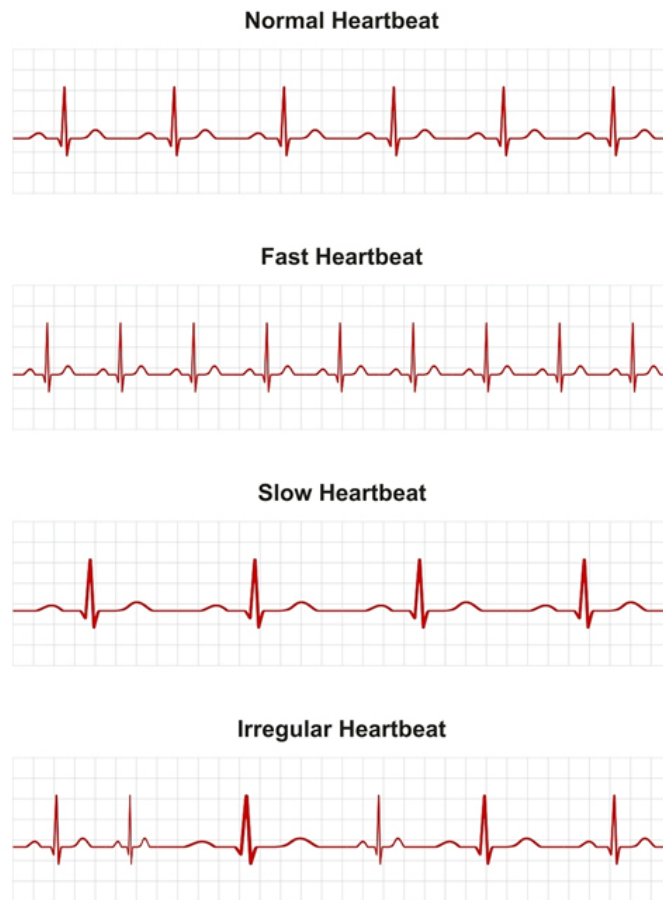


Figure 1.1.1. EKG showing irregular beating of the heart [2].

Arrhythmia can be categorized based on the speed of the heartbeat (fast, slow, irregular) and location (atrium, ventricle). Moderate arrhythmias, such as bradycardia (slow heartrate), can often be treated with a pacemaker (Figure 1.1.2), and surgery inside the heart is not required.

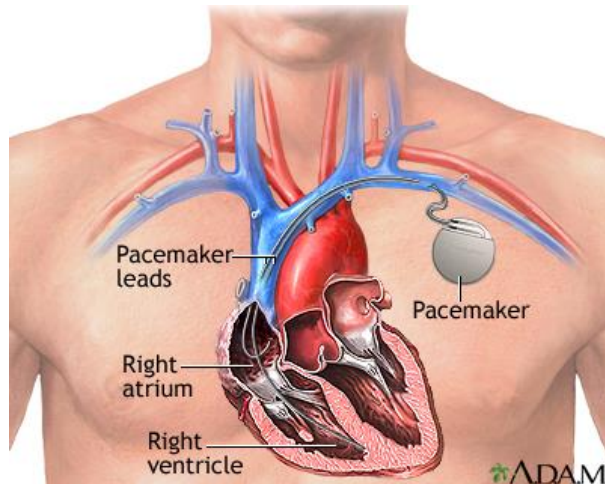


Figure 1.1.2. Treatment of bradycardia with a pacemaker [3].

For tachycardia (fast heart rate), treatment is often in the form of medication or cardioversion. Other forms of arrhythmia may also include irregular heartbeats caused by an abnormal electrical signal either in the atrium (atrial fibrillation) or in the ventricle (ventricular fibrillation) of the heart. Both types of arrhythmias are serious as they can cause stroke or failure of heart pumping. Such arrhythmias can be treated with an implantable cardioverter-defibrillator or with medication depending on the severity [4]. However, the drawback of all the above-mentioned treatments is that the patient has to rely on medication and devices, and these devices could malfunction [5]. Thus, a more permanent solution to arrhythmia is in the form of catheter ablation (Figure 1.1.3).

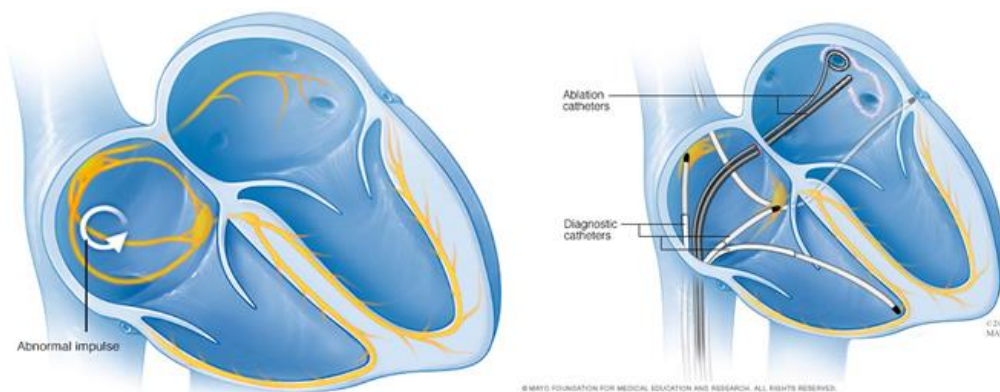


Figure 1.1.3. Catheter ablation [6], [7].



Catheter ablation is frequently used for arrhythmia-related surgeries, because the procedure is minimally invasive and has the highest success rates [8]. This form of treatment requires using a medical catheter to be inserted into the patient's heart. The catheter tip is guided through the heart, and radiofrequency (RF) thermal energy is applied to blood vessels/tissues which emit wrong heartbeat signal. Thus, this surgery requires knowing where the catheter tip is in relation to the affected blood vessels. Existing methods of catheter positioning locate the catheter tip through medical imaging tools, such as X-ray and echocardiography. During operation, a surgeon relies on those images to operate on the heart.

However, such medical imaging tools have significant drawbacks. The aforementioned imaging techniques require contrast agents to improve image resolution in order to provide real-time assessment of cardiac blood flow [9]. These contrast agents are known to cause complications to certain groups of patients. The symptoms that patients experience can be either moderate, such as vomiting and hives, or severe, such as kidney failure [10], [11]. It has been documented that contrast dyes used in catheter ablation surgery may damage kidneys, shown in Figure 1.1.4. Hospitals rely on patient screening to bar patients with a higher risk of exhibiting such complications. However, the screening cannot completely eliminate these complications from occurring.

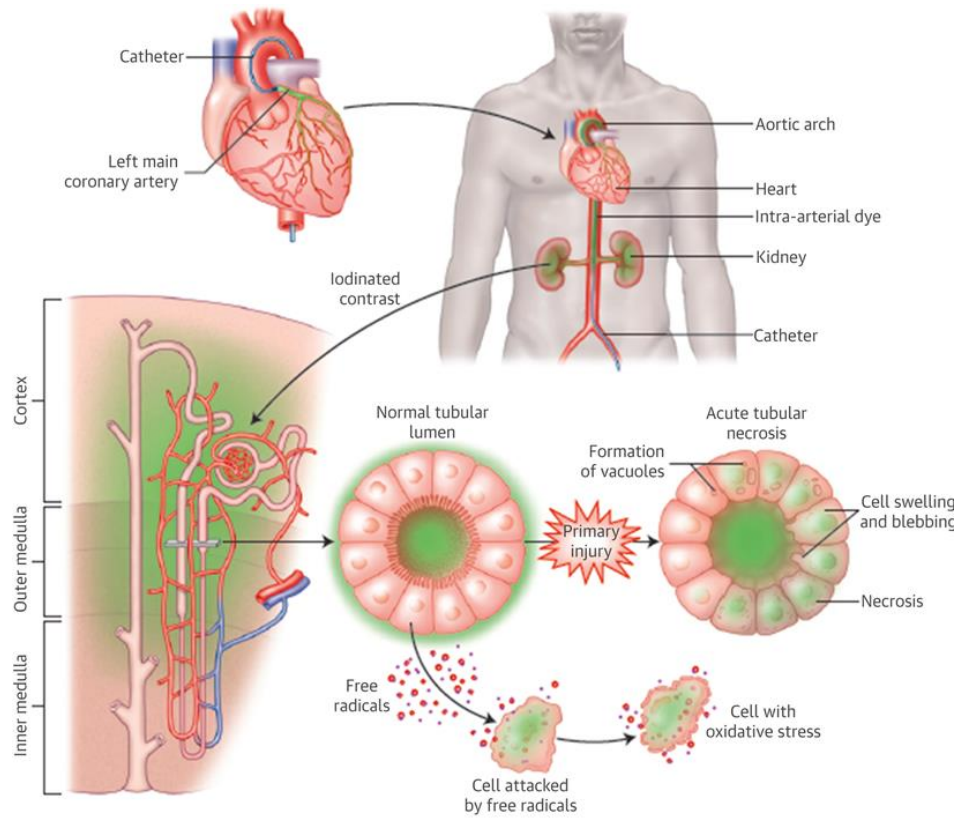


Figure 1.1.4. Contrast agents may cause damage to kidney [10].

Other imaging techniques which do not use contrast dyes, such as magnetic resonance imaging (MRI) are expensive and cannot be widely used in numerous small medical centers. In addition, MRI patient monitoring has limited use in medical facilities because of the need of patient motion correction which would correct errors in the spatial representation of the imaging when the patient moves or has changes in respiration during surgery [12]. The goal of this research is to develop a minimally invasive catheter tracking system to find the mapping catheter tip's position and orientation. This catheter tracking system will allow for application to a much broader patient base with arrhythmia, eliminating the risk of complications from contrast dyes used in existing imaging techniques. The fast update rate and compactness of the proposed tracking system will pave the way for implementation for other types of medical tracking applications.

## 1.2 Objective

For this thesis, a position tracking system is implemented to map the shape of the heart for catheter ablation (Figures 1.2.1 and 1.2.2). An accurate, precise tracking system is necessary to

correctly locate the position of the catheter in the heart. Such a positioning system is vital to tell the surgeon the location which emits abnormal heart rhythm.



Figure 1.2.1. Heart surgery.

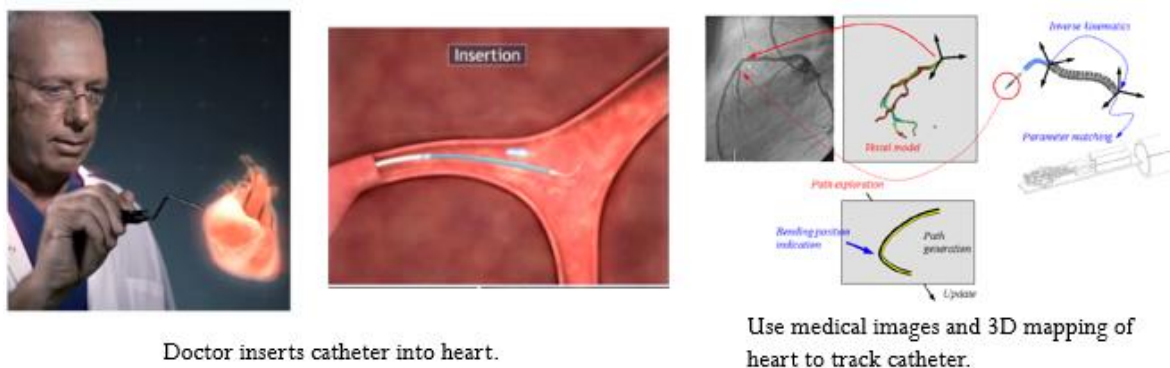


Figure 1.2.2. Catheter used in heart surgery.

For surgeries, there are multiple types of catheters for different applications and for different purposes. Thus, catheters come in different sizes. Table 1.2.1 shows the diameters of catheters in French units. Figure 1.2.3 illustrates the diameters of heart arteries and veins. In general, catheters for heart surgery are under 8 French in order to fit into the smallest arteries and veins.

Table 1.2.1. French catheter scale [13].

French gauge	Circumference (mm)	Outer diameter	
		(mm)	(inches)
3	3.14	1	0.039
4	4.19	1.333	0.053
5	5.24	1.667	0.066
6	6.28	2	0.079
7	7.33	2.333	0.092
8	8.38	2.667	0.105
9	9.42	3	0.118
10	10.47	3.333	0.131
11	11.52	3.667	0.144
12	12.57	4	0.158
13	13.61	4.333	0.170
14	14.66	4.667	0.184
15	15.71	5	0.197
16	16.76	5.333	0.210
17	17.81	5.667	0.223
18	18.85	6	0.236
19	19.90	6.333	0.249
20	20.94	6.667	0.263
22	23.04	7.333	0.288
24	25.13	8	0.315
26	27.23	8.667	0.341
28	29.32	9.333	0.367
30	31.42	10	0.393
32	33.51	10.667	0.419
34	35.60	11.333	0.445

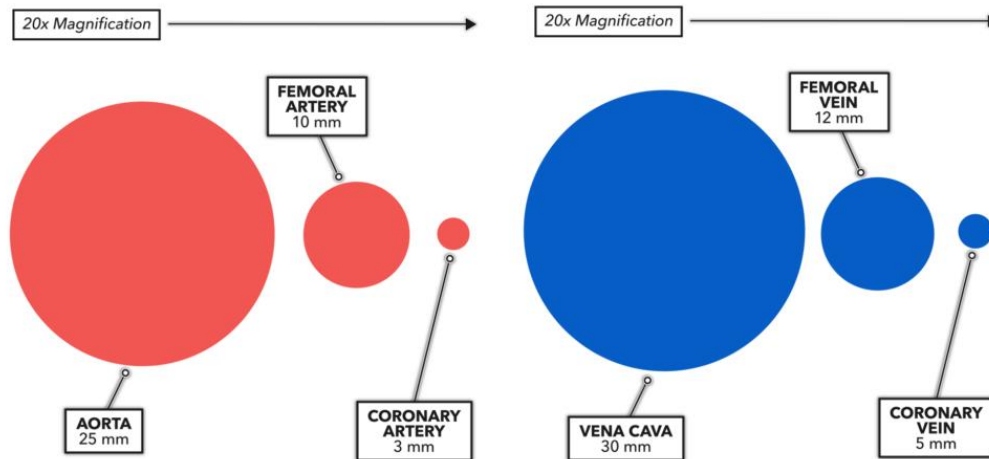


Figure 1.2.3. Diameters of heart arteries and veins [14].

Catheter-based surgeries use multiple catheters. As stated earlier, RF ablation is applied to the area which emits wrong heart signal. The surgeon needs information on the location of the wrong heartbeat signal relative to the RF ablation catheter. This is done through heart shape mapping using diagnostic cardiac catheterization. Diagnostic cardiac catheterization is the process of introducing, under local anesthesia, diagnostic catheter(s) (7 French in diameter) into veins and/or arteries in the neck, leg, or arm, from which they are advanced to the right and/or left sides of the heart [15]. Once the diagnostic catheters are inside the heart chambers, blood samples and blood pressure can be taken. This is done through the EKG platinum band sensors placed around the catheter tip, which helps the doctor determine the location of wrong heartbeat signal, as depicted in Figure 1.2.4.



Figure 1.2.4. Diagnostic mapping catheter tip with platinum band EKG sensors [16].

Normally, for imaging-based techniques such as X-ray mentioned earlier, contrast fluid dye is injected through a process called angiography to track the location of the diagnostic catheter (Figure 1.2.5).

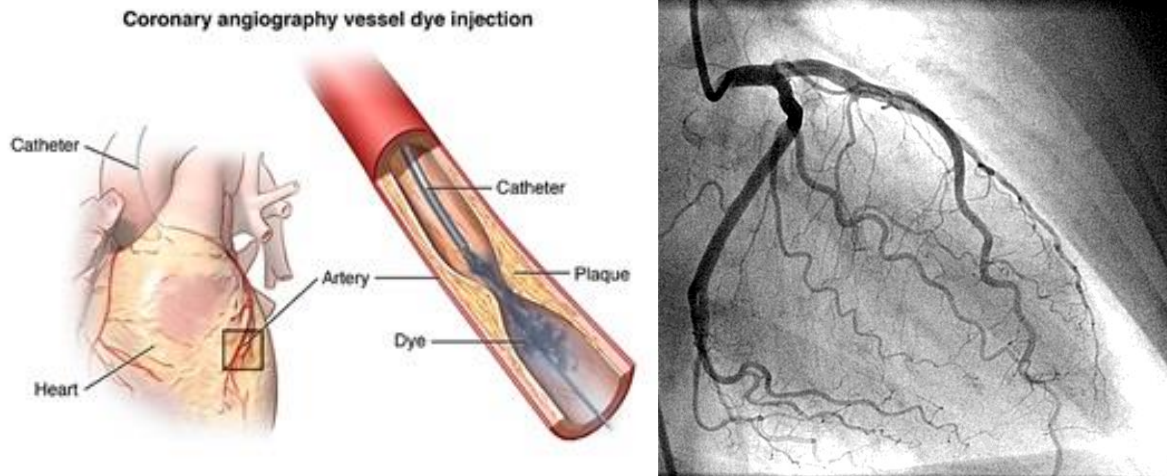


Figure 1.2.5. Angiography for heart mapping [17]–[19].

Due to the complications caused by angiography, there is a need for an alternative tracking system. For the proposed electromagnetic (EM) tracking system, an electromagnetic coil will be attached to the tip of the 7 French diagnostic catheter, and this coil's position will be tracked relative to reference EM coils placed in reference locations.

### 1.3 Magnetic Positioning System

EM tracking is based on determining the position and orientation of an object by measuring magnetic field strength at a certain location [20]. Magnetic positioning is prevalent among most modern medical tracking systems because it brings many benefits including no line of sight and high accuracy.

Magnetic tracking can be separated into DC and AC based magnetics. DC magnetics is unsuitable for position tracking because it is vulnerable to distortion caused by ferromagnetic materials [21]. However, it is popular for catheter-based navigation and steering where magnetic deflection is used to control the catheter's movement inside a human body. For our application, we focus on the tracking aspect and use AC-based tracking as it is more immune to ferrite-based metals.

For this research, an experimental setup is constructed to investigate the feasibility of AC magnetic positioning of a coil on a diagnostic catheter tip to be used as planned. The positioning

system is designed to offer precise and quick tracking of the catheter tip, so that the surgeon can observe its position and orientation. Through the experiment, we demonstrate the viability of the proposed system in terms of its accuracy, precision, and speed. Because arteries and veins in the heart are very small, primary challenges include designing a small coil to fit on the diagnostic catheter of 7 French. In addition, the small vessels mean that the accuracy of the tracking system should be at millimeter-level precision and with a refresh rate of 200 Hz.

## **2. LITERATURE REVIEW**

### **2.1 Tracking Systems**

There are a wide variety of tracking systems for different applications, such as vehicle GPS tracking [22] and personal indoor area tracking with radiofrequency, infra-red, and ultra-sound sensors [23]–[25]. However, these systems are unsuitable for tracking applications in biomedicine because of insufficient parameters such as precision, accuracy, and line of sight requirement. For biomedicine applications, such as computer assisted surgery (CAS), the positioning error should be in the millimeter range [26]. Optical and electromagnetic tracking systems are the two main types of tracking systems integrated into commercially-available computer assisted surgery so far [27] because of their high precision. For the proposed catheter tracking system in heart surgery, an optical tracking system is infeasible due to the need of a direct line of sight between optical markers and camera sensors, and such line of sight is not possible when one has to be placed inside the body and the other outside the body. Thus, this study focuses on electromagnetic tracking with applications in biomedicine for CAS [28].

### **2.2 Electromagnetic Positioning System Models**

#### **2.2.1 Medical Applications**

As discussed in the introduction, RF ablation involves one medical catheter with RF electrodes on the tip and other diagnostic catheters to be inserted into the patient's body. The diagnostic catheter's platinum EKG sensors, which help identify the location of the irregular heartbeat, are on the tip of the catheter shaft. During the ablation surgery, knowledge of the position and orientation of the catheter tip is essential for correctly applying RF ablation.

Before selecting a specific EM tracking system for our application of RF ablation, we review existing systems described in the literature. In general, magnetic tracking for medical applications has been a growing area of research, with publications increasing from 10 per year in the 1990s to over 50 per year past 2012, with over 24 different commercially available EM tracking systems on the market [28], [29]. A comprehensive review of electromagnetic tracking in medicine has been provided in [28]. A review of patents can be found in [30]. Typically, tracking devices



are composed of magnetic field sources, magnetic field detectors, control electronics, and signal processing unit (computer) which executes algorithms capable to calculate the position and orientation of the magnetic marker. There are generally two types of systems [30]: (1) the magnetic field, produced by a set of coils driven by currents and positioned externally to the patient, is measured by sensors installed on an intra-body probe (e.g., the Aurora system), see Figure 2.2.1 (left); and (2) the magnetic field, produced by a transmitter installed on an intra-body probe, is measured by magnetic field sensors positioned outside the patient body. The latter also covers passive transponder system (e.g., Calypso system), see Figure 2.2.1 (right) [28].

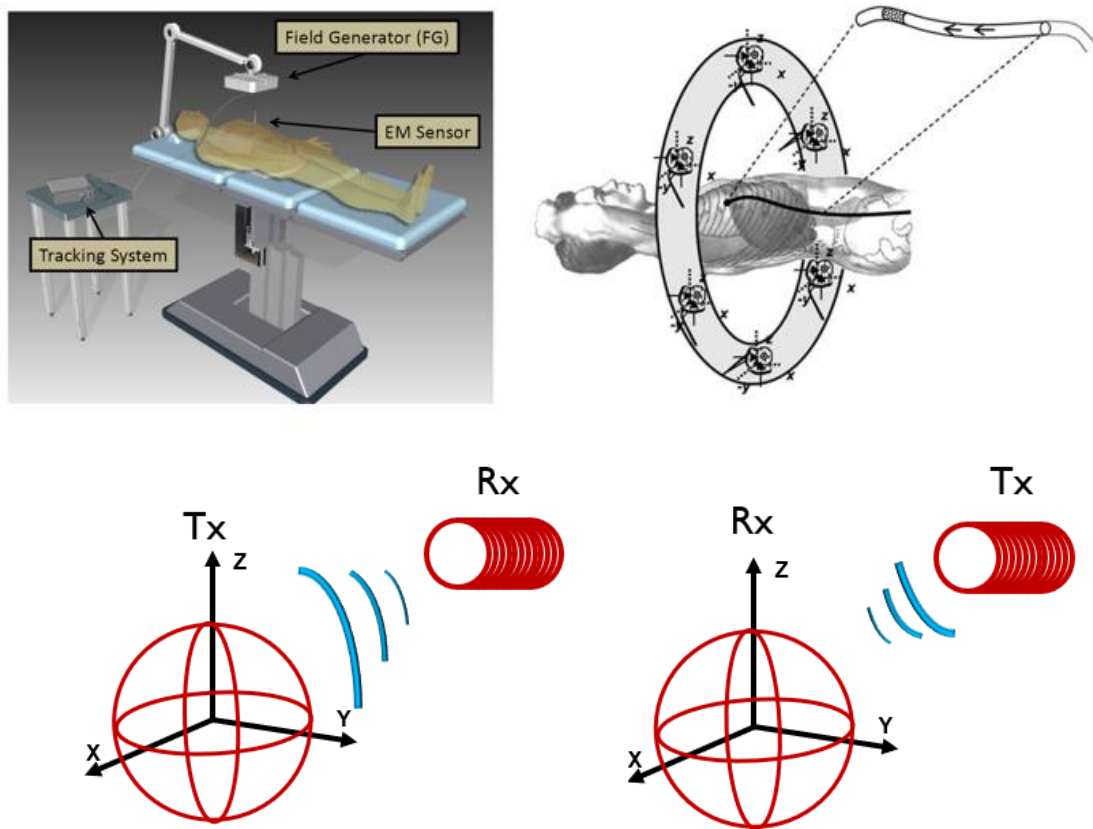


Figure 2.2.1. Two types of medical tracking systems: tracking receiver (Rx) inside a patient (left) and tracking transmitter (Tx) inside a patient (right).

The first type system is to track a tiny millimeter-sized magnetic sensor. Several tracking systems based on this concept have been developed for the medical industry for catheter ablation and other surgical procedures, which require millimeter-level accuracy and precision [31]–[34].

For instance, the NDI Aurora, Ascension [31], and Polhemus tracking systems use a planar field generator placed in a reference location. The generator consists of multiple coils that are sequentially activated, and a tiny single sensing coil is placed on the object being tracked (Figure 2.2.2).

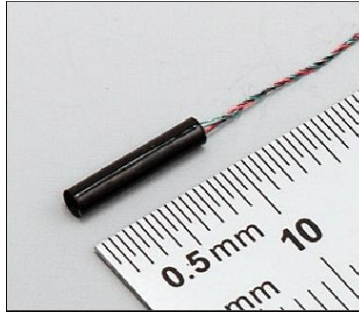


Figure 2.2.2. NDI Aurora sensing coils.

In such sensing systems, only 1-D information can be obtained, hence it is necessary to have multiple transmitters to identify the receiver position and orientation [32]. Systems, such as [33], have transmitting coils sequentially activated, which means that a longer time is required for the iterative position calculations, prohibiting real-time tracking with high update rate ( $> 50$  Hz). Furthermore, because these methods employ a large number of transmitting coils, the systems are typically bulky and difficult to use in a clinical environment. Systems used commercially, developed by NDI and Ascension, have been tested by researchers independently by Wilson et al. [35] and Yaniv et al. [36]. Through these tests, it has been found that although these systems have high accuracy and precision for CAS systems, they suffer from poor update rates (40 Hz). Other faster methods to separate the transmitter coils, such as frequency division multiplexing (FDM) reported in [34], suffer from frequency mixing which would be measured by the sensing coil. Demodulation techniques and correction techniques proposed by [34] attempting to fix these limitations may cause inaccurate measurements of magnetic-field magnitude, and in turn inaccurate position estimates. These fixes also slow down the system refresh rate. A study comparing the system update rates of FDM method and the time division multiplexing (TDM) method finds that FDM is only six times faster [37]. Systems such as the one described in [38] use multi-sensor fusion through inertial measurement units (IMUs) consisting of gyroscope, magnetometer, and accelerometer in order to overcome the need of multiple transmitting coils.

However, such systems have been shown to only fit on catheters which are of 18 French (6 mm) or larger (for large organ tracking) and thus cannot be used for a 7 French heart ablation catheter.

Another design somewhat related to the above method is a magnetic navigation system (MNS), a device that generates an external magnetic field to manipulate objects made of magnetic materials. Under the magnetic field, these objects experience magnetic torque and force, which enable them to move and perform various tasks. However, these devices are bulky and complex, and their focus is on navigation rather than positioning [39]–[41].

In summary, there are several limitations of the architecture of the first type of system which has been widely examined. In contrast, the second type of system has not been investigated fully, which is the focus of our analysis.

The second type system is to track an electromagnetic transmitter. This is achieved by placing a circular magnetic transmitter coil on the catheter tip. The diameter of the coil is smaller than that of the catheter shaft in order for the outer diameter of the coil housing to fit. The coil is powered by an external transmitter driver, which is connected to the coil using a thin twisted pair wire, twisted around the catheter shaft. This coil generates an AC magnetic field, which is measured by reference sensor coils placed in fixed positions, such as under the operating table that the patient lies on, or on the sidewalls close to the operating table. These sensor coils convert the magnetic field into voltage based on the sensitivity of the sensor. The position and orientation of the transmitter coil can then be calculated based on the measured magnetic field using an iterative algorithm.

This second type of system overcomes the main drawbacks of the above first type of EM tracking system (i.e., tracking receiver) by having one transmitter. It means that the system's speed is limited by the measuring/sampling rate of the receiver coil, which can operate much faster than TDM/FDM based transmitter separation. In addition, triaxial sensing coils can be used to enable a simple and low-cost system. We are unaware of any existing system using this type of architecture. Most commercially available systems use the type one model, and few systems which use the type two model such as Calypso require optical along with magnetic tracking to function; the tracking coil is passive, not an active transmitter coil. McGary [42] described a type two design involving the implementation of superconducting quantum interference device (SQUID) magnetometers to measure a transmitting field. He has shown through simulations the potential high accuracy and precision of such a system, but such a system has not been realized in the industry. The proposed

tracking system will implement a type two system design with high precision and update rate, while maintaining a small form factor and low cost through the use of triaxial sensing coils.

### 2.2.2 Dipole Based Model

To determine the position of the transmitter and receiver coils relative to one another, the equation relating magnetic field to a distance vector is solved. Magnetic field equations are highly nonlinear, and exact magnetic field equations for circular coils, taking geometry, skin effect, core permeability, and other nonidealities, have added complexity. For this system, transmitting and receiving coils are approximated by magnetic dipoles in free space. This approximation is valid when the distance between transmitter and receiver is large compared to the size of the coil, and in this system the range of tracking is between 10 and 50 cm with the coil size being 1.5 mm in diameter.

Magnetic tracking systems generally operate in the frequency range of 30–300 kHz because their wavelengths range from 10 to 1 km [43]. For this system, the target operating frequency is 32 kHz, which has a wavelength of 9.37 km. This means that the phase variation of the magnetic field over the covering area of the magnetic tracking system is small. In addition, at 32 kHz, the human body can be considered transparent to the emitted magnetic field, implying that there is minimal absorption of EM radiation by the patient [44]–[46].

The magnetic vector potential is defined as follows:

$$\mathbf{A}(\mathbf{r}) = \frac{\mu_0}{4\pi} \left( \frac{\mathbf{M} \times \mathbf{r}}{r^3} \right) \quad (2.2.2.1)$$

where  $\mu_0$  is the permeability of free space,  $\mathbf{M}$  the dipole moment vector of the transmitting coil, and  $\mathbf{r}$  the vector of length  $r$  from the position of transmitter (Tx) to the receiver (Rx). The magnetic flux density is:

$$\mathbf{B} = \nabla \times \mathbf{A}(\mathbf{r}) \quad (2.2.2.2)$$

$$\mathbf{B} = \frac{\mu_0}{4\pi} \left( \frac{3(\mathbf{M} \cdot \mathbf{r})\mathbf{r}}{r^5} - \frac{\mathbf{M}}{r^3} \right) \quad (2.2.2.3)$$

If a receiver coil is placed in the transmitter magnetic field, a voltage  $V$  will be induced in the coil Rx. According to Faraday's law, this can be expressed as:

$$V = -j\omega\alpha_{rec}\mathbf{m} \cdot \mathbf{B} \quad (2.2.2.4)$$

where  $\omega$  is the angular frequency,  $\alpha$  the number of turns times the area of the Rx, and  $\mathbf{m}$  the dipole moment vector of the Rx.

$$V = -j\omega\alpha_{rec}\alpha_{trans}I_{trans}\left[\frac{\mu_0}{4\pi}\left(\frac{3(\mathbf{M}\cdot\mathbf{r})(\mathbf{m}\cdot\mathbf{r})}{r^5} - \frac{\mathbf{M}\cdot\mathbf{m}}{r^3}\right)\right] \quad (2.2.2.5)$$

where  $I_{trans}$  is the amplitude of the current in Tx.

### 2.2.3 Tracking the Transmitter

The type two system [30] is implemented using the near field magnetic flux density ( $\mathbf{B}$ ) equation (2.2.2.3). Specifically, the magnetic field generated by a transmitting coil can be approximated by the dipole field equation:

$$\mathbf{B} = \frac{\mu_0}{4\pi}\left(\frac{3(\mathbf{m}\cdot\mathbf{r})\mathbf{r}}{r^5} - \frac{\mathbf{m}}{r^3}\right) \quad (2.2.3.1)$$

where  $\mu_0$  is the permeability of free space,  $\mathbf{m}$  the dipole moment vector of the transmitting coil, and  $\mathbf{r}$  the vector of length  $r$  from the position of transmitter (Tx) to the receiving coil (Rx) at the position  $\mathbf{r}^{rec}$  (shown below in Figure 2.2.3).

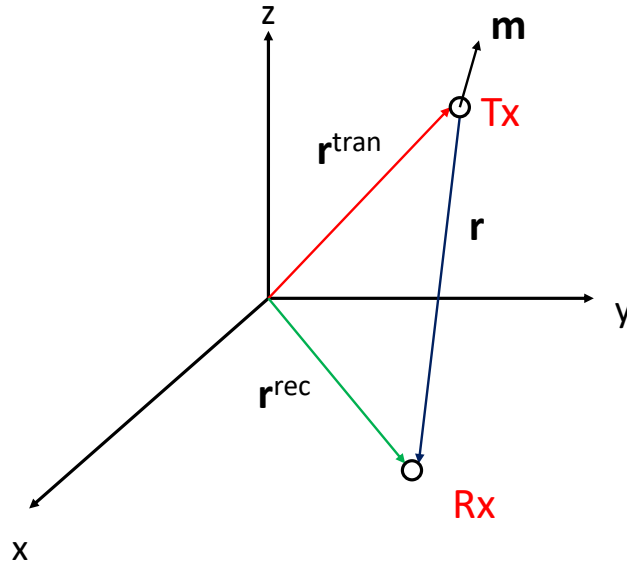


Figure 2.2.3. Tracking the transmitter (fixed receiver).

McGary [42] presented a procedure to solve the position and orientation of the transmitter, which is detailed in Section 3.4. Essentially, the procedure involves the isolation of  $\mathbf{m}$  in (2.2.3.1):

$$\mathbf{m} = \frac{4\pi r^3}{\mu_0} \left( \frac{3\mathbf{r}\mathbf{r}^T}{2\mathbf{r}^T\mathbf{r}} - \mathbf{I} \right) \mathbf{B} \quad (2.2.3.2)$$

Suppose that there are two 3-coil receivers that measure  $\mathbf{B}_1$  and  $\mathbf{B}_2$  transmitted from the single transmitter with  $\mathbf{m}$ . Since the locations of the two receivers are known, and the distance vector between them is  $\mathbf{p}$ , the vector  $\mathbf{r}_1$  from the position of transmitter (Tx) to the first triaxial receiver (Rx<sub>1</sub>) can be calculated using (2.2.3.3):

$$F_1(\mathbf{r}_1) = r_1^3 \left( \frac{3\mathbf{r}_1\mathbf{r}_1^T}{2\mathbf{r}_1^T\mathbf{r}_1} - \mathbf{I} \right) \mathbf{B}_1 - \|\mathbf{p} + \mathbf{r}_1\|^3 \left( \frac{3(\mathbf{p} + \mathbf{r}_1)(\mathbf{p} + \mathbf{r}_1)^T}{2(\mathbf{p} + \mathbf{r}_1)^T(\mathbf{p} + \mathbf{r}_1)} - \mathbf{I} \right) \mathbf{B}_2 = \mathbf{0} \quad (2.2.3.3)$$

This is a system of three nonlinear equations with three unknowns  $\mathbf{r}_1 = (r_{1x}, r_{1y}, r_{1z})$ , which can be solved by Newton's method. Using the result of  $\mathbf{r}_1$ , the transmitter position  $\mathbf{r}^{tran} = (x, y, z)$  can be identified.

The accuracy and precision of such a system is often limited by unstable magnetic field caused by the fluctuation in Tx coil current. This affects both the  $\mathbf{B}$  and  $\mathbf{m}$ . However, the setup in (2.2.3.3) eliminates  $\mathbf{m}$ , and both  $\mathbf{B}_1$  and  $\mathbf{B}_2$  are affected by the same change in Tx coil current, so that the effects of current fluctuation are minimized.

## 2.2.4 Tracking the Receiver

Most published and existing systems use the type 1 system [30], also called active transmitter system [28]. Here, we summarize the model developed by Plotkin and Paperno [33] and explain its limitations compared to the type 2 system. The system requires multiple transmitters to identify the position and orientation of the Rx. The dipole field model of transmitting coil  $i$  is:

$$\mathbf{B}_i^t = \frac{\mu_0}{4\pi} \left( \frac{3(\mathbf{M} \cdot \mathbf{r}_i)\mathbf{r}_i}{r_i^5} - \frac{\mathbf{M}}{r_i^3} \right) \quad (2.2.4.1)$$

where  $\mathbf{M}$  is the dipole moment vector of the transmitting coil, and  $\mathbf{r}_i$  is the vector from the transmitting coil  $i$  (Tx) to the receiving coil (Rx) (Figure 2.2.4).

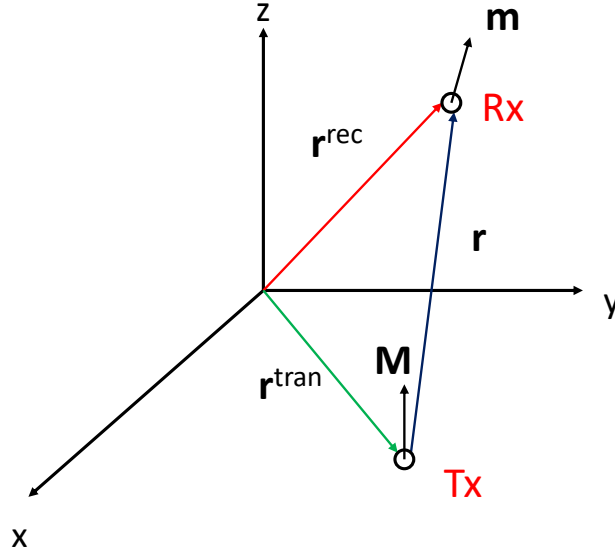


Figure 2.2.4. Tracking the receiver (fixed transmitter).

The field seen by the receiving coil is:

$$B_i^{rec} = \mathbf{B}_i^t \cdot \mathbf{m} \quad (2.2.4.2)$$

where  $\mathbf{m}$  is the dipole moment vector of the receiving coil. In this model, the transmitter is pointed in the  $z$ -direction:

$$\mathbf{M} = (0, 0, M) \quad (2.2.4.3)$$

The orientation of the receiver is:

$$\mathbf{n} = \frac{\mathbf{m}}{m} = (n_x, n_y, n_z) \quad (2.2.4.4)$$

Substituting (2.2.4.1), (2.2.4.3), and (2.2.4.4) into (2.2.4.2), we obtain:

$$B_i^{rec} = \frac{\mu_0}{4\pi} m M \frac{1}{r_i^5} [3z(\mathbf{r}_i \cdot \mathbf{n}) - n_z r_i^2] \quad (2.2.4.5)$$

The above equation can be rewritten as:

$$B_i^{rec} - \frac{\mu_0}{4\pi} m M \frac{1}{r_i^5} [3z(\mathbf{r}_i \cdot \mathbf{n}) - n_z r_i^2] = 0 \quad (2.2.4.6)$$

The LHS is the error between field strength measured by the receiving coil and the field seen by the receiver at position  $\mathbf{r}_i$  and orientation  $\mathbf{n}$ .

From Figure 2.2.4, we have:

$$\mathbf{r}_i = \mathbf{r}^{rec} - \mathbf{r}_i^{tran} = \begin{bmatrix} r_x^{rec} \\ r_y^{rec} \\ r_z^{rec} \end{bmatrix} - \begin{bmatrix} r_{ix}^{tran} \\ r_{iy}^{tran} \\ 0 \end{bmatrix} \quad (2.2.4.7)$$

where the transmitter location  $\mathbf{r}_i^{tran}$  is known.

Substituting (2.2.4.7) into (2.2.4.6), rewriting it as  $F_i(\mathbf{r}^{rec}, \mathbf{n}) = 0$ , and assuming that there are  $k$  transmitters, we have a system of  $k$  nonlinear equations:

$$\begin{aligned} F_1(\mathbf{r}^{rec}, \mathbf{n}) &= 0 \\ &\vdots \\ F_i(\mathbf{r}^{rec}, \mathbf{n}) &= 0 \\ &\vdots \\ F_k(\mathbf{r}^{rec}, \mathbf{n}) &= 0 \end{aligned} \quad (2.2.4.8)$$

There are six unknowns: receiver position  $\mathbf{r}^{rec} = (x, y, z)$  and its orientation  $\mathbf{n} = (n_x, n_y, n_z)$ . Thus, it is necessary that  $k \geq 6$ . The system of equations (2.2.4.8) can be solved as a nonlinear least square minimization problem:

$$\min \Phi = \sum_{i=1}^k F_i(\hat{\mathbf{r}}^{rec}, \hat{\mathbf{n}})^2 \quad (2.2.4.9)$$

We estimate  $\hat{\mathbf{r}}^{rec}$  and  $\hat{\mathbf{n}}$  by minimizing the sum of squared errors of  $k$  transmitters using the observed data  $(B_1^{rec}, \dots, B_i^{rec}, \dots, B_k^{rec})$ . The problem can be solved by the Levenberg-Marquardt method. One of the drawbacks of the type 1 architecture is that the transmitter magnetic moment  $M$  cannot be isolated for equation (2.2.4.9) as in (2.2.3.3). As a result, the system is more sensitive with respect to power fluctuations due to the relationship among  $B_i^{rec}$ ,  $m$ , and  $M$  in (2.2.4.6). Thus, in the type 1 system, the power fluctuations of each transmitter must be carefully considered.

In summary, the two types of systems work as follows. In [42], two triaxial receivers (Rx<sub>1</sub> and Rx<sub>2</sub>) track a single transmitter (Tx)'s position. Using the B-field equation to isolate the magnetic moment vector of the Tx ( $\mathbf{m}$ ), vector  $\mathbf{r}$  is calculated (using iterative algorithm described below) by equating  $\mathbf{m}$  seen by Rx<sub>1</sub> and Rx<sub>2</sub> (i.e., the measured  $\mathbf{B}_1$  and  $\mathbf{B}_2$ ). The  $(x, y, z)$  position can then be solved using  $R$  and the Rx positions.

In [33],  $n$  uniaxial transmitters are arranged in an array in  $(x, y, z)$  frame to track a uniaxial receiver's position. The uniaxial receiver (Rx) gets only one measurement (current), and the specific vector component is unknown. Thus, multiple transmitters must be used to identify the position and orientation of the Rx. The B-fields from the  $n$  transmitters are measured by the Rx, and its position  $(x, y, z)$  and orientation  $(m_x, m_y, m_z)$  (magnetic moment vector) are solved by an iterative algorithm.

The general idea for tracking the receiver is illustrated in Figure 2.2.5.



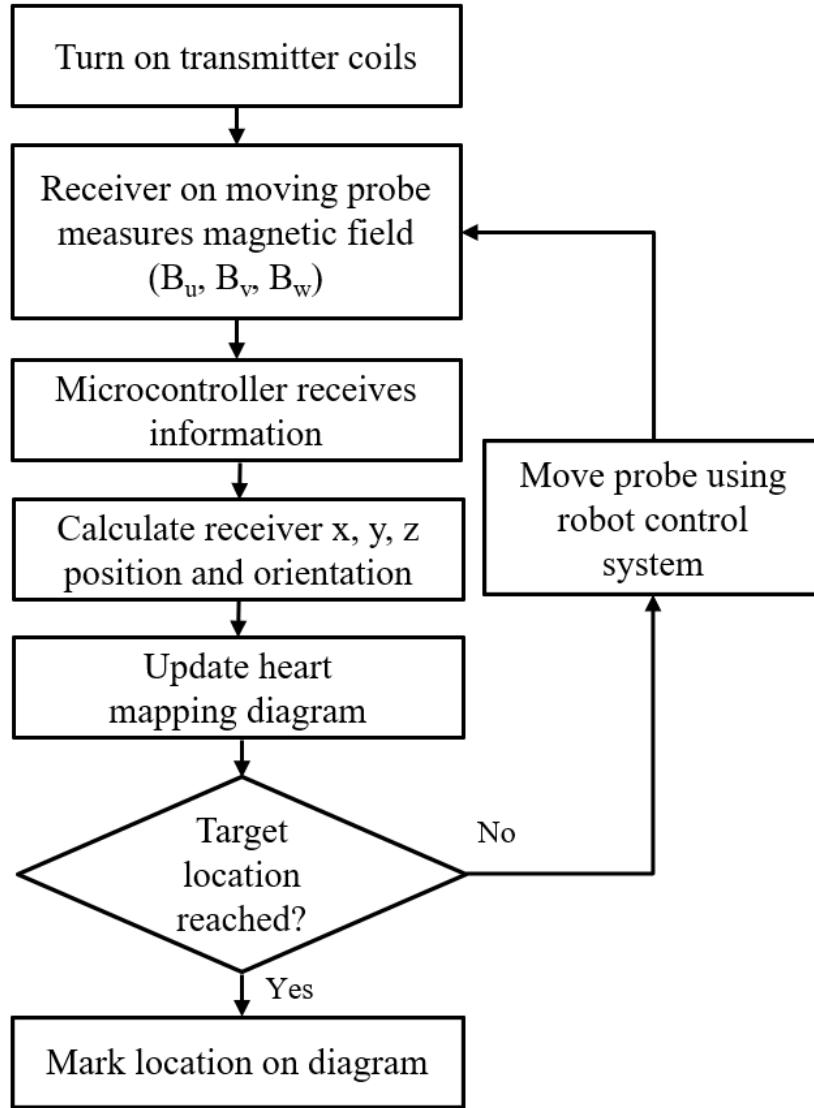


Figure 2.2.5. Type 1 tracking receiver system overview.

## 2.3 Optimization Methods for Position Calculation

### 2.3.1 Optimization Methods

Position calculation often involves solving roots for a system of equations [42] or nonlinear least square minimization [33]. Methods summarized in this section are detailed in [47]. The basic idea is as follows. Suppose that we have a function  $f$  of a single variable  $x$ , the minimization of  $f$  can also be viewed as a way to drive the first derivative of  $f$  to zero, that is  $g(x) = f'(x) = 0$ , which is to solve the roots for  $g(x)$ . For example, in (2.2.3.3), an optimization algorithm is used to minimize the error between the magnetic moments seen by the two triaxial receivers. In (2.2.4.9)

an optimization algorithm is used to minimize the errors between the B-fields measured by the receiver and the B-fields calculated from the dipole equation across multiple transmitters.

### ***Newton's Method***

For a function

$$f: \mathbb{R}^n \rightarrow \mathbb{R} \quad (2.3.1.1)$$

The gradient of  $f$  is:

$$\nabla f(\mathbf{x}) = \begin{bmatrix} \frac{\partial f}{\partial x_1} \\ \vdots \\ \frac{\partial f}{\partial x_n} \end{bmatrix} \quad (2.3.1.2)$$

and the Hessian matrix of  $f$  is:

$$\mathbf{F}(\mathbf{x}) = \begin{bmatrix} \frac{\partial^2 f}{\partial x_1^2} & \frac{\partial^2 f}{\partial x_2 \partial x_1} & \cdots & \frac{\partial^2 f}{\partial x_n \partial x_1} \\ \frac{\partial^2 f}{\partial x_1 \partial x_2} & \frac{\partial^2 f}{\partial x_2^2} & \cdots & \frac{\partial^2 f}{\partial x_n \partial x_2} \\ \vdots & \vdots & \ddots & \vdots \\ \frac{\partial^2 f}{\partial x_1 \partial x_n} & \frac{\partial^2 f}{\partial x_2 \partial x_n} & \cdots & \frac{\partial^2 f}{\partial x_n^2} \end{bmatrix} \quad (2.3.1.3)$$

Define:

$$\mathbf{g}^{(k)} = \nabla f(\mathbf{x}^{(k)}) \quad (2.3.1.4)$$

The method of steepest descent is given by the recursive formula below:

$$\mathbf{x}^{(k+1)} = \mathbf{x}^{(k)} - \alpha_k \nabla f(\mathbf{x}^{(k)}) \quad (2.3.1.5)$$

where  $\alpha_k$  is a positive scalar called the step size, and

$$\alpha_k = \arg \min_{\alpha \geq 0} f(\mathbf{x}^{(k)} - \alpha \nabla f(\mathbf{x}^{(k)})). \quad (2.3.1.6)$$

The steepest descent algorithm proceeds as follows: at each step  $k$ , starting from the point  $\mathbf{x}^{(k)}$  we conduct a line search in the direction  $-\nabla f(\mathbf{x}^{(k)})$  until a minimizer,  $\mathbf{x}^{(k+1)}$ , is found.

The Newton's method requires computation of inverse of the Hessian matrix:

$$\mathbf{x}^{(k+1)} = \mathbf{x}^{(k)} - \mathbf{F}(\mathbf{x}^{(k)})^{-1} \mathbf{g}^k \quad (2.3.1.7)$$

Note that Newton's method can be used to solve the roots for:

$$\mathbf{g}(\mathbf{x}) = \mathbf{0} \quad (2.3.1.8)$$

### ***Levenberg-Marquardt Modification***

If the Hessian matrix  $\mathbf{F}(\mathbf{x}^{(k)})$  is not positive definite, then the search direction  $\mathbf{d}^{(k)} = -\mathbf{F}(\mathbf{x}^{(k)})^{-1}\mathbf{g}^k$  may not point in a descent direction. The Levenberg-Marquardt modification ensures that the search direction is a descent direction.

$$\mathbf{x}^{(k+1)} = \mathbf{x}^{(k)} - (\mathbf{F}(\mathbf{x}^{(k)}) + \mu_k \mathbf{I})^{-1}\mathbf{g}^k \quad (2.3.1.9)$$

where  $\mu_k \geq 0$ .

When  $\mu_k \rightarrow 0$ , (2.3.1.9) represents the Newton's method, and when  $\mu_k \rightarrow \infty$ , the algorithm approaches a pure gradient method with small step size.

### ***Nonlinear Least-Squares Problem***

A nonlinear least-squares problem has the form:

$$\min \sum_{i=1}^m (r_i(\mathbf{x}))^2 \quad (2.3.1.10)$$

where  $r_i: \mathbb{R}^n \rightarrow \mathbb{R}$ ,  $i = 1, \dots, m$ , are given functions. Define:

$$\mathbf{r} = [r_1, \dots, r_m]^T \quad (2.3.1.11)$$

$$f(\mathbf{x}) = \mathbf{r}(\mathbf{x})^T \mathbf{r}(\mathbf{x}) \quad (2.3.1.12)$$

Jacobian matrix of  $\mathbf{r}$  is:

$$\mathbf{J}(\mathbf{x}) = \begin{bmatrix} \frac{\partial r_1}{\partial x_1}(\mathbf{x}) & \cdots & \frac{\partial r_1}{\partial x_n}(\mathbf{x}) \\ \vdots & \ddots & \vdots \\ \frac{\partial r_m}{\partial x_1}(\mathbf{x}) & \cdots & \frac{\partial r_m}{\partial x_n}(\mathbf{x}) \end{bmatrix} \quad (2.3.1.13)$$

The gradient of  $f$  is:

$$\nabla f(\mathbf{x}) = 2\mathbf{J}(\mathbf{x})^T \mathbf{r}(\mathbf{x}) \quad (2.3.1.14)$$

The Hessian matrix of  $f$  is:

$$\mathbf{F}(\mathbf{x}) = 2\mathbf{J}(\mathbf{x})^T \mathbf{J}(\mathbf{x}) + \mathbf{S}(\mathbf{x}) \quad (2.3.1.15)$$

where  $\mathbf{S}(\mathbf{x})$  is the matrix with the  $(k, j)$ th component as:

$$r_i(\mathbf{x}) \frac{\partial^2 r_i}{\partial x_k \partial x_j}(\mathbf{x}) \quad (2.3.1.16)$$

Newton's method applied to the nonlinear least-squares problem is given by:

$$\mathbf{x}^{(k+1)} = \mathbf{x}^{(k)} - (\mathbf{J}(\mathbf{x})^T \mathbf{J}(\mathbf{x}) + \mathbf{S}(\mathbf{x}))^{-1} \mathbf{J}(\mathbf{x})^T \mathbf{r}(\mathbf{x}) \quad (12.3.1.7)$$

When ignoring the second derivatives ( $\mathbf{S}(\mathbf{x}) = 0$ ), we have the Gauss-Newton method:

$$\mathbf{x}^{(k+1)} = \mathbf{x}^{(k)} - (\mathbf{J}(\mathbf{x})^T \mathbf{J}(\mathbf{x}))^{-1} \mathbf{J}(\mathbf{x})^T \mathbf{r}(\mathbf{x}) \quad (2.3.1.18)$$

The recursive formula of Levenberg-Marquardt algorithm is:

$$\mathbf{x}^{(k+1)} = \mathbf{x}^{(k)} - (\mathbf{J}(\mathbf{x})^T \mathbf{J}(\mathbf{x}) + \mu_k \mathbf{I})^{-1} \mathbf{J}(\mathbf{x})^T \mathbf{r}(\mathbf{x}) \quad (2.3.1.19)$$

where  $\mu_k \mathbf{I}$  may be viewed as an approximation to  $\mathbf{S}(\mathbf{x})$  in Newton's method.

When  $\mu_k$  is zero, (2.3.1.19) becomes the Gauss-Newton method. As  $\mu_k$  tends to infinity, the search direction  $(\mathbf{x}^{(k+1)} - \mathbf{x}^{(k)})$  tends towards the steepest descent direction. The term  $\mu_k$  can be controlled to ensure descent even when second-order terms, which restrict the efficiency of the Gauss-Newton method, are encountered. Thus, the Levenberg-Marquardt method uses a search direction that is a cross between the Gauss-Newton direction and the steepest descent direction.

In summary, tracking position calculation involves solving roots of nonlinear functions using optimization methods. Typically, a nonlinear optimization method is implemented by an iterative algorithm as follows:

1. Start with the initial guess position  $\mathbf{x}^{(0)}$  for objective function  $f(\mathbf{x})$ .
2. Determine the direction and step length of search (*update*).
3. Update the initial guess to obtain a new position  $\mathbf{x}^{(1)}$ .

$$\mathbf{x}^{(1)} = \mathbf{x}^{(0)} + \text{update}$$

4. Repeat until the position is found (error minimized).

$$\mathbf{x}^{(k+1)} = \mathbf{x}^{(k)} + \text{update}$$

Graphically, the above algorithm is shown in Figures 2.3.1 and 2.3.2.

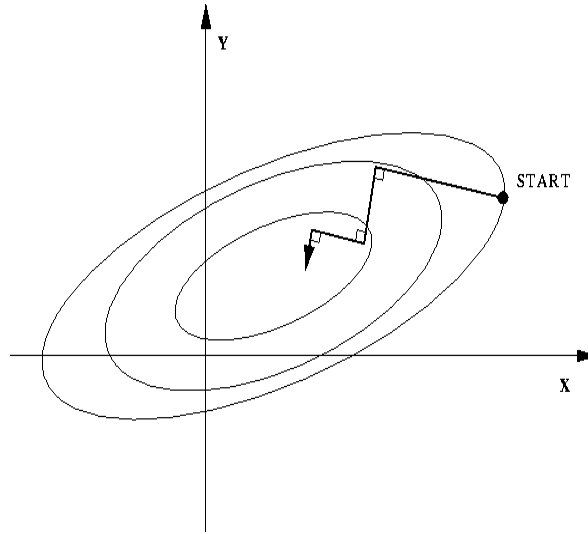


Figure 2.3.1. Search path to an optimal solution.

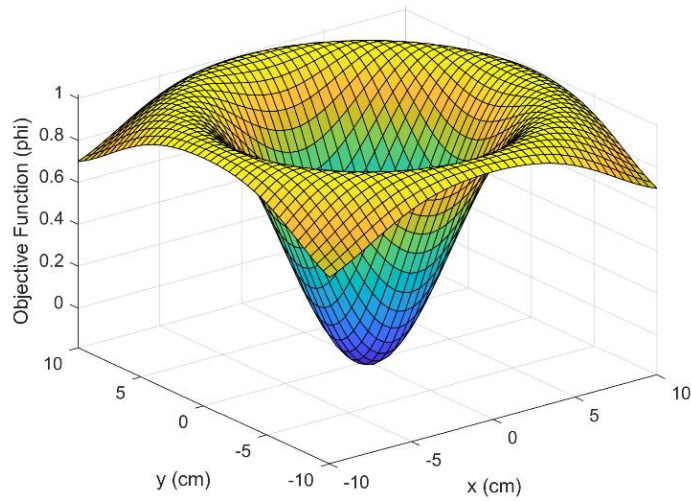


Figure 2.3.2. Objective function showing position errors, optimal position at  $(x, y) = (0\text{cm}, 0\text{cm})$ .

### 2.3.2 Other Optimization Methods

There are other optimization methods used in position calculations in electromagnetic tracking. For example, the Nelder-Mead simplex method is used to determine position and orientation  $(x, y, z, \theta, \phi)$  in a system for tongue tracking used in therapy for aphasia patients [48] (Figures 2.3.3–2.3.5).

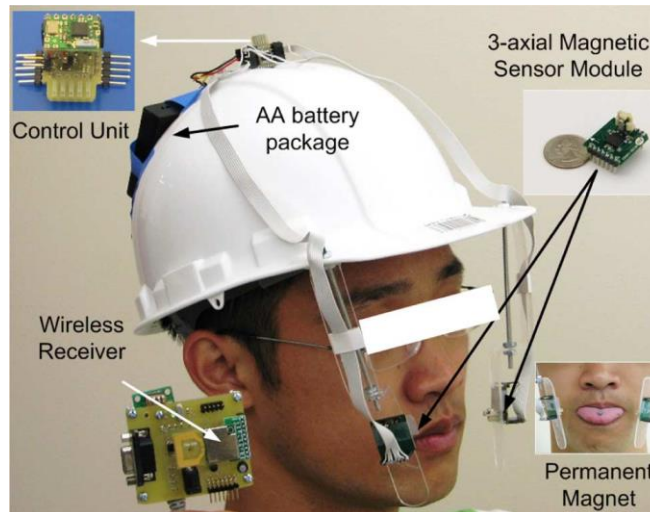


Figure 2.3.3. A system for tongue tracking.

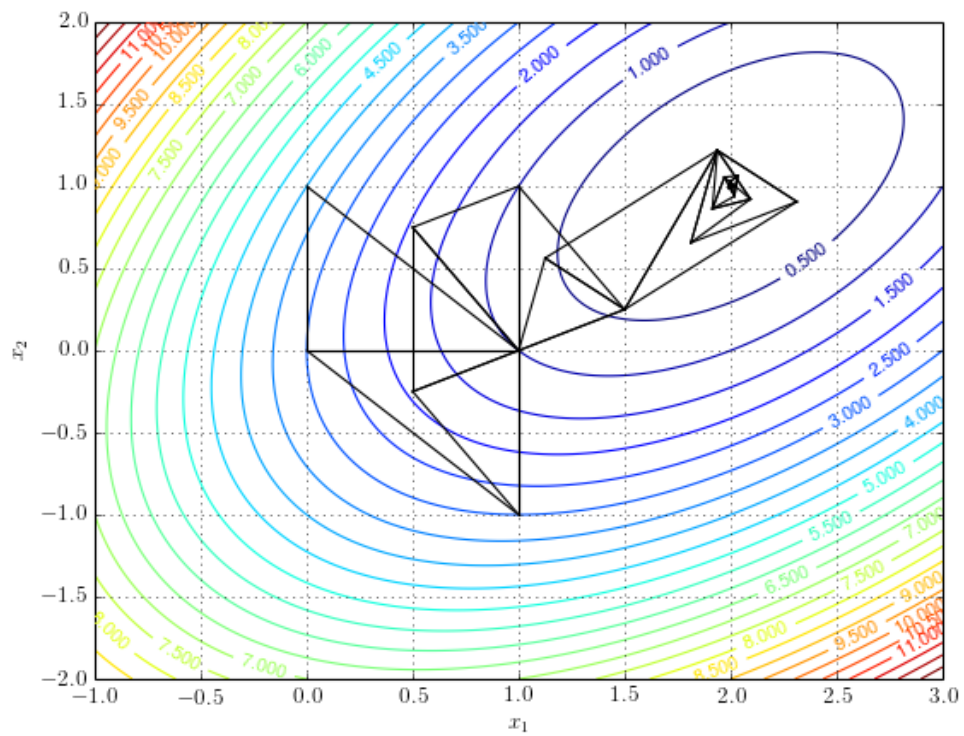


Figure 2.3.4. Simplex method to find optimal solution.

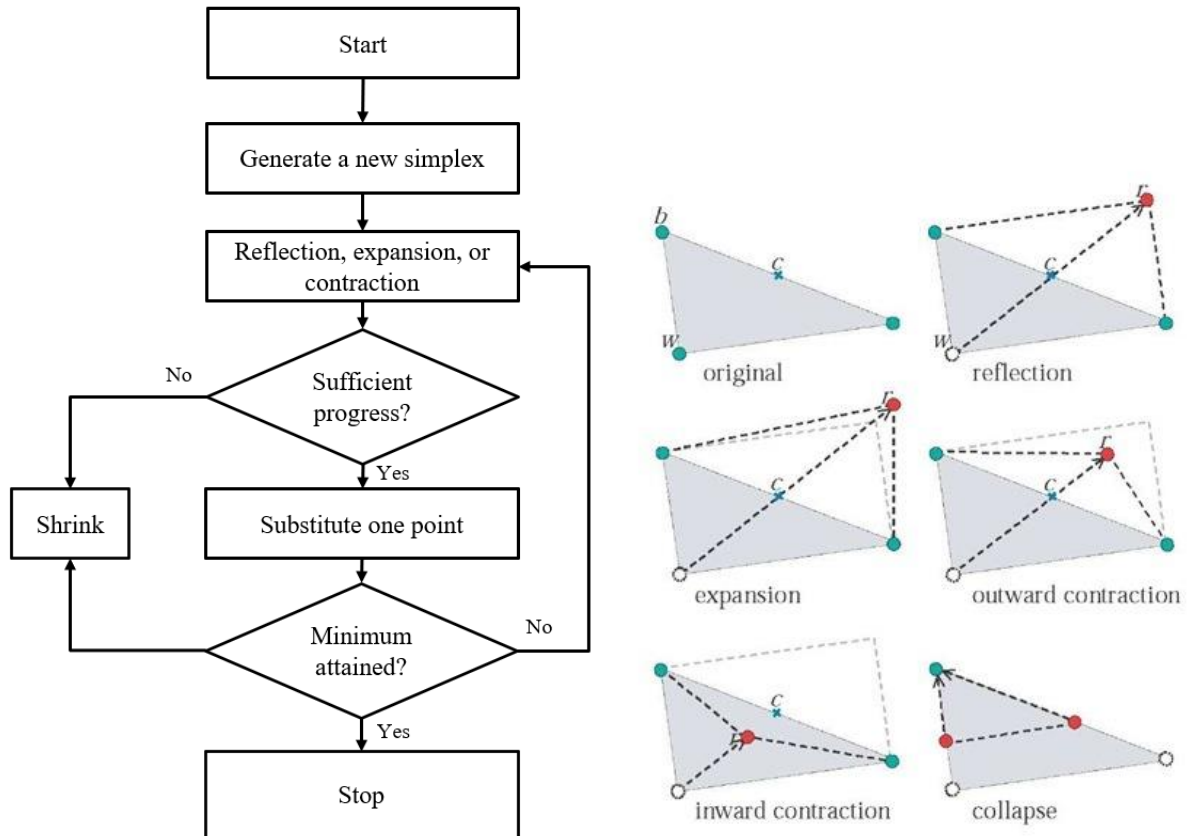


Figure 2.3.5. Algorithm for Nelder-Mead simplex method.

A global search algorithm is the particle swarm optimization [49]. It is a population-based optimization involving particles which move around in search space. The goal is to find the best particle using fitness function, to determine its position and velocity, to identify correct direction, and to minimize the objective function (Figure 2.3.6).

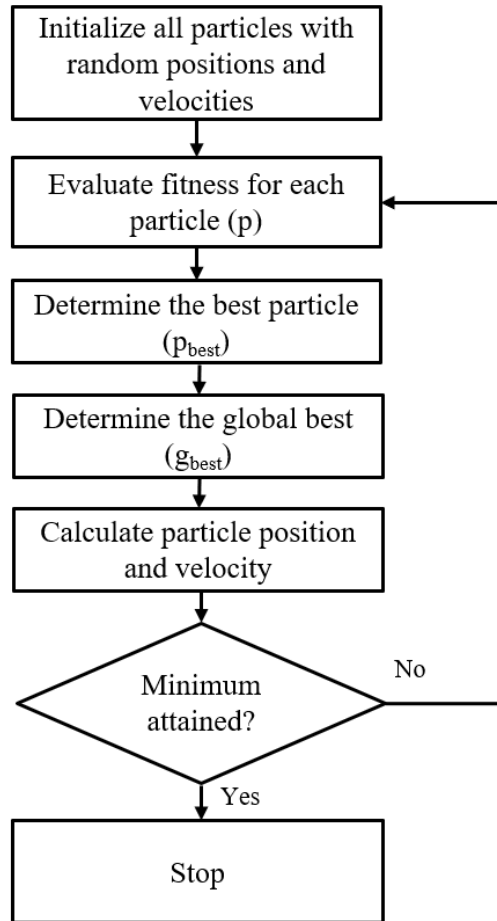


Figure 2.3.6. Algorithm for particle swarm optimization.

In summary, optimization techniques are essential to tracking systems. Position calculation involves solving roots for a system of equations [42] or nonlinear least square minimization [33]. Optimization methods are used to determine the optimal fixed sensor or transmitter locations [50]–[52], optimal coil size [53], optimal targeting volume [54], and optimal filter parameter estimations in tracking data processing [23], [55]–[57].

## 2.4 Electromagnetic Tracking Sensors

Extensive research has been done on tiny coils to be fitted on catheters of different shapes and sizes. Most involve sensing coils because most EM tracking systems adopt the type 1 system. An example of a tiny sensor is made by Ascension Technology Corporation [58] (Figure 2.4.1).





Figure 2.4.1. Ascension sensing coils.

These sensors measure magnetic field generated by planar field generators in the tracking area. Existing systems use either a five or six degrees of freedom (DOF) sensor (as small as 0.3 mm in diameter). In a 5DOF sensor, magnetic wire is wrapped around a ferromagnetic core which boosts the sensed magnetic field strength, due to the high magnetic permeability of the core. Examples of patented sensor designs are shown in Figure 2.4.2. In order to make sure that the sensors are durable, reinforcement can be made either by gluing wire onto solid core or by putting a plastic cover over the coil. The adhesive application needs to be precise. Nevertheless, these sensors often have limited durability. There is a weak point where the wire and the plastic meet, which can easily break. Generally, the design of the tiny coil used for a catheter tracking system requires careful consideration.

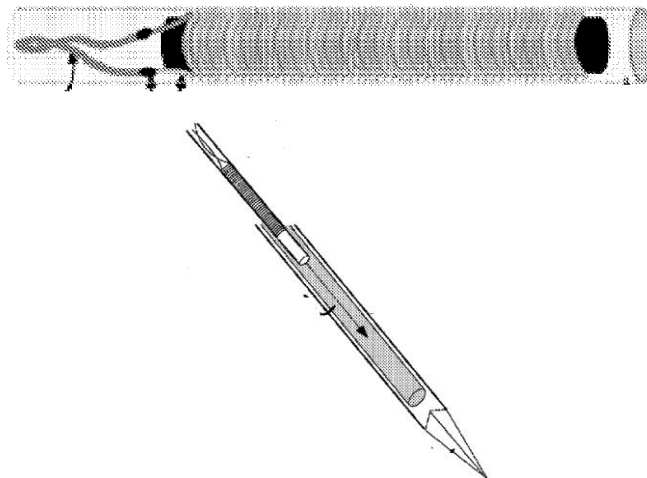


Figure 2.4.2. Magnetically tracked sensors [59], [60].

For 6DOF sensors, the complexity of coil design increases. Tracking 6DOF with a single coil is not possible because of the axial symmetry of the cylindrical coil, implying that the rotation angle of the coil on its own axis cannot be determined. Thus, most 6DOF sensors include two coils so that the two B-fields measured are not axially symmetric with each other. Figure 2.4.3 shows a patented design using two coils, which has been realized in NDI Aurora system where they offer both 5DOF and 6DOF sensors for their tracking systems.

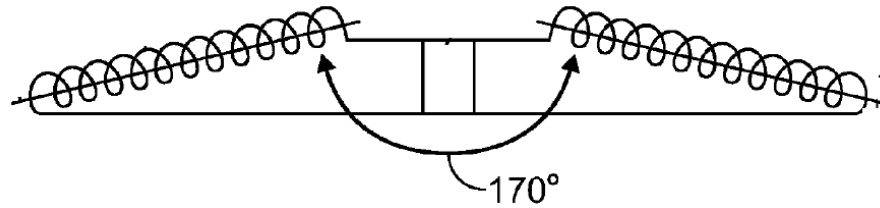


Figure 2.4.3. Magnetically tracked 6DOF sensors [58].

In the proposed heart mapping system, a 6DOF tracking sensor is not necessary because knowledge of orientation of the catheter itself around its own axis is not required. This is because the catheter tip's platinum EKG sensor is wrapped all the way around the catheter shaft. The EKG sensor reading is independent of the catheter's rotational angle about its axis.

### **3. TRACKING SYSTEM DESCRIPTION AND HARDWARE DESIGN**

#### **3.1 System Description**

Magnetic positioning involves setting up transmitters that transmit magnetic field and receivers that measure the transmitted magnetic field. The system can be set up so that either the receiver or the transmitter can be tracked as in the types 1 and 2 systems described in the previous chapter. For cardiac ablation, the object being tracked is a diagnostic mapping catheter. For this project, the type 2 system is implemented, where the transmitter coil fitted on the catheter is tracked to help determine the position of the moving probe, and the receiver coils are in the reference frame.

The proposed diagnostic catheter tracking system, consisting of one transmitter coil and two triaxial receiver coils, along with the relevant hardware, is illustrated in Figure 3.1.1. This chapter describes the development of the tracking system including design considerations for each component, hardware and software implementation, and testing.

As detailed below, the tracking system involves two triaxial sensor coils placed under a patient's bed. Although this configuration allows for a simple implementation of a type 2 system, the compensation of mutual coupling among the triaxial coils due to winding and geometric imperfections must be carefully considered. The transmitting coil attached to the catheter tip has a size constraint, and the coil's outer diameter cannot exceed the catheter shaft's diameter of 7 French so that it is small enough to fit into a human heart. This necessitates a custom coil designed for the size of the catheter. This transmitter coil is connected by a twisted-pair wire which connects to the system hardware.

The system hardware must be carefully designed to minimize the effects of noise and distortion. This is vital because of the weak magnetic field generated from the tiny transmitter coil as well as the need to control the heat generated from the coil. As described below, the transmitter driver design consists of an active feedback sensing system in the form of a phase locked loop (PLL) to reduce phase and sideband noise of the transmitting magnetic field.

A firmware implementation of the mathematical positioning algorithms and software calibration allows for a rapid real-time tracking system. This is in part due to the fast sampling rate of the microcontroller (2.4 MSPS) and fast post-processing (1.6 kHz) for the position calculation.

The magnetic field measurements are sampled using the microcontroller's onboard analog to digital converter (ADC). Finally, the data, which consist of position and orientation, are visually relayed to the surgeon on a computer screen.

Figure 3.1.1. Catheter tracking system illustration.

The following sections describe in detail the hardware design of the system. For the transmitter system design, the coil geometry and driver circuitry are optimized to maximize the B-field strength while minimizing the noise and distortion for catheter tracking. For the sensing system design, the sensitivity of the triaxial coil, along with the minimization of noise to maximize sensing signal to noise ratio (SNR) and to minimize position jitter, is considered.

### 3.2 Transmitter Analysis

### 3.2.1 Transmitter Magnetic Field Model Selection

The selection of a magnetic field model used in the position algorithm involves the consideration of minimizing the computational cost while providing accurate position and orientation calculation. There are multiple methods to approximate the magnetic field generated from coils in air. The following models were evaluated for the study:

- (1) Point source model - the entire Tx coil is treated as a single point source;
- (2) Circular model - the model was developed by NASA engineers to simulate the B-field generated by a circular coil [61]. The method requires the use of elliptical integrals, which are very process intensive.

Simulations were conducted on both models to verify their accuracy using Matlab. We assume that the circular model provides the most accurate description of the B-field generation because its mathematical equations account for the entirety of the coil geometry. The circular model assumes only a single loop. However, since the coil used in this system is a long solenoid, the turn density (turns/m) will affect the B-field strength. We compare the model calculated B-field results of models (1) and (2) in terms of magnitude and percent differences. The percent difference error is calculated as follows, assuming that the circular model produces the true B-field:

$$\%error = \frac{abs(B_{pointsource} - B_{circular})}{B_{circular}} \times 100\% \quad (3.2.1.1)$$

where  $B_{circular}$  and  $B_{pointsource}$  denote magnetic flux density of the circular model and point source model, respectively.

For the simulations, the coil is placed at  $(x, y, z) = (0, 0, 0)$  cm in the  $xy$  plane. The B-field strength is recorded for  $x$ ,  $y$ , and  $z$  components at different positions. Figures 3.2.1 through 3.2.4 depict the B-field magnitudes along with the percent errors. The point source approximation is accurate for the  $x$  and  $y$  components. As seen in Figure 3.2.2, the maximum percent error does not exceed 0.2%. However, the  $z$  component approximation is poor when the measuring distance is not significantly larger than the coil radius of 1.5 mm. This can be clearly seen in Figures 3.2.2 and 3.2.4. For  $z$  positions greater than 5 cm, the errors are under 0.1% for all three components. From these tests, it is concluded that the point source model is an accurate model as long as the measuring distance is significantly larger than the coil radius.

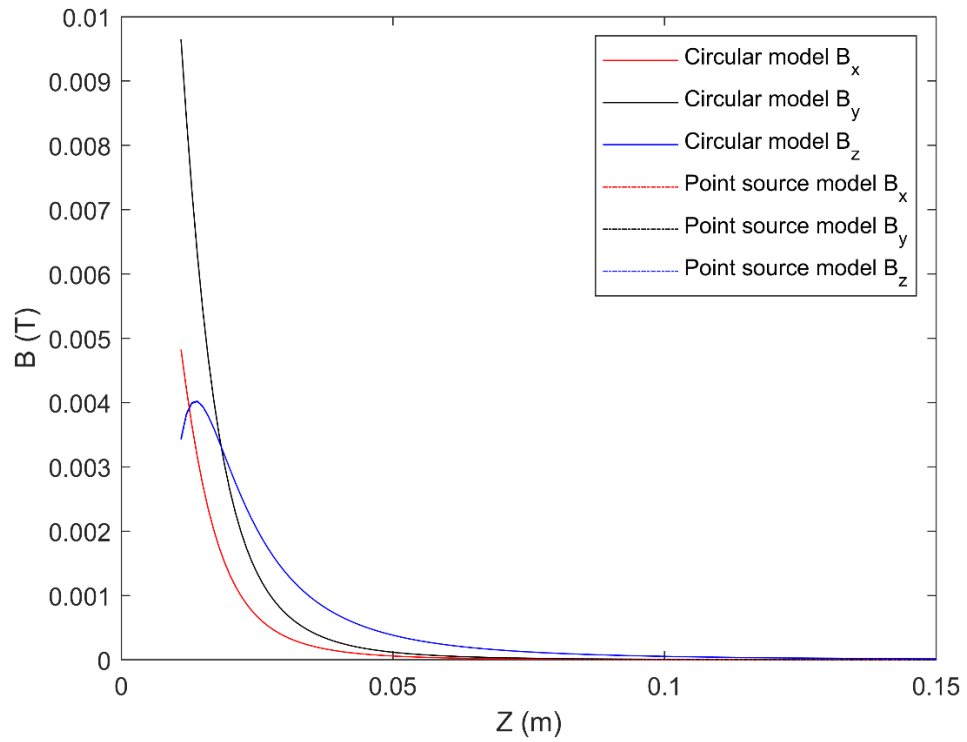


Figure 3.2.1. Simulated B-field at  $x = 0.5\text{cm}$ ,  $y = 1\text{cm}$ ,  $z$  varying between 1 and 15cm.

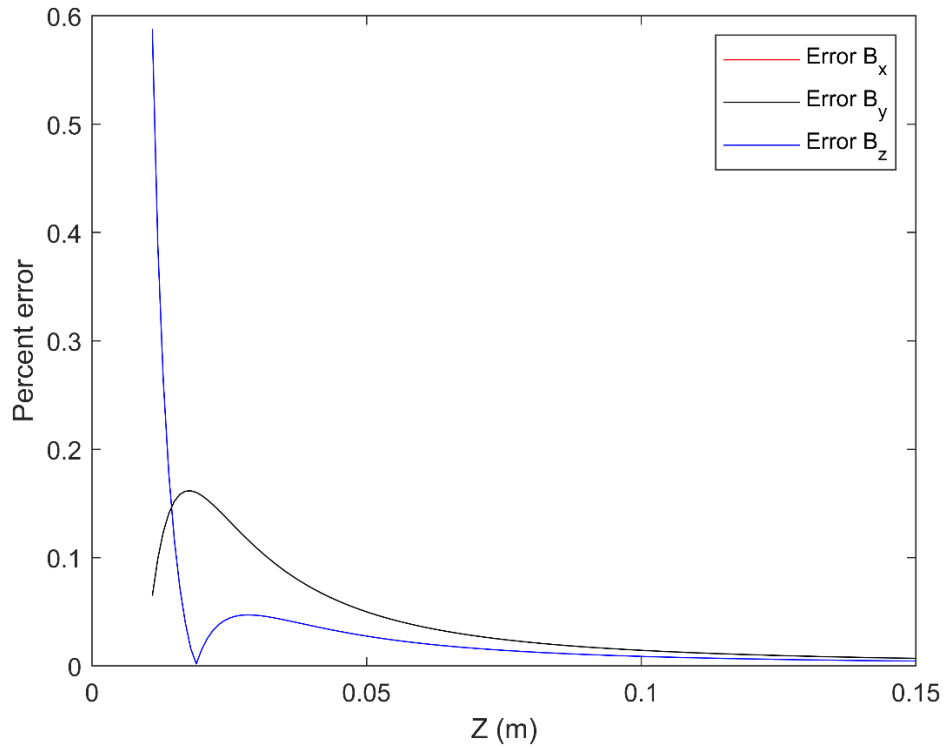


Figure 3.2.2. Errors at  $x = 0.5\text{cm}$ ,  $y = 1\text{cm}$ ,  $z$  varying between 1 and 15cm.

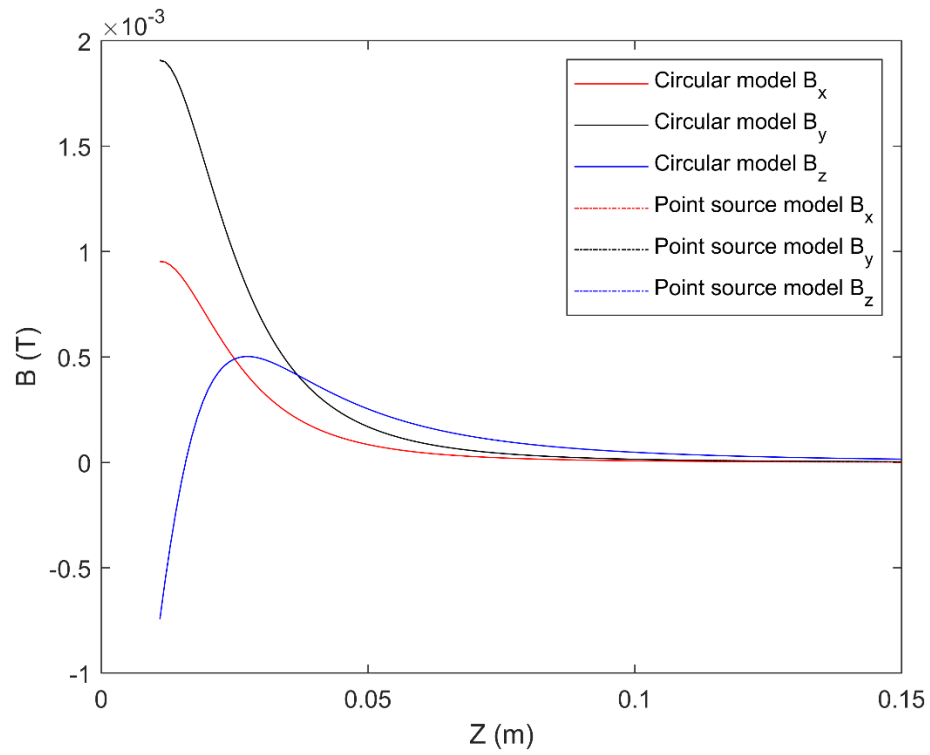


Figure 3.2.3. Simulated B-field at  $x = 1\text{cm}$ ,  $y = 2\text{cm}$ ,  $z$  varying between 1 and 15cm.

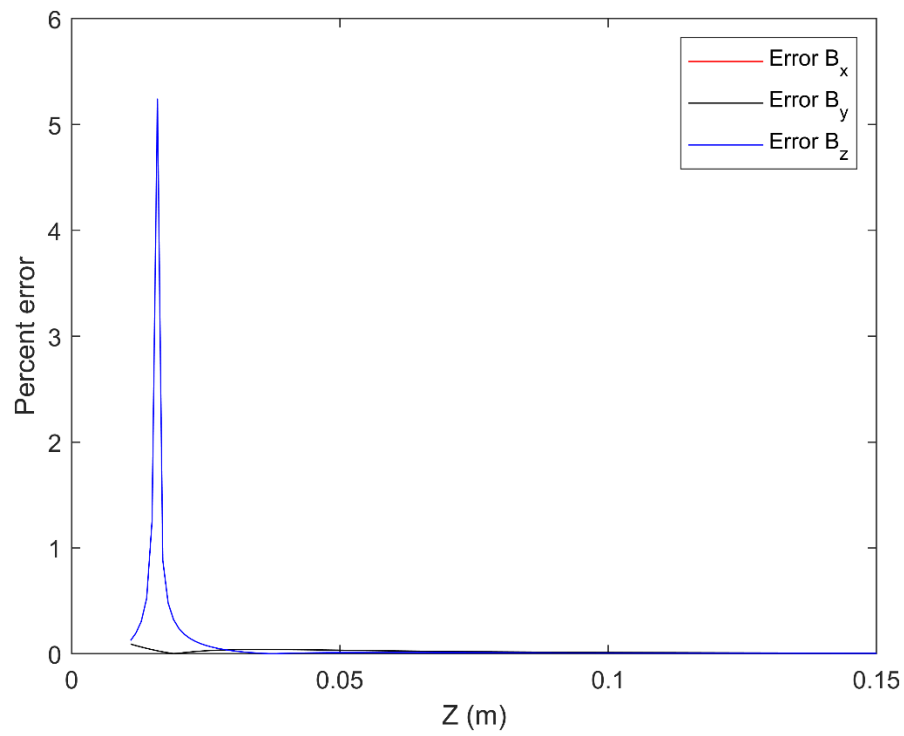


Figure 3.2.4. Errors at  $x = 1\text{cm}$ ,  $y = 2\text{cm}$ ,  $z$  varying between 1 and 15cm.

### 3.2.2 Transmitter Coil Introduction

In this section, the design of the transmitter coil, based on the catheter size constraint is discussed. Because this coil is used to track the catheter tip, it should be sufficiently small to be placed onto a catheter probe of 7 French in diameter (see Section 1.2). The transmitter coil used for the tracking system went through different iterations. First, commercially available coils were tested as a proof of concept. Afterwards, a custom transmitter coil was designed to optimize the transmitter coil's B-field in the limited area. This introduction provides a brief overview of the initial coils tested in the proof of concept stage and the drawbacks found through these tests.

First, tests have been performed on commercially available coils. Table 3.2.1 below shows the coils analyzed.

Table 3.2.1. Comparison of commercially available coils.

Manufacturer	Part Number	Dimensions (W×H×L) (mm)	Inductance (mH)	Core	Calculated DC Resistance ( $\Omega$ )	Calculated ESR ( $\Omega$ )	Calculated Q at 32kHz
Coilcraft	4312RV	3.45×2.34×11.38	1	Ferrite*	27.21	27.23	8
EPCOS/TDK	B82450A*E	2.7×2.7×7.8	1	Ferrite	29	29.02	9.07
Neosid	MS2074	2×2×7.9	2	Ferrite	21.11	21.13	6

First, commercially available coils by Coilcraft 4312RV and EPCOS B82450A\*E were examined (Figure 3.2.5). These tests showed that these coils could generate a B-field strong enough to be successfully implemented in a tracking system. This is due to their high core permeability, which boosts the coil's quality factor.



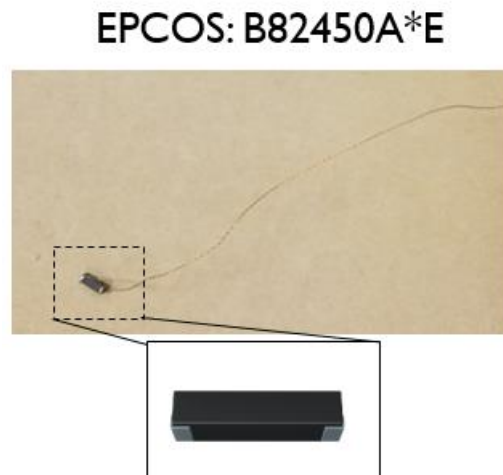
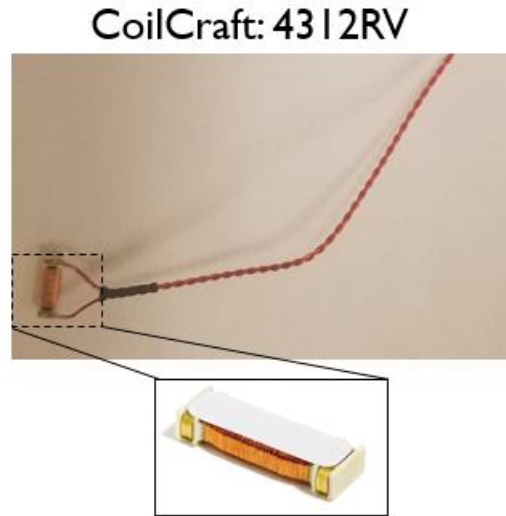


Figure 3.2.5. Commercially available coils tested.

However, these coils and other commercial based coils are not viable because they either have a ferrite core, which causes nonlinear changes in magnetic field resulting in distortion, or do not have specifications required to generate a strong B-field measurable by receivers 20–30 cm away from the transmitter coil, while maintaining a small form factor required for this system. Most of the problems associated with ferrite core transmitters is core saturation when the core is fully magnetized, producing maximum magnetic flux. This causes a distorted waveform for the AC current as seen in Figure 3.2.6 below.

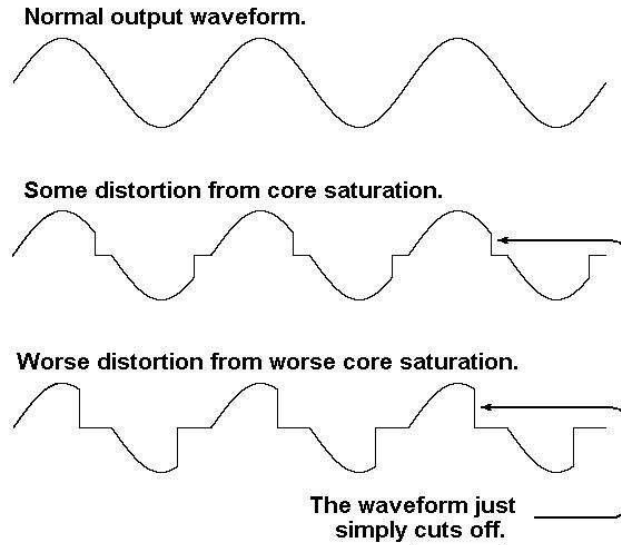


Figure 3.2.6. Core saturation waveform behavior [62].

Tests of the Coilcraft and EPCOS coils show that there is core saturation behavior seen in the oscilloscope output (Figure 3.2.7). Here, a simple H-bridge coil driver is run with a pulse width modulated signal (blue), and the voltage across the inductor (magenta) is measured. The core saturation behavior can be clearly seen.

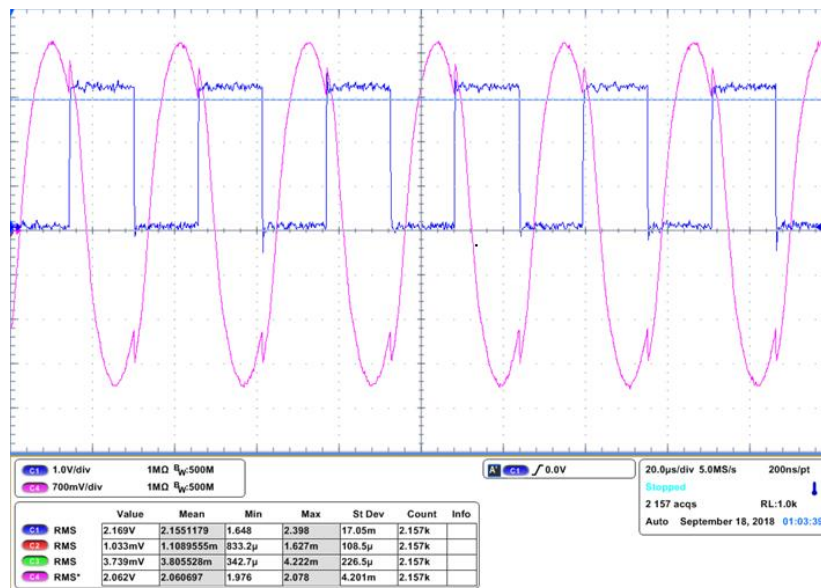


Figure 3.2.7. Oscilloscope output of EPCOS B82450A\*E coil: clock signal for transmitter driver (blue) and transmitter coil inductor voltage waveform (magenta).

Another problem with commercially available coils is their sizes. Both commercial coils tested have dimensions that exceed the constraint of 7 French (2.3 mm in diameter) (Figure 3.2.8). Coils such as NDI/Ascension small sensors contain ferrite, which have the same drawbacks as the Coilcraft and EPCOS coils with significant distortion.



Figure 3.2.8. Catheter tip.

Because of these drawbacks, a custom air core coil is designed. Air core coils do not have the core saturation problem and thus are viable for the proposed system. However, they must be designed carefully due to their low inductance and quality factor, compared to ferrite coils. Their size and geometry must be optimized to maximize the magnetic field generated, while minimizing distortion and noise, and considering fitness for the catheter. Thus, for this positioning system a coil was custom made with a plastic core and wrapped with the thinnest readily available copper wire to fit within the constraints of catheter tip. Core and wire constraints will be discussed in the following sections.

Since the catheter's diameter is 2.3 mm, the diameter of the plastic coil holding frame should not exceed this size. In addition, the vertical length of free space at the end of the catheter was specified to be 1.5 cm. Thus, the target coil dimensions are 1.5 mm in diameter and 10 mm in length. The plastic core and frame have an outer diameter of 2 mm and length of 12 mm. Figure 3.2.9 shows the evolution of the transmitter coils used for the tracking system design with the bottom right coil being the final implementation of the transmitter coil design used for the proposed system.

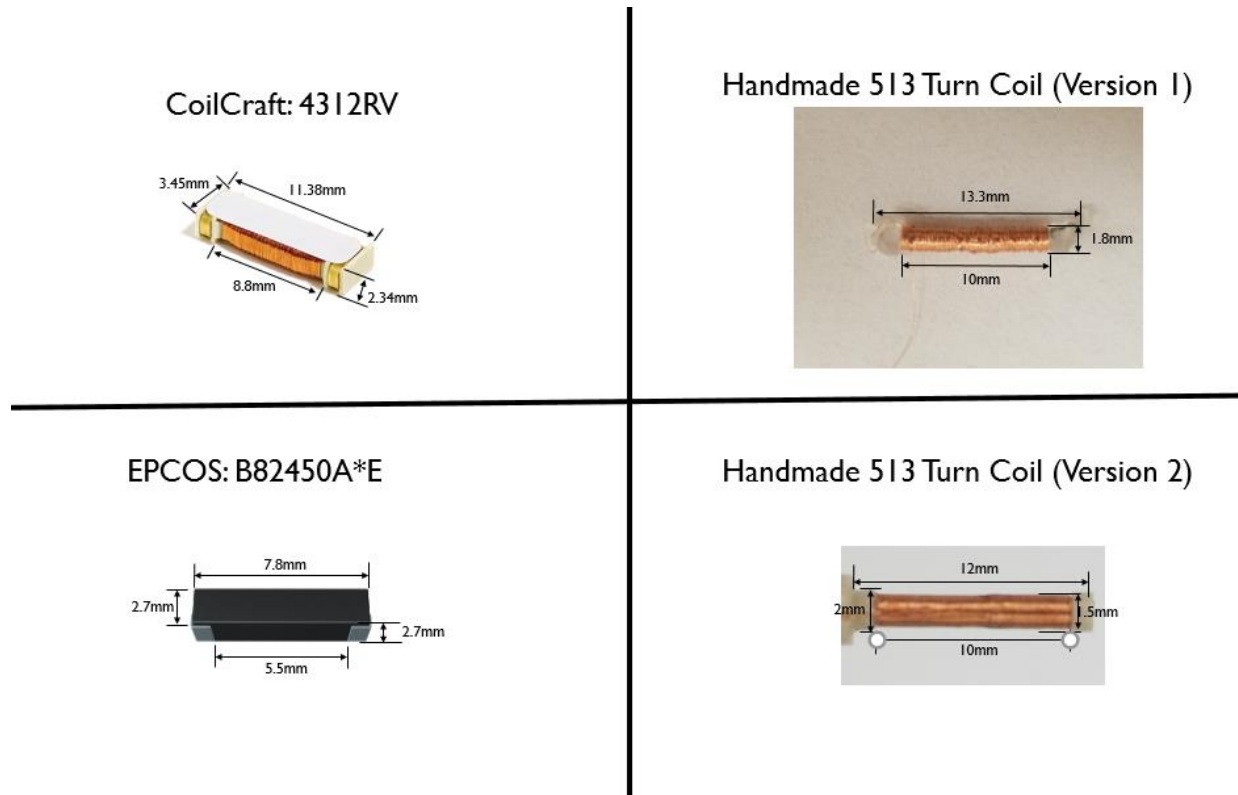


Figure 3.2.9. Different plastic cores for transmitter coil.

### 3.2.3 Transmitter Core

The core of the coil that was wound around was custom made using a Formlabs 3-D printer with an SLA plastic clear resin (0.1 mm printing precision). Figure 3.2.10 below shows the plastic core. The inner diameter of the core is designed to be 1.2 mm so that when the wire is wrapped around, the outer diameter is 1.5 mm. The length is 10 mm. 1 mm stubs are placed at each end so that the coil would remain in place and not slide off the core during testing. The smallest plastic core diameter that can handle the mechanical stress for winding copper wire is 1.2 mm.



Figure 3.2.10. Plastic core for the proposed transmitter coil.

### 3.2.4 Transmitter Coil Design

For the transmitter coil, the design must be evaluated to maximize transmitting magnetic field and minimize inefficiency from nonidealities such as skin effect and current crowding.

Skin effect is where the current density is not uniform inside the conductor and is mostly concentrated on the wire's edges. The AC resistance increases by square root of frequency as follows [63].

$$R_{AC} = R_{DC} \cdot k\sqrt{f} \quad (3.2.4.1)$$

where  $R_{AC}$  and  $R_{DC}$  are the AC and DC resistances, respectively;  $f$  is the frequency in Hz; and  $k$  depends on the wire's diameter on American scale AWG.

The equation for current density  $J$  in a depth is:

$$J = J_s e^{\frac{-d}{\delta}} \quad (3.2.4.2)$$

where  $J_s$  is the surface current density;  $d$  is the conductor's diameter; and  $\delta$  is the skin depth given by the electric resistivity  $\rho$ , magnetic permeability  $\mu$ , and angular frequency  $\omega$  as follows:

$$\delta = \sqrt{\frac{2\rho}{\omega\mu}} \quad (3.2.4.3)$$

For the proposed system, the operating frequency is 32 kHz. This low frequency means that skin effect is negligible. As seen in Figure 3.2.11 below, the test on a 1.32 mm wire shows that the change in current density from the edges to the center of the wire is minimal.

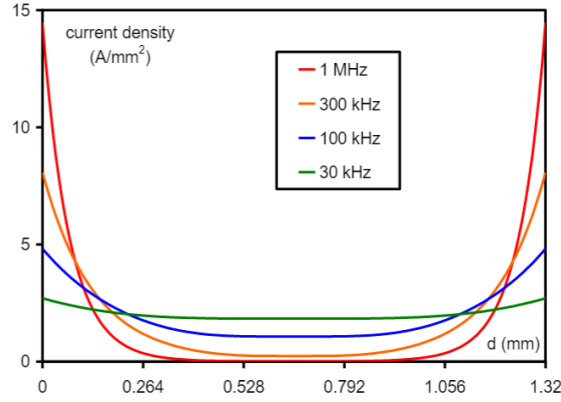


Figure 3.2.11. Current density in a 1.32mm diameter wire [64].

In this system, the smallest available copper wire, 44 AWG (0.05 mm in diameter), is used to maximize the number of turns of the coil. Higher AWG allows for more turns in the limited space on a small coil but has the drawback of higher impedance. Figure 3.2.12 illustrates the increase in resistance as AWG increases.

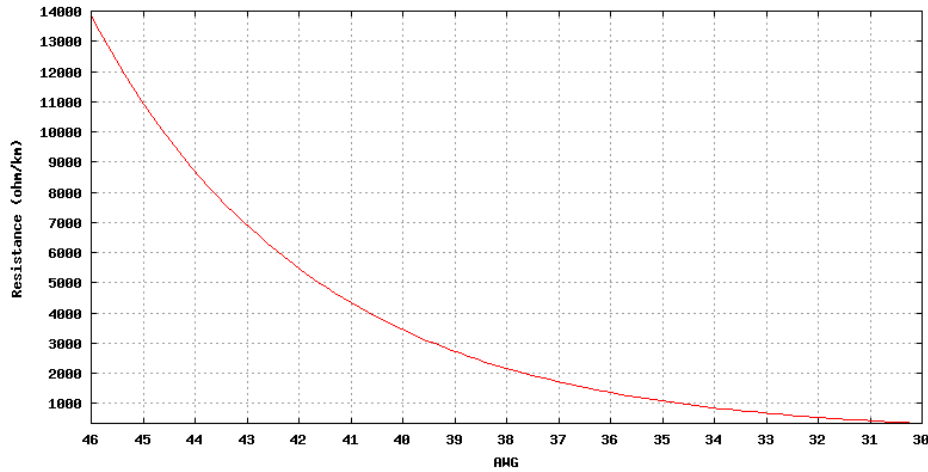


Figure 3.2.12. Resistance of wire in relation to AWG [65].

On the other hand, a lower AWG may seem better from the relationship shown in Figure 3.2.12, but based on Ampere's law, a larger number of turns leads to a stronger magnetic field, and due to the coil size constraint, maximizing the number of turns is vital.

Next, the magnetic field strength from the transmitter is evaluated to ascertain that it is measurable in the target tracking range of 10–50 cm. In addition, the magnetic field must also be measurable at 1 m range to satisfy the critical SNR target. The critical SNR is the smallest SNR

that the sensing coils can detect the transmitting field. Assuming a driving voltage ( $V_{DD}$ ) of 5 V, the magnetic field and the required voltage were estimated.

To estimate the magnetic field strength, we also need to consider the number of layers for the coil. Proximity effect loss due to multilayer based coil designs has been well documented [66]. Figure 3.2.13 shows how the net current decreases for the inner layers compared to the outer layers due to skin and proximity effect. This leads to AC conduction loss and a weaker magnetic field than the one determined by the Ampere's law.

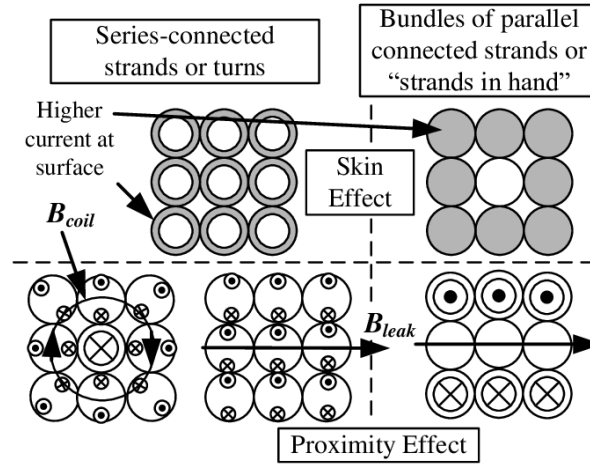


Figure 3.2.13. Skin and proximity effects on coils [67].

Another factor to consider is the shape of transmitter coil. The shape is defined by the coil's radius  $R$  relative to its length  $l$  and coil thickness  $c$ . Figure 3.2.14 below depicts the possible coil formations.

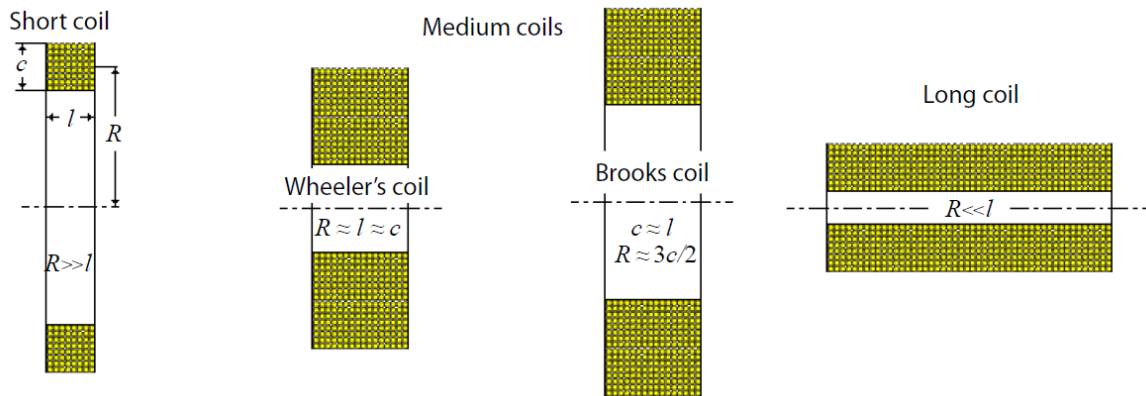


Figure 3.2.14. Multi-layer coil shapes [68].

Optimal geometry of the coil has been studied extensively. The optimal coil geometry is selected based on minimization of losses due to skin and proximity effect. The Brook's coil geometry in Figure 3.2.14 has been shown to be the most optimal coil in terms of its minimum non-ideal effects [69]. However, for the proposed design, the size of  $R$  is severely constrained, and thus a Brook's coil geometry is not possible. Because the available length  $l$  of the catheter shaft (10 mm) is significantly larger than the radius  $R = 1.5$  mm, the coil geometry used is that of a long coil, often called a solenoid. The coil geometry is shown in Figure 3.2.15 below.

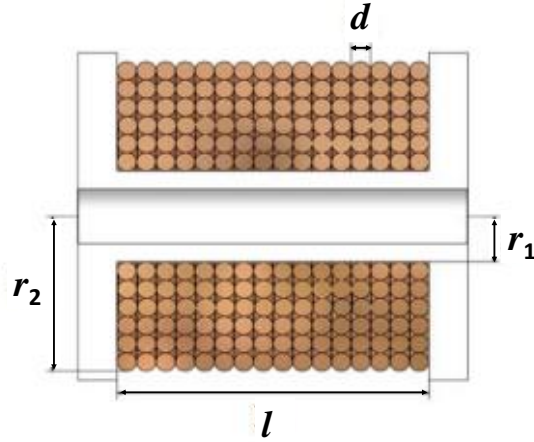


Figure 3.2.15. Geometry of a long coil [70].

The number of turns  $n$  depends on the diameter  $d$  of the magnetic wire, the coil packing factor  $k$ , and the inner and outer radii  $r_1$  and  $r_2$  [70]:

$$n = \frac{kl(r_2 - r_1)}{d^2} \quad (3.2.4.4)$$

The length of wire needed,  $l_w$ , is given by

$$l_w = \pi \frac{(r_2^2 - r_1^2)}{d^2} l \quad (3.2.4.5)$$

and the cross-sectional area of the magnetic wire is given by

$$A_w = \pi \frac{d^2}{4} \quad (3.2.4.6)$$

Using (3.2.44) to (3.2.4.6), we can obtain the ohmic resistance of the coil

$$R_{DC} = \frac{l_w}{A_w \sigma_{cu}} \quad (3.2.4.7)$$

where  $\sigma_{cu}$  is the copper conductivity. The inductance of a multilayered solenoid coil is given by



$$L = \frac{78.7n^2d_m^2}{3d_m + 5(d_2 - d_1) + 9l} \quad (3.2.4.8)$$

where  $L$  is in  $10^{-7}\text{H}$ ,  $d_1 = 2r_1$ ,  $d_2 = 2r_2$ ,  $d_m = (d_1 + d_2)/2$ , and all diameters and  $l$  are in meters.

For proximity effect, the relationship between AC resistance  $R_{AC}$  and DC resistance  $R_{DC}$  is based on the Dowell's equation [71]–[73]. For a multilayer solenoid, the  $R_{AC}$ , relative to  $R_{DC}$ , can be expressed as [72]:

$$R_{AC} = \Delta \left[ G_1(\Delta) + \frac{2}{3}(n_l^2 - 1)G_2(\Delta) \right] R_{DC} \quad (3.2.4.9)$$

with  $G_1$  and  $G_2$  representing the geometry of the coil

$$G_1(\Delta) = \frac{\sinh 2\Delta + \sin 2\Delta}{\cosh 2\Delta - \cos 2\Delta} \quad (3.2.4.10)$$

$$G_2(\Delta) = \frac{\sinh \Delta - \sin \Delta}{\cosh \Delta + \cos \Delta} \quad (3.2.4.11)$$

where  $n_l$  is the number of layers in the coil, and  $\Delta$  is the ratio of the layer height to the skin depth described above in (3.2.4.3)

$$\Delta = \frac{d}{\delta} \sqrt{\frac{\pi}{2}} \quad (3.2.4.12)$$

The skin effect equation (3.2.4.3) can be rewritten in terms of  $\sigma_{cu}$

$$\delta = \sqrt{\frac{2}{\sigma_{cu} \omega \mu}} \quad (3.2.4.13)$$

Table 3.2.2 and Figure 3.2.16 below show the ratio of AC to DC resistance for different numbers of layers. Here the packing factor  $k$  is assumed to be 0.9, and the wire is 44AWG (0.0508 mm in diameter) enameled copper wire with a conductivity of  $\sigma = 5.81\text{E}7$  ( $1/(\Omega \cdot \text{m})$ ). The skin depth at the operating frequency of 32 kHz is 0.369 mm. The maximum diameter for the coil design is set at 1.5 mm based on the catheter diameter. The inner diameter is shrunk by 0.1 mm for every layer added on the design to make space for the enameled copper wire.

Table 3.2.2.  $R_{ac}/R_{dc}$  for each layer.

Number of Layers	Inner Diameter (mm)	Outer Diameter (mm)	Number of Turns	Inductance (H)	$R_{dc}$ (ohms)	$R_{ac}$ (ohms)	Overall $R_{ac}/R_{dc}$
1	1.4	1.5	174	5.30E-06	7.495	7.495	1.000
2	1.3	1.5	348	1.97E-05	14.473	14.478	1.000
3	1.2	1.5	523	4.11E-05	20.934	20.952	1.001
4	1.1	1.5	697	6.75E-05	26.878	26.919	1.002
5	1	1.5	871	9.71E-05	32.305	32.384	1.002

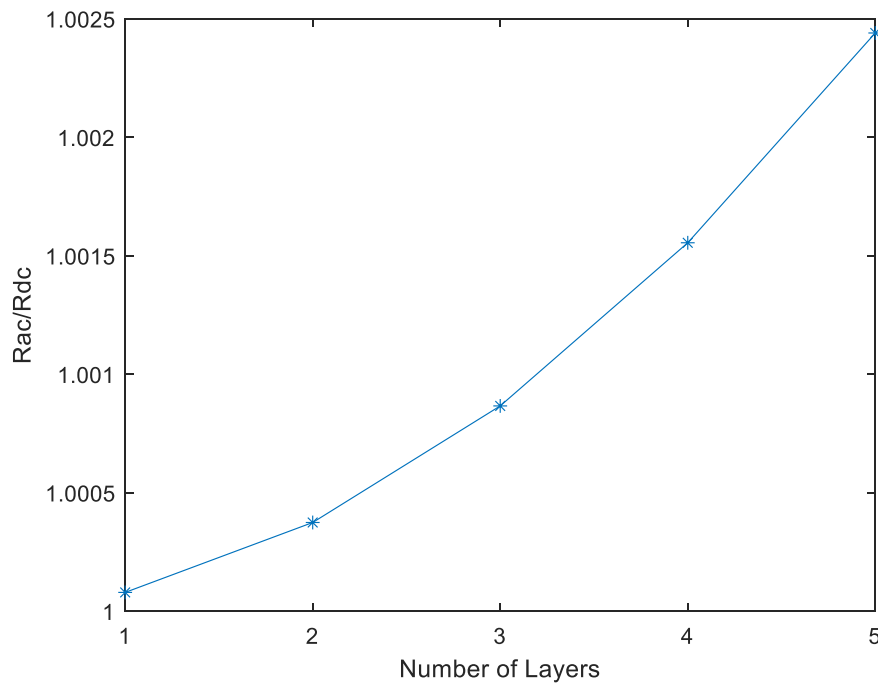


Figure 3.2.16. Ratio of AC to DC resistance by the number of layers.

As the number of layers increases, the AC resistance increases relative to the DC resistance. It is imperative to select a coil design that will generate a strong enough magnetic field, while reducing non-idealities from skin and proximity effect. For the proposed system, the optimal number of layers in the transmitter coil is determined to be either 3 or 4 (Table 3.2.3). This design allows for a detectable magnetic field on the level of  $4E-11T$ . The 3-layer design is opted since it has a stronger B-field, and due to reduced non-idealities, the AC resistance will be 0.1% higher than the DC resistance. In contrast, the 4-layer design requires a smaller plastic core of 1 mm in

diameter to have the same 1.5 mm outer diameter as the 3-layer design, which leads to a more fragile coil.

Table 3.2.3. Hand calculated B-field and voltage estimations of the transmitter coil.

Specification	EPCOSA*E	3 Layer Design	4 Layer Design
Inductance	1.01mH	39μH	68μH
Outer Diameter	2mm	1.5mm	1.5mm
Inner Diameter	1.7mm	1.15mm	1.035mm
Length	7mm	10mm	10mm
Wire AWG	44	44	44
#Turns	315	513	684
Core Perm.	25	1	1
RAC	15.3Ω	17.36Ω	22.23Ω
B-field at 1m	4.96E-11T	4.38E-11T	3.68E-11T
Voltage at 1m	40μV	35μV	38μV
Operating Freq	32kHz	32kHz	32kHz
Q	6.56	0.6	0.79
RMS Current	250.8mA	241.7mA	193.9mA
RMS Power	1.254W	1.21W	0.9695W
Real Power	0.962W	1.014W	0.835W

### 3.2.5 Heat Considerations

Next, we evaluate the heat generated by the transmitter, which is a particularly important factor for biomedical applications. The simplest model relates heat energy to mass and change in temperature by the specific heat capacity formula below [74]:

$$C = \frac{Q}{m\Delta T} \quad (3.2.5.1)$$

where  $C$  is the specific heat capacity of the liquid in joule per kilogram degrees Celsius;  $Q$  is the heat energy transferred in joules;  $m$  is the mass of the liquid being heated in kg; and  $\Delta T$  is the change in temperature in degrees Celsius. However, this model cannot be used for modeling heat in human blood because blood is constantly flowing through the heart and throughout the body

over time (Figure 3.2.17), and the above static model will overestimate the temperature increase in a local region being heated by the transmitter coil.

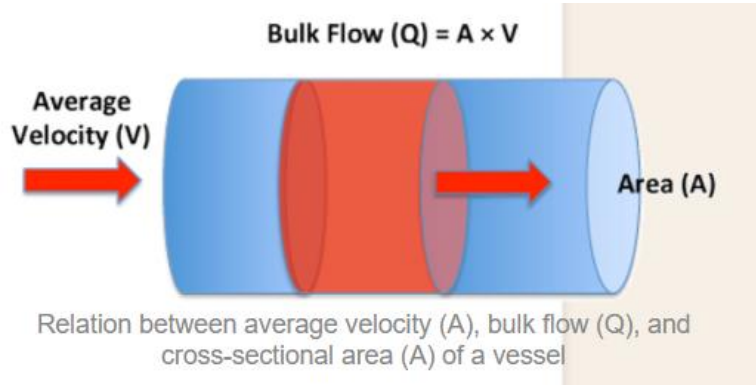


Figure 3.2.17. Fluid bulk flow in relation to cross-sectional area and average velocity.

A more accurate method is to use the Pennes bioheat equation [75], [76]. This heat equation models the transient temperature in the domain of human blood and tissue as a result of oscillating heating condition (for this system it will be from the oscillating current across the transmitter coil). The 1-D Pennes bioheat transfer equation is:

$$\rho c \frac{\partial T}{\partial t} = \nabla \cdot (k \nabla T) - W \rho_{bl} c_{bl} (T - T_{bl}) + Q + \rho SAR \quad (3.2.5.2)$$

where  $t$  is the time,  $\rho$  the tissue mass density,  $c$  the specific heat capacity of tissue,  $T$  the tissue temperature,  $W$  the blood perfusion rate,  $\rho_{bl}$  the blood density,  $c_{bl}$  the specific heat capacity of blood,  $T_{bl}$  the supplying arterial blood temperature,  $k$  the tissue thermal conductivity,  $Q$  the heat generated by human metabolism, and SAR the specific absorption rate, which is a measure of the rate at which energy is absorbed per unit mass by the human body when it is exposed to EM fields.

Using the above model and an anatomical model, the time profiles of temperature and SAR can be simulated. This type of simulation is often performed when the effect of MRI exams on patients is tested, as published in [75] (Figure 3.2.18). As shown in (3.2.5.2), the maximum temperature varies with the perfusion rate and starting temperature. In general, the precise prediction of local temperature change is challenging and beyond the scope of this study. Based on the International Electrotechnical Commission (IEC) standards, the coil temperature should not cause the core body temperature to rise higher than 38°C and the local heart blood temperature to

exceed  $40^{\circ}\text{C}$ . In addition, the specific absorption rate of the magnetic field (SAR) is limited to 20 W/kg in the local heart area and 4 W/kg in the whole body (Figure 3.2.14).

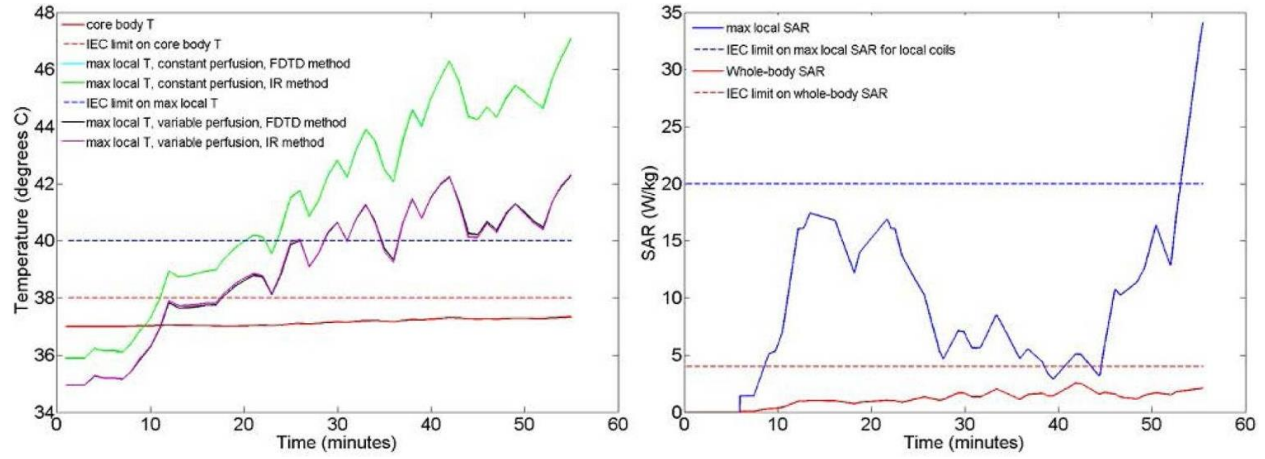


Figure 3.2.18. Simulated temperature compared to IEC temperature limit (left) and simulated magnetic radiation (SAR) compared to IEC magnetic radiation limit (right) [75].

For the proposed system, we consider local SAR = 20 W/kg as the constraint for the transmitter. The local SAR is determined over the mass of 10 g [77]. As discussed below, the custom-made transmitter coil for the proposed system meets the target specifications without violating any restrictions set by the IEC. Specifically, the parameters for the proposed Tx are:  $R = 25\ \Omega$ ,  $I = 80\ \text{mA}$ , and  $P = 0.16\text{W}$ . For the mass of 10g, the SAR = 16W/kg.

### 3.2.6 Transmitter Coil Winding

Next, the winding of the transmitter coil is discussed. Figure 3.2.19 below shows the winding apparatus.

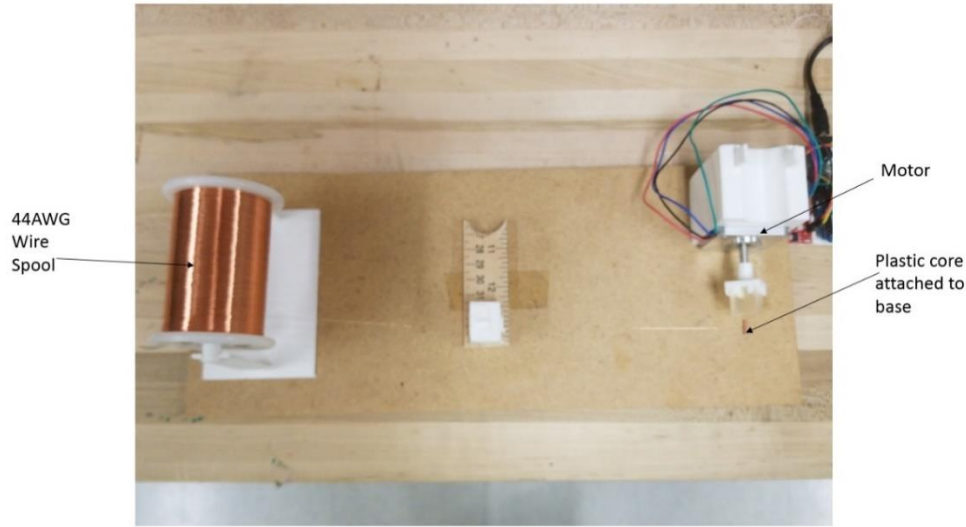


Figure 3.2.19. Coil winding apparatus.

The copper wire spool supplies 44 AWG wire that winds around the plastic core. The small plastic core was attached to a 1 cm<sup>3</sup> cube, made of the same resin material (Figure 3.2.20). This cube allows the core to be attached to a motor shaft, so the copper wire could be wound around the core. The motor was programmed to spin around 513 revolutions. Afterwards, the coil along with the cube was taken off the motor attachment. The coil was cut from the cube base, and the transmitter coil was ready for use. Figure 3.2.20 below shows coil fixtures used.

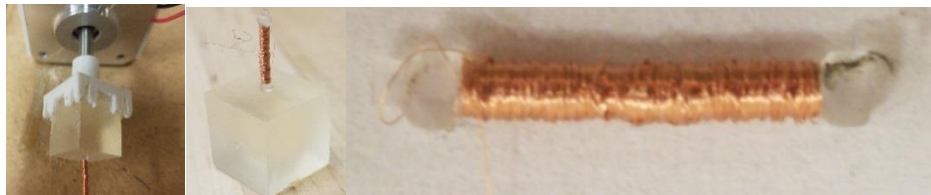


Figure 3.2.20. Coil being wound (left), coil winding completed (middle), version 1 transmitter coil (right).

### 3.2.7 Transmitter Coil Specifications

The inductance, along with the resistance of the coil, is measured using an LCR meter. Table 3.2.4 below shows both the 3-layer and 4-layer coil designs. Multiple versions of the 3-layer design of the transmitter coil were made. For the first version, the coil was wound using the apparatus shown above, without a microscope. However, the resulting coil had uneven windings,

depicted in Figure 3.2.20 (right). Thus, a second version was made, using a microscope to ensure that all coil turns had equal spacing and no overlapping windings between layers. A final version was made with exactly 3 layers (470 turns).

Table 3.2.4. Comparison of designed coils (no external connections).

Coil	Length (mm)	Outer Diameter (mm)	Inner Diameter (mm)	Number of Turns	Number of Layers	Wire AWG	Inductance (mH)	Core	ESR ( $\Omega$ )	Measured Q at 32kHz
3 Layer (Ideal)	10	1.5	1.2	513	3	n/a	0.0424	Plastic	17.36	n/a
4 Layer (Ideal)	10	1.5	1.035	684	4	n/a	0.0636	Plastic	22.23	n/a
3 Layer (version 1)	10	1.5	1.2	513	4.2	44	0.0294	Plastic	17.66	0.321
3 Layer (version 2)	10	1.5	1.2	513	3.4	44	0.04352	Plastic	21.68	0.404
3 layer (final version)	10	1.5	1.2	470	3	44	0.0402	Plastic	20.78	0.406

The second version coil inductance is shown below in Figure 3.2.21.

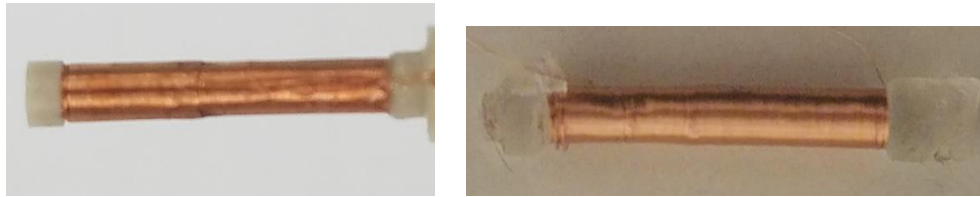


Figure 3.2.21. Transmitter coil version 2 (left) and final version (right).

This transmitter coil is driven by an LC tank circuit. The capacitor, along with the driving circuit, is placed in a reference location approximately 1 m away from the patient. The driving circuit PCB's form factor is too large (cm sized) and cannot be placed on or near the catheter. Thus, a cable is required to connect the transmitter driver and the transmitter coil itself. The cable length required is at least 1 m, and the long cable's parasitic resistance and inductance must also be considered, along with secondary magnetic field induced by the cable.

Since this cable carries mA level current for the transmitter coil, it is a key for the wires to be wound in twisted pair formation to reduce the electromagnetic induction between the two wires connecting the transmitter coil. The twisted pairs for versions 1 and 2 are made using 26 and 30 AWG, respectively, enameled copper wire hand twisted. Figure 3.2.22 below shows the twisted pair wires used for version 2.



Figure 3.2.22. 30AWG twisted pair wire version 2.

A final version was created by a professional medical company involved in the larger sponsored project on heart shape mapping. This coil is made using the same specifications from the version 2 design, with commercially available 30 AWG twisted pair wire. This coil is attached onto the catheter tip, illustrated in Figure 3.2.23.



Figure 3.2.23. Transmitter coil (final version) attached to catheter tip.

Table 3.2.5 below shows the specifications of the cable connecting the driver and coil along with the coil specifications when the parasitic resistance and inductance are factored in.

Table 3.2.5. Comparison of designed coils (with twisted pair wire).

Coil	Twisted Pair Length (cm)	Twisted Pair AWG	Wire Type	Total Inductance (mH)	Total ESR ( $\Omega$ )	Measured Q at 32kHz
3 Layer (version 1)	50	26	Enameled Copper	0.02978	18.14	0.332
3 Layer (version 2)	120	30	Enameled Copper	0.04308	22.78	0.380
3 Layer (final version)	140	30	Copper, Insulated Commercially Twisted	0.06099	26.36	0.465



In conclusion, for this system, a tiny air-core coil allows for easy integration on the tip of a medical catheter and can generate B-field strong enough to be measurable by magnetic sensors placed 10 to 50 cm away from the transmitter.

### 3.2.8 Transmitter Driver Design

The following sections describe the driving circuit. First, the LC loop is discussed. The transmitter coil is driven using an LC loop. The LC loop consists of a transmitter coil and a tuning capacitor. The tuning capacitor's capacitance is set based on the operating frequency ( $f$ ) of 32 kHz. The capacitance can be obtained by the equation below:

$$f = \frac{1}{2\pi\sqrt{LC}} \quad (3.2.8.1)$$

For the final version coil, the capacitance used is 660 nF.

Next, we describe the driver circuit design constraints. The transmitter driver is optimized to maximize the magnetic field strength generated by the coil at the 32 kHz frequency, while minimizing total harmonic distortion (THD) and various noises, such as flicker noise, resistor noise, and phase noise. As discussed in the coil design, the small coil generates copious amounts of heat. To meet the target heat specifications based on the calculations from the Pennes bioheat equation, noise and distortion must be kept at a minimum to maximize the total power delivered to the 32 kHz target magnetic field.

Two main architectures were carefully assessed for the proposed system. An H-bridge driver and an op-amp driver. The first iteration investigated an H-bridge driver. In an H-bridge driver, the power required is significantly lower than that of an op-amp driver. However, through preliminary tests, the frequency response of the inductor current is significantly distorted with harmonics and other frequency components not at the main tone. This is because an H-bridge driver uses a pulse width modulated (PWM) wave, which translates to a square wave. The proposed system uses an air core inductor, which has low Q. This low Q causes a wide passband, resulting in the input square wave harmonics to propagate to the inductor current [78]. As a result, this driver was not selected due to its inefficiency. An op-amp driver requires significantly more power than an H-bridge driver but has the benefit of minimal distortion because the AC input is

not a square wave. However, minimal distortion can only be realized with a clean AC sinusoidal input. In the discussion of H-bridge driver design below, we will describe the drawbacks of such a design encountered in the research process.

### ***Transmitter Driver (H-Bridge) Simulation and Evaluation***

An H-bridge driver consists of four transistors with a common application of driving brushed DC motors [79]. The transistors act as a switch changing the polarity of the drive direction. A pulse width modulation (PWM) signal can change the power delivered to the motor, where smaller percentage duty cycle leads to less power, and a higher percentage duty cycle leads to more power.

Although most published applications of H-bridge drivers are for motors, an H-bridge can be used to drive other types of inductive loads, such as the transmitter coil for this application. This section investigates the advantages and disadvantages of an H-bridge driver for the transmitter coil.

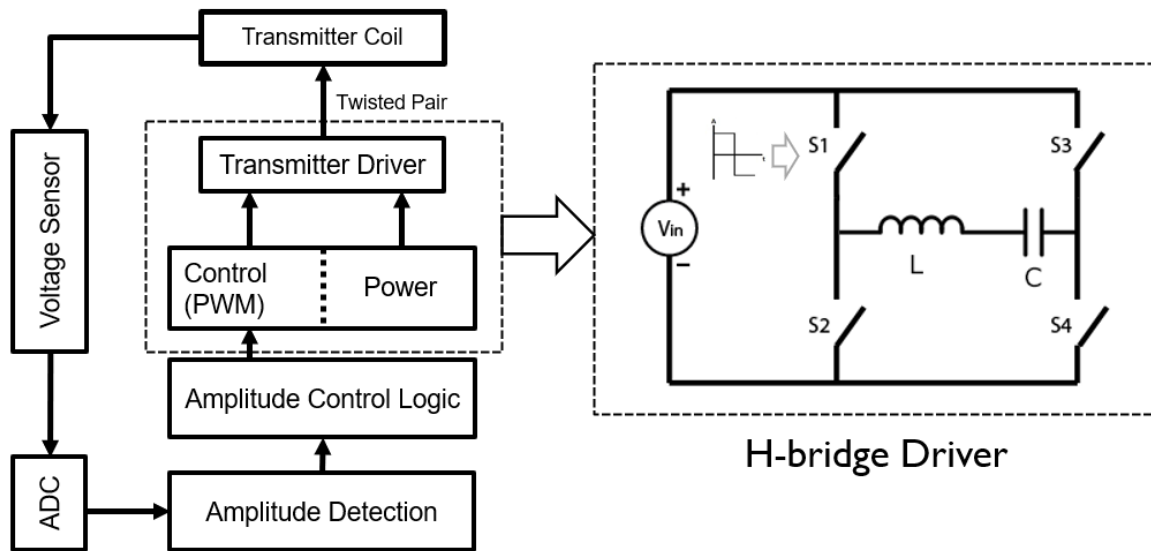


Figure 3.2.24. Possible transmitter system with an H-bridge driver.

Minimal changes are required when an H-bridge is designed for the inductor coil instead of a motor (Figure 3.2.24). For the switching circuit, this H-bridge consists of 4 switches including 2 pairs of single pole double throw switches (SPDTs). Two SPDTs allow for synchronous control,

and the switch selected is a commercially available integrated circuit (IC) ADG884, which has the additional break before making property [80]. This property prevents both pairs of SPDTs from being closed at one time, which prevents momentary connection of all 4 switches, as shown in Figure 3.2.25 below.

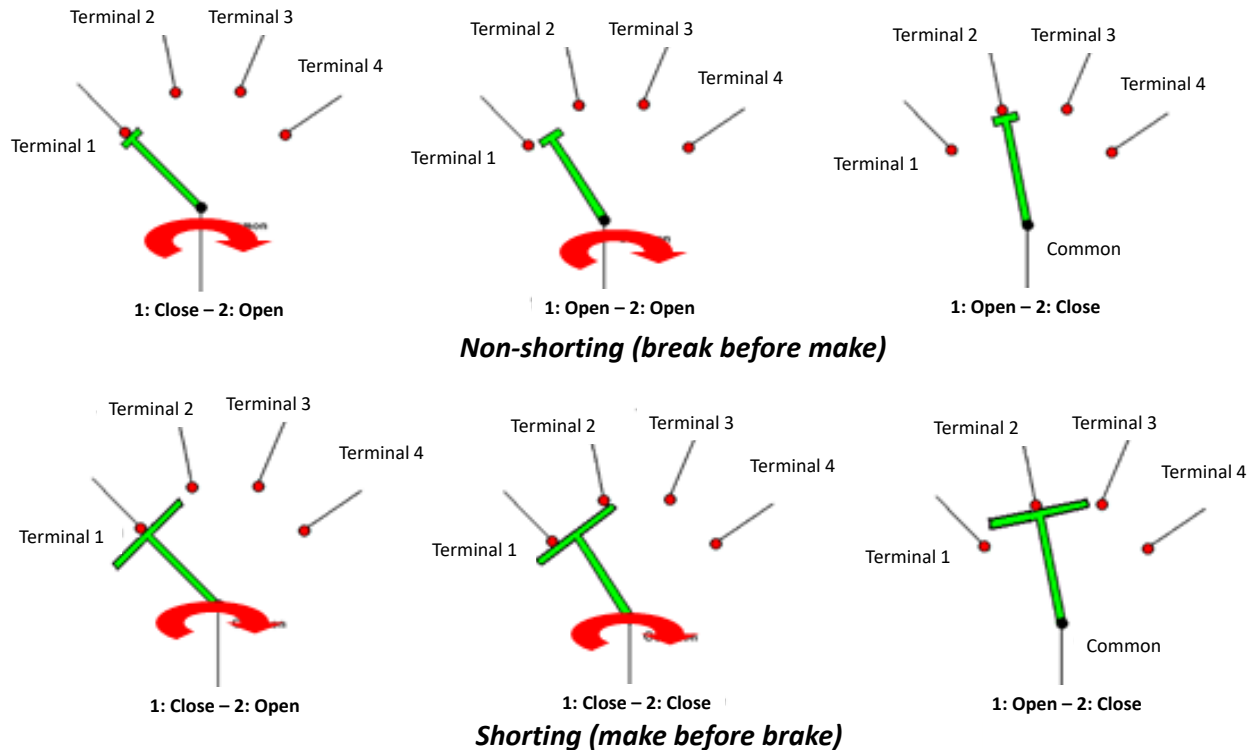


Figure 3.2.25. Break before make allows for shorting prevention [81].

The four switches are controlled by a microcontroller PWM signal at the operating frequency of 32 kHz. Figure 3.2.24 shows the implementation of an H-bridge driver. The inductive load will have a tuning capacitor in parallel. This tuning capacitor allows charge to flow back and forth between the plates of the tuning capacitor and the transmitter coil [82], which enables the circuit to oscillate at the operating frequency and the transmitter coil to generate AC magnetic field. In addition to the tank circuit, a voltage sensing feedback circuit is used to regulate the current of the inductor. This is created using 3 resistors, dividing the voltage to be recorded using microcontroller ADC. From there, the duty cycle of the PWM can be adjusted based on the inductor current magnitude. Figure 3.2.26 shows the driver design.

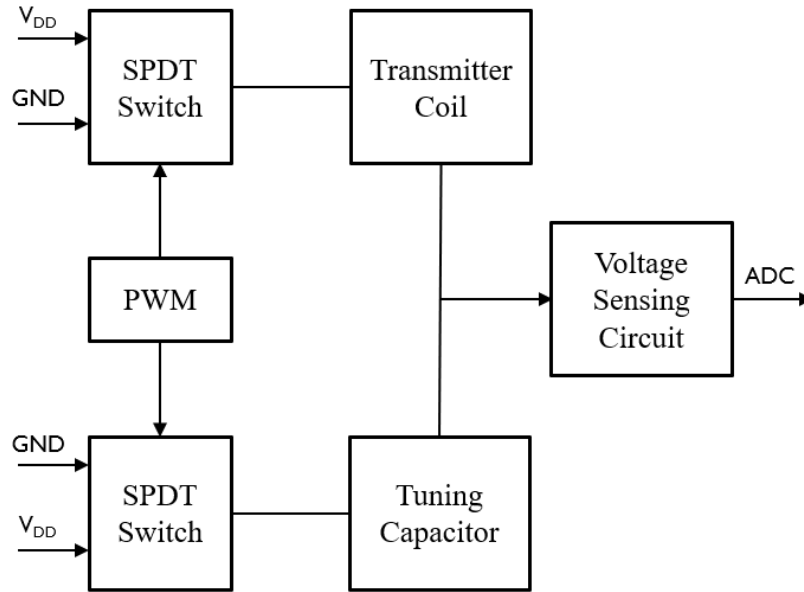


Figure 3.2.26. H-bridge driver design with voltage sensing feedback circuit.

To evaluate the H-bridge drive implementation, it is imperative to analyze the noise sources in the circuit. There are several possible noise sources. The first possible noise source is PWM phase noise. The noise is in-band at the carrier frequency of 32 kHz. This phase noise (jitter) is a key here since it affects the pulse width of the PWM. Changing the pulse width directly affects the transmitter coil's current, which in turn affects the strength of the generated magnetic field.

Also, if the transmitter coil's power is increased, the generated noise increases. Hence, it is imperative to keep this noise in mind. Amplitude noise can be ignored because the PWM is a control signal (either logic 1 or logic 0), so the slight changes in voltage level will not affect the current in the transmitter coil. Figure 3.2.27 below summarizes the possible noises seen in this system, where the red signal is the noiseless 32 kHz inductor current, and the gray signal depicts all the noise sources.

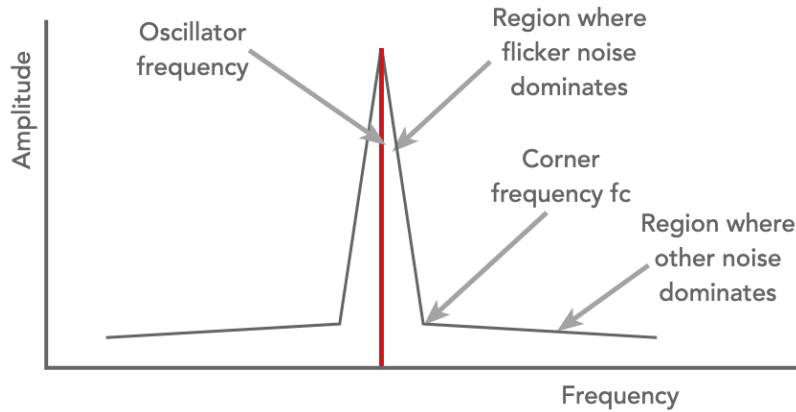


Figure 3.2.27. Hypothetical frequency domain curve of noise sources (gray) relative to transmitter coil inductor current (red).

Next, the resistor and channel noise sources are examined. There are many resistors in the circuit, including switching regulator internal resistance, SPDT on resistance, and coil resistance noise. Since the switching regulator and SPDT on resistances are  $< 1 \Omega$ , these resistors can be ignored in the noise analysis. This also means that the switch flicker ( $1/f$ ) noise can be ignored due to  $R_{switch} \ll R_{coil}$ . Tests are needed to confirm whether the flicker noise is negligible. Based on both time domain and frequency domain plots at low frequencies, a conclusion can be made on if this hypothesis is true. Figure 3.2.28 below illustrates flicker noise waveform.

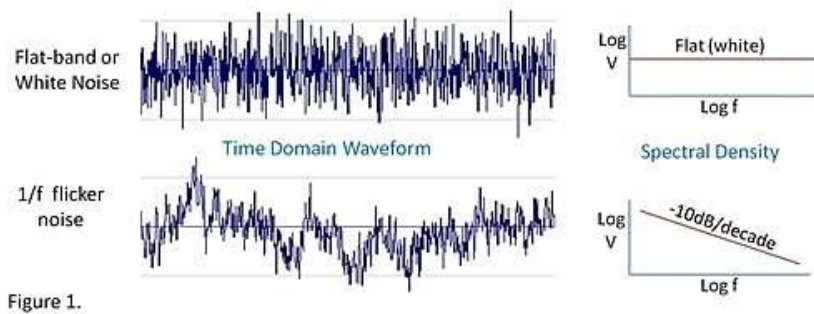


Figure 3.2.28. Flicker noise waveform pattern relative to white noise.

If the flicker noise is negligible, then only the coil resistor noise needs to be analyzed. This noise source is shaped by the LC resonator, which means that the noise center frequency depends on the LC tuning frequency, not the PWM control (i.e., operating) frequency.

With a general overview of the possible noise sources in the transmitter H-bridge driver circuit implementation, it is imperative to select the proper circuit parts and optimize the design.

A couple of methods are used to lower the effect of the PWM phase noise. One is the use of a low noise crystal. Instead of generating PWM using an internal microcontroller crystal, an external crystal is used. A digital low pass filter and feedback with hysteresis is implemented. As noted above, the H-bridge SPDTs are implemented using commercially available single pole double throw switches in a single integrated circuit (IC) package (ADG884). Figure 3.2.29 below shows the schematic of this series LC loop. The driver is powered with three different voltages: 5 V, 3 V, 2.2 V. The first is through USB, and the latter 2 are generated using switching regulators. Two 22  $\mu\text{F}$  capacitors are used at each of the switching regulator output to mitigate the noise. The 3 V is used for the voltage sensing feedback for the PWM duty cycle control (not shown in schematic). The 5 V is used for the SPDT  $V_{\text{DD}}$  line. The 2.2 V is the analog  $V_{\text{DD}}$  of the coil. The original 5 V analog  $V_{\text{DD}}$  design described above for the hand calculations in Table 3.2.3 was not used because the coil RMS current exceeds 150 mA, which means that the coil operating temperature will not be below the threshold determined by the bioheat equation. Thus, the  $V_{\text{DD}}$  selected was 2.2 V, which results in a 70 mA RMS current. This current is satisfactory for the initial test of tracking the catheter in a 20 cm distance.

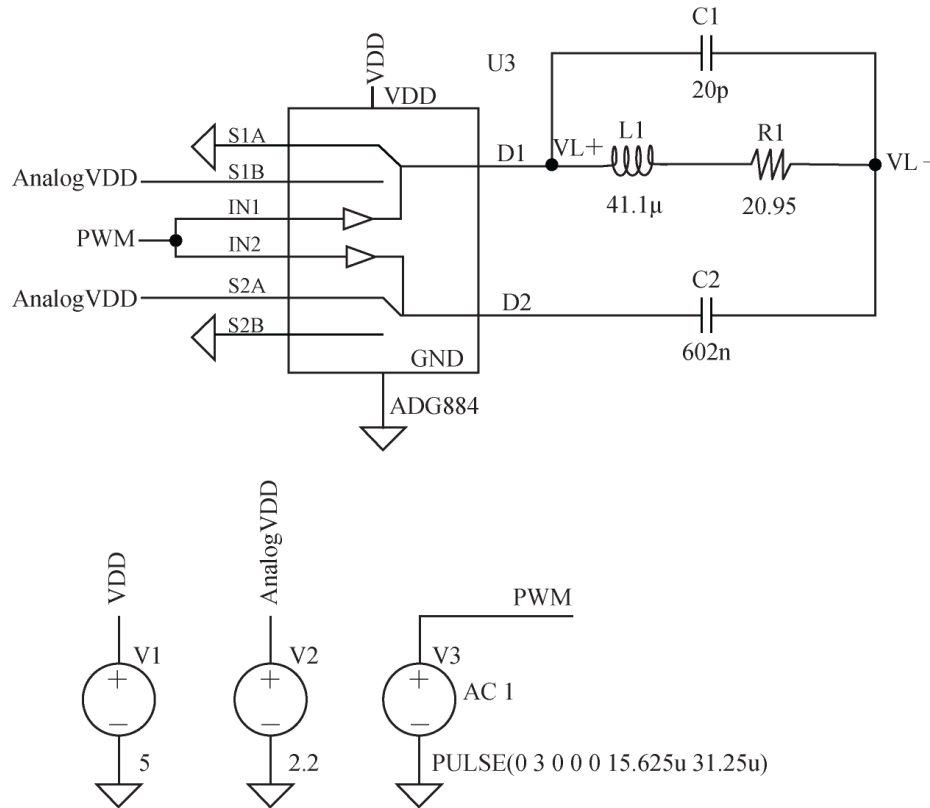


Figure 3.2.29. Transmitter driver LC loop (final version coil).

The voltage and current across the inductor (L1 in schematic) are determined in simulation. Figure 3.2.30 and Table 3.2.6 below show the simulation result for the tested circuit.

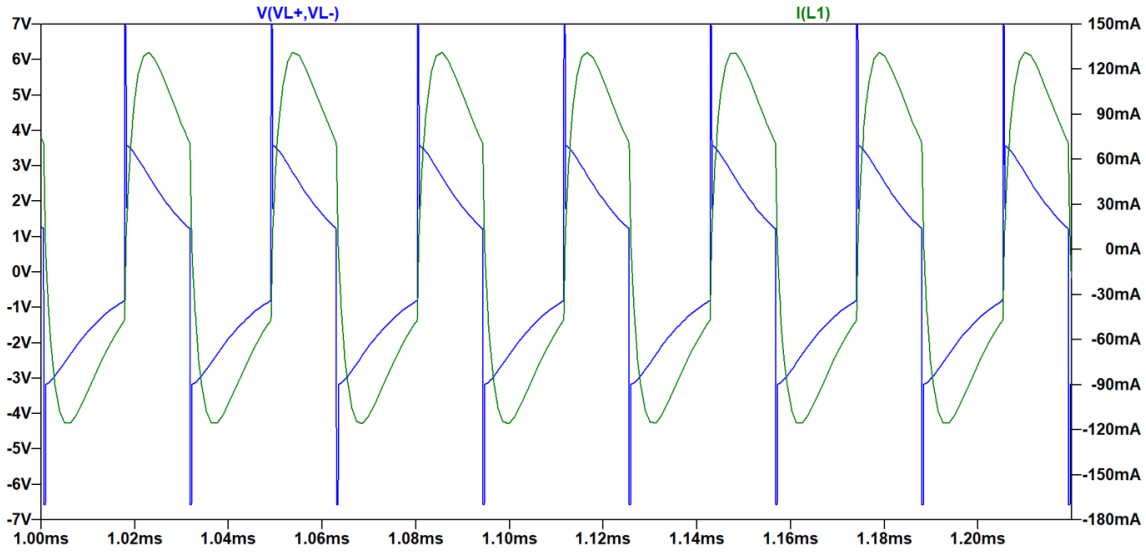


Figure 3.2.30. Simulation results: blue line: voltage across inductor and green line: current through inductor.

Table 3.2.6. RMS current and power of coil at 32kHz for various operating voltages.

	RMS Voltage Across Inductor (V)	RMS Current Across Inductor (mA)	RMS Power (mW)
Simulated	2.52	71.10	179.36
Measured	2.45	69.16	169.69

In addition, a Fourier Analysis was performed to evaluate the power of the fundamental tone and the efficiency of the transmitter driver. As seen in Figures 3.2.31, there is significant odd harmonic distortion. Although the difference between the 1<sup>st</sup> and 2<sup>nd</sup> order harmonics is greater than 100 dB, the difference between the 1<sup>st</sup> and 3<sup>rd</sup> order harmonics is less than 15 dB, which means a large amount of power wasted on the 3<sup>rd</sup> tone and other higher order odd harmonics. For the proof of concept stage of the tracking system, this H-bridge driver architecture is used in the tracking system, but in the final implementation, an alternative design has to be considered to lower the effect of total harmonic distortion (THD). This alternative design is the op-amp driver discussed in the introduction of the driver section.

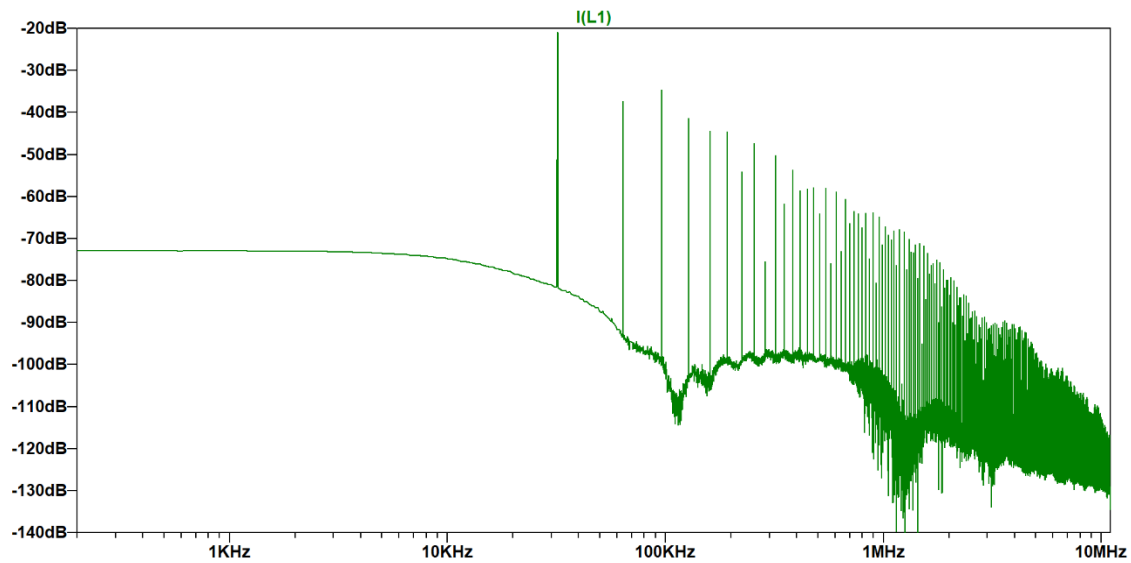


Figure 3.2.31. Frequency domain simulation results of current across inductor.

The circuit shown above, along with the switching regulators and feedback voltage sensing resistors, is fabricated on a PCB shown below in Figure 3.2.32.

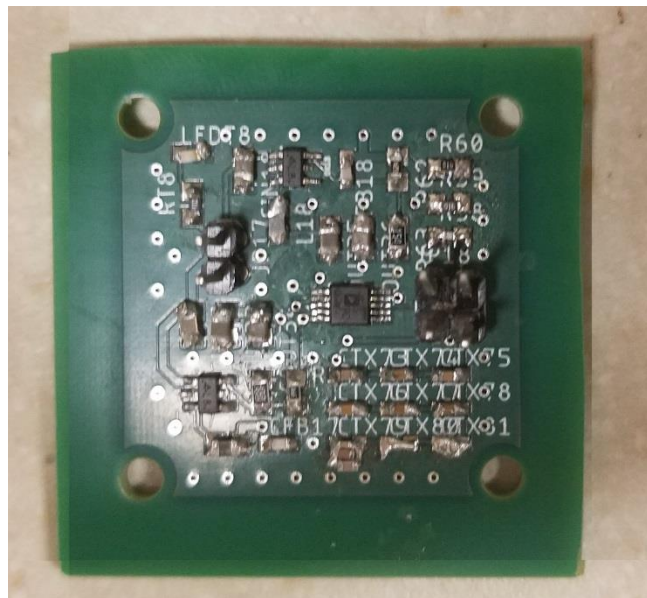


Figure 3.2.32. PCB for H-bridge transmitter driver.



The transmitter coil designed is attached to the twisted-pair cable which is in turn connected to the driver on the PCB (Figure 3.2.32). With the driver powered on, the coil power specifications are recorded by measuring the voltage across the coil to verify its function using the simulation results obtained earlier. Figure 3.2.33 below shows the voltage across the transmitter coil in time domain.

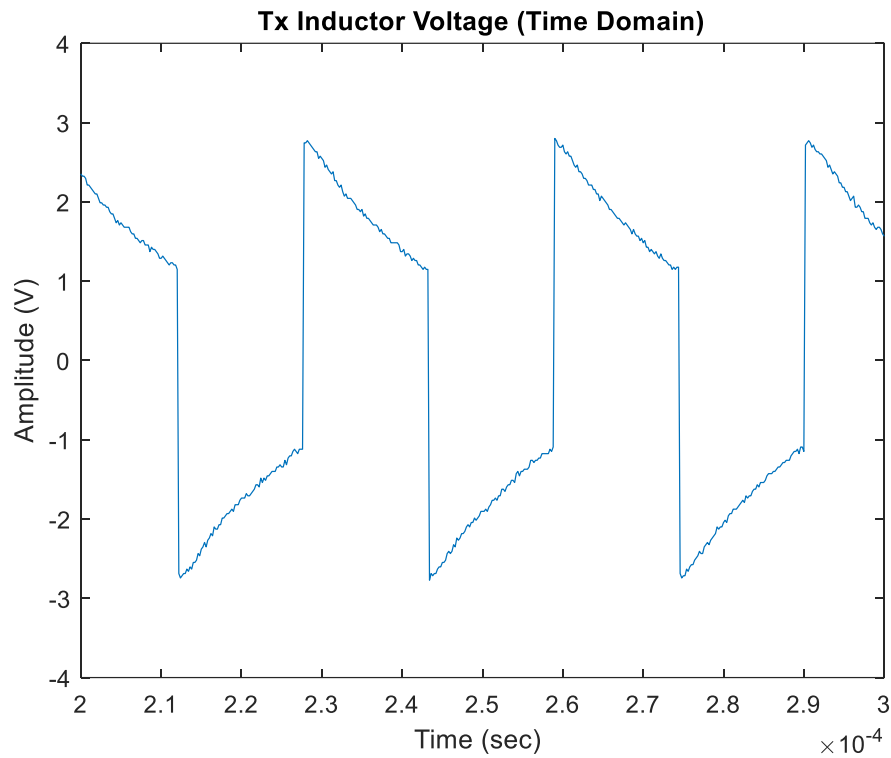


Figure 3.2.33. Measured voltage across the transmitter coil.

Table 3.2.7 below compares the powers of the simulated and measured systems. The measured voltage and current are roughly similar to the simulation results, where the RMS power of the coil is 170 mW.

Table 3.2.7. RMS current and power of final version transmitter coil 32kHz.

	RMS Voltage Across Inductor (V)	RMS Current Across Inductor (mA)	RMS Power (mW)
Simulated	2.52	71.10	179.36
Measured	2.45	69.16	169.69

The frequency domain plot of the voltage across the inductor is shown below. The effects of higher order harmonics, along with noise, are analyzed for the actual coil.

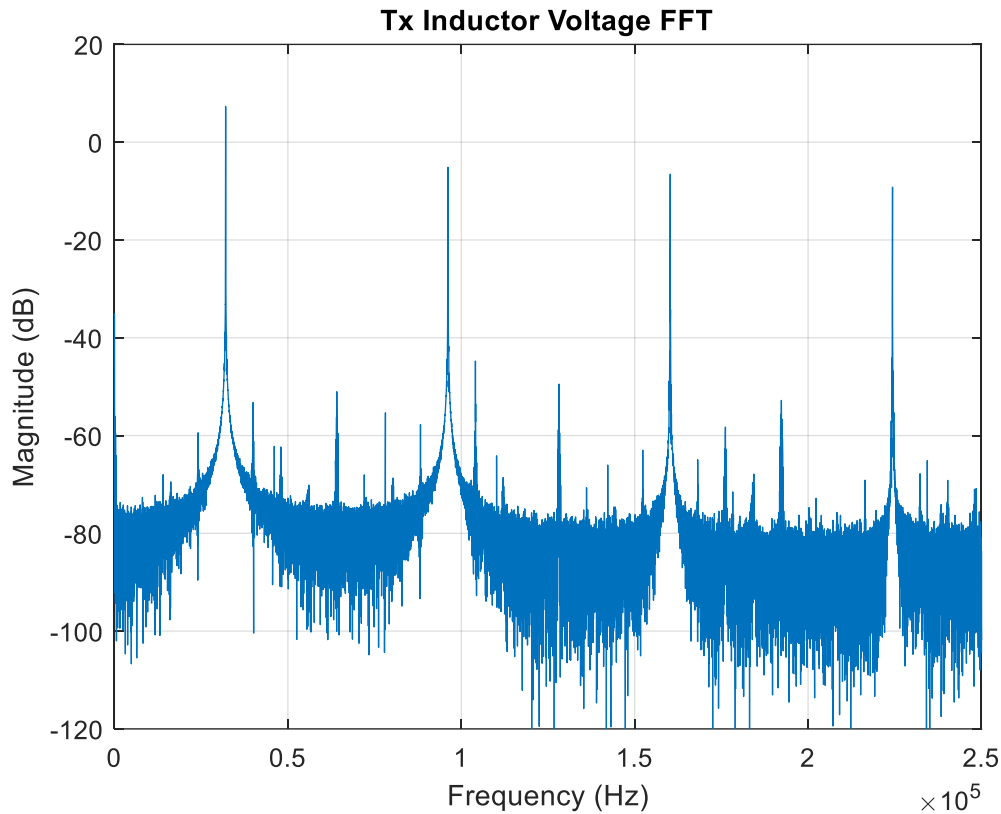


Figure 3.2.34. Frequency domain plot of voltage across the transmitter coil.

As in Figure 3.2.34 above, very similar harmonic distortions can be seen in the actual measured voltage across the transmitter coil. The main tone is at 32 kHz with 2<sup>nd</sup> harmonic at 64 kHz and 3<sup>rd</sup> harmonic at 96 kHz. The difference between the 1<sup>st</sup> and 3<sup>rd</sup> harmonics is on the order of 10 dB, which corresponds to what is determined from the simulation result (Table 3.2.8). Other higher order harmonics show similar results, and thus these harmonics are not negligible and need to be factored in future analysis.

Table 3.2.8. Comparison of simulated and measured harmonic tones.

Data Type	Fundamental Tone (dB)	2nd Harmonic (dB)	3rd Harmonic (dB)	Difference between 1st and 2nd Harmonics	Difference between 1st and 3rd Harmonics
Simulated Inductor Current	-19.64	-125.25	-33.15	105.61	13.51
Simulated Inductor Voltage	9.56	-92.27	-0.046	101.83	9.61
Measured Inductor Voltage	8.91	-44.87	-1.54	53.78	10.45

To evaluate the noise in the transmitter circuit, an FFT is run on the node between the inductor (coil) and the tuning capacitor. Through the FFT results, we can test the above stated hypothesis that flicker noise and other nondominant low frequency noise sources are negligible. Figure 3.2.35 below shows the frequency domain plot of the voltage at the LC node of the circuit. This frequency domain plot was obtained on oscilloscope to maximize window length and obtain more precise frequency plot. A zoom in of the first and second harmonics is shown to check the mixing frequencies. There are a lot of mixing frequencies, hence a lot of side lobes. Define  $\Delta f$  as the change in frequency between mixing frequency components. All higher order harmonics (e.g., 3<sup>rd</sup>, 4<sup>th</sup>, 5<sup>th</sup>, etc.) exhibit the same mixing frequencies, along with the same  $\Delta f$ . As mentioned in the transmitter driver introduction, the large magnitude of higher order harmonics and mixing is due to the low quality factor (Q) of the coil having a wide passband and a noisy PWM signal (with high order harmonics) which introduces significant distortion to the AC current in the inductor.

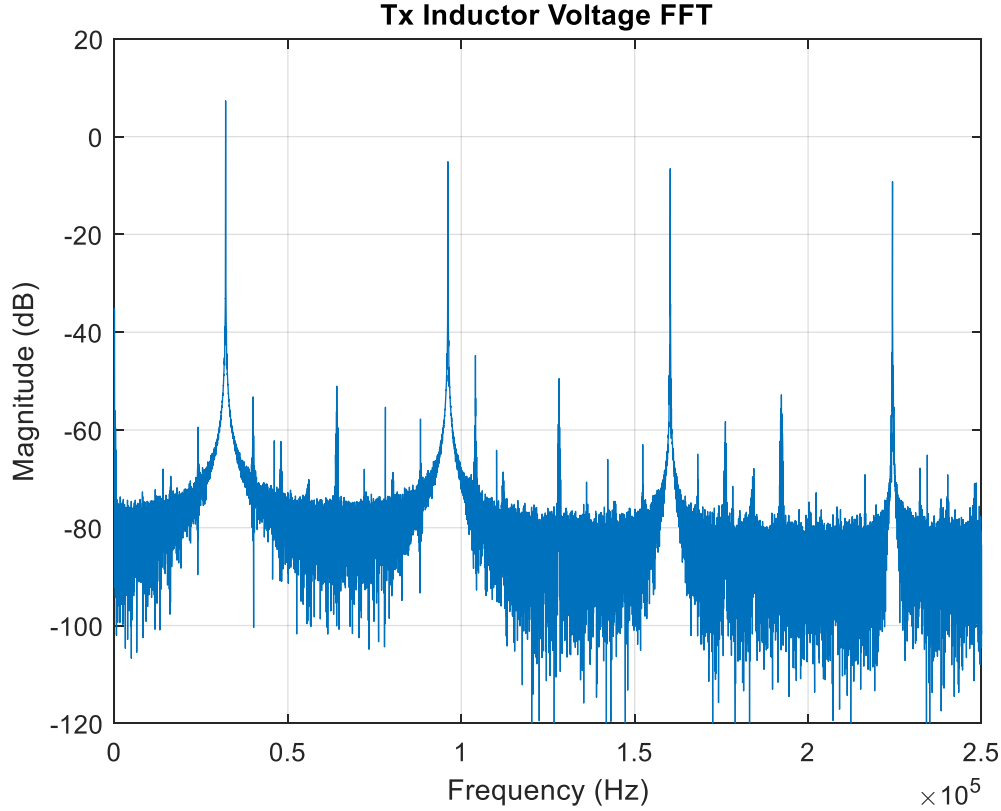


Figure 3.2.35. Frequency domain plot of voltage at LC node and mixing frequencies for 1<sup>st</sup> and 2<sup>nd</sup> order harmonics.

From these results, it can be concluded that the H-bridge driver produces large higher order harmonic signals in addition to the main tone. This driver was used in the early testing stages and proof of concept verification for the heart shape mapping system. However, for the final implementation, an alternate transmitter driving circuit design is proposed as discussed below.

#### ***Transmitter Driving Circuit (Op-Amp Based Driver) and Coil Connection***

This section describes the evaluation of the second transmitter driver design for the proposed system. The transmitter is powered using a custom-built LC tank driving circuit. This circuit is required to drive the inductor coil at the operating frequency of 32 kHz with minimal noise and distortion so that the transmitted magnetic field is maximized subject to the heat constraints of the Pennes bioheat equation. Minimizing the noise and distortion allows for less heat dissipation.

The methods to reduce noise and distortion are discussed first. It is necessary to optimize the AC control signal to minimize noise and improve stability, because noise in the control signal can propagate to the current across the transmitter coil resulting in a noisy magnetic field. This will be done through an active feedback sensing system. Figure 3.2.36 below is the proposed transmitter system diagram.

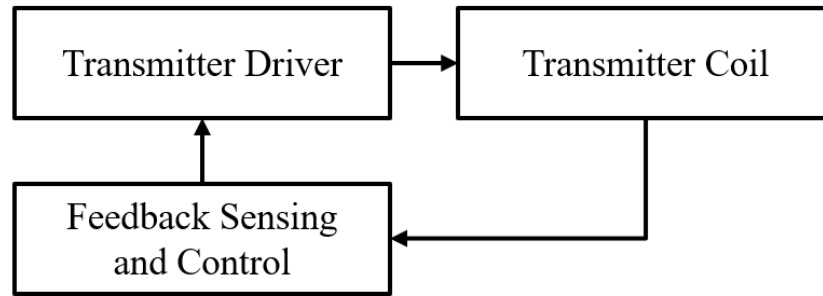


Figure 3.2.36. Transmitter system diagram.

The analysis from the H-bridge driver has shown that the low quality factor ( $Q$ ) of an air core transmitter coil results in a wide passband causing harmonics from the PWM control signal propagating to the inductor current, which leads to a distorted B-field signal. A new current driver circuit which reduces harmonics along with frequency mixing is considered. For this we look to an op-amp driver.

The op-amp driver amplifies an AC input signal with a clean DC battery power source to provide current. The op-amp design has the function of high current amplification along with low total harmonic distortion (THD). The current across the inductor is sensed using a clamping and voltage dividing circuit, and a firmware feedback sensing and control adjusts the AC control signal (Figure 3.2.37).

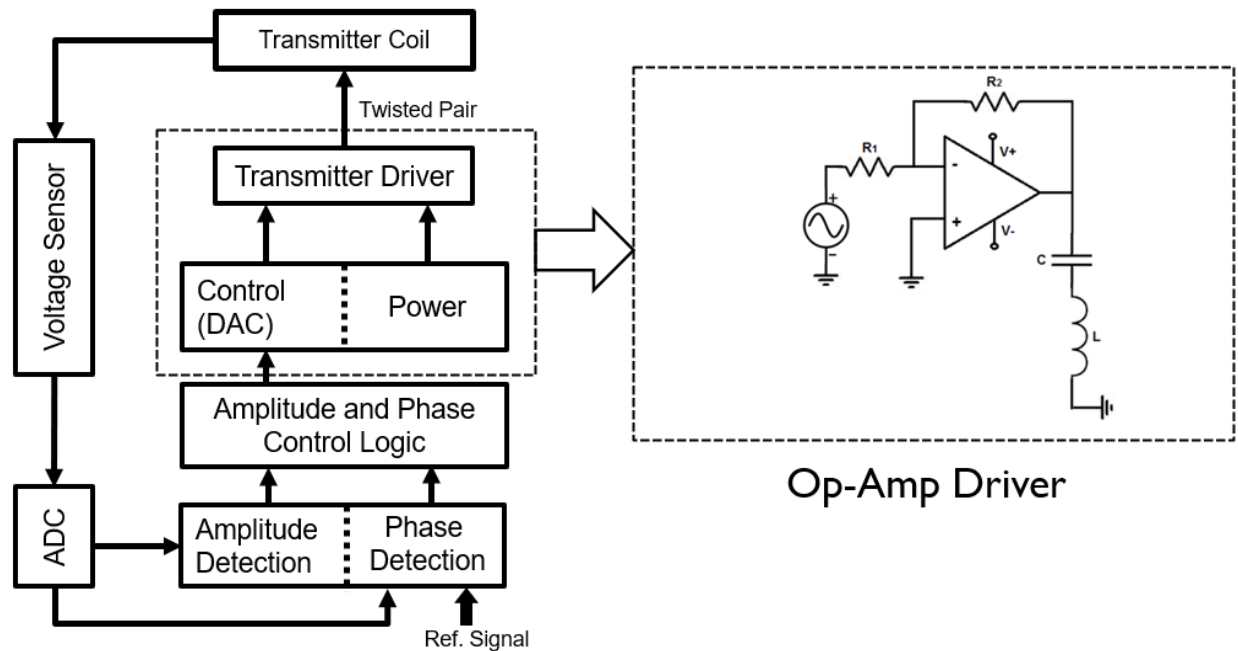


Figure 3.2.37. Block diagram of the transmitter system.

Other design features optimizing the driver include shielding the twisted pair wire with mu-metal to reduce the parasitic magnetic field generated by the high current wire.

### 3.2.9 AC Input Signal Generation and Feedback

32 kHz AC input signal generation is discussed in this section. The input signal is generated using a microcontroller programmable signal. For this, either a digital to analog converter (DAC) or a pulse-width modulated (PWM) signal can be utilized. For the proposed system, a DAC is used instead of a PWM signal because of the higher resolution and low power of high order harmonics of DAC. A 12-bit DAC signal is generated at a sampling rate of 2.4 MSPS. Oversampling the DAC causes the quantization noise to be moved away from the 32 kHz signal band, which results in noise shaping.

A test was performed to compare the frequency responses of a DAC signal with a PWM signal, using the same temperature compensated low phase noise crystal (TCXO) as a clock source for the microcontroller. From the experiment, we can observe from Figure 3.2.38 the reduction of sideband noise when it is changed from the PWM signal (blue curve) to the DAC signal (red curve). This is crucial as this sideband noise would appear in all harmonic components resulting in the

frequency mixing behavior observed in the earlier magnetic field produced by the H-bridge driver transmitter.

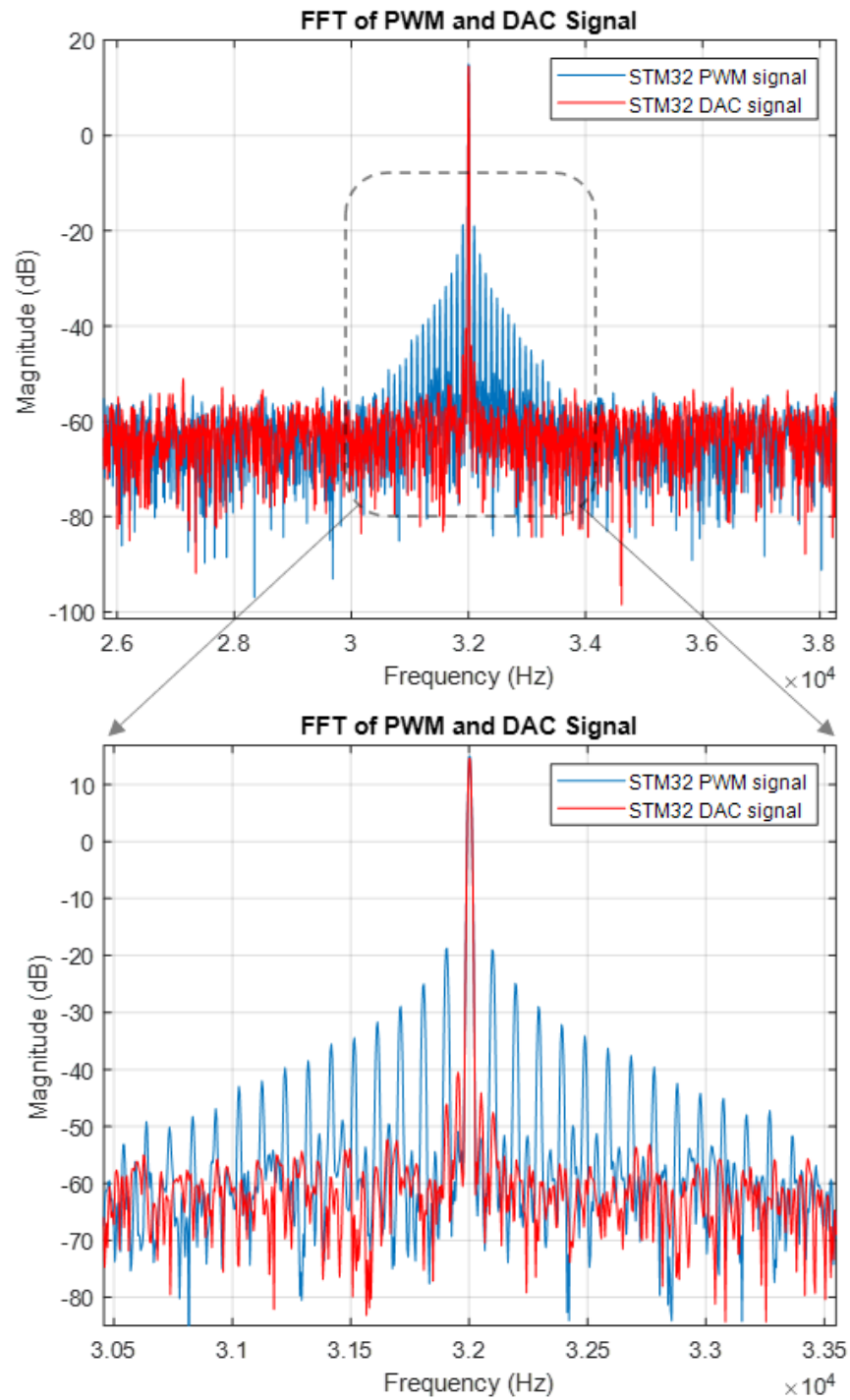


Figure 3.2.38. Comparison of STM32F4 PWM (blue) and DAC (red).

We now examine the feedback system. The goal is to further reduce the phase noise. The functionality of the DAC in relation to the transmitter (Tx) driver is shown in Figure 3.2.39. The DAC signal is generated based on the amplitude and phase measured from the transmitter coil. This measurement is done through an ADC. Afterwards, post-processing is performed on the sensed signal, and a digital comparator algorithm is used to obtain the phase of the transmitter signal in relation to the reference 32 kHz signal generated by the crystal on the microcontroller STM32F4 board. This forms a phase locking system, which syncs up the DAC signal to the reference. A temperature compensated low phase noise crystal (TCXO) along with the phase locking system allows for a low-noise clean AC control signal which leads to a transmitter magnetic field with minimal noise.

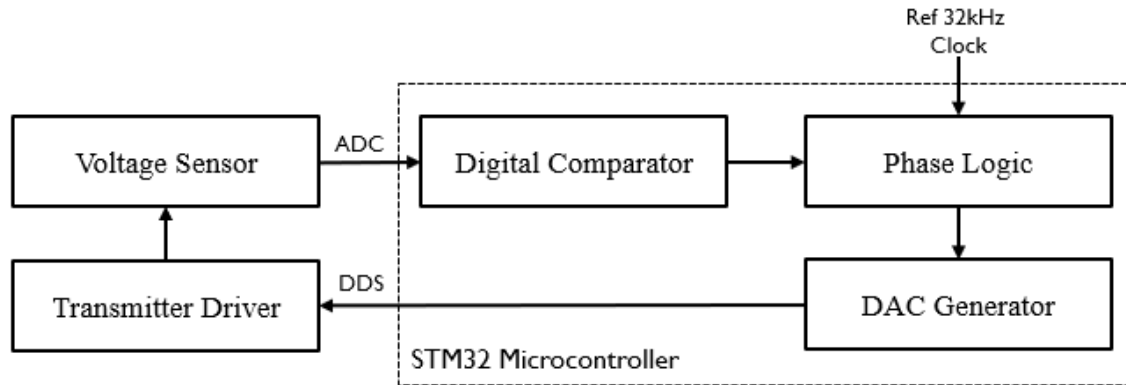


Figure 3.2.39. Phase and amplitude-controlled DAC with Tx driver.

Next, the op-amp driver is designed. The overall schematic of the op-amp driver is shown in Figure 3.2.39. The op amp is powered by single supply with a 5 V DC battery source boosted to 12 V. The boosting is performed using a switching regulator, which allows for a clean high current power source, with minimum ripple.

For the LC tank configuration, the LC can be designed either in series or parallel with each other. For the proposed system, a series LC is implemented. Hand calculations below show why this formation is preferable. First, the AC inductor current relative to the op-amp current is calculated. The goal is to select the formation with the most efficient conversion from the op-amp current to the AC inductor current. A higher op-amp current results in larger op-amp output THD.



For a parallel LC, the inductor current ( $I_L$ ) is about  $Q$  times of the op-amp output current ( $I_{OP-AMP}$ ), as shown in the equation below:

$$I_L = \left( \frac{\frac{1}{j\omega C_{total}}}{\frac{1}{j\omega C_{total}} + R + j\omega L} \right) I_{OP-AMP} \quad (3.2.9.1)$$

$$= \left( \frac{1}{1 - \omega^2 LC_{total} + j\omega RC_{total}} \right) I_{OP-AMP} \approx \frac{1}{j\omega RC_{total}} I_{OP-AMP} \approx \frac{Q}{j} I_{OP-AMP}$$

In series LC, the inductor current is almost the same as the op-amp output current.

$$I_L \approx I_{OP-AMP} \quad (3.2.9.2)$$

The transmitter coil has a  $Q$  value of 0.4. Thus, if the parallel formation were used, about 60% of the op-amp output current would be wasted to the capacitor in parallel formation, as the current had to split between the inductor branch and capacitor branch. In the series formation, no op-amp output current is wasted because there is only one current path at the output. The above analysis was verified by simulations (Figure 3.2.40–3.2.42).

Another issue with the parallel configuration is that the terminal of the inductor not connected to the op-amp output has to be biased to the output DC voltage of the op amp. In contrast, the bottom of the inductor in series can be connected to a ground terminal. This is because in the series configuration, there is only one current branch at the op-amp output, and when the capacitor is attached to the output of the op amp, it blocks the DC output current from flowing across the inductor to ground. Hence, in the series configuration, the output does not need a DC bias circuit, and the op amp auto-biases the output.

Finally, the frequency response behavior is analyzed. This is done by running a simple LTSPICE simulation with values based on the transmitter coil used in the H-bridge design (Figure 3.2.40). V1 and V2 simulate AC voltage at the output of the op amp. A 20 pF capacitor is added based on the self-capacitance formula of the coil. Because the skin and proximity effects have been shown to be minimal for the coil design, the formula for a single layer coil is used for simplicity.

$$C_s = \frac{2\pi d_m}{\cosh^{-1} p/d} = 20 \text{ pF} \quad (3.2.9.3)$$

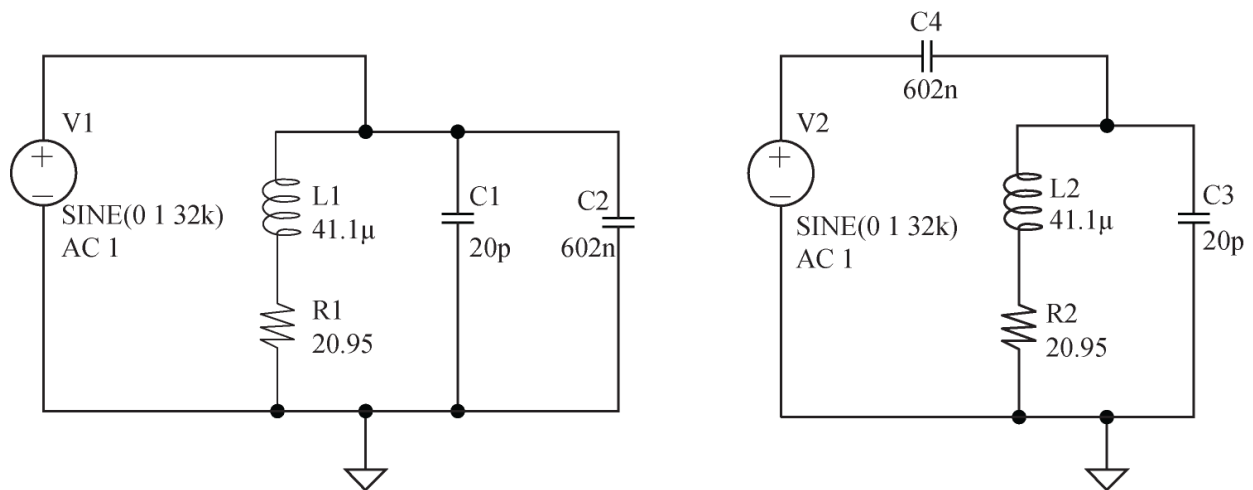


Figure 3.2.40. Simulation schematic of parallel LC (left) and series LC (right).

The magnitude Bode plot is obtained from an AC sweep simulation, and the inductor current behaviors for the parallel  $I(L1)$  and series  $I(L2)$  are plotted in Figure 3.2.41. In addition, a transient simulation is performed to confirm the inductor current to op-amp current efficiency hand calculations.

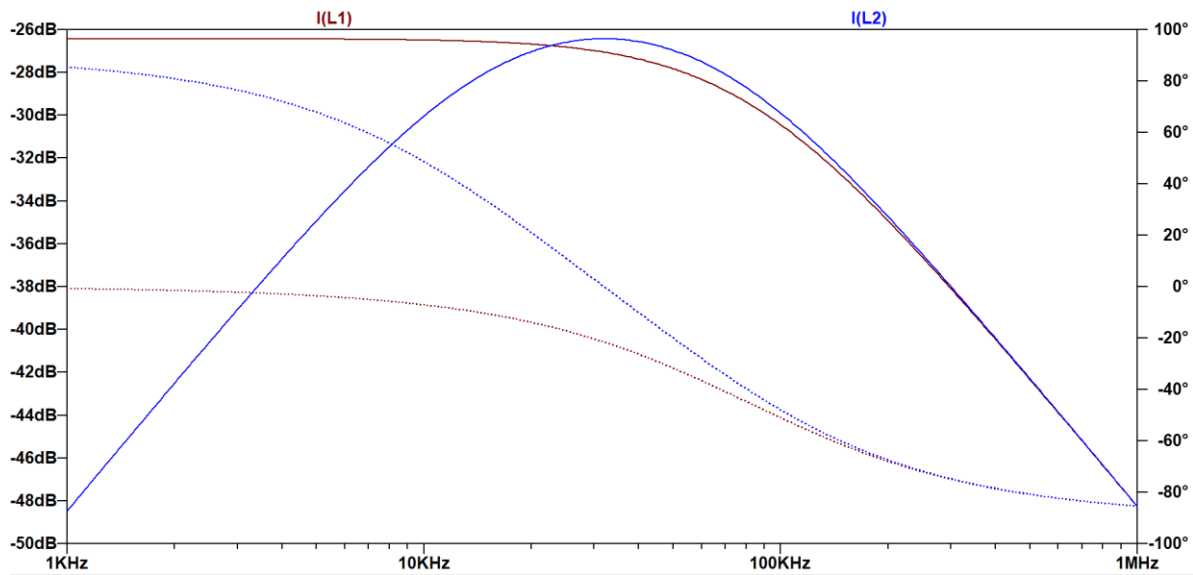


Figure 3.2.41. Simulation Bode plot of transmitter inductor current for parallel LC  $I(L1)$  and series LC  $I(L2)$  driver circuits.

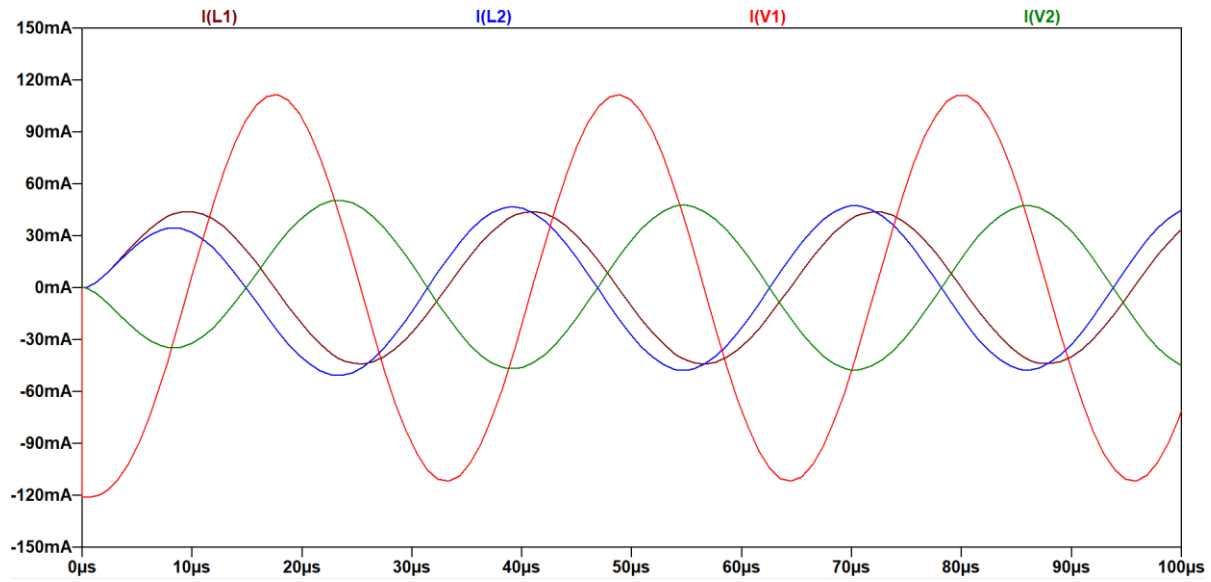


Figure 3.2.42. Simulation transient plot of op-amp and inductor currents for parallel LC ( $I(V1)$  and  $I(L1)$ ) and series LC ( $I(V2)$  and  $I(L2)$ ) driver circuits.

The transient simulation confirms our results from hand calculations. Both formations are simulated with the same AC voltage source, which mimics the op-amp output AC voltage. This results in the same inductor current  $I(L1) = I(L2)$ . The currents drawn from the op-amp output  $I(V1)$  and  $I(V2)$  are examined. Thus, the required op-amp output current for parallel  $I(V1)$  is 40% larger than that of series  $I(V2)$ , and we can see that  $I(V2) \approx I(L2)$  in Figure 3.2.42. From the Bode plot (Figure 3.2.41), the frequency response for the parallel formation is lowpass for inductor current  $I(L1)$ , and the frequency response for the series formation is bandpass for inductor current  $I(L2)$ . The bandpass response of the series formation is because the inductor current is shared with the capacitor in the same branch, which allows for both low frequency and high frequency rejections, optimizing the current for the transmitter at the 32 kHz operating frequency. From the above analysis, a series LC configuration is selected for the transmitter driver.

Finally, the closed loop gain architecture and sensing circuit are considered. The inverting amplifier formation is selected. Although the inverting amplifier has poor input impedance because of the resistance connected at the input, the non-inverting amplifier has more significant drawbacks, resulting in increased noise and distortion. This is due to the non-inverting formation having no virtual ground, resulting in poor common mode anti-interference [83].

A voltage sensing circuit is used to measure the voltage across the Tx coil, which is converted into current to determine the coil B-field strength. This circuit is passive and must have

minimal interference with the Tx inductor current, while still being able to extract the coil current magnitude. First, the signal must be attenuated (from 6 V<sub>p-p</sub> down to 2.5 V<sub>p-p</sub>) so that it can fit within the ADC voltage sampling range (0 to 3 V max range) of the microcontroller. This attenuation is performed in a tandem circuit consisting of a resistor divider and a clamping circuit. The resistor divider lowers the voltage amplitude to meet the ADC range and resolution specifications, and the clamping circuit removes the negative cycle of the wave since ADC cannot measure negative voltage. In addition, a second switching regulator is added as part of the clamping circuit to offset the negative voltage shift due to the forward biasing of the clamping circuit diode.

The op-amp driver schematic is illustrated in Figure 3.2.43. A 12 V DC source is used (in implementation, a 5 V battery boosted to 12 V using a switching regulator). A 1 pF self-capacitance of the inductor is assumed for this simulation. In addition, a resistor divider network is used for op-amp biasing. The op amp is in inverting formation, meaning that the gain is  $R_2/R_1 = -2$ . Thus, with an input of 3 V<sub>p-p</sub> the output has an amplitude of 6 V<sub>p-p</sub>. The voltage sensing circuit is composed of a resistor divider ( $R_3$ ,  $R_4$ ) and a clamping circuit ( $R_5$  and diode). The resistor divider consists of a 1 M $\Omega$  and a 750 k $\Omega$  resistors, which is used to divide the Tx coil voltage because the peak to peak amplitude of the coil voltage exceeds the maximum ADC input voltage. As noted above, a clamping circuit is used to remove the negative half of the AC signal to fit ADC of the microcontroller to measure the Tx power. A switching regulator is used to generate 0.7 V DC  $V_{bias}$  to DC shift the AC signal.

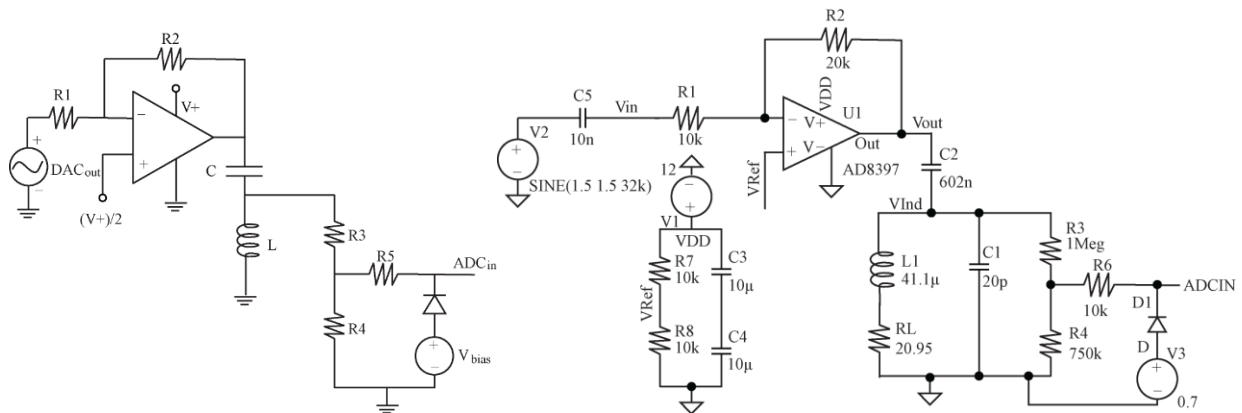


Figure 3.2.43. Schematic of op-amp based transmitter driver with sensing circuit (left) and LTSPICE simulation (right).

The complete op-amp driver and voltage sensing circuit is simulated in LTSPICE. Time domain and frequency domain simulations are performed on the inductor current  $I(L1)$ . Figure 3.2.44 shows the time domain simulation results of the op-amp output voltage  $V(vout)$  and the current across the inductor  $I(L1)$ . The  $V(vout)$  curve shows that the op amp is capable of driving the series LC with a 6 V<sub>p-p</sub> swing based on the design parameters. However, the most important result is the shape of the  $I(L1)$  curve, since it directly impacts the transmitting magnetic field. The AC current across the transmitter coil is 240 mA<sub>p-p</sub>, which is within the maximum current determined from the Pennes bioheat equation. According to the frequency domain plot in Figure 3.2.45, the simulated noise and distortion is minimal, where most of the power is successfully delivered to the main operating frequency (32 kHz). The highest harmonic component is the 3<sup>rd</sup> order with a 38.5 dB difference from the fundamental tone. This means that the simulated current that contributes to distortion is 80 times smaller than the fundamental tone.

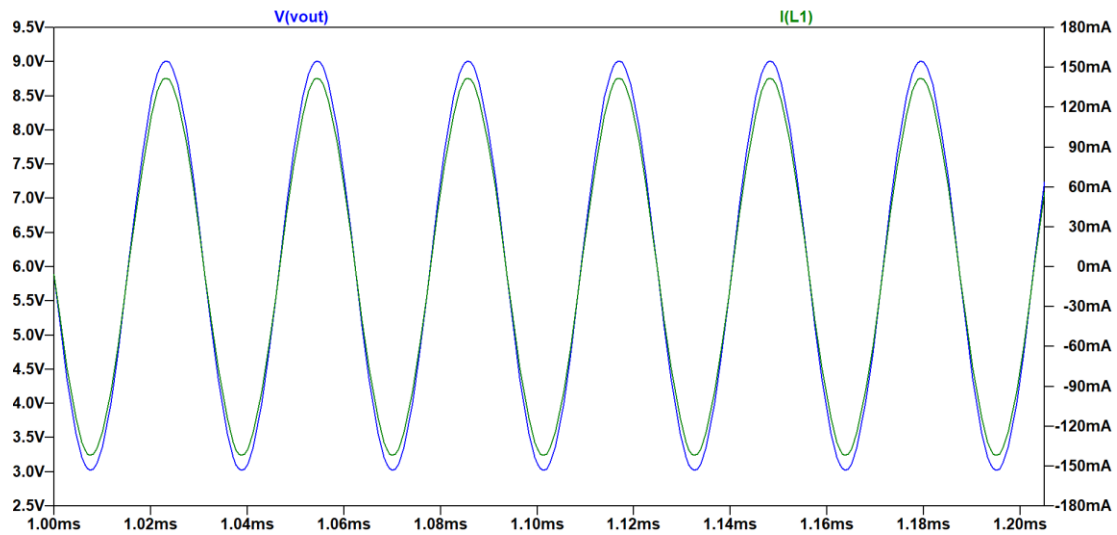


Figure 3.2.44. Time domain simulation results of op-amp based transmitter driver.

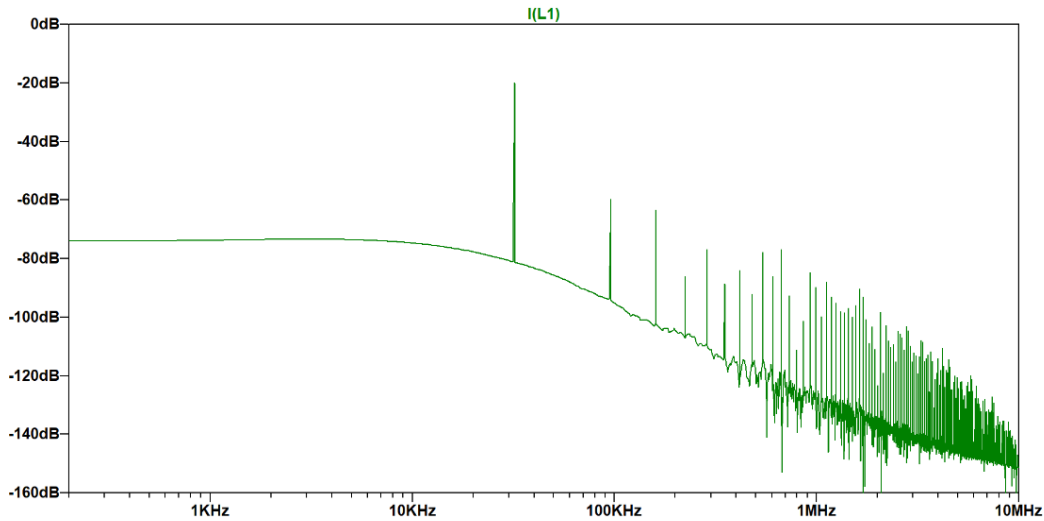


Figure 3.2.45. Frequency domain simulation results of op-amp based transmitter driver.

In the next step, this op-amp driver, along with the feedback sensing circuit and transmitter coil connection using the twisted pair wire, is tested. Time domain results are obtained using an oscilloscope measuring the voltage at the op-amp output and the voltage across the inductor, which are then converted to current through Ohm's law to compare with the simulation results. The experimental results show very similar op-amp peak to peak voltage and voltage across inductor of 6 V<sub>p-p</sub> (Figure 3.2.46). Convert this to current results in the same 240 mA<sub>p-p</sub>. In addition, through a fast Fourier transform, the frequency response of the measured inductor voltage is determined. Compared to the simulation results, the 2<sup>nd</sup> order harmonic is more prevalent. However, even with a noticeable 2<sup>nd</sup> order harmonic component, the 3<sup>rd</sup> order harmonic has a significantly smaller magnitude with a 53.5 dB difference between 3<sup>rd</sup> order and main tone. The 2<sup>nd</sup> order component is in a 40.8 dB difference between 3<sup>rd</sup> order and the main tone. Here we assume that the magnitudes of inductor current and voltage frequency response can be converted based on the DC+AC resistance of the coil. From Figure 3.2.47, the total harmonic distortion of the inductor voltage is approximately 110 times smaller than the fundamental tone, where the significant contribution of distortion comes from the 2<sup>nd</sup> and 3<sup>rd</sup> order harmonics. The above analysis verifies the functionality of the op-amp driver, along with its improvements compared to traditional LC tank circuits such as an H-bridge driver.

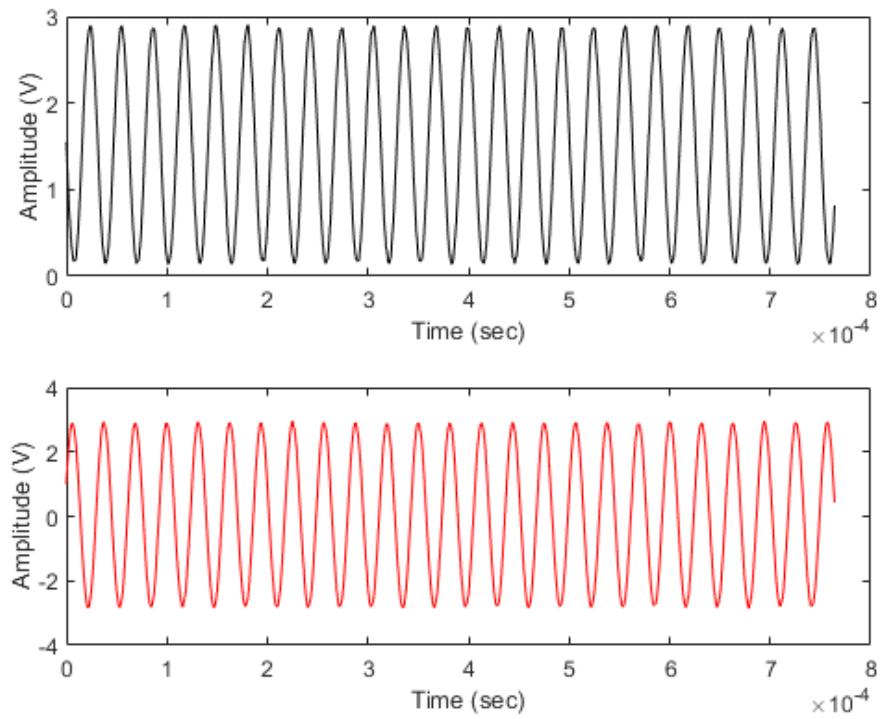


Figure 3.2.46. Time domain voltage of DAC signal (upper) and inductor voltage (lower).

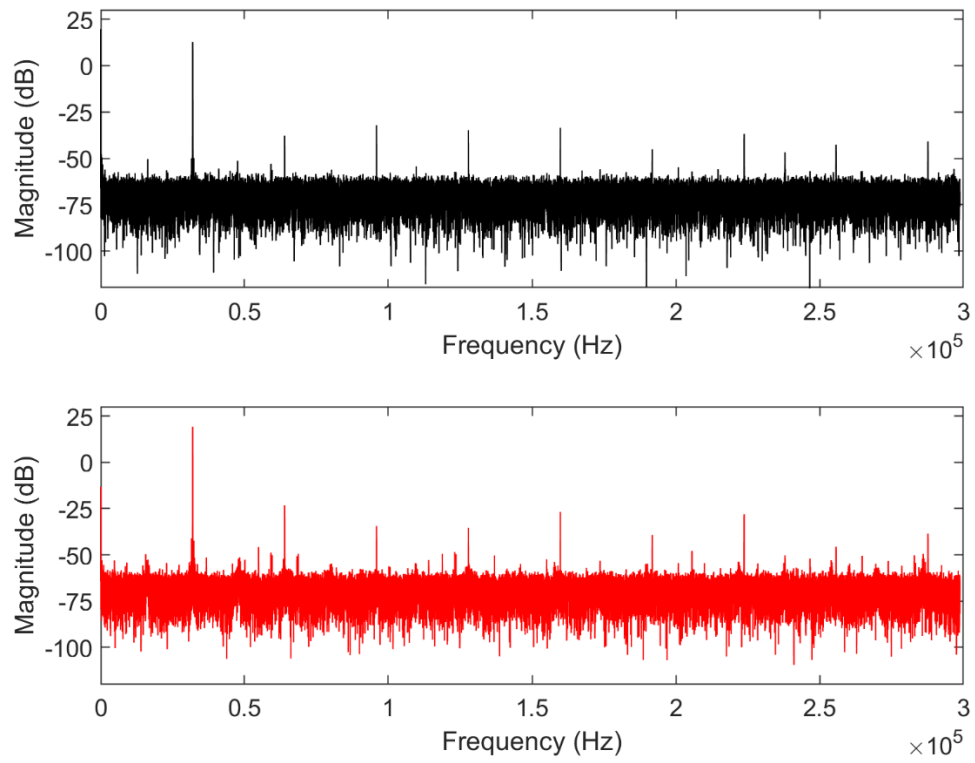


Figure 3.2.47. Fast Fourier transform (FFT) of DAC signal (upper) and inductor voltage (lower).

In addition, the reduction in higher order harmonics (peaks with frequencies of multiples of 32 kHz) allows for a higher operating current of 100 mA RMS than the 80 mA RMS current used in the preliminary H-bridge design because more power can be provided to the main tone of the signal.

However, one significant drawback of the op-amp design is that it requires higher voltage and current from a power supply than traditional LC tank circuits, though the additional voltage and current (12 V and 500 mA, respectively) required are lower than that of most other magnetic positioning systems [84]. Even with this drawback, the measurement tests show that the transmitter coil frequency response is better than the H-bridge design.

The power consistency of the Tx coil using the op-amp design is verified by extracting the RMS Tx coil voltage over time. This is shown in Figure 3.2.48.

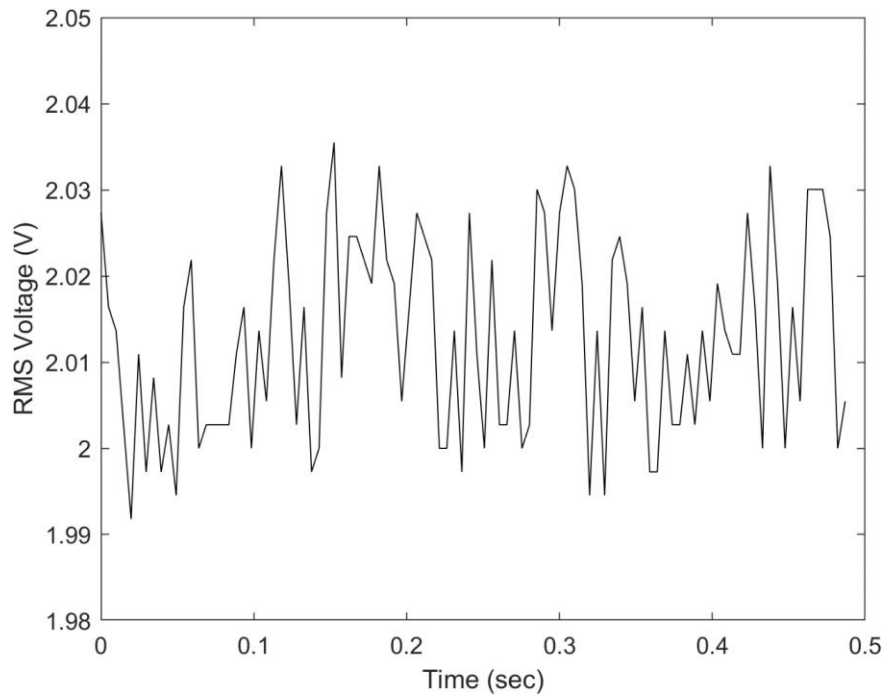


Figure 3.2.48. Transmitting coil RMS voltage over time.

In this design, the target current is 100 mA RMS. With a DCR of approximately  $25 \Omega$ , this means that the RMS voltage needs to be at 2 V, which is confirmed in Figure 3.2.48. In addition, the maximum voltage deviation from the nominal voltage is 30 mV (0.07 percent change of the original power level), meaning that the B-field generated by the transmitter coil is stable.



In conclusion, despite the above-mentioned drawbacks of the op-amp design, both simulation and measurement results indicate that its noise and higher order harmonic magnitudes are significantly lower than those of the H-bridge driver described in the previous section. In the proposed tracking system, the op-amp driver with voltage sensing circuit and DAC control signal is used to transmit an AC B-field.

### 3.2.10 Transmitter Integration into System Level

This section describes the integration of the op-amp driver and voltage sensing circuit into the complete system with the sensing circuit. Figure 3.2.49 below shows the block diagram of the transmitter system, along with its connection to relevant hardware.

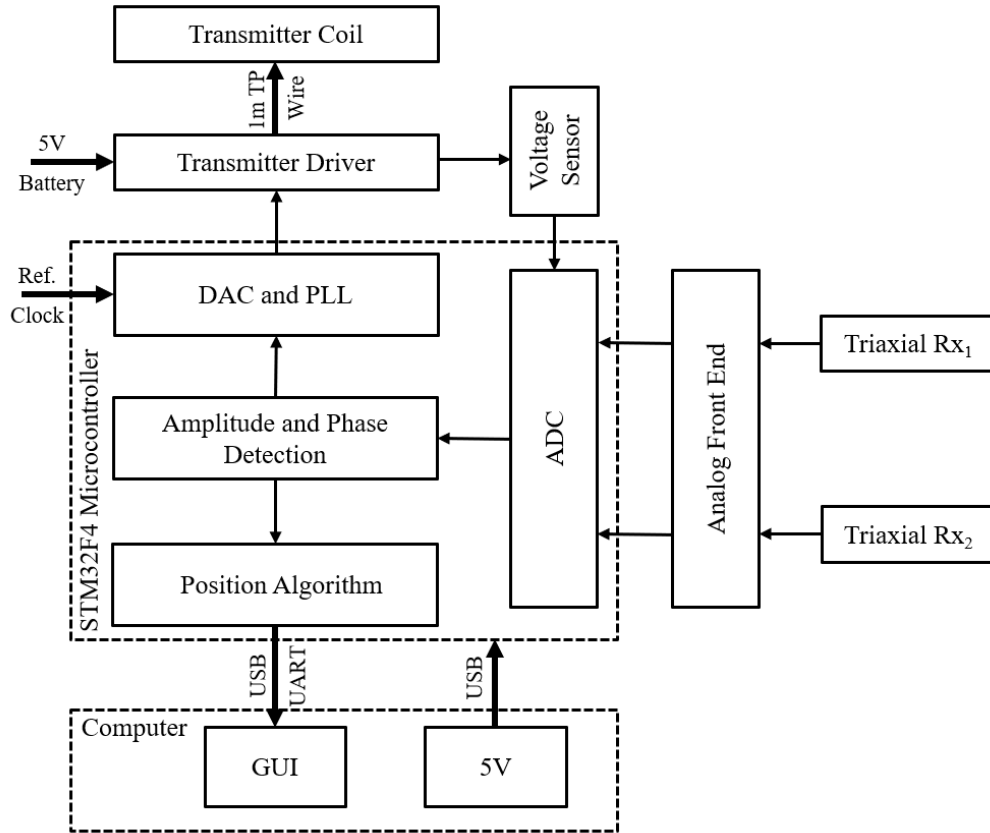


Figure 3.2.49. Block diagram of complete system.

The transmitter driver along with the coil is shown by the two top left blocks. The system has 3 external connections. One connection is the power connection for the driver. The power for

the driver is a Klein Tools (KBT2) 13400 mAh battery providing 5 V DC through USB connection (Figure 3.2.50). This battery is selected because it can provide the current needed to boost up to 12 V DC to operate op amp, as well as providing 100 mA RMS current to the coil.

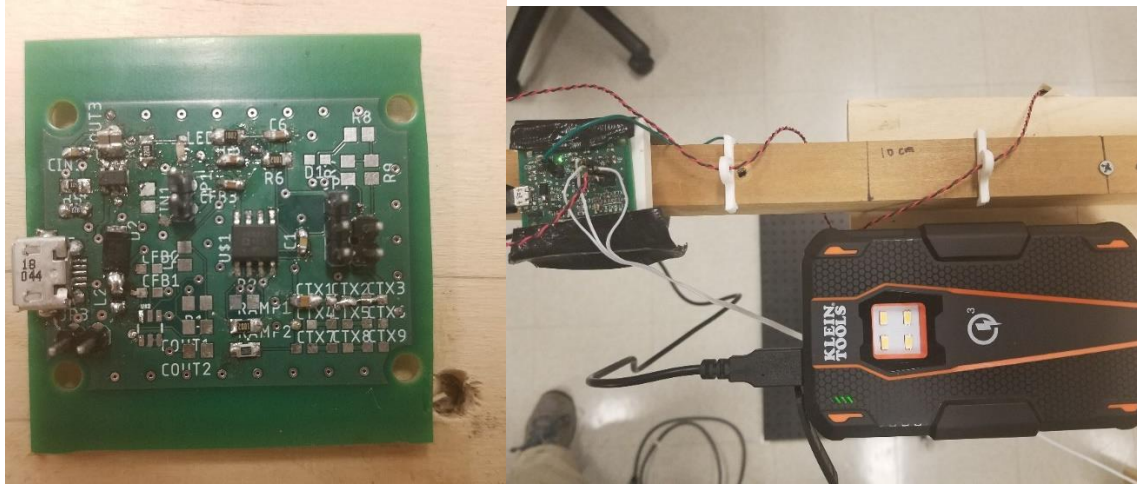


Figure 3.2.50. Transmitter driver with feedback sensing circuit (left), battery and coil twisted pair wire connected to transmitter driver (right).

As stated earlier, the microcontroller DAC is programmed to generate a  $3\text{ V}_{\text{p-p}}$  sinusoidal signal with a frequency of 32 kHz to make the Tx coil emanate B-field at 32 kHz. To check if the Tx coil's power is consistent, the proposed feedback voltage sensing circuit is used. This feedback circuit senses the voltage across the transmitter coil and is read by the microcontroller ADC. The voltage values are processed, and the amplitude is computed. If the amplitude changes from its nominal value, the amplitude of the DAC signal is adjusted to increase/decrease the power of the transmitter coil.

### 3.3 Sensing Coil Analysis

In this section, details of the sensing coils in the proposed tracking system are discussed. The sensing coils are placed in the reference frame, and the coils measure the magnetic field generated by the transmitter attached to the diagnostic mapping catheter. The size, sensitivity, geometry, and positioning of the coils have a large impact on the measurement accuracy which in turn affects tracking algorithm performance and convergence rate. Thus, it is necessary to carefully examine each of the relevant parameters.

### 3.3.1 Selection of Sensing Coils

The positioning algorithm (described below) requires solving for three position values ( $x$ ,  $y$ ,  $z$ ) and three magnetic moment values ( $m_x$ ,  $m_y$ ,  $m_z$ ) of the transmitter coil, and through these magnetic moment values, the azimuth and elevation orientation angles of the transmitting coil can be determined. For the six unknowns, we collect six B-field measurements.

As noted above in the literature review, most systems are under the type 1 design which uses multiple reference transmitters. Reversing a type 1 system to a type 2 system is undesirable. Most of these reference transmitting coils are bulky, and when they are used as sensing coils, magnetic uniformity assumption would be violated, which means that B-field magnitudes at specific points cannot be accurately captured.

McGary [42] proposed an implementation of SQUID (superconducting quantum interference device) in a type 2 system. These magnetometers have extremely high sensitivity (at aT level) but require liquid nitrogen cooling to maintain superconductivity during measurements. This leads to substantially higher cost and difficult implementation as storage and handling of the cryogenic fluid must be carefully considered. In addition, according to [85], various unexpected and unexplained phenomena have been reported for these superconducting sensors. By analyzing the quantitative data obtained from the magnetometers, the authors conclude that superconducting devices may not function well enough to capture a magnetic dipole of constant magnitude. This implies that the magnetic uniformity assumption can fail, which results in incorrect and misleading results. Thus, despite the high sensitivity of these superconducting magnetometers, the shortcomings reported make it undesirable to be used in the proposed real-time tracking system, in which fast update rates are achieved via simple and fast post-processing algorithms. Complex compensation methods will lead to a slower tracking system.

Uniaxial coils can be used as well. Six uniaxial sensing coils may be placed at different positions and orientations in the operating room to measure the transmitted magnetic field. However, placement of the six uniaxial coils needs to be optimized to minimize divergence of the positioning algorithm. To make the sensing system compact, triaxial sensing coils are considered. Two triaxial coils are used with six coils in total satisfying the need to solve for the six unknown position and orientation values. According to [86], triaxial sensing coils have the drawback of non-ideal sensing behavior due to imperfections in coil winding which leads to orthogonality errors, such as mutual coupling among the 3 coils. In addition, the sensing coils will be of different sizes

and diameters, so that the difference in quality factor Q also needs additional consideration. For the proposed system, mutual coupling compensation and coil gain mismatch compensation are developed to address relevant sensing errors.

These two triaxial coils are placed in reference locations in the operating room, and there is little restriction on size of the sensing coils. However, due to the magnetic uniformity assumption, large sensing coils are not preferable. Many commercially available triaxial coils were tested and compared (Table 3.3.1). An air core coil made in the Professor Jung's Analog Group Lab at Purdue University is used as a control. A ferrite core coil has higher sensitivity but with the drawback of reduced linearity and magnetic saturation limitations. While this was mentioned as a severe problem when designing the transmitter coil, for the sensing coil, the magnetic field is very weak in the tracking range, and a high sensitivity coil needs to be used. The following coils were tested:

- 3d-printed coil (Created in Jung's Analog Group Lab) 15 mm diameter air core coil
- Grupo Premo 10 mm diameter ferrite core coil (3dcc10 low and high inductances)
- Grupo Premo 20 mm diameter ferrite core coil (3dcc20 low and high inductances)
- Grupo Premo 15 mm diameter ferrite core flat coil (3dv15)

Table 3.3.1. Comparison of triaxial sensing coils.

	L (mH)	DCR (ohm)	R (32kHz)	QL (32kHz)	Sense (mV)	STD (mV)	fself (kHz)	Cpara (nF)	Cext (nF)	Fres (kHz)
3d printed coil (Jung Lab)	1.87	128.1	128.1	2.94	160.505	1.256	81.65	2	10	33.33
	1.92	129.9	129.9	2.97	42.13dB					
	1.86	125.6	125.6	2.98	0.78%					
3dcc10 (Low Ind)	0.59	23.7	21.31	5.44	116.536	1.024	500	0.17		
	0.63	21.2	20.11	6.56	41.1232dB		500	0.16		
	0.645	20.5	19.58	6.88	0.88%		500	0.16		
3dcc10 (High Ind)	7.3	240	233	6.40	459.572	1.862	120	0.24	3.3	31.30
	8	240	225	7.04	47.8475dB		150	0.14	3.0	31.26
	8	240	219	7.04	0.41%		150	0.14	3.0	31.26
3dcc20 (Low Ind)	0.3	2.8	2.64	20.96	245.068	1.473	500	0.34		
	0.295	2.8	2.5	22.88	44.4217dB		500	0.34		
	0.3	2.6	2.47	24.16	0.60%		500	0.34		
3dcc20 (High Ind)	1.11	5.4	6.17	40.16	484.692	2.01	250	0.37		
	1.14	4.9	6.12	44.48	47.6454dB		250	0.36		
	1.16	5.1	6.1	42.08	0.41%		250	0.35		
3DV15 (Flat coil)	6	104.91	109.8	11.33	173.807	1.468	250	0.07		
	6	107.73	111.7	11.81	41.4668dB		250	0.07		
	6.96	160.35	163.08	8.92	0.84%		600	0.01		

Note:

	From spec sheet	Measured	Matlab simulation	Excel calculation	Experimental results
--	-----------------	----------	-------------------	-------------------	----------------------

Each coil was tested and evaluated based on its mean and standard deviation of sensed voltage at a fixed position from a transmitting Helmholtz coil. From this, the SNR can be determined for the coil. The test results suggest that the best coil is the Grupo Premo 3DCC10 (Hi inductance) coil, which features three perpendicular coils housed in a cube structure with an outer diameter of 10 mm (Figure 3.3.1). It boasts high quality factor  $Q$  and high sensitivity for its size. Further tests show that orthogonality errors are minimal for these coils. Each of the three coils is oriented in  $X$ ,  $Y$ , and  $Z$  directions, respectively. This allows for three unique directional B-field values to be recorded.

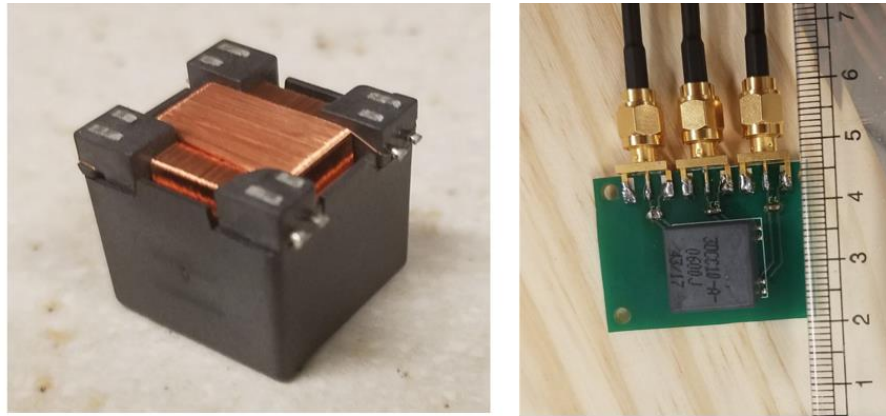


Figure 3.3.1. 3DCC10 triaxial sensing coil (left) and PCB sensing LC circuit (right).

Table 3.3.2 below shows the specifications of the coil standalone, without PCB connection.

Table 3.3.2. 3DCC10 triaxial sensing coil specifications.

Coil Type	Coil Axis	L (mH)	Rdc max (ohms)	Rmeasured @32kHz (ohms)	QL (32kHz)	Self Resonant Frequency (kHz)	Cparasitic (nF)
3DCC10 (Hi Ind)	Z	7.3	240	233	6.40	120	0.24
	Y	8	240	225	7.04	150	0.14
	X	8	240	219	7.04	150	0.14

### 3.3.2 Connection of Sensing Coils to Microcontroller

Next, we discuss the connection of the sensing coils to the microcontroller. The triaxial sensing coils measure magnetic field from the tiny transmitter coil. Noise on the sensing side

directly impacts the precision (jitter) of the calculated position. Distortion on the sensing side directly impacts the accuracy of the calculated position. The heat constraint on the maximum amplitude of the transmitting field means that the noise and distortion is non-negligible for this system.

To reduce noise, each of the three coils is connected to a tuning capacitor in parallel (on the PCB in Figure 3.3.1) which tunes the LC circuit to 32 kHz operating frequency. This boosts the SNR at the main tone frequency. Each of the coils is also connected through an SMA connection, which provides a shielded cable connection to an amplification circuit (Analog Front End) amplifying the magnetic field measured by the sensing coils. The amplification circuit must satisfy a large dynamic range because the near field magnetic field strength is within the range of  $10^{-10}$  T to  $10^{-7}$  T (assuming free air permeability).

Table 3.3.3 below shows the actual coil specifications of the two triaxial coils used in testing, with the PCB and SMA connector attached, along with the tuning capacitor value.

Table 3.3.3. Triaxial sensing coil specifications with PCB and SMA connector attached.

Triaxial Rx 1	Inductance (mH)	Resistance ( $\Omega$ )	Q (32kHz)	Tuning Capacitance (nF)
Z	7.63	256.8	6.22	3.29
X	8.4	238.6	7.37	3.01
Y	8.16	238.9	7.20	3.06
Triaxial Rx 2	Inductance (mH)	Resistance ( $\Omega$ )	Q (32kHz)	Tuning Capacitance (nF)
Z	7.69	262.1	6.15	3.25
X	8.41	235.1	7.47	3.02
Y	8.15	238.6	7.10	3.05

Each of the signals measured is weak and needs to be amplified. 6 SMA coaxial cables are used to connect the 6 coils to amplifiers. The coaxial cables are shielded and provide a clean way to get the measured signal to amplifiers.

### 3.3.3 Sensing Coil Resistor Noise Analysis

The dominant noise of the sensing coil is the coil wire resistance. The white resistor noise ( $v_{n,R}$ ) is shaped by the Rx LC resonator and boosted by Q at the resonant frequency. If  $V_{in,emf}$  is the total received voltage seen at the input to the op amp, and  $V_{in,noise}$  is the total input noise due to

the coil resistance, two equations can be written for these two different voltages in (3.3.3.1) and (3.3.3.2) (Figure 3.3.2).

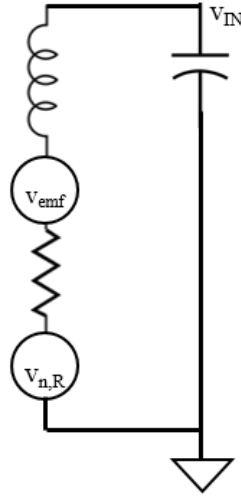


Figure 3.3.2. Sensing coil resistor noise ( $v_{n,R}$ ) in relation to measured signal ( $v_{emf}$ ).

$$v_{in,noise} = \left( \frac{\frac{1}{j\omega C}}{R + j\omega L + \frac{1}{j\omega C}} \right) \sqrt{4kTR} = \left( \frac{1}{1 - \omega^2 LC + j\omega RC} \right) \sqrt{4kTR} \quad (3.3.3.1)$$

$$v_{in,emf} = \left( \frac{\frac{1}{j\omega C}}{R + j\omega L + \frac{1}{j\omega C}} \right) v_{emf} = \left( \frac{1}{1 - \omega^2 LC + j\omega RC} \right) v_{emf} \quad (3.3.3.2)$$

It is important to note that the received signal voltage ( $V_{in, emf}$ ) has a strong dependence on the LC tuned frequency. This means that if the LC operating frequency deviates from the tuned frequency, the main tone signal will be significantly weaker, but the noise will still have roughly the same magnitude, resulting in a poor SNR. Note that the SNR depends on tracking distance, meaning that a poor base SNR results in a lower tracking range, making the system incapable for the applied heart mapping system. The SNR value, which defines the threshold at which the tracking system fails, is called critical SNR. This concept is illustrated in Figure 3.3.3.

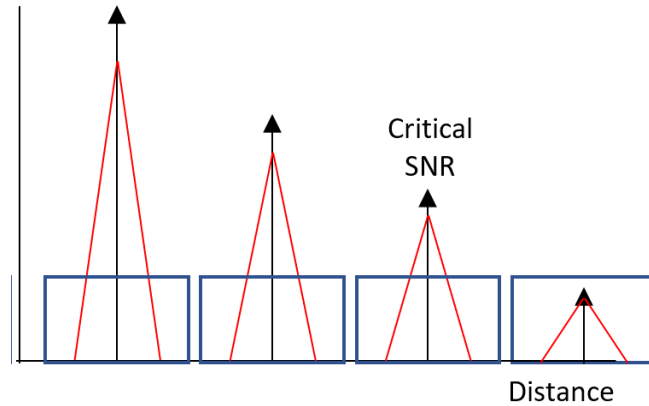


Figure 3.3.3. Signal (red) and noise (blue) over distance.

Thus, it is imperative to make sure that the receiver LC circuit is tuned exactly at the operating frequency of 32 kHz to ensure maximum SNR. For this design, since the sensing coil signal must be amplified using an op amp, the op-amp noise must be considered. The coil resistor noise is bigger than the op-amp noise around the operating signal frequency. This is because with a high Q coil, the received signal will be boosted, along with the coil resistance noise. However, the op-amp noise is not boosted by Q because the op amp comes after the LC circuit. As a result, a high Q receiver coil is necessary to ensure that the received signal is larger than the amplifier noise. This is illustrated in Figure 3.3.4.

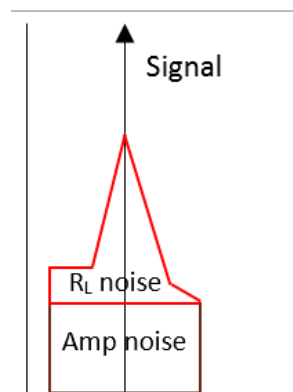


Figure 3.3.4. Effect of Q on resistor and amplifier noise.

Even if a high Q receiver is selected, it may still be possible for the received signal magnitude to be below the amplifier noise floor. As a result, the received signal is undetectable.



### 3.3.4 Analog Front End (Amplifiers)

The sensing signal magnitude range must be within the resolution of the microcontroller's 12-bit ADC. The ADC allows for a maximum  $3 V_{p-p}$ . Based on the analysis of the Q of the sensing coils and the coil sensitivity of 50 mV/A/m, the measured sensing signal RMS voltage is on the order of 10  $\mu$ V to 10 mV. To maximize the ADC range utilized, amplifiers are designed to have the proper gain and bandwidth. The target amplified RMS voltage should be between 10 mV and  $3 V_{p-p}$ . The challenge faced here is that the operating tracking range is less than 50 cm distance between Tx and Rx, which means that the magnetic field (B-field) follows the near-field characteristics. The decline in B-field strength over distance ( $r$ ) follows  $1/r^3$  or  $1/r^5$  relationship. With a minimum tracking distance of 5 cm from Tx to Rx, this means that within the heart mapping area the amplifiers must be able to accept a range of  $10^{-7}$  to  $10^{-10}$  B-field. The dynamic range required in voltage is by a factor of  $10^3$ , while the target 12-bit resolution ADC dynamic range is only 10 mV to 3V which roughly translates to a factor of  $10^3$  measurement input range. Thus, the designed amplification system needs to allow a large input dynamic range. There are three common amplifier designs which maximize dynamic range:

- Variable gain amplifier (VGA)
- Programmable gain amplifier (PGA)
- Multistage amplifier (Cascade)

For the amplifier bandwidth we may take into consideration the following two designs:

- Narrowband amplifier
- Wideband amplifier

Both VGA and PGA amplifiers are unsuitable for this application due to their shortcomings. For a feedback-based VGA design, the gain bandwidth is constant. As a result, a large gain will have very low bandwidth, which results in high sensitivity to process, voltage, and temperature (PVT) variations. An analog multiplier-based VGA has its gain linearity dependent on control voltage (linearity decreases inversely with respect to control voltage). This results in a low active gain range. Thus, most VGAs are undesirable due to PVT variations. Circuits to compensate such variations (especially temperature compensation circuits) are often complex and still have linearity error.

Two of the most common PGA architectures are resistive and capacitive PGAs. For a resistive PGA, the closed loop formation suffers from an input stage distortion, and the common

mode is amplified as well, resulting in poor common mode rejection. A capacitive PGA, on the other hand, fixes the problems with the resistive PGA, but has problems with capacitor mismatch errors, resulting in gain deviation and distortion. Fixing such mismatch requires dynamic element matching (DEM) in microcontroller unit (MCU) DAC. This means that the MCU must be carefully designed to accurately control input and gain.

For this system, a two-stage amplifier is designed to amplify the weak signals and accommodate a large dynamic range. A wideband amplification circuit is used for each stage to reduce the circuit's sensitivity to PVT. In order to design correct gain stages, the effect of noise on multi-stage amplifiers is analyzed.

### Op-Amp Noise

The analysis for the op-amp noise contribution assumes that the noise level is solely based on the input referred voltage and current noise [87]. This is commonly done when calculating the noise figure for op amps. Because of the multi-gain stage design, the input referred noise will be amplified after each stage. We consider an amplification design with only two stages. We start with the investigation of the input referred noise relative to the closed loop circuit design.

In general, the input referred noise can be expressed as either superposition of the input signal and the noise or part of a closed loop, because a closed loop op amp has the same input referred noise voltage as the open-loop op amp, illustrated in Figure 3.3.5.

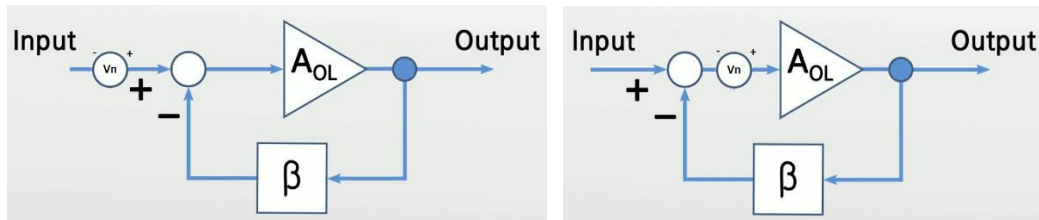


Figure 3.3.5. Block diagram of amplifier transfer function showing input referred noise having same magnitude whether it is inside or outside the feedback loop.

Thus, the two diagrams depicted above have the same transfer function:

$$v_{out} = (v_{in} + v_n) \frac{A_1}{1 + \beta A_1} \quad (3.3.4.1)$$

where  $v_n$  is the input referred noise of the open-loop circuit with the gain of  $A_1$ .

Now, the gain stage magnitude and order are optimized based on the input referred noise. The two gain stages used for the proposed design are of 10 and 100, which satisfies the magnetic field dynamic range of triaxial sensors within the 50 cm range. Each gain stage is designed using the same closed loop circuit to minimize different SNRs between different gain stages.

The effect of order of gain stages on the input noise seen at the output is analyzed below. The design is optimized with minimum amplification of the input referred noise. The second stage noise is examined in detail because this stage is used when tracking signal is very weak, where SNR is very low. The first stage noise analysis is not as significant because the first stage is used alone only when the second stage is saturated, i.e., the first stage alone will not be used when the signal is weak. Define input referred noise as  $v_{n,in}$ . In the first stage,  $v_{n,in}$  is multiplied by the closed loop gain. At the input of the second stage, the total noise seen is the sum of the input referred noise of the second stage input plus the output amplified noise from the first stage (added in power domain). This total noise is now multiplied by the gain of the second stage to get the total output noise. Figure 3.3.6 compares the two possible designs.

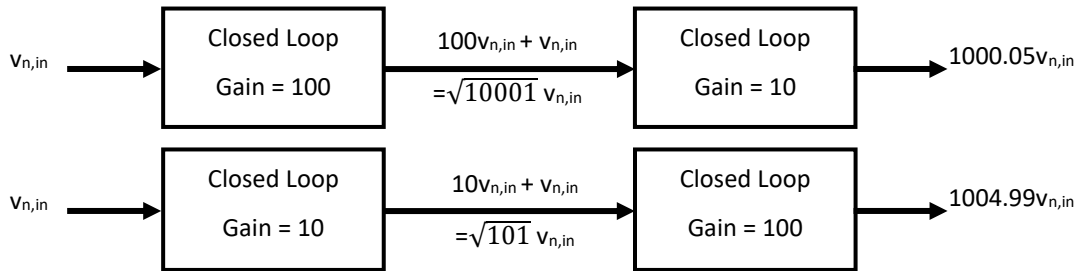


Figure 3.3.6. Two possible gain stage designs.

From this analysis, the design of a larger gain in the first stage with a smaller gain in the second has a lower output noise with a  $4.94 v_{n,in}$  reduction. This translates into nearly 5 times lower input referred noise at the second stage op-amp output. The noise behavior of the second stage is vital because most of the long-distance tracking involves weak signals, where only the second stage is used. Thus, the two-stage op amp is designed with a gain of 100 in the first stage and a gain of 10 in the second stage. The op-amp input referred noise is controlled by selecting a low-noise op amp for the design to minimize the effect of op-amp noise on the measured sensing signal. The op amp used in this design is AD8692 by Analog Devices. It has an input referred noise of

6.5 nV/sqrt (Hz) at 10 kHz when operating with single supply at 3 V, which matches the input range of the ADC for this system.

This two-stage dynamic range amplifier is simulated to verify its amplification and noise figure. Figure 3.3.7 below shows the circuit of this two-stage amplifier. The bandwidth is required so that the gain is maximized at 32 kHz, the frequency used for this system. As mentioned earlier, since the circuit architecture features wide bandwidth, slight mismatch in resistor and capacitor values will not cause the gain to change much.

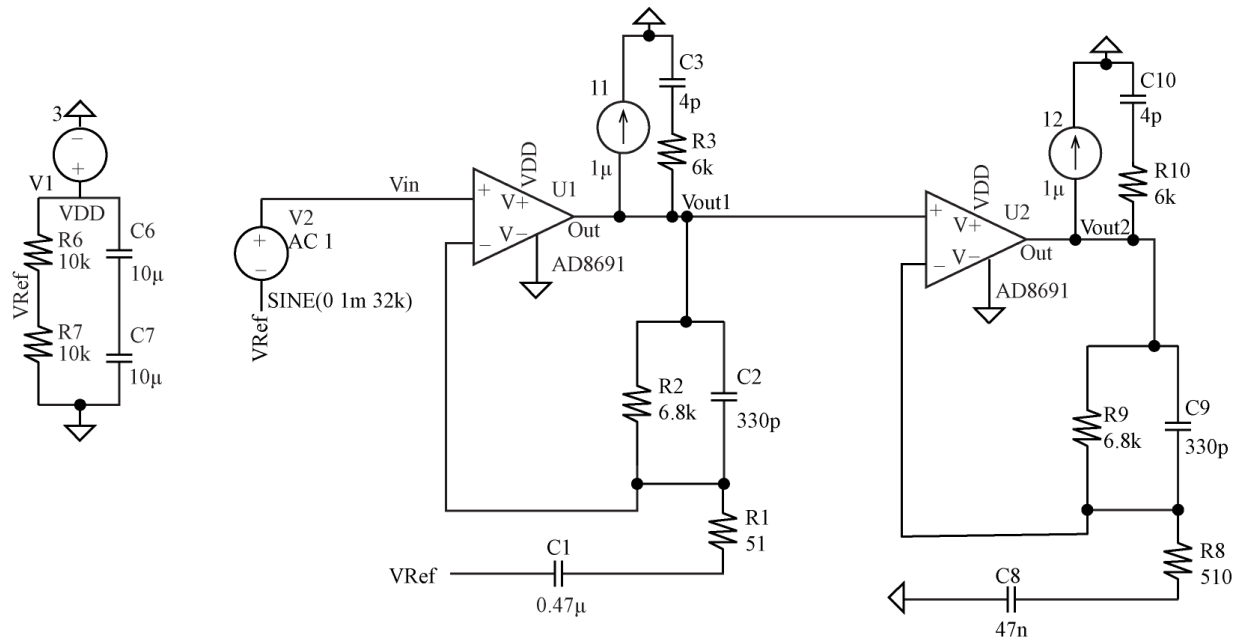


Figure 3.3.7. Two-stage amplifier.

Figure 3.3.8 below shows a frequency sweep simulation plotting magnitude (dB) and phase (deg). Stage 1 curve is in green, and the curve for stages 1 and 2 combined is in blue. The results show a gain of over 100 (40 dB) for the first stage and 1000 (60 dB) for the second stage, clearly within the target.

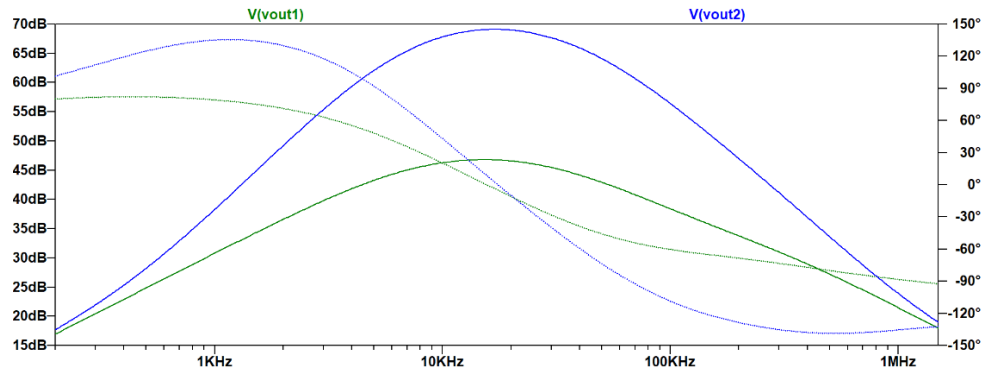


Figure 3.3.8. Frequency sweep simulation.

Next, the DC offset at the output is analyzed. The input DC of the op amp is biased at  $V_{dd}/2 = 3/2 \text{ V} = 1.5 \text{ V}$ . This DC offset voltage must be kept with minimal change once it gets to the output of the second stage into ADC. The datasheet value of the offset of AD8691 is 2 mV. With a gain of 10 in the second stage, the offset at the output will be around 20 mV. This means that the input into the ADC could have a DC offset of around 4 mV, which is negligible relative to the 3 V swing available.

This hypothesis was tested in simulation, where a  $2 \text{ mV}_{p-p}$  32 kHz sine wave was stimulated into the two-stage amplifier. The DC output of the first stage (i.e., input of the second stage amp) and the DC output of the second stage amp are measured. Figure 3.3.9 shows the results. Both the yellow and purple lines show DC shifts under 1 mV, which accurately reflects the theoretical prediction (the DC offset should be under 4 mV).

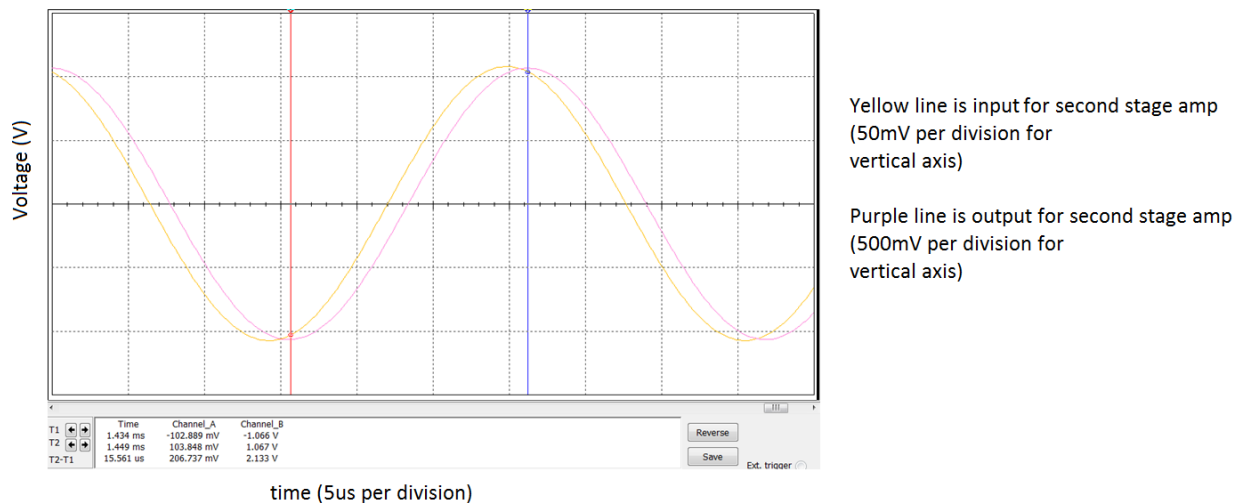


Figure 3.3.9. Simulation for DC offset shift.

Next, the frequency tones and higher order harmonics are analyzed for the circuit to verify the two-stage amplifier circuit's linearity. An FFT is run on the simulated voltage for both the input and output of the 1<sup>st</sup> stage of amplification shown below in Figure 3.3.10.

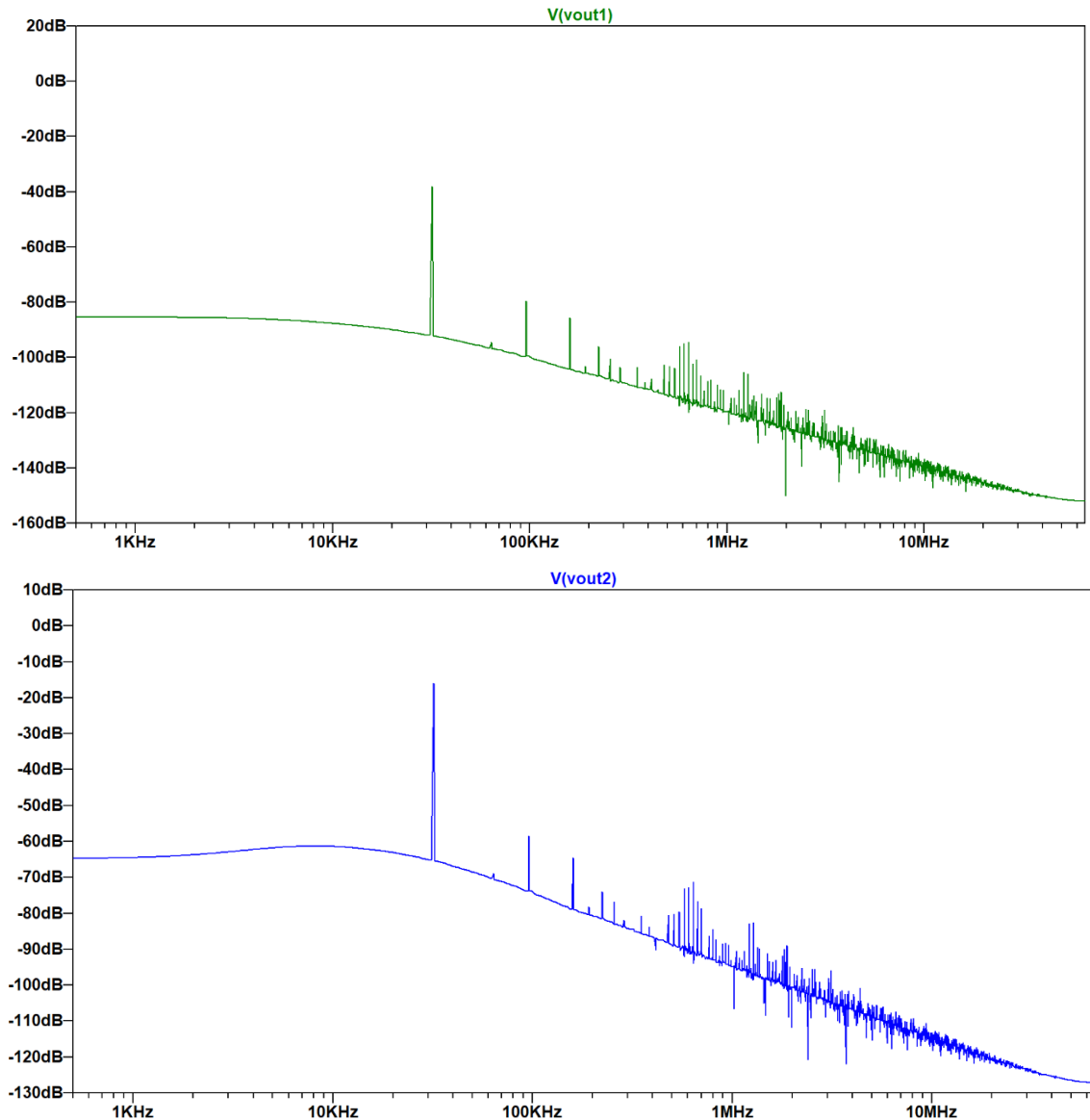


Figure 3.3.10. Fourier analysis simulation closed loop amplification of stage 1 (V(vout1)) and stage 1+2 (V(vout2)).

After that, a parametric sweep for input voltages ranging from 300  $\mu$ V to 30 mV is performed on the FFT. These simulated values are compared to the measured ones. Table 3.3.4 and Figure 3.3.11 below depict the results. As shown by the results, similar to the transmitter, the

2<sup>nd</sup> order harmonic can be safely ignored, with more than 20 dBv difference between the 2<sup>nd</sup> harmonic and the fundamental tone. However, the 3<sup>rd</sup> order harmonic cannot be ignored. Thus, post-processing software filters are used to reject this tone.

Table 3.3.4. Simulated frequency domain magnitudes of 1<sup>st</sup>, 2<sup>nd</sup>, and 3<sup>rd</sup> harmonics with unit in dBv (a) and unit in dBm (b).

(a)

Input (dBv)	Fundamental Tone (dBv)	Output 2nd Harmonic (dBv)	Output 3rd Harmonic (dBv)
-30.47	5.18	-18.33	-7.88
-33.99	4.82	-18.61	-11.66
-35.92	4.09	-21.67	-19.48
-40.07	0.50	-38.72	-42.29
-42.51	-2.00	-41.23	-44.71
-46.03	-5.52	-44.80	-48.30
-52.08	-11.54	-50.71	-53.91
-55.16	-14.64	-53.97	-57.21
-57.09	-16.45	-86.59	-82.48
-58.43	-17.78	-111.35	-119.09
-60.01	-19.41	-114.33	-126.14
-61.95	-21.31	-118.35	-135.30
-64.45	-23.81	-123.67	-147.13
-67.97	-27.33	-130.72	-145.04

(b)

Input (dBm)	Fundamental Tone (dBm)	Output 2nd Harmonic (dBm)	Output 3rd Harmonic (dBm)
-17.47	18.18	-5.33	5.12
-20.99	17.82	-5.61	1.34
-22.92	17.09	-8.67	-6.48
-27.07	13.50	-25.72	-29.29
-29.51	11.00	-28.23	-31.71
-33.03	7.48	-31.80	-35.30
-39.08	1.46	-37.71	-40.91
-42.16	-1.64	-40.97	-44.21
-44.09	-3.45	-73.59	-69.48
-45.43	-4.78	-98.35	-106.09
-47.01	-6.41	-101.33	-113.14
-48.95	-8.31	-105.35	-122.30
-51.45	-10.81	-110.67	-134.13
-54.97	-14.33	-117.72	-132.04

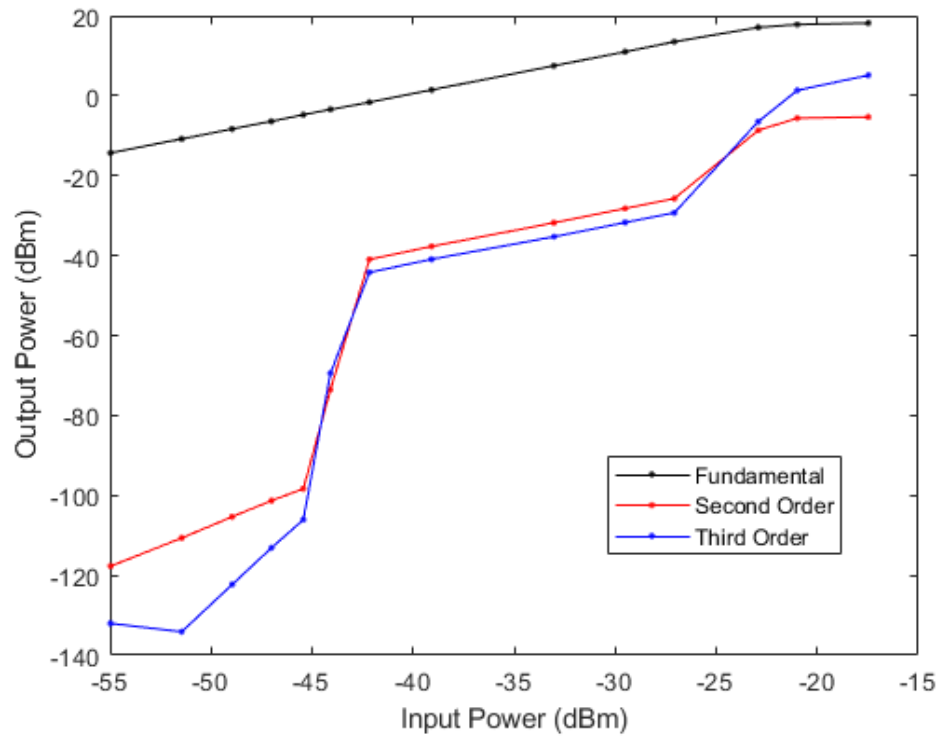


Figure 3.3.11. IP2 and IP3 plots of 1<sup>st</sup> stage amplifier.

### 3.3.5 Analog Front End Integration

The analog front end integration involves amplifying a pair of triaxial coils. Thus, the designed two-stage dynamic range amplifier circuit is replicated 6 times, one for each sensing coil. Figure 3.3.12 below shows the PCB of the analog front end.



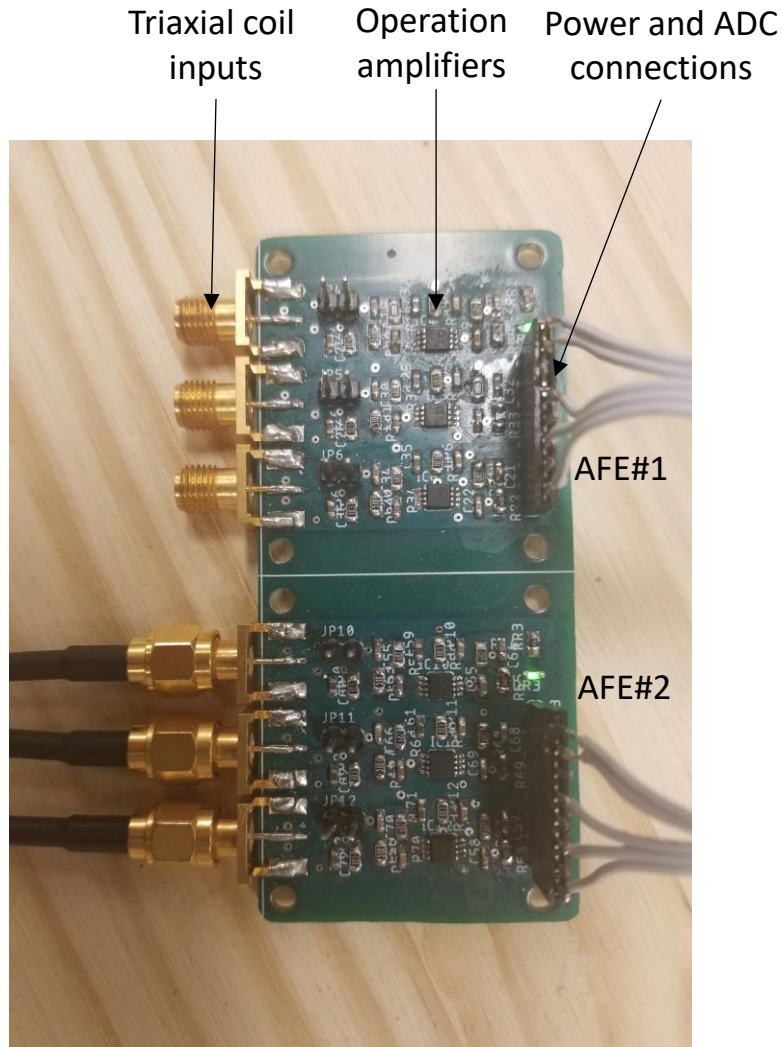


Figure 3.3.12. Analog front end.

The triaxial coils on the LC sensing PCB are connected to the analog front end via SMA cables. Analog front end #1 is for one triaxial coil, and analog front end #2 is for the second triaxial coil. Note that the two analog front ends are identical in design, with the only exception of their wired connection to triaxial coils and to the microcontroller ADC. Figure 3.3.13 below shows the block diagram for the integration of the analog front end into the system. Both stages of the amplified signals are fed into the microcontroller ADC. Thus, the sensing system utilizes 12 channels for 12 signals (6 coils with 2 possible amplifications). The STM32 microcontroller ADC used for the proposed system consists of 3 ADCs. Because of this restriction, only 3 coils in one triaxial receiver are sampled at a time. A firmware amplitude detection algorithm extracts the 32

kHz measured B-field, and an amplifier selection algorithm with hysteresis selects the appropriate gain. For instance, if the amplitude detection is used on the second stage, and the signal is saturated or near 3 V, the ADC will select the first stage channel for that individual coil in the next cycle. In contrast, if the first stage amplification amplitude drops below 300 mV, the second stage is selected. Hysteresis in the gain selection process is performed by having a tolerance between the thresholds specified so that borderline measurements will not flip-flop amplifier selections every time cycle. This is vital because the relative SNRs of the different stages are not the same, which may lead to a reduction in calculated position precision.

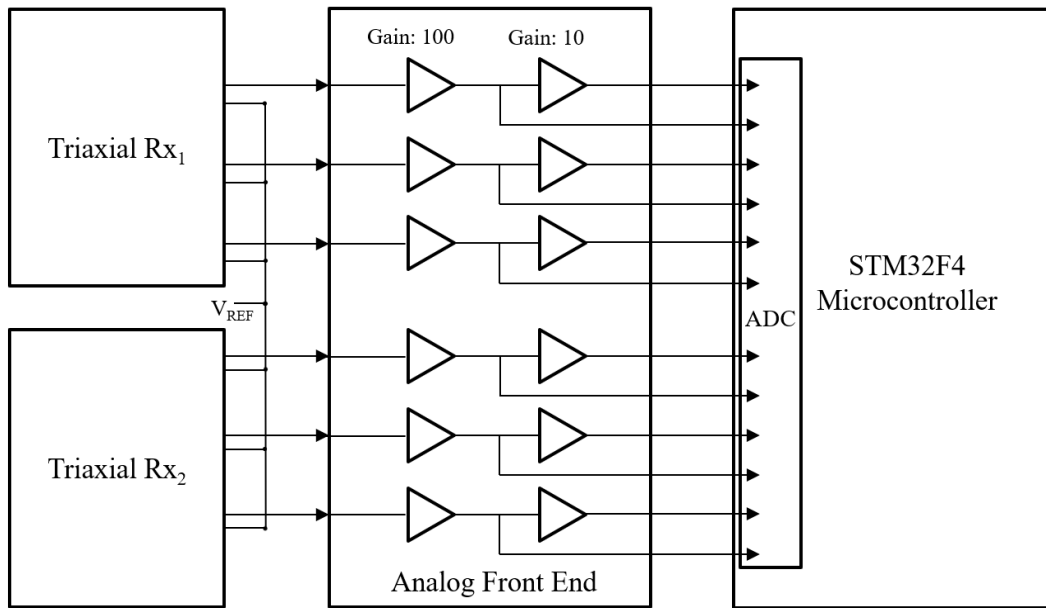


Figure 3.3.13. Block diagram of analog front end.

We now test the entire transmitter and sensing system to confirm that measured properties are consistent with those from simulations. We examine the SNR for the B-field measurement over distance and estimate the position jitter based on the positioning algorithm detailed in the next chapter. For this design, the 3DCC10 sensing coil and 1.5 mm diameter designed plastic transmitter coil are tested, along with the transmitter LC tank circuit and sensing LC tank circuit. For the position determination, the SNR needs to be above the noise floor over the test range. Specifically, for the system to function at 50 cm distance, all 3 individual coils in each triaxial receiver should have SNRs above the noise floor. In the study, we define the noise floor using the

sensing (Rx) system noise and the measured B-field in fundamental tone as the measured signal. The measurement SNR needs to be above the critical SNR, a threshold where the measured B-field amplitude is equal to the Rx system noise magnitude. This can be seen in Figure 3.3.14.

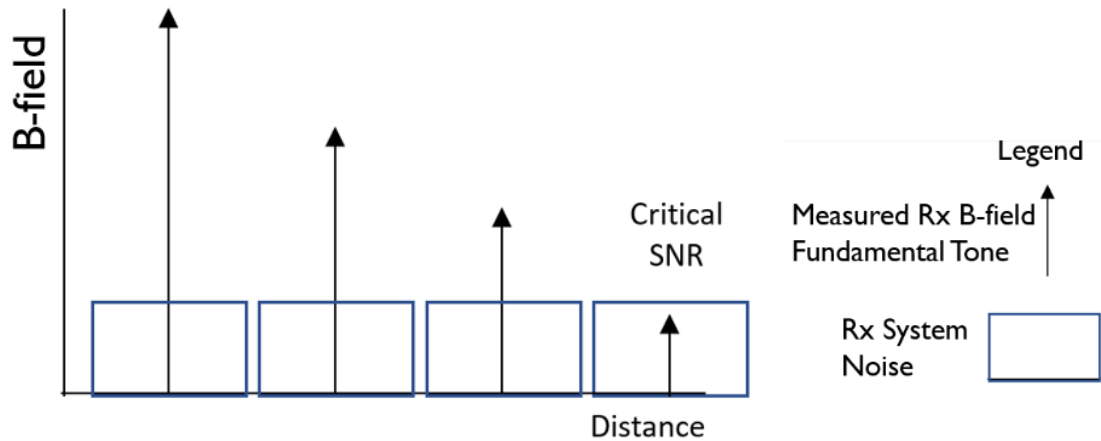


Figure 3.3.14. Voltage level at different distances, with emphasis on critical SNR.

First, a preliminary test is performed. The sensing coil (Rx) and transmitter coil (Tx) are placed 20 cm apart. The voltage across the sensing coil (after amplification) is recorded. The amplifier used here is the second stage because the second stage amplifier is used for weak signals with poor SNR, the bottleneck of the system for position precision. Afterwards, the sensing coil and transmitter are moved farther apart by 10 cm, and then the voltage is recorded again. The two coils are slowly moved farther apart until the sensor coil voltage is no longer measurable, where measurable threshold is defined by the oscilloscope noise profile. The oscilloscope is set at a fixed amplification throughout the tests. The triaxial coil voltages were recorded across 3 channels (Ch1, Ch2, and Ch3). First, the oscilloscope's baseline noise floor was determined. The 3 channels were grounded, and the reference and trigger channels were changed through these tests. The test setup is shown in Figure 3.3.15. Tables 3.3.5 and 3.3.6 show the null measurement results, by analyzing the mean and standard deviation of the measured voltages across each grounded channel.



Figure 3.3.15. Oscilloscope null noise measurement test.

Table 3.3.5. Null noise measurement with transmitter coil as reference.

	Mean (mV)	Stdev (uV)	SNR (dB)
Ch1	4.40	94.86	33.33
Ch2	3.68	97.70	31.52
Ch3	2.57	86.17	29.48

Table 3.3.6. Null noise measurement with Ch4 probe as reference.

	Mean (mV)	Stdev (uV)	SNR (dB)
Ch1	4.28	117.40	31.24
Ch2	3.31	113.50	29.30
Ch3	2.43	102.80	27.47

From these tests, it was concluded that voltage measurement values below 5 mV RMS were inaccurate.

In this preliminary test below, we want to find out whether the sensor coil voltage is measurable beyond 50 cm. The RMS voltage is recorded across distance (Figures 3.3.16 and 3.3.17).

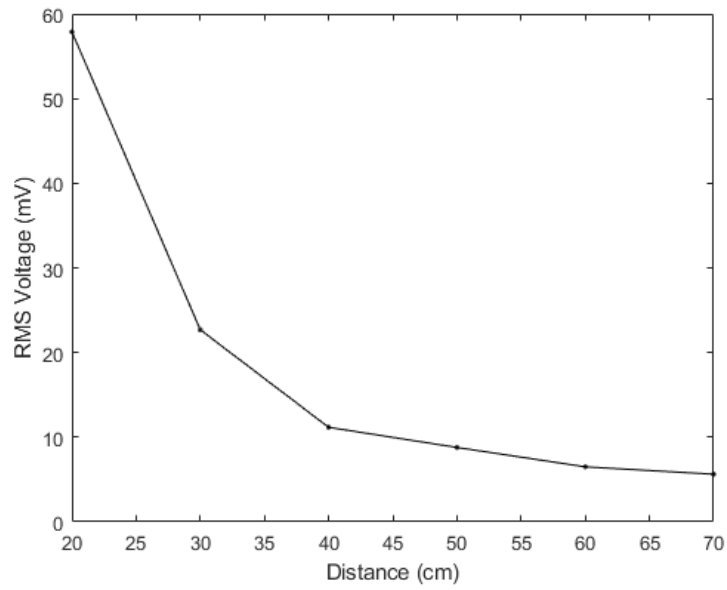


Figure 3.3.16. Measured voltage by distance between Tx and Rx.

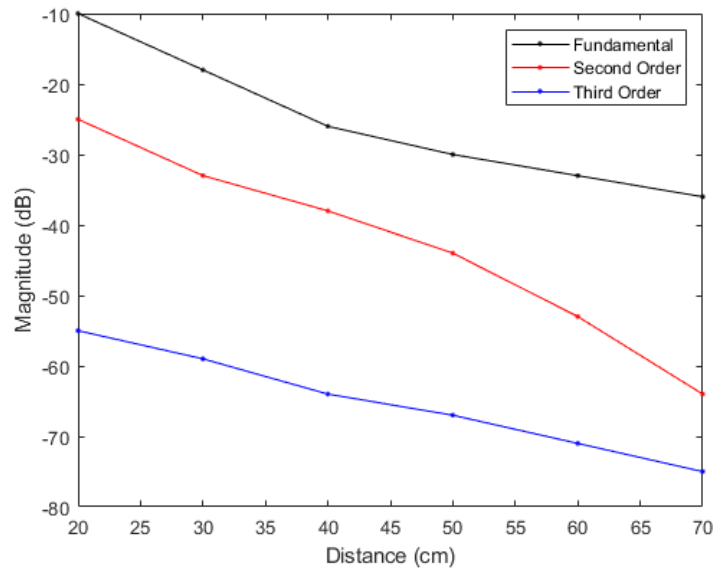


Figure 3.3.17. Measured voltage by distance between Tx and Rx in terms of separate harmonic tones.

The results indicate that at ranges 70 cm or greater, the measured voltage drops below 5 mV, which is 5  $\mu$ V unamplified. Based on this test, the absolute maximum range for reliable detection is 70 cm for the system. Table 3.3.7 summarizes the voltage magnitude over distance between the transmitter coil (Tx) and the sensing triaxial coils (Rx).

Table 3.3.7. Voltage level and measured frequency domain magnitudes of 1<sup>st</sup>, 2<sup>nd</sup>, and 3<sup>rd</sup> harmonics.

Distance between Tx and Rx (cm)	Measured RMS Voltage (mV)	Fundamental Tone (dB)	2nd Harmonic (dB)	3rd Harmonic (dB)	Difference between 1st and 2nd Harmonics	Difference between 1st and 3rd Harmonics
20	57.88	-10	-25	-55	15	45
30	22.69	-18	-33	-59	15	41
40	11.17	-26	-38	-64	12	38
50	8.79	-30	-44	-67	14	37
60	6.5	-33	-53	-71	20	38
70	5.63	-36	-64	-75	28	39

The IP2 and IP3 plots for the amplifier are obtained by measuring the first 3 harmonic magnitudes over distances ranging 5–50 cm (Table 3.3.8). Ranges greater than 50 cm were not measured because noise levels were too high, which would cause the data unreliable. Figure 3.3.18 shows the IP plot of the analog front end used for the system.

Table 3.3.8. Measured frequency domain magnitudes for first three harmonic tones.

	Distance (cm)	Input (dBm)	Stage 1 Output (dBm)	Stage 1+2 Output (dBm)
Fundamental Tone	5	-29.7	-9.8	2.1
	10	-31.5	-13.0	-3.1
	15	-36.2	-16.3	-6.3
	20	-38.0	-21.2	-8.3
	25	-40.9	-24.6	-11.9
	30	-41.5	-25.7	-13.4
	35	-43.8	-28.0	-15.9
	40	-46.6	-30.6	-19.2
	45	-47.2	-32.2	-20.3
	50	-47.6	-35.0	-23.4
Second Order Harmonic	5		-35.5	-25.8
	10		-30.5	-20.2
	15		-31.2	-20.9
	20		-35.1	-21.8
	25		-35.8	-22.6
	30		-36.2	-24.3
	35		-36.0	-25.6
	40		-35.9	-25.0
	45		-37.1	-26.7
	50		-36.2	-27.1
Third Order Harmonic	5		-28.8	-8.6
	10		-31.8	-25.2
	15		-34.0	-26.4
	20		-39.4	-27.4
	25		-42.6	-29.1
	30		-43.1	-29.4
	35		-43.1	-31.0
	40		-44.4	-31.9
	45		-45.0	-32.7
	50		-45.0	-34.0

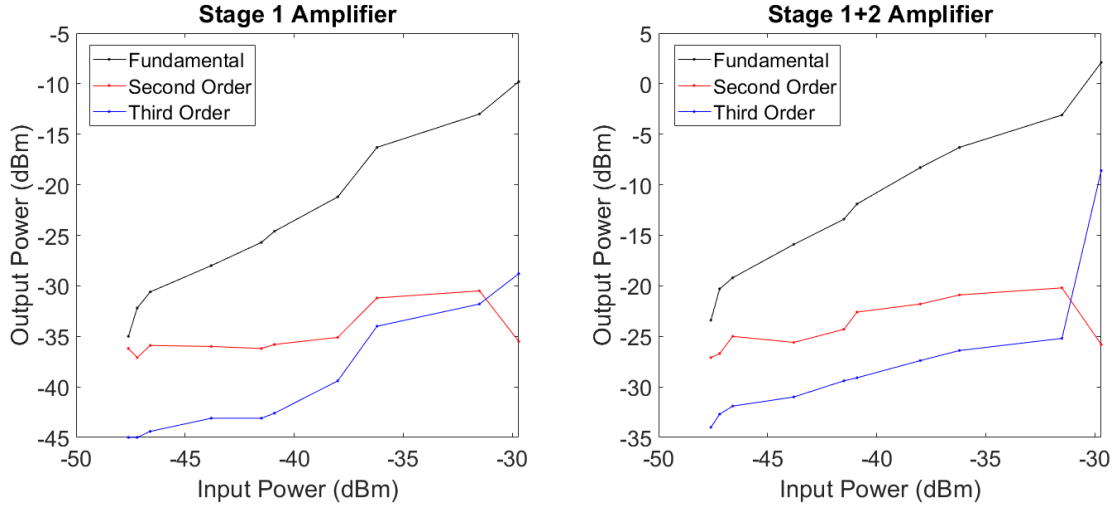


Figure 3.3.18. IP2 and IP3 plots of the 1<sup>st</sup> stage amplifier (left) and 2<sup>nd</sup> stage amplifier (right).

### 3.3.6 Sensitivity

Next, the frequency response of the measured signal is obtained. This is to investigate the effect of sensitivity at various positions. The B-field sensed by a triaxial receiver is measured at various distances relative to the transmitter coil, and the SNR is determined, where the noise is defined by the standard deviation of the signal received. This is to verify that the SNR within the tracking range is significantly higher than the critical SNR. In addition, using the positioning algorithm, the position and orientation errors are simulated at different B-field SNRs. White noise is simulated with a constant magnitude at 32 kHz. The white noise magnitude is adjusted based on the simulated SNR in Matlab. From the simulation, we see that the target SNR is 40 dB for the proposed system. Figure 3.3.19 depicts the simulated position and orientation error at an SNR of 40 dB.

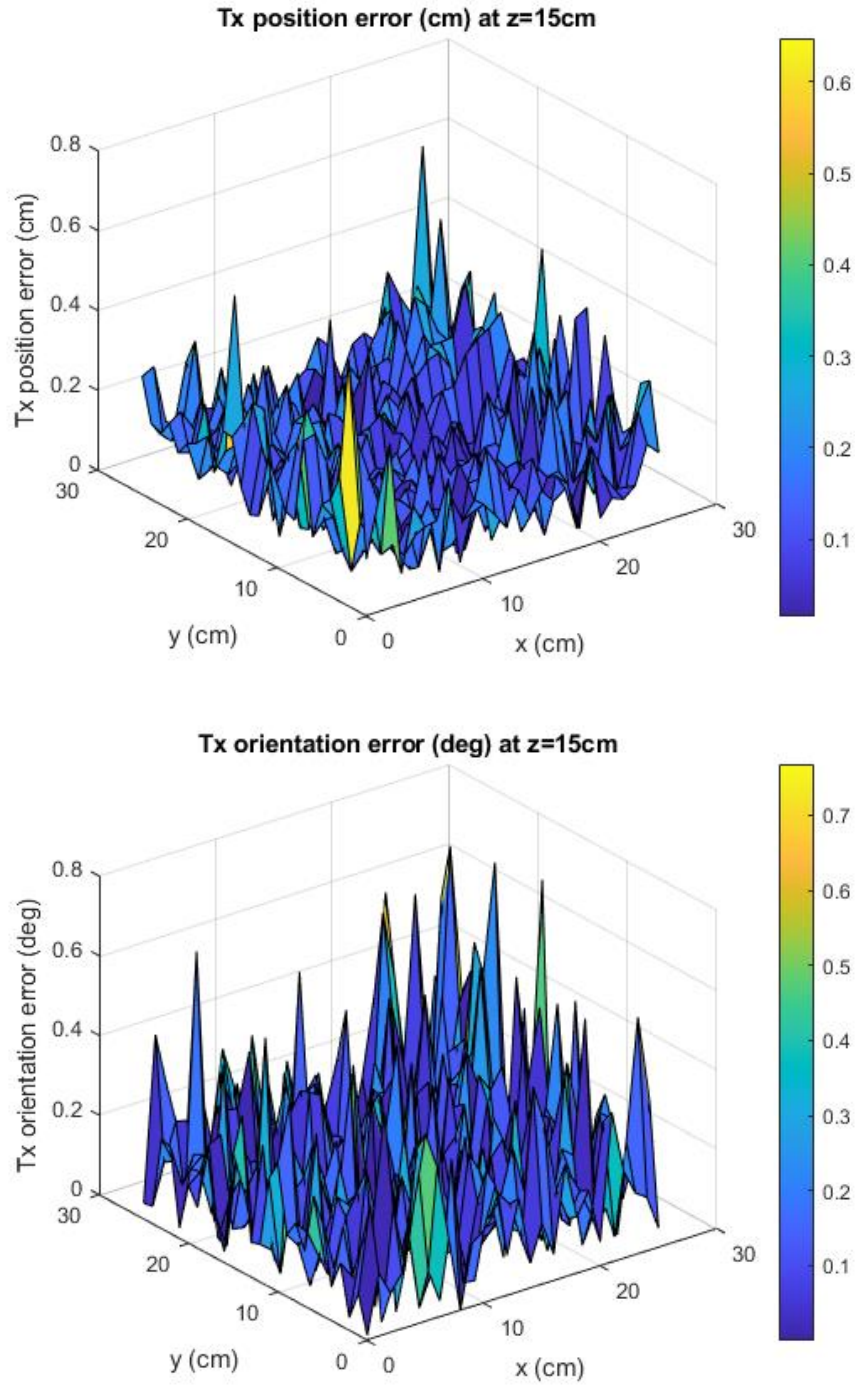


Figure 3.3.19. Position algorithm error when SNR = 40 dB (no filter applied).

The goal is to have a deviation of position under 5 mm and 1 deg (unfiltered) so that the filtered deviation will be under 1 mm and 0.1 deg. Next, the sensing coil is measured at two different distances. Figure 3.3.20 below depicts the frequency responses of measured triaxial



receiver signals ( $x$ ,  $y$ ,  $z$ ) at two of the tested distances of  $x = 20$  cm and  $x = 40$  cm. The Tx orientation is in the  $+x$  direction.

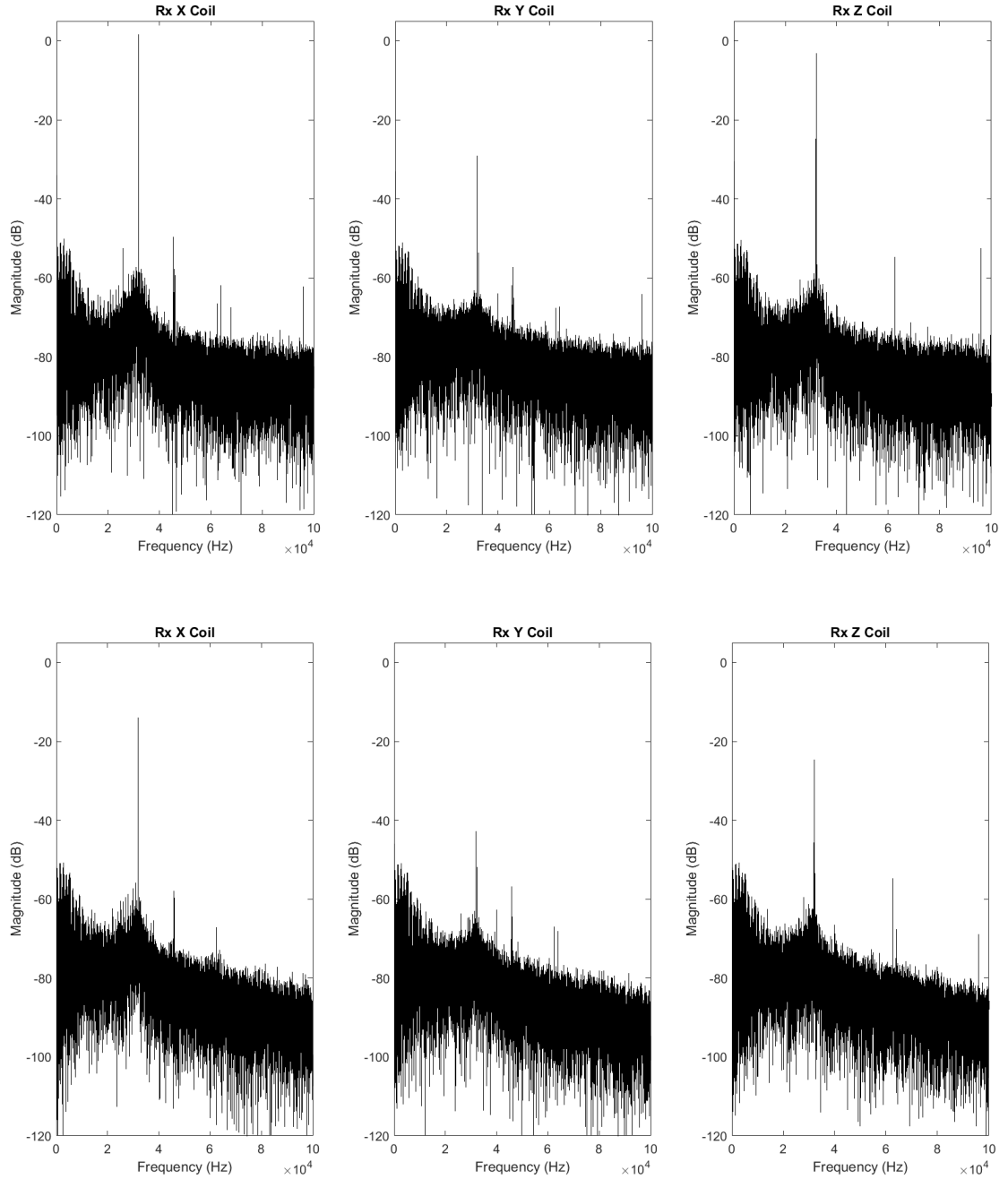


Figure 3.3.20. Frequency response of receiving  $x$ ,  $y$ ,  $z$  coils measured at 20 cm in  $x$  distance from Tx to Rx (upper) and 40 cm in  $x$  distance (lower).

The frequency response plots (Figure 3.3.20) indicate that at 20 cm, the SNR for the strongest fields is approximately 60 dB, and at 40 cm, the SNR is approximately 40 dB. The measurement test results of the coils verify that the actual position jitter will be within the 5 mm target at 40 cm.

Coil sensitivity is defined as the conversion of H-field to measurable voltage. A higher conversion allows for a higher voltage. All three triaxial coils have roughly equal sensitivity of 50 mV/A/m. To confirm this sensitivity value, the measured voltage at known positions was converted to H-field in unit of A/m. The test consists of the Tx coil oriented in the positive  $x$  direction at  $y = 0$  cm,  $z = 8$  cm, and varying  $x$ . The  $H_x$ ,  $H_y$ , and  $H_z$  of the sensing coil are recorded. A COMSOL simulation of the transmitter coil with the same geometry and number of turns is run in the AC/DC module. The test results show that the measured magnetic field strength is consistent with the magnetic field simulated using COMSOL's AC/DC module. Figure 3.3.21 illustrates the Tx performance with the coil's axis oriented in the  $x$ -direction.

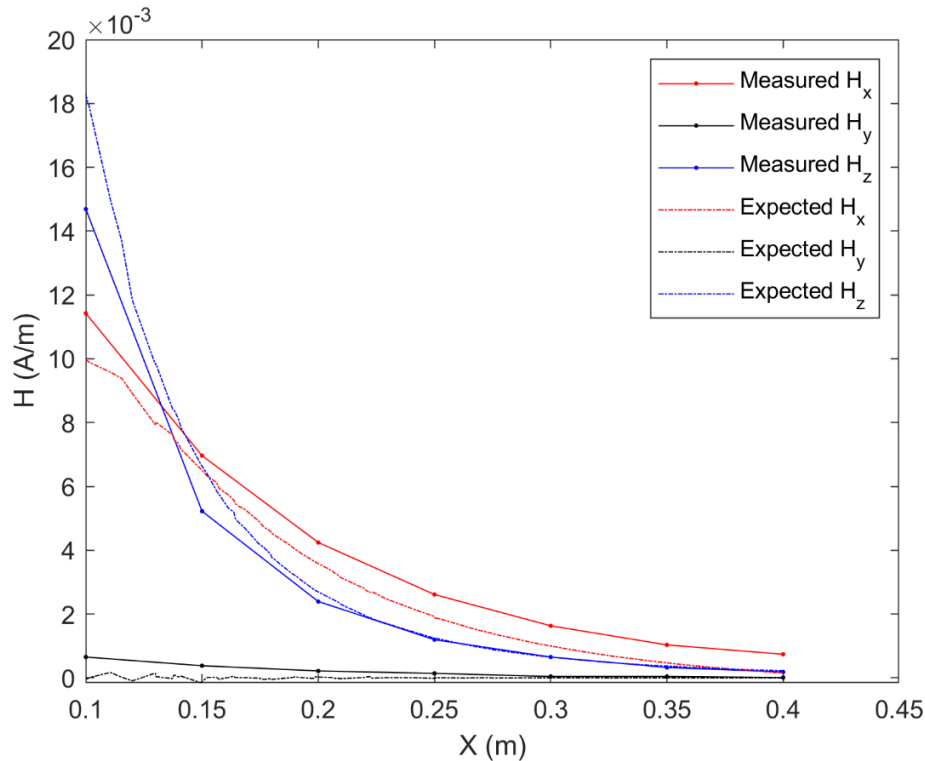


Figure 3.3.21. Measured vs. simulated magnetic field strength.

### 3.3.7 Sensing Coil Test

The previous test was performed using an oscilloscope to measure the amplified sensing voltage. However, the sensing system measurements in the proposed system are performed using the STM32 microcontroller ADC during live-time tracking. The noise profile of the ADC may not be the same as that of the oscilloscope. Because of this, a separate test is performed to verify the SNR results obtained through the oscilloscope.

The same 3DCC10 sensing coil and the designed 1.5 mm diameter plastic transmitter coil are used in the tests. In these tests, the sensing coil and transmitter coil are placed 15–20 cm apart in the  $z$  direction, and the two sensing coils are placed 32.53 cm apart from one another, which was the optimal distance determined as detailed below. The signed peak-to-peak voltage across the sensing coil (after amplification) is recorded using the STM32 microcontroller ADC for each test position within the tracking area over time. A set of 100 samples are recorded for each position, and from these 100 samples, the mean and standard deviation are determined. The SNR can then be back calculated from these values. All 3 coils within each triaxial coil are tested separately for the verification.

First, the total harmonic distortion of the sensing coils, measured after 2 stages of amplification, using the analog front end, is evaluated over different positions. Tables 3.3.9 and 3.3.10 below along with Figures 3.3.22 and 3.3.23 show the measured fundamental tone and the second and third order harmonics (at 64 kHz and 96 kHz, respectively). From these data summarized in the tables and figures, the total harmonic distortion can be computed and analyzed.

Table 3.3.9. Rx1: Fundamental tone and harmonic magnitudes.

$x$ distance (cm)	Fundamental tone (dB)			2nd order harmonic (dB)			3rd order harmonic (dB)		
	$x$ coil	$y$ coil	$z$ coil	$x$ coil	$y$ coil	$z$ coil	$x$ coil	$y$ coil	$z$ coil
10	10.29	-16.88	12.35	-59.22	-63.41	-47.83	-56.67	-46.54	-52.00
15	5.96	-24.84	3.42	-57.97	-64.18	-54.68	-70.32	-60.95	-46.14
20	1.65	-29.19	-3.15	-61.92	-67.41	-54.68	-62.28	-64.12	-52.58
25	-2.83	-33.94	-9.43	-67.27	-67.53	-55.42	-64.99	-72.36	-58.66
30	-7.06	-38.32	-15.19	-67.98	-66.95	-55.32	-72.52	-78.40	-63.29
35	-10.85	-41.35	-20.30	-67.84	-66.71	-55.08	-79.80	-80.65	-63.40
40	-14.02	-42.85	-24.57	-67.15	-66.97	-54.72	-78.55	-80.93	-68.90
45	-16.89	-44.34	-28.69	-67.53	-65.45	-54.68	-66.05	-79.55	-72.60
50	-19.58	-43.46	-32.39	-68.03	-64.98	-55.24	-81.52	-78.07	-79.53

Table 3.3.10. Rx2: Fundamental tone and harmonic magnitudes.

$x$ distance (cm)	Fundamental tone (dB)			2nd order harmonic (dB)			3rd order harmonic (dB)		
	$x$ coil	$y$ coil	$z$ coil	$x$ coil	$y$ coil	$z$ coil	$x$ coil	$y$ coil	$z$ coil
10	6.97	-8.05	12.00	-66.78	-67.33	-58.81	-42.43	-45.58	-51.69
15	4.40	-17.33	3.58	-61.43	-70.18	-59.57	-61.91	-48.90	-47.34
20	-0.05	-25.79	-4.05	-71.91	-69.56	-59.34	-71.41	-56.58	-53.61
25	-4.38	-32.91	-10.54	-72.66	-70.32	-59.78	-68.74	-69.58	-60.84
30	-8.27	-38.49	-16.04	-72.68	-69.11	-58.86	-74.50	-80.80	-66.31
35	-11.80	-43.08	-20.71	-72.56	-68.16	-59.02	-79.00	-81.40	-73.16
40	-14.96	-46.19	-24.69	-70.15	-68.35	-59.32	-80.21	-80.33	-70.21
45	-17.77	-48.38	-28.03	-70.81	-70.60	-59.31	-79.13	-81.43	-79.20
50	-20.41	-48.75	-30.90	-72.66	-69.08	-60.10	-79.95	-80.81	-80.75

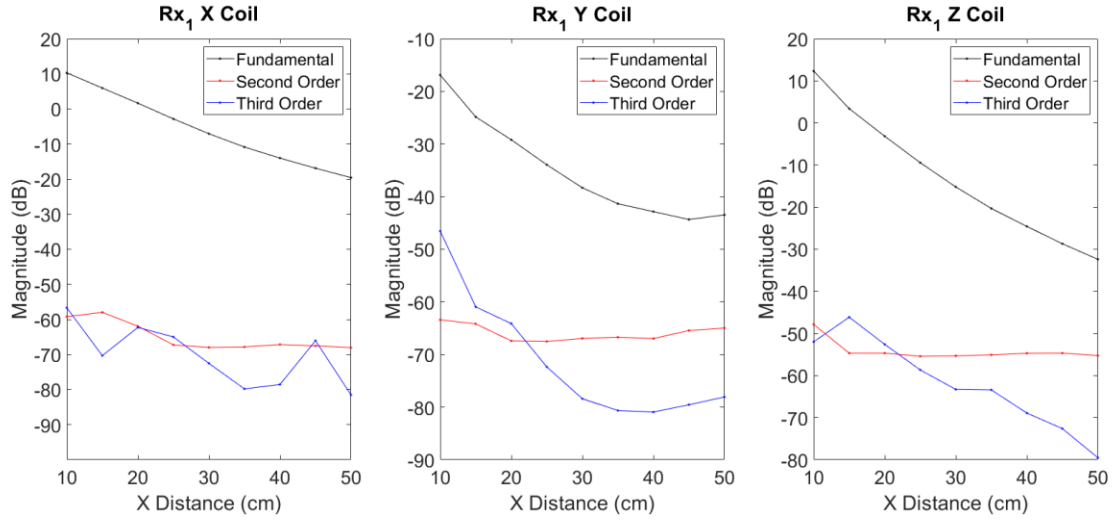


Figure 3.3.22. Rx<sub>1</sub> measured voltage values at different  $x$  distances.

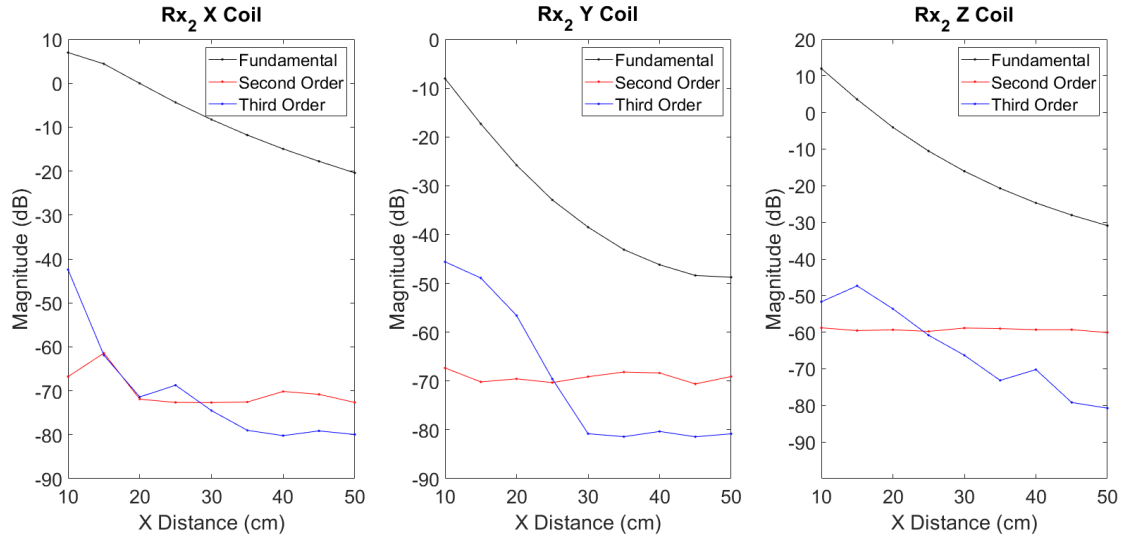


Figure 3.3.23. Rx<sub>2</sub> measured voltage values at different  $x$  distances.

From these results, we see that the harmonic distortion is only significant at far distance (–30 dB attenuation of harmonic relative to the fundamental, which is 3% THD between Tx and Rx, dominated by the second order harmonic. This is because the second order harmonic does not vary over distance. 3% THD is negligible for the proposed system and only happens in the worst case

at 50 cm distance, outside of the heart mapping area. Most points have  $-50$  dB attenuation of harmonic relative to the fundamental, resulting in only 0.3% THD.

Figures 3.3.24 and 3.3.25 below show the signed peak-to-peak measured voltage (as the measure of B-field generated from the transmitter) in relation to the simulated ideal voltage at different test positions (distance in cm) for the 6 coils. The standard deviation (indicated by error bars) ranges from 1 to 3 mV for all test positions. From this, we can determine that the average SNR is in fact 40 dB based on a 200 mV average amplitude and 2 mV standard deviation. This matches the frequency tests performed on the coil in Figure 3.3.20. This 40 dB SNR allows us to track the position of the Tx coil with a deviation in position no larger than 5 mm and 1 deg unfiltered or 1 mm and 0.2 deg filtered. In other words, this system will be able to track position and orientation accurately at the target specifications, within the target range.

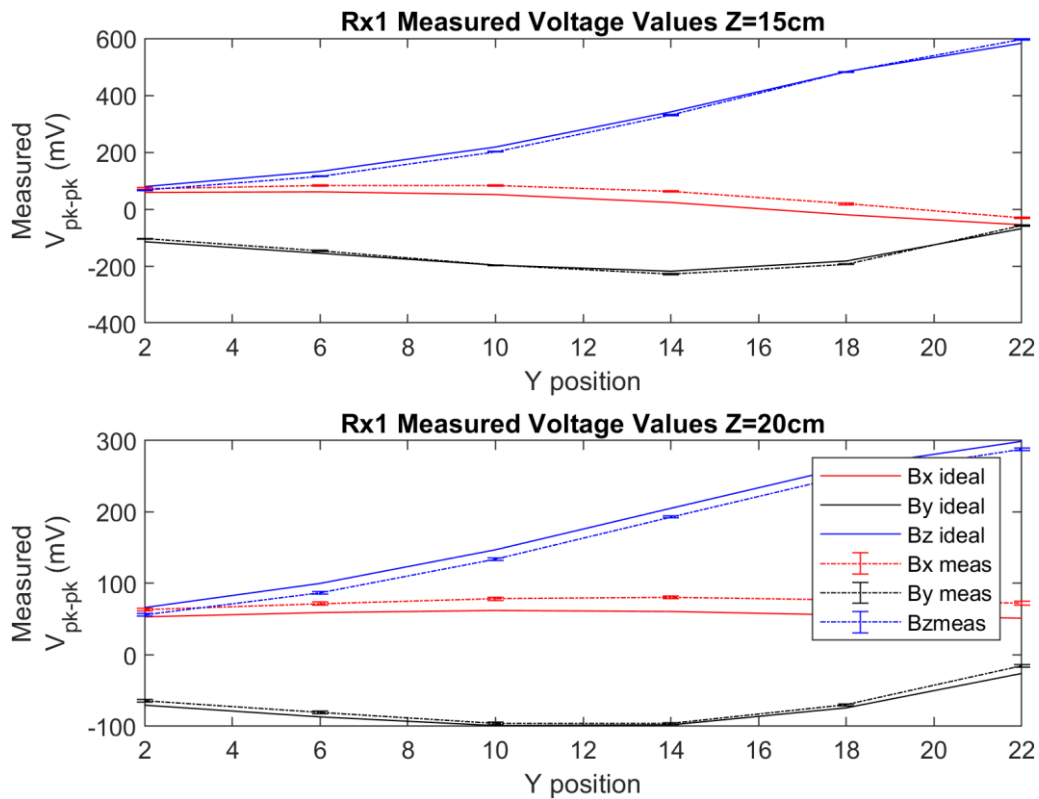


Figure 3.3.24. Rx<sub>1</sub> measured voltage values at different positions.

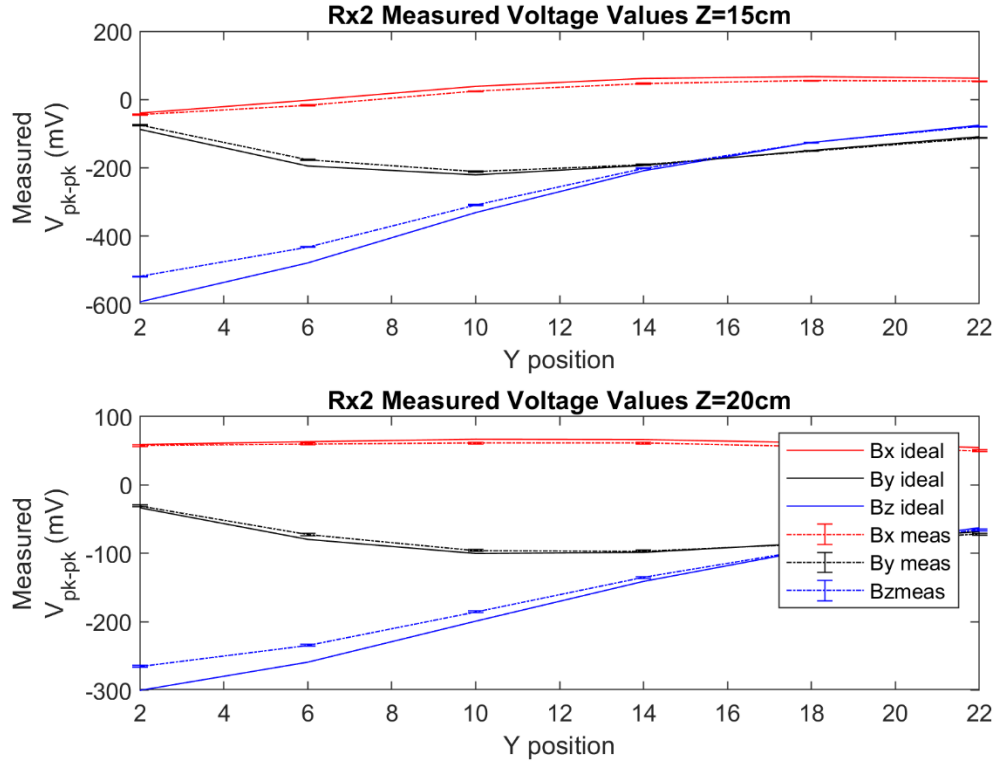


Figure 3.3.25. Rx<sub>2</sub> measured voltage values at different positions.

### 3.3.8 Sensing Coils Configuration

To achieve the effective tracking of a transmitter, sensors must be optimally placed to maximize magnetic field measured by the coils, providing necessary data to allow position calculation [50]–[52]. For our simple system with two triaxial sensing coils, we choose the sensor positions recommended in [42]. Specifically, for the system to track a catheter in a  $25 \times 25 \times 25$  cm volume, the receiver coils are placed at the corners of the tracking area  $(0, 0, -0.5)$  cm and  $(23, 23, -0.5)$  cm. Figure 3.3.26 below shows the setup of the two Rx coils along with this connection.

Based on the results of multiple simulations for two receivers, McGary [42] reports that a diametrically opposed detector configuration is the best for minimizing position errors. Similar findings are also reported by Talcoth and Rylander [50], using an optimization method, for multiple receivers or transmitters in a circular arrangement. The distance between the receivers is determined by the sensitivity of the sensing coils and empirical tests (receivers in the  $xy$  plane, and Tx in the positive  $z$  direction).

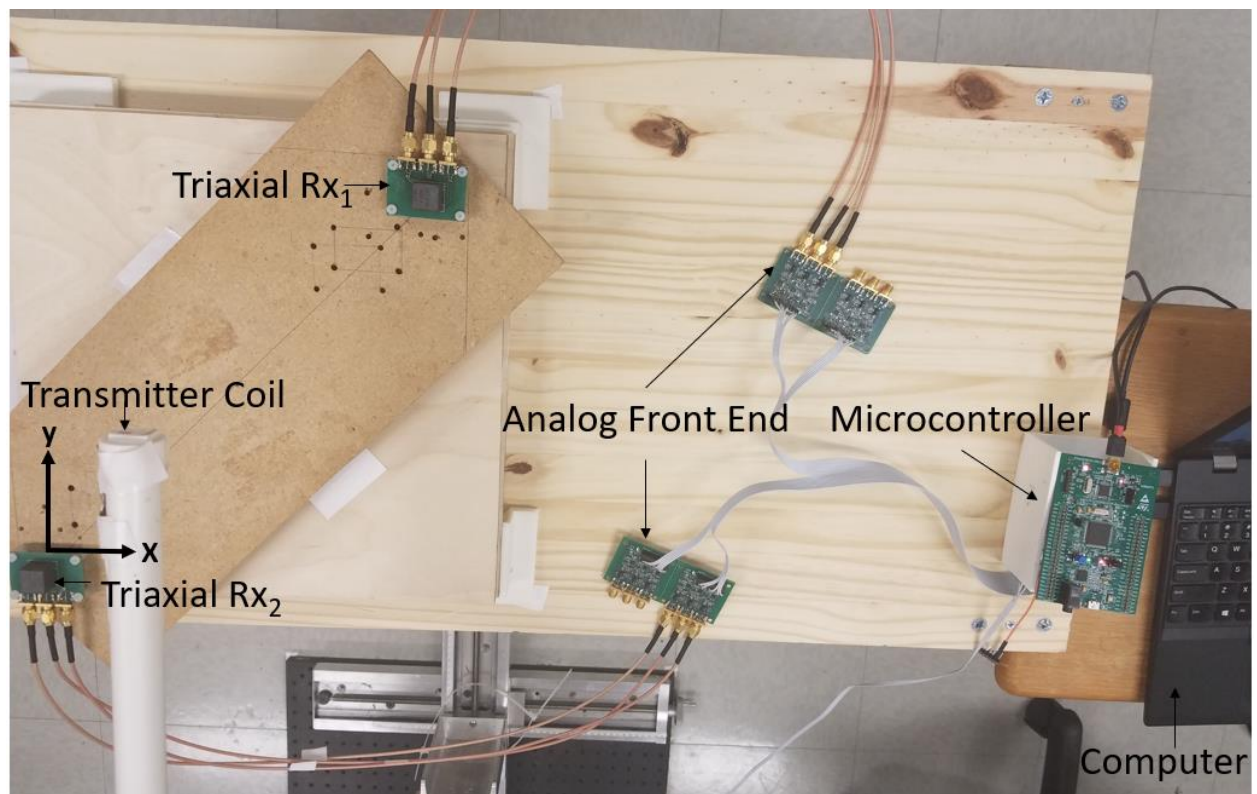


Figure 3.3.26. Two 3DCC10 sensing coil setup.



## 4. MAGNETIC POSITIONING FIRMWARE

### 4.1 Firmware Optimization

In this chapter, we describe the magnetic tracking models and the selection of positioning algorithm for the firmware to translate the sensed B-field from the transmitter into the transmitter coil's position and orientation. The post-processing is performed all on the microcontroller. This is necessary to achieve the fast position update rate required for live-time position tracking.

The firmware code is optimized for parallel processing, which allows for the microcontroller to multitask. For the proposed system, the microcontroller is programmed to sample the amplified sensing coil signals, while simultaneously computing the position using measured signals in the previous cycle. Each position calculation involves five steps. First, the three ADCs in the microcontroller sample in parallel the three B-field signals. The sampling rate is 2.4 MSPS, well above the 32 kHz operating frequency. There are seven signals to measure, including six from the sensing coils and one from the transmitter coil. The signal from the transmitter coil is required for computing its phase relative to those of the sensing coils. These seven signals are split into three groups. The first group includes three measured sensing coil signals from one triaxial receiver. The second group consists of the other three signals from the second triaxial receiver. The third group includes the transmitter coil voltage along with two sensing coils signals, one from each triaxial receiver. This forms the active feedback sensing described above in Section 3.2.9.

These groups are sampled cyclically, with only one group sampled per position calculation cycle. The other two groups are stored in memory for position calculation in this cycle. In step 2, amplitude and phase are extracted using an amplitude and phase detection algorithm (a matched filter). In step 3, calibration and compensation are performed based on non-idealities determined for each coil. The calibration is described in the calibration section in the next chapter. Once the sign and magnitude of the B-field are determined for the group, the position algorithm takes the six signed amplitude values from sensing coils and computes the position in step 4. In the last step, a Kalman filter reduces the noise in the computed position and orientation based on the position and orientation values from previous cycle. The filter delay cannot be significantly higher than five milliseconds; otherwise, the system latency will be poor.

Figure 4.1.1 shows the entire firmware cycle, depicting how the Rx and Tx coils are sampled simultaneously by three ADCs and how the data are used to compute the position.

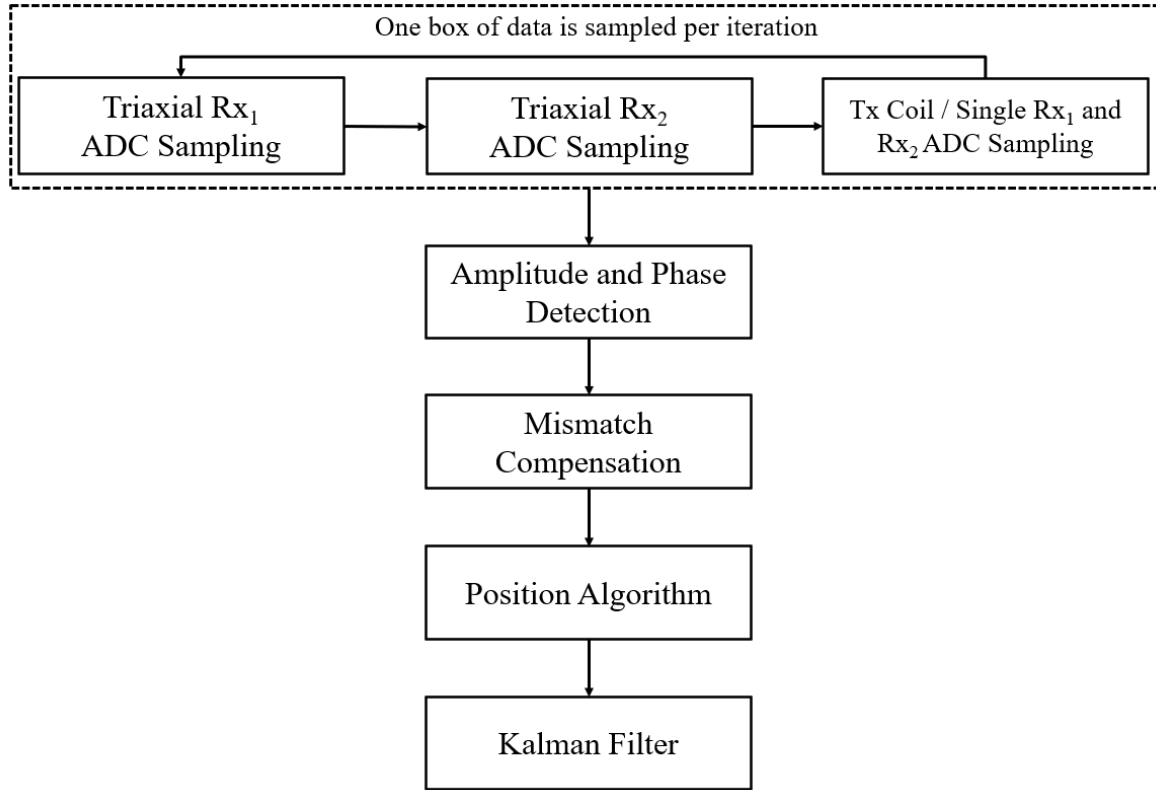


Figure 4.1.1. ADC data sample for position calculation.

Next, the timing is described along with the position data transfer from the microcontroller to the GUI on a computer. The target update rate is 200 readings/sec, which allows for a rapid live-time tracking much faster than sensing coil tracking systems (type 1). As illustrated in Figure 4.1.2, the cycle starts with  $t_0-t_1$  for the ADC sampling. The sampling of the next group signals is performed in parallel with the amplitude detection, position computation, and filtering of the previous cycle's data. Thus, the total cycle time of single position update is given by  $t_1-t_4$ .

The total cycle time is estimated by coding an LED blink for each cycle. The LED voltage is recorded on an oscilloscope. Using time domain trace, the period of the LED blink is computed, and the total time for one cycle is 0.63 ms. The single cycle time is significantly faster than the target 200 readings/sec. Because of this, the time  $t_n$  (sending data to GUI ) occurs after every 8

cycles of  $t_1$ – $t_4$ . This allows for a reduction in perceived filter latency. The position gets updated to the user visually at a rate of 200 readings/sec.

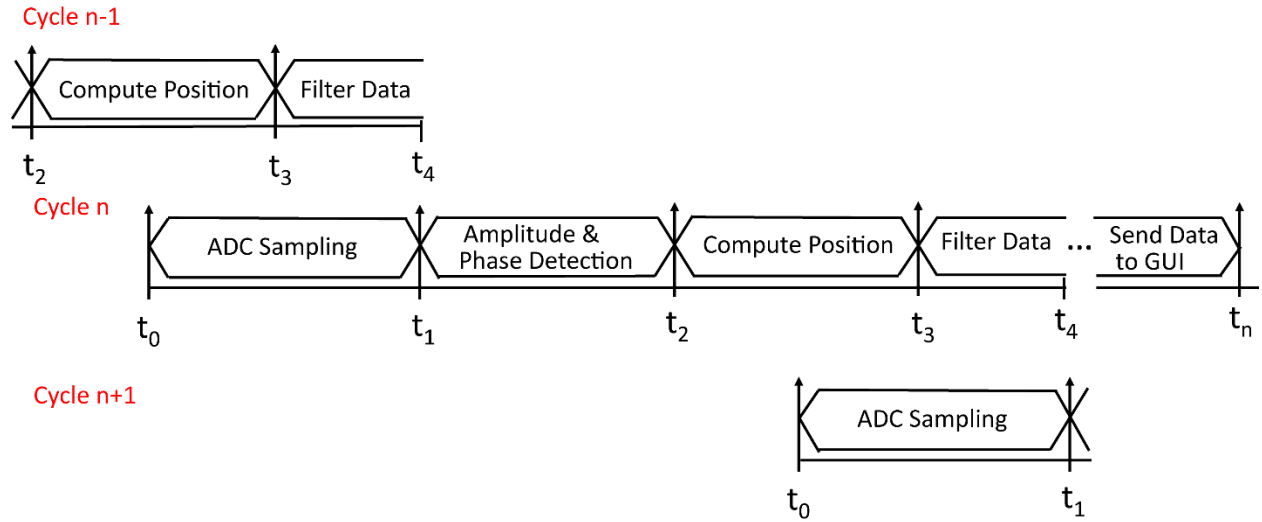


Figure 4.1.2. Timing of microcontroller computations.

## 4.2 Positioning Algorithm

In this section, we discuss the positioning algorithm. The goal of the algorithm is to calculate the position ( $x$ ,  $y$ , and  $z$  in a reference frame) and orientation (azimuth and elevation) of the transmitter using the 6 signed B-field magnitudes measured from sensing coils. The magnetic moment vector of the transmitting coil ( $m_x, m_y, m_z$ ) is used to compute the azimuth and elevation angles. Thus, a minimum of six independent equations are required to solve the six unknowns [28], [30]. The general idea for tracking the transmitter is illustrated in Figure 4.2.1.

The major challenge in selecting a positioning algorithm is the high degree of nonlinearity in the B-field equations. It means that an iterative position algorithm typically cannot ensure universal convergence in the tracking area. To mitigate the problem, we examined and tested two possible algorithms that can be used for this 1 transmitter 2 triaxial sensing system.

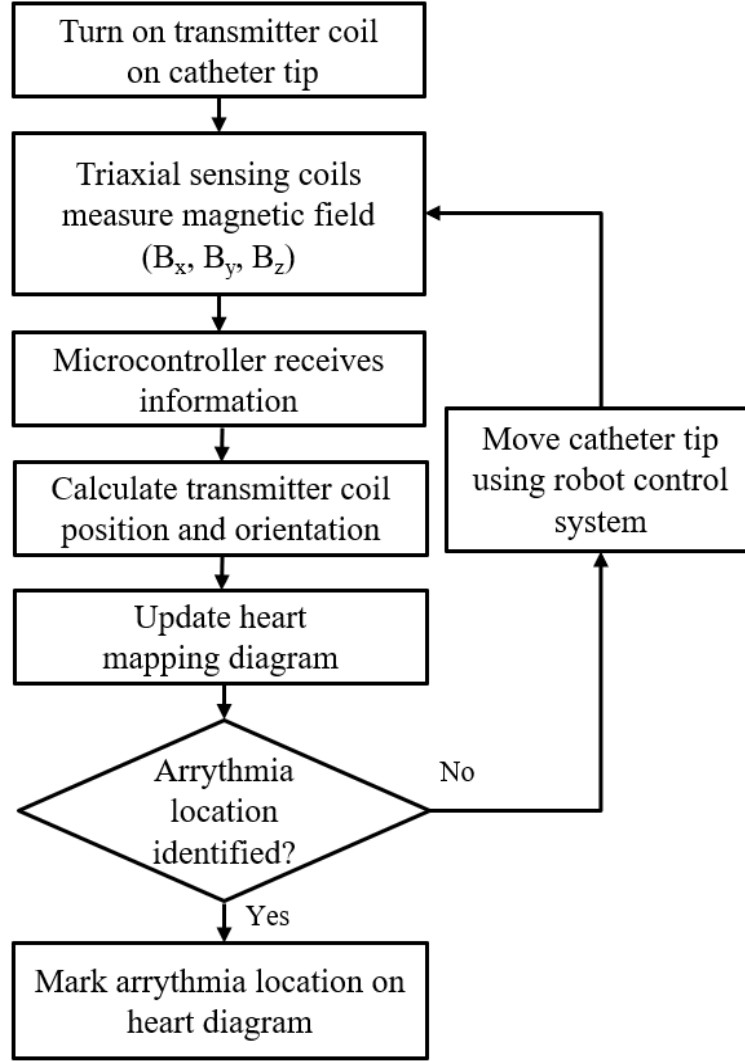


Figure 4.2.1. Tracking system overview.

#### 4.2.1 Algorithm 1: Position Solver

The first algorithm is based on the dipole field model as described in Section 2.2.3. The near field generated by a transmitting coil can be approximated by the following dipole field equation:

$$\mathbf{B} = \frac{\mu_0}{4\pi} \left( \frac{3(\mathbf{m} \cdot \mathbf{r})\mathbf{r}}{r^5} - \frac{\mathbf{m}}{r^3} \right) \quad (4.2.1.1)$$

where  $\mu_0$  is the permeability of free space,  $\mathbf{m}$  the dipole moment vector of the transmitting coil, and  $\mathbf{r}$  the vector of length  $r$  from the position of transmitter (Tx) to the receiving coil (Rx) at the position  $\mathbf{r}^{rec}$ .

We define the tracking coordinate frame with the receiving coils as reference. Each of the three coils in a triaxial receiver is oriented in the  $x$ ,  $y$ , and  $z$  direction, respectively. Equation (4.2.1.1) can be rewritten in explicit vector components of  $x$ ,  $y$ , and  $z$  by letting:

$$\mathbf{B} = \begin{bmatrix} B_x \\ B_y \\ B_z \end{bmatrix} \quad \mathbf{m} = \begin{bmatrix} m_x \\ m_y \\ m_z \end{bmatrix} \quad \mathbf{r} = \begin{bmatrix} r_x \\ r_y \\ r_z \end{bmatrix} \quad (4.2.1.2)$$

Substituting (4.2.1.2) into (4.2.1.1), we have:

$$\begin{bmatrix} B_x \\ B_y \\ B_z \end{bmatrix} = \frac{\mu_0}{4\pi} \left( \frac{3(m_x r_x + m_y r_y + m_z r_z)}{r^5} \begin{bmatrix} r_x \\ r_y \\ r_z \end{bmatrix} - \frac{1}{r^3} \begin{bmatrix} m_x \\ m_y \\ m_z \end{bmatrix} \right) \quad (4.2.1.3)$$

and

$$r = \|\mathbf{r}\| = \sqrt{r_x^2 + r_y^2 + r_z^2} \quad (4.2.1.4)$$

$B_x$ ,  $B_y$ , and  $B_z$  are the three B-field signed values measured by a receiver. Using these measured B-fields values, the position algorithm calculates vector  $\mathbf{r}$  and the transmitter orientation defined by vector  $\mathbf{m}$ . Note that  $\mathbf{r}$  is the distance vector from transmitter to receiver, and we define the position of transmitter  $\mathbf{r}^{tran}$  using both  $\mathbf{r}$  and receiver location  $\mathbf{r}^{rec}$ . This is done by using the coordinate frame defined in Figure 2.2.3, and thus

$$\mathbf{r} = \mathbf{r}^{rec} - \mathbf{r}^{tran} \quad (4.2.1.5)$$

where

$$\mathbf{r}^{rec} = \begin{bmatrix} r_x^{rec} \\ r_y^{rec} \\ r_z^{rec} \end{bmatrix} \quad \mathbf{r}^{tran} = \begin{bmatrix} r_x^{tran} \\ r_y^{tran} \\ r_z^{tran} \end{bmatrix} = \begin{bmatrix} x \\ y \\ z \end{bmatrix} \quad (4.2.1.6)$$

Note that the receiver location  $\mathbf{r}^{rec}$  is known and fixed. Thus, when the algorithm computes distance vector  $\mathbf{r}$ ,  $\mathbf{r}^{tran} = (x, y, z)$  (Tx position) can be determined.

The dipole equation (4.2.1.3) is only for one triaxial receiver and transmitter relation. The position algorithm utilizes two  $\mathbf{B}$  vectors measured by two separate triaxial receivers,  $\mathbf{B}_1$  and  $\mathbf{B}_2$ , each with three components in  $x$ ,  $y$ , and  $z$ . The distances from the transmitter to the two triaxial receivers are  $\mathbf{r}_1$  and  $\mathbf{r}_2$ , respectively. These dipole equations need to be rearranged to obtain an efficient algorithm. As explained by McGary [42], the same magnetic moment of the transmitter  $\mathbf{m}$  is observed by both triaxial receivers, and thus  $\mathbf{m} = \mathbf{m}_1 = \mathbf{m}_2$ . Essentially, the algorithm involves the minimization of the difference between  $\mathbf{m}_1$  and  $\mathbf{m}_2$ ,  $\min [abs(\mathbf{m}_1 - \mathbf{m}_2)]$ , or finding the roots for  $\mathbf{m}_1 - \mathbf{m}_2 = \mathbf{0}$  by solving  $\mathbf{r}_1$  through iterations.

Specifically, the dipole equation (4.2.1.1) is written in matrix notation:

$$\mathbf{B} = \frac{\mu_0}{4\pi r^3} \left( \frac{3\mathbf{r}^T \mathbf{m}}{\mathbf{r}^T \mathbf{r}} \mathbf{r} - \mathbf{m} \right) \quad (4.2.1.7)$$

The transmitter magnetic moment  $\mathbf{m}$  can be isolated for a triaxial receiver away from the transmitter described by vector  $\mathbf{r}$ :

$$\mathbf{m} = \frac{4\pi r^3}{\mu_0} \left( \frac{3\mathbf{r}\mathbf{r}^T}{2\mathbf{r}^T \mathbf{r}} - \mathbf{I} \right) \mathbf{B} \quad (4.2.1.8)$$

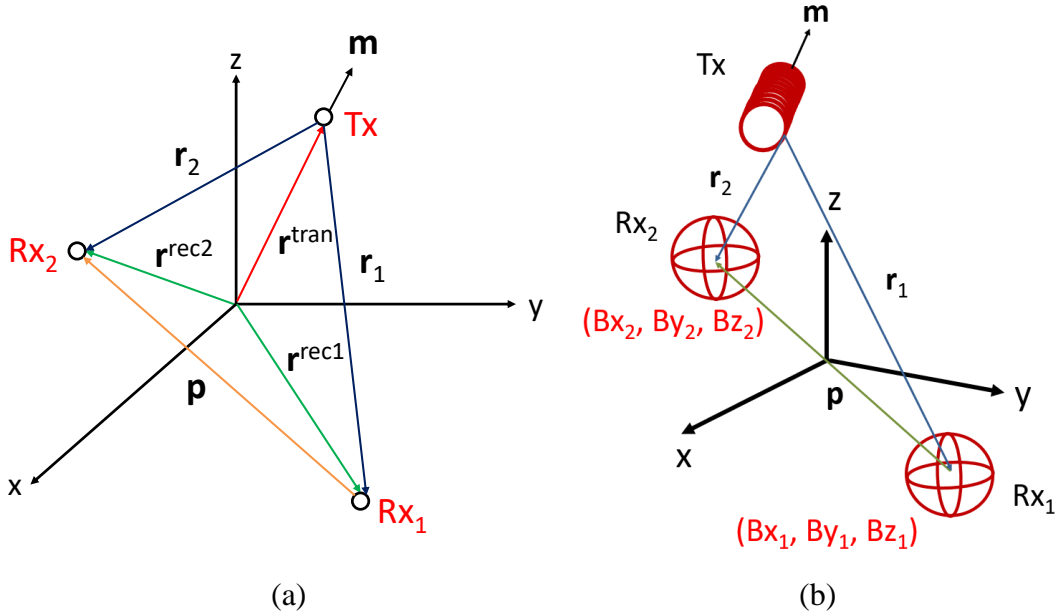


Figure 4.2.2. Tracking the transmitter with two fixed receivers.

Because we have two triaxial sensing coils that measure  $\mathbf{B}_1$  and  $\mathbf{B}_2$  transmitted from the single transmitter with  $\mathbf{m}$  shown above in Figure 4.2.2, we have  $\mathbf{m} = \mathbf{m}_1 = \mathbf{m}_2$  or:

$$\frac{\mu_0 \mathbf{m}}{4\pi} = r_1^3 \left( \frac{3\mathbf{r}_1 \mathbf{r}_1^T}{2\mathbf{r}_1^T \mathbf{r}_1} - \mathbf{I} \right) \mathbf{B}_1 = r_2^3 \left( \frac{3\mathbf{r}_2 \mathbf{r}_2^T}{2\mathbf{r}_2^T \mathbf{r}_2} - \mathbf{I} \right) \mathbf{B}_2 \quad (4.2.1.9)$$

Because the locations of the two receivers are known, define the distance between them as  $\mathbf{p}$ :

$$\mathbf{p} = \mathbf{r}_2 - \mathbf{r}_1 \quad (4.2.1.10)$$

and

$$\mathbf{r}_2 = \mathbf{p} + \mathbf{r}_1 \quad (4.2.1.11)$$

Since  $\mathbf{p}$  is known, (4.2.1.9) can be rewritten as a function of  $\mathbf{r}_1$  only by plugging (4.2.1.11) into (4.2.1.9), and we obtain the expression for  $\mathbf{m}_1 - \mathbf{m}_2 = \mathbf{0}$  as:

$$F_1(\mathbf{r}_1) = r_1^3 \left( \frac{3\mathbf{r}_1\mathbf{r}_1^T}{2\mathbf{r}_1^T\mathbf{r}_1} - \mathbf{I} \right) \mathbf{B}_1 - \|\mathbf{p} + \mathbf{r}_1\|^3 \left( \frac{3(\mathbf{p} + \mathbf{r}_1)(\mathbf{p} + \mathbf{r}_1)^T}{2(\mathbf{p} + \mathbf{r}_1)^T(\mathbf{p} + \mathbf{r}_1)} - \mathbf{I} \right) \mathbf{B}_2 = \mathbf{0} \quad (4.2.1.12)$$

This is a vector function for a system of three nonlinear equations with three unknowns  $\mathbf{r}_1 = (r_{1x}, r_{1y}, r_{1z})$ , which can be solved by Newton's method (see (2.3.1.8) in Section 2.3.1). Using the result of  $\mathbf{r}_1$ , we can calculate the transmitter position  $\mathbf{r}^{tran} = (x, y, z)$  using (4.2.1.5) and its orientation using (4.2.1.8). The transmitter position is calculated by solving  $F_1(\mathbf{r}_1) = 0$  (4.2.1.12) as a nonlinear least-squares problem. In this case, we implement Newton's method following McGary [42] by defining:

$$H(\mathbf{r}, \mathbf{B}) = \frac{3}{2}(r\mathbf{r}^T\mathbf{B})\mathbf{r} - r^3\mathbf{B} \quad (4.2.1.13)$$

The Jacobian of  $H$  is:

$$H'(\mathbf{r}, \mathbf{B}) = \frac{3}{2} \left( (r\mathbf{r}^T\mathbf{B})\mathbf{I} + \frac{\mathbf{r}^T\mathbf{B}}{r}\mathbf{r}\mathbf{r}^T + r\mathbf{r}\mathbf{B}^T \right) - 3r\mathbf{B}\mathbf{r}^T \quad (4.2.1.14)$$

The derivative of  $F_1$  in (4.2.1.12) is:

$$F_1'(\mathbf{r}) = F_1'(\mathbf{r}, \mathbf{B}_1, \mathbf{B}_2) = H'(\mathbf{r}, \mathbf{B}_1) - H'(\mathbf{r} + \mathbf{p}, \mathbf{B}_2) \quad (4.2.1.15)$$

$$\mathbf{r}^{(k+1)} = \mathbf{r}^{(k)} - [F_1'(\mathbf{r})]^{-1}F_1(\mathbf{r}) \quad (4.2.1.16)$$

The above equation is used to solve  $\mathbf{r}_1$ . Using the result of  $\mathbf{r}_1$ , we can calculate the transmitter position  $\mathbf{r}^{tran} = (x, y, z)$  using (4.2.1.5) and its orientation using (4.2.1.8).

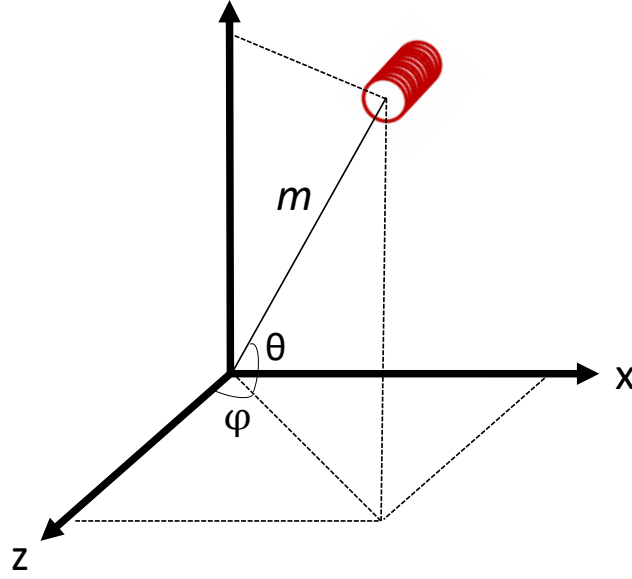


Figure 4.2.3. Orientation angles.

Using the estimated orientation  $\hat{\mathbf{m}}$ , azimuth angle  $\varphi$  and elevation angle  $\theta$  (Figure 4.2.3) can be calculated as follows:

$$m = \sqrt{m_x^2 + m_y^2 + m_z^2} \quad (4.2.1.17)$$

$$\theta = \sin^{-1} \frac{-m_y}{m} \quad (4.2.1.18)$$

$$\varphi = \tan^{-1} \frac{m_x}{m_z} \quad (4.2.1.19)$$

This positioning algorithm was simulated with a Tx to Rx  $z$  distance of 15 cm. B-field with SNR of 60 dB was simulated at various  $x$  and  $y$  positions within the heart mapping area. Its expected performance is shown below in Figure 4.2.4.



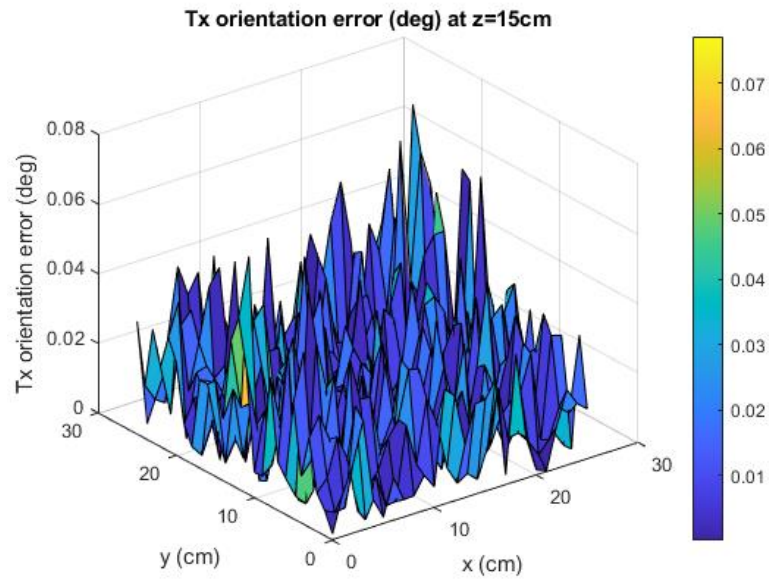
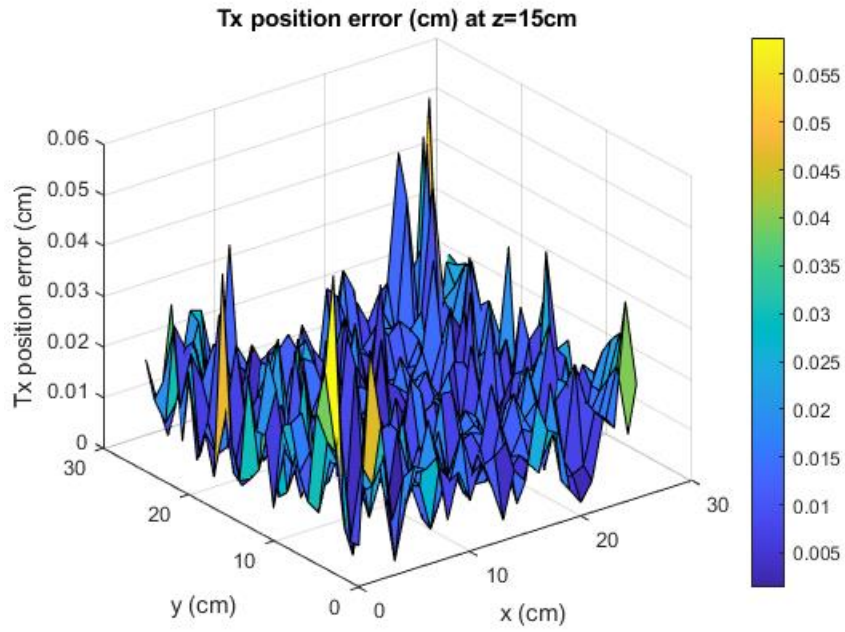


Figure 4.2.4. Simulated position and orientation errors.

### 4.2.2 Algorithm 2: Position Search

The second algorithm tested is based on a position search method. Unlike the first algorithm, based on the McGary algorithm [42], which uses triaxial receiver coils as the reference frame, this algorithm searches for possible receiver positions of  $Rx_1$  and  $Rx_2$ , based on the reference transmitter coil position, where the transmitter is located at the origin of the coordinate frame.

First, define the magnetic dipole equation in this coordinate frame. Here, we assume that the transmitter is oriented in the  $+z$  direction,  $\mathbf{m} = (0, 0, m_z)$  [86]. Because the transmitter location is fixed at the origin, a triaxial sensing coil is located at  $\mathbf{r} = (r_x, r_y, r_z)$ , and from (4.2.1.3), we have the three transmitting B-field components:

$$B_x = \frac{\mu_0}{4\pi} \left( \frac{3m_z r_x r_z}{r^5} \right) \quad (4.2.2.1)$$

$$B_y = \frac{\mu_0}{4\pi} \left( \frac{3m_z r_y r_z}{r^5} \right) \quad (4.2.2.2)$$

$$B_z = \frac{\mu_0}{4\pi} \left( \frac{m_z (2r_z^2 - r_x^2 - r_y^2)}{r^5} \right) \quad (4.2.2.3)$$

However, the measured three B-field components from the triaxial receiver are not in the transmitter's coordinate frame as the  $x$ ,  $y$ , and  $z$  components. Instead, the measured B-field is in the receiver's coordinate frame  $u$ ,  $v$ , and  $w$ , as  $B_u$ ,  $B_v$ , and  $B_w$  from each of the coils in the triaxial receiver. Figure 4.2.5 shows the coordinate frames. This algorithm is different from the above discussed first algorithm in that the positions for Receivers 1 and 2 are unknown in the  $xyz$  frame at the beginning of the search. The goal is to estimate the  $Rx_1$  and  $Rx_2$  positions and orientation in the  $uvw$  frame relative to the Tx centered at  $(0, 0, 0)$  with  $+z$  orientation in the  $xyz$  frame.

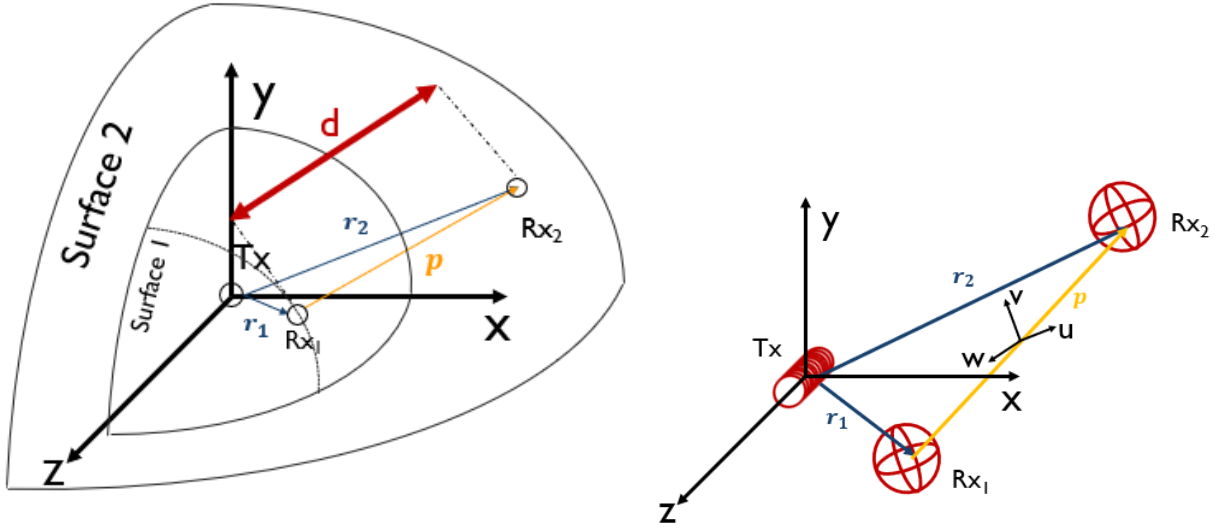


Figure 4.2.5. Transmitter as reference frame and two receivers on iso-power surface.

We need to relate  $B_x$ ,  $B_y$ , and  $B_z$  in the transmitter coordinate frame to the  $B_u$ ,  $B_v$ , and  $B_w$  in the sensing coordinate frame. Note that, despite in different frames, the B-field magnitudes in transmitter's  $xyz$  frame and receiver's  $uvw$  frame should be identical  $B_{uvw} = B_{xyz}$ , i.e.,

$$\sqrt{B_u^2 + B_v^2 + B_w^2} = \sqrt{B_x^2 + B_y^2 + B_z^2} \quad (4.2.2.4)$$

The fact that the B-field magnitudes are the same is important here, because the B-field magnitude represents an iso-power surface of the transmitter. From this, we may define iso-power surfaces of Tx for Rx1 (surface 1) and Rx2 (surface 2), respectively. These surfaces include all the possible positions for Rx1 and Rx2. Using these iso-power surfaces, the Rx1 and Rx2 positions and orientation are estimated.

The search algorithm starts by determining the Rx1 position on surface 1 using the measured B-field magnitude. Using Equations (4.2.2.1) through (4.2.2.3), we can express the B-field magnitude on surface 1 in terms of the elements of vector  $\mathbf{r}_1$  for Rx1 as:

$$\begin{aligned} B_{1xyz} &= \frac{\mu_0 m_z}{4\pi} \sqrt{\frac{r_{1x}^4 + r_{1y}^4 + 4r_{1z}^4 + 2r_{1x}^2 r_{1y}^2 + 5r_{1x}^2 r_{1z}^2 + 5r_{1y}^2 r_{1z}^2}{(r_{1x}^2 + r_{1y}^2 + r_{1z}^2)^5}} \\ &= G(r_{1x}, r_{1y}, r_{1z}) \end{aligned} \quad (4.2.2.5)$$

At this step, the transmitter to receiver orientation is not considered because measurements in the sensing coil frame  $uvw$  are translated into  $xyz$  using the iso-power relationship, and  $B_{1xyz}$  is known.

The position of the first triaxial sensing coil is now estimated through a search process. Start with a guess position,  $(r_{1x}^0, r_{1y}^0, r_{1z}^0)$ , which is not necessarily on surface 1. To obtain the next position on surface 1  $(r_{1x}, r_{1y}, r_{1z})$ , for a fixed  $r_{1x}$ ,  $r_{1y}$  is calculated as:

$$r_{1y} = \frac{r_{1y}^0}{r_{1z}^0} r_{1z} \quad (4.2.2.6)$$

Now solve  $r_{1z}$  using:

$$B_{1xyz} = G\left(r_{1x}, \frac{r_{1y}^0}{r_{1z}^0} r_{1z}, r_{1z}\right) \quad (4.2.2.7)$$

Next, search through  $r_{1y}$  by varying the slope in (4.2.2.6) as:

$$\frac{r_{1y}^0 \pm \Delta r_{1y}}{r_{1z}^0} \quad (4.2.2.8)$$

In summary, the search proceeds by solving  $r_{1z}$  on surface 1 first, then  $r_{1y}$ , and finally  $r_{1x}$ . For each search position, Equations (4.2.2.1) through (4.2.2.3) are used to calculate  $\mathbf{B}_{1xyz}$  which is measured by  $R_{x1}$  as  $\mathbf{B}_{1uvw}$ . Note that since  $R_{x1}$  is in the  $uvw$  frame, a perfect match can only be found if we rotate  $\mathbf{B}_{1xyz}$  (changing the Tx orientation  $\mathbf{m}$ ):

$$\mathbf{B}_{1uvw} = \mathbf{R}\mathbf{B}_{1xyz} \quad (4.2.2.9)$$

where  $\mathbf{R}$  is the rotation matrix. Similar to algorithm 1, we do not consider rotation around the  $z$ -axis of the transmitter for a 5DOF system:

$$\mathbf{R} = \mathbf{R}_z(0)\mathbf{R}_y(\theta)\mathbf{R}_x(\varphi) = \mathbf{R}_y(\theta)\mathbf{R}_x(\varphi) \quad (4.2.2.10)$$

$$\mathbf{R} = \begin{bmatrix} \cos\theta & \sin\varphi\sin\theta & \cos\varphi\sin\theta \\ 0 & \cos\varphi & -\sin\varphi \\ -\sin\theta & \sin\varphi\cos\theta & \cos\varphi\cos\theta \end{bmatrix} \quad (4.2.2.11)$$

So, using Equation (4.2.2.9), the transmitter's orientation  $\mathbf{R}$  can be computed given  $\mathbf{B}_{1uvw}$  and  $\mathbf{B}_{1xyz}$ .

After that, the position of sensing coil 2 on surface 2 is determined. Since  $\text{Tx}_2$  is also fixed in the  $uvw$  frame, and the transmitter to sensing coil orientation is already known from the rotation matrix  $\mathbf{R}$ , a closed form solution can be used. Specifically,  $\mathbf{B}_{2uvw}$  measured by  $\text{Rx}_2$  and the same  $\mathbf{R}$  can be used to calculate the B-field in the  $xyz$  frame  $\mathbf{B}_{2xyz}$ . In other words, the measured  $uvw$  components of the three sensing coil voltages are converted into B-field  $xyz$  components:

$$\mathbf{B}_{2xyz} = \mathbf{R}^{-1}\mathbf{B}_{2uvw} \quad (4.2.2.12)$$

Once  $\mathbf{B}_{2xyz}$  is known,  $\mathbf{r}_2$  on surface 2 can be computed ( $\mathbf{B}_{2xyz} = \mu_0\mathbf{H}_{2xyz}$ ) as in [88]:

$$r_{2x} = \frac{H_{2x}}{H_{2\rho}}\rho \quad (4.2.2.13)$$

$$r_{2y} = \frac{H_{2y}}{H_{2\rho}}\rho \quad (4.2.2.14)$$

$$r_{2z} = k\rho \quad (4.2.2.15)$$

where

$$H_{2\rho} = \sqrt{H_{2x}^2 + H_{2y}^2} \quad (4.2.2.16)$$

$$\rho = \sqrt[3]{\frac{3m_z k_2}{4\pi(1+k^2)^{\frac{5}{2}}H_{2\rho}}} \quad (4.2.2.17)$$

$$k_2 = \frac{\pm 3H_{2z}}{4H_{2\rho}} + \frac{\sqrt{9\left(\frac{H_{2z}}{H_{2\rho}}\right)^2 + 8}}{4} \quad (4.2.2.18)$$

Finally, the distance between  $\text{Rx}_1$  on surface 1 and  $\text{Rx}_2$  on surface 2 is calculated as follows:

$$d = \sqrt{(r_{2x} - r_{1x})^2 + (r_{2y} - r_{1y})^2 + (r_{2z} - r_{1z})^2} \quad (4.2.2.19)$$

From Figure 4.2.5, the distance between  $\text{Rx}_1$  and  $\text{Rx}_2$  is  $p$ . The magnitude of vector  $\mathbf{p}$  should be equal to the computed distance  $d$  for the correct relative positions among the transmitter and the two receivers.

If  $d = p$ , then the positions of  $R_{x1}$  and  $R_{x2}$  in the  $xyz$  frame are correct, and the  $T_x$  position can be estimated; otherwise, the search on surface 1 repeats. Thus, the objective of the algorithm is to minimize the error in magnitude of  $d$  and  $p$ :

$$\min(d - p) \quad (4.2.2.20)$$

Figure 4.2.6 summarizes the above algorithm 2 in a block diagram.

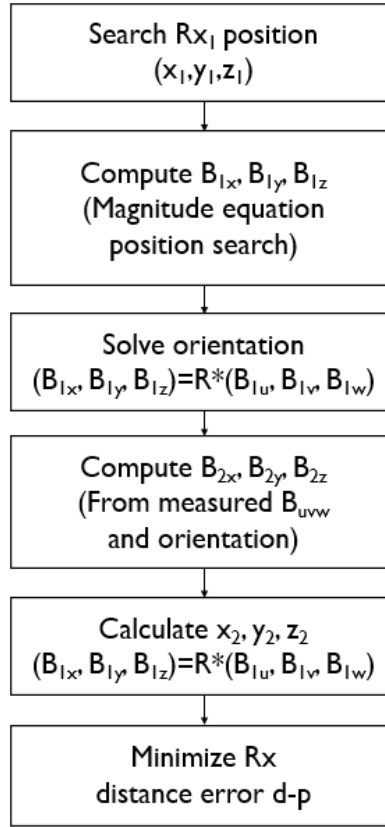


Figure 4.2.6. Block diagram for position search algorithm.

Both of these algorithms are tested using simulations in Matlab. Test positions are swept through the tracking area, and system SNR is set at 40 dB. The system test results suggest that algorithm 2 does not offer better performance in terms of computation speed and precision in position estimation than algorithm 1. Thus, algorithm 1 is used in the final system testing.

### 4.3 Kalman Filter

This section describes the filtering applied to the position and orientation computed from the position algorithm. This is necessary for achieving millimeter level accuracy and 0.1 mm variation in position because the post-process filtering can lower the position variation. The filter is constrained by latency, where filter latency may not exceed the system update rate by 5 frames. Gaussian/IIR filters are easier and more efficient to implement in real-time, but suffer from poor response time, resulting in high latency.

In addition, Gaussian/IIR filters suffer from high pole sensitivity, which leads to instability [89]. FIR/moving average filters have the advantage of stability and linear phase shift but require a sizable buffer resulting in more post-processing time. Kalman filters can achieve substantially improved performance although at the cost of computational complexity. Thus, a Kalman filter is implemented in the system. Kalman filter is a unique filter that has minimal latency, while being able to significantly reduce the noise in the system. Most Kalman filters are applied in tracking systems with multi-sensor fusion, where the data from multiple types of sensors (e.g., accelerometer, gyroscope, and magnetometer) are integrated, and the position is determined [55], [90]. However, integrating additional sensors in the catheter is not feasible. A catheter with IMU described in [38] is 6 mm in diameter and 25 mm in length. In this system, in order to have enough data to improve tracking precision, the position algorithm runs multiple times at 1.6 kHz, and the position is updated to user interface at 200 Hz, so 8 data points are filtered for each position update. The Kalman filter is applied to each position calculation.

A Kalman filter tracks the estimated (prediction) state of an object and updates the estimate based on measurements and state transition models [91]. In the prediction step, the Kalman filter estimates the next state vector at current time  $t$  based on the previous state vector results at time  $t-1$ , which consists of position values ( $x, y, z$ ) and two orientation values (yaw and pitch). At the update step, measurement values are the position and orientation estimates from the positioning algorithms (Figure 4.3.1). Since the positioning algorithm involves an iterative solver to find roots of a system of equations, the inverse Jacobian of the objective function affects the convergence of the position solution. The reciprocal of the determinant of the Jacobian is a good measure of the variance of measurement noise and is used to construct the Kalman gain (the weight for the correction). The system noise covariance matrix is optimally tuned to produce the best estimations. This process is repeated for every position calculated by the algorithm. By applying a Kalman

filter on the position calculation for five times before the position is visually updated, the position error/variance can be reduced, while the latency is kept low at around 50 ms.

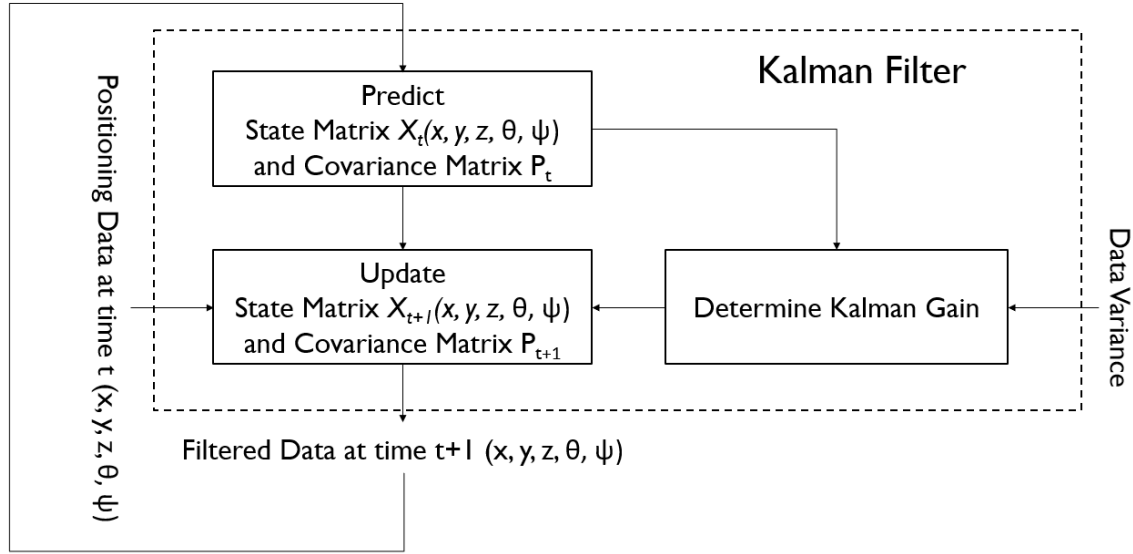


Figure 4.3.1. Kalman filter algorithm flow.

Specifically, the Kalman filter works as follows:

$$\hat{\mathbf{x}}_{t|t-1} = \mathbf{F}_t \hat{\mathbf{x}}_{t-1|t-1} \quad (4.3.1)$$

where  $\hat{\mathbf{x}}$  is prior prediction ( $2 \times 5$ ) with the first row including three position and two orientation values estimated at  $t-1$ , and initial values in the second row are set to zeros;  $\mathbf{F} = [1 \text{ dt}; 0 \text{ } 1]$  with  $\text{dt} = 0.001$  as the sampling interval.

The initial error covariance matrix  $\mathbf{P}$  ( $2 \times 2$ ) and system noise  $\mathbf{Q}$  ( $2 \times 2$ ) are empirically determined.

$$\mathbf{P}_{t|t-1} = \mathbf{F}_t \mathbf{P}_{t-1|t-1} \mathbf{F}_t^T - \mathbf{Q}_t \quad (4.3.2)$$

The Kalman gain is:

$$\mathbf{K}_t = \mathbf{P}_{t|t-1} \mathbf{H}_t^T (\mathbf{H}_t \mathbf{P}_{t|t-1} \mathbf{H}_t^T + \mathbf{R}_t)^{-1} \quad (4.3.3)$$

where  $\mathbf{H} = [1 \text{ } 0]$ , and  $\mathbf{R}$  is the inverse of the Jacobian determinant (a scalar).

The measurement vector  $\mathbf{z}$  ( $1 \times 5$ ) is given by the three position and two orientation values estimated at  $t$ :

$$\mathbf{z}_t = \mathbf{H}_t \mathbf{x}_t \quad (4.3.4)$$

The posterior prediction estimates are:



$$\hat{\mathbf{x}}_{t|t} = \hat{\mathbf{x}}_{t|t-1} + \mathbf{K}_t(\mathbf{z}_t - \mathbf{H}_t\hat{\mathbf{x}}_{t|t-1}) \quad (4.3.5)$$

with error covariance matrix being updated as:

$$\mathbf{P}_{t|t} = \mathbf{P}_{t|t-1} - \mathbf{K}_t\mathbf{H}_t\mathbf{P}_{t|t} \quad (4.3.6)$$

#### 4.4 Optimal Detection

This section describes the methodology for extracting the amplitude and phase of the measured sensing signals. This system only operates at a single frequency of 32 kHz. Thus, only a single tone digital filter is necessary. The single tone filter used for the proposed design is a matched filter. Note that higher order harmonics (especially 3<sup>rd</sup> harmonic as seen in IP3 plot of the amplifier) will be rejected and thus do not need to be considered.

The mathematical operation of the matched filter works as follows. If the received signal is considered to be a sinusoidal wave where its phase is unknown, then the signal can be expressed as a superposition of its sine and cosine components where amplitude  $A$  is the sine component amplitude and amplitude  $B$  is the cosine component amplitude:

$$A\sin\theta + B\cos\theta \quad (4.4.1)$$

The sine and cosine components are extracted using a reference sine wave and a cosine wave. These two waves have the same 2.4 MHz sampling rate as well as the same amplitude.

$$(A\sin\theta + B\cos\theta)\sin\theta = A\sin^2\theta + B\sin\theta\cos\theta \quad (4.4.2)$$

By multiplying these reference waves and accumulating the computed values through addition, a time average of the 32 kHz sine and cosine components of the measured signal sample points is obtained.

$$\frac{2}{n} \sum_{i=1}^n A\sin^2\theta_i + B\sin\theta_i\cos\theta_i = \frac{2}{n} n \left( A * \frac{1}{2} + B * 0 \right) = A \quad (4.4.3)$$

Similarly, amplitude  $B$  can also be obtained by using a reference cosine:  $\cos\theta$ .

Through these components, the magnitude is extracted through an RMS average of the two components, and phase is extracted through arctan of sine and cosine components:

$$Amplitude = \sqrt{A^2 + B^2} \quad (4.4.4)$$

$$\tan (Phase) = \frac{A}{B} \quad (4.4.5)$$

$$Phase = \tan^{-1} \frac{A}{B} \quad (4.4.6)$$

The block diagram below illustrates how the amplitude and phase of the received signal are determined (Figure 4.4.1). This optimal detection method is applied to all 6 signals from the 6 sensing coils and to the voltage of sensing transmitter coil signal.

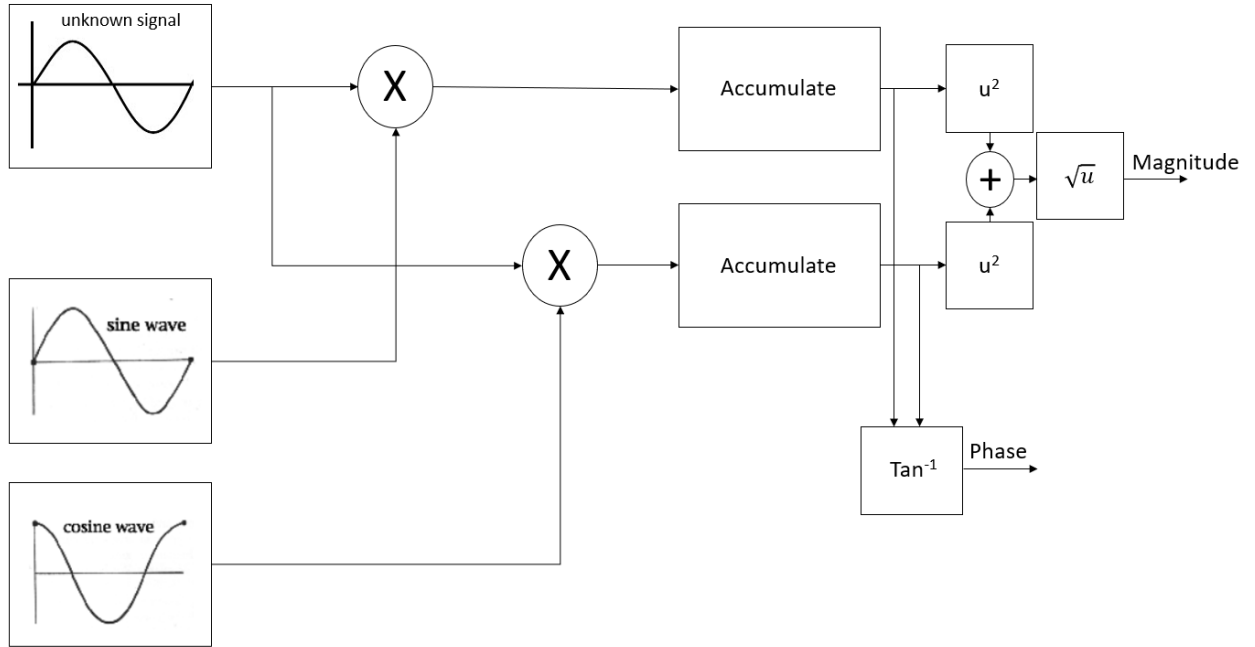


Figure 4.4.1. Optimal detection.

The phase directly translates into the sign of the AC wave. The signed amplitudes obtained from this method are then used to calculate the position of the transmitter.

## 4.5 Algorithm Convergence Speed

The system solves the position of the Tx coil using positioning algorithm 1. The algorithm is adopted from McGary [42] which calculates the transmitter position by solving a system of equations. The goal is to verify that the algorithm can correctly solve for the position in the tracking area and can function with high accuracy and speed, even when SNR is low. Figure 4.5.1 shows a simulation of a  $25 \times 25$  cm  $x$ - $y$  area with the simulated B-field used in the algorithm having an SNR of 30 to 40 dB, with no post-processing filter applied. As seen in Figure 4.5.1, the number of iterations that the position algorithm takes to converge is around 3–5. The condition of convergence is when the distance between the current and next calculated position is less than 0.01 mm.

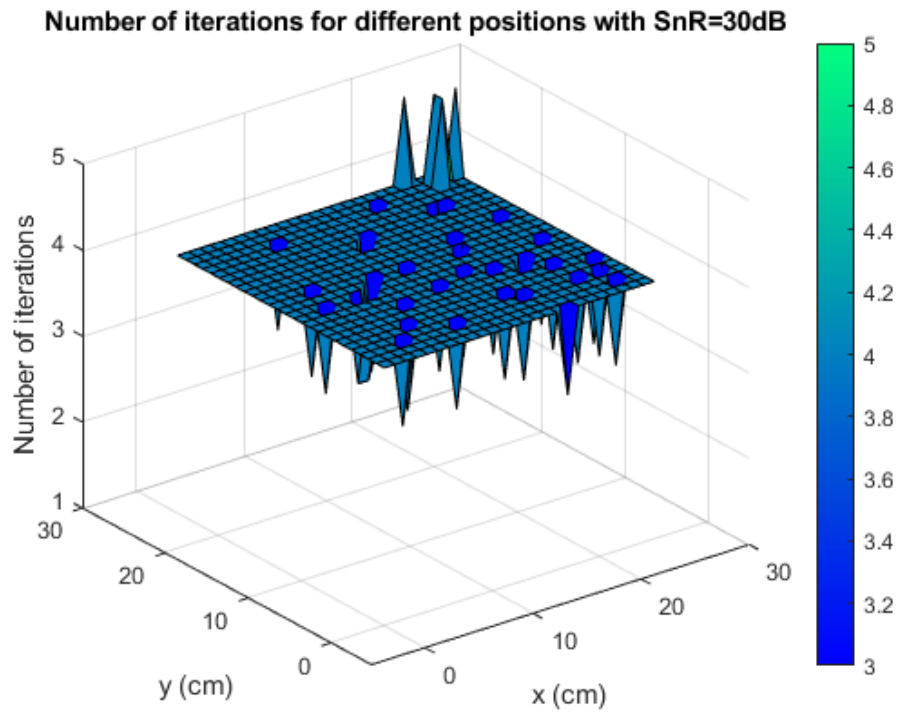
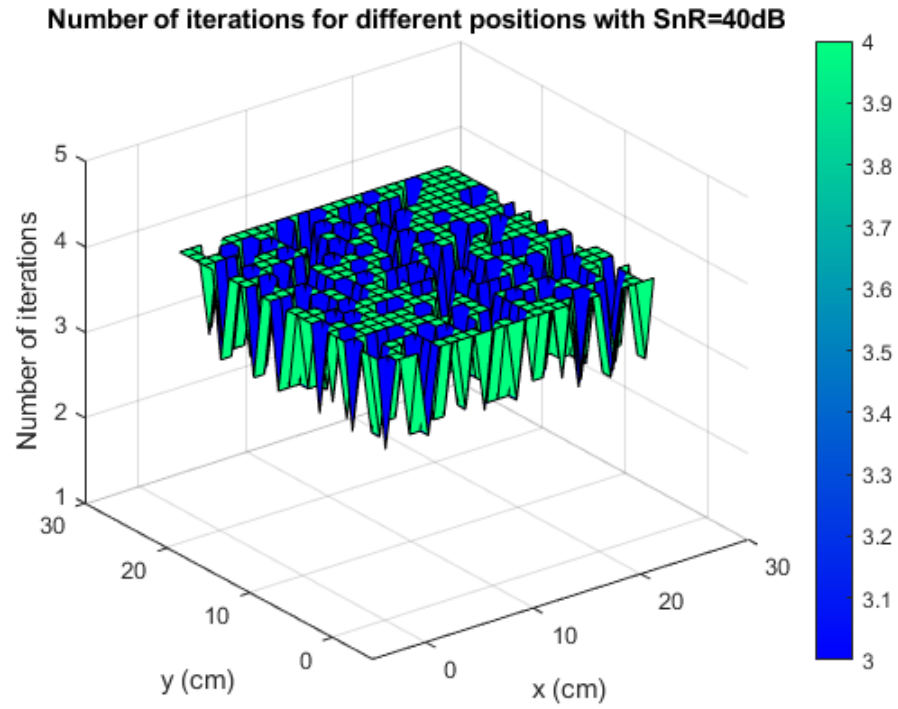


Figure 4.5.1. Number of iterations to converge in position algorithm.

## 4.6 Computational Cost

The method to compute the algorithm computational cost is described below. To estimate the simulation execution time, first, the execution time of Matlab simulation on a desktop computer is obtained for the algorithm. Using the model detailed in [92], the average execution time per time step is determined. Afterwards, this execution time step is used to estimate the execution time on the STM32 microcontroller used for this system.

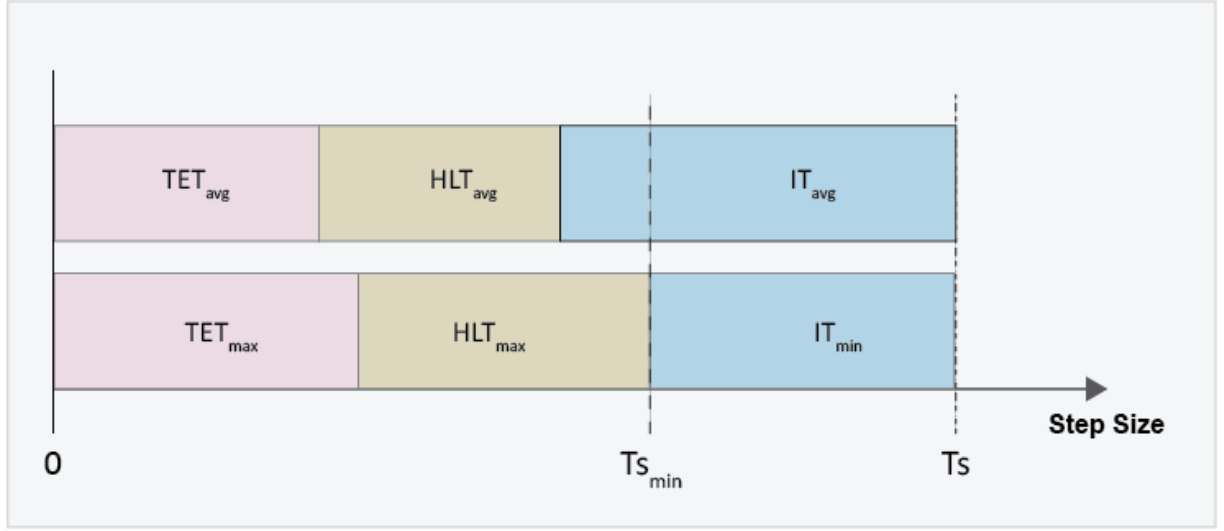


Figure 4.6.1. Computational cost – the execution time per time step [92].

This total time is separated into two parts: the task execution time (TET) and the hardware latency time (HLT). The time that the program is not running is considered the idle time (IT). As illustrated in Figure 4.6.1,

$$Ts_{min} = TET_{max} + HLT_{max} \quad (4.2.1.20)$$

For the proposed system, the goal is to make the time step smaller than 5 ms for all combined post-processing portions. Thus, the minimum step size  $Ts_{min} = 5$  ms, where the maximum execution and latency time cannot exceed this value.

Besides the minimum step size, we examine the computational cost, the cost of addition, multiplication, and other mathematical operations based on the Big O notation. The Big O notation defines the upper bound of the algorithm cost, meaning that it provides the worst case computation cost [93].

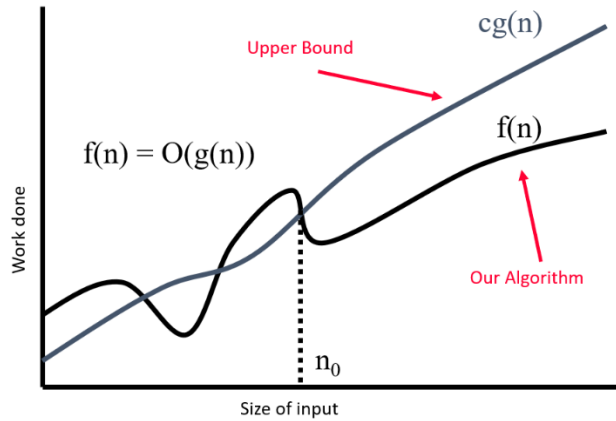


Figure 4.6.2. Visual Big O meaning [94].

For a given function  $g(n)$ ,  $O(g(n))$  is defined to be the set of functions shown in Figure 4.6.2:

$$O(g(n)) = \{f(n): \text{there exist positive constant } c \text{ and } n_0 \text{ such that} \quad (4.2.1.21) \\ 0 \leq f(n) \leq cg(n) \text{ for all } n \geq n_0\}$$

Functions commonly used in the analysis of algorithms is shown in Figure 4.6.3.

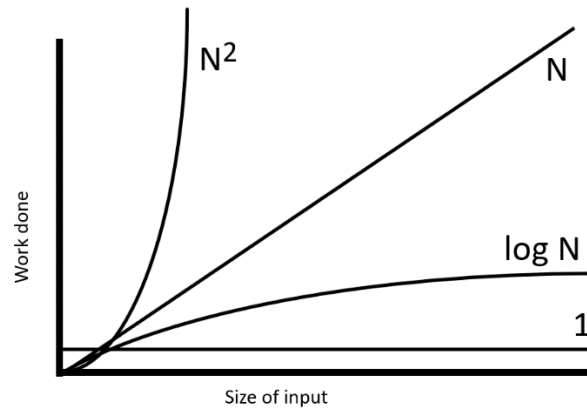


Figure 4.6.3. Comparing factors [94].

To calculate the overall Big O, the algorithm is broken up into individual operations. The Big O of each operation is calculated and then summed up. The constants are not considered when determining the Big O. After the summation, the highest order term is considered the Big O for time complex [95].

Big O is focused on the asymptotic properties. However, for the proposed system, the input size is limited due to the limited measurement within a relatively small tracking range. Thus, we analyze the computational cost based on the clock cycles of the STM32 microcontroller. Specifically, the number for each type of mathematical operations (e.g., multiplication and addition) is first counted for each firmware block in Tables 4.6.1–4.6.3. Then, the numbers of operations are summed across all blocks for one iteration (i.e., one position estimation) in Table 4.6.4. Next, the corresponding clock cycles for these operations are calculated using data on clock cycles per operation for each type of operation from the microcontroller’s data sheet from STMicroelectronics [96] also in Table 4.6.4. Finally, the computation time for one position update is estimated using the time per clock cycle also from the data sheet (Table 4.6.5). The resulting  $8.92\text{E-}04\text{s} = 0.892\text{ms} < 5\text{ms}$ .

Table 4.6.1. Computation cost for optimal detection and mismatch.

Line	Computation	Big O	Multiplication	Division	Addition	Square root	Trigonometric	Conversion, absolute, or negation
1	Sine Accumulate (1 Sample)	$O(n^2)$	1	0	2	0	0	1
2	Cosine Accumulate (1 Sample)	$O(n^2)$	1	0	2	0	0	1
3	614 Samples Line 1 and Line 2 Total		1228	0	2456	0	0	1228
	Magnitude and Phase Extraction							
4	Magnitude Calculation	$O(n^2)$	2	0	1	1	0	0
5	Phase Calculation (angle conversion)		1	1	0	0	0	0
6	Phase Calculation (inverse tangent)					0	1	0
7	Lines 3,4, 5, 6 total (for 3 Rx coils)		3693	3	7371	3	3	3684
	Phase calculation 3 Rx coils (worst case assumes sign switching and phase shift)							
1	Calculating phase difference between Tx and Rx		0	0	6	0	0	0
2	Shift phase to normalize around 0 degrees		0	0	3	0	0	2
3	Switch sign		0	0	0	0	0	3
4	Lines 1-3 total		0	0	9	0	0	5
	<b>Total for optimal detection</b>		<b>3693</b>	<b>3</b>	<b>7389</b>	<b>3</b>	<b>3</b>	<b>3694</b>
	<b>Mismatch (3 Rx coils)</b>							
	Gain mismatch		3	0	0	0	0	0
	Orientation mismatch		9	0	6	0	0	3
	Coupling correction		9	0	6	0	0	3
	Position mismatch		0	0	6	0	0	6
	<b>Total for mismatch</b>		<b>21</b>	<b>0</b>	<b>18</b>	<b>0</b>	<b>0</b>	<b>12</b>



Table 4.6.2. Computation cost for position algorithm.

Line	Computation	Big O	Multiplication	Division	Addition	Square root	Trigonometric	Conversion, absolute, or negation
	Resfun (residual function)							
1	$x'*x$	$O(3)$	3	0	2	0	0	0
2	$x*x'$	$O(9)$	9	0	0	0	0	0
3	$((\text{line } 1)^{(3/2)})$	$O(n^{1.5})$	0	0	0	1	0	0
4	$(3*(\text{line } 2)/(2*(\text{line } 1))-\text{eye}(3))$	$O(n^2)$	0	10	3	0	0	0
5	(line 4 expression)*B1	$O(9)$	9	0	6	0	0	0
6	line 5 x line 3	$O(n^2)$	3	0	0	0	0	0
7	lines 1-6 total for x		24	10	11	1	0	0
8	$x+p$		0	0	3	0	0	0
9	lines 1-6 total for $x+p$ and subtraction from line 7		24	10	14	1	0	0
10	lines 7-9 total		48	20	28	2	0	0
	Jacfun (Jacobian function)							
11	$(\text{line } 1)^{(1/2)}$	$O(n^{0.5})$	0	0	0	1	0	0
12	$x*B1$	$O(3)$	3	0	2	0	0	0
13	(line 11)x(line 12)	$O(n^2)$	1	0	0	0	0	0
14	(line 12)/(line 11)x(line 2)	$O(n^3)$	9	1	0	0	0	0
15	$x*B1'$	$O(9)$	9	0	0	0	0	0
16	(line 11)x(line 15)	$O(n^2)$	9	0	0	0	0	0
17	$B1*x'$	$O(9)$	9	0	0	0	0	0
18	$3*(\text{line } 11)*(\text{line } 17)$	$O(n^2)$	10	0	0	0	0	0
19	$(3/2)*[(\text{line } 13)*\text{eye}(3)+\text{line } 14+\text{line } 18]$		9	0	12	0	0	0
20	lines 11-19 total for x		59	1	14	1	0	0
21	lines 11-19 total for $x+p$ and subtraction from line 12		59	1	23	1	0	0
22	lines 20-22 total		118	2	37	2	0	0
	Update							
23	inv(Jacfun)	$O(27)$	36	1	14	0	0	4
24	line 23*resfun	$O(9)$	9	0	6	0	0	0
25	$x-\text{line } 24$		0	0	3	0	0	0
26	Total		45	1	23	0	0	4
	Complete position algorithm (1 iteration)							
	Resfun(line 10) +Jacfun(line 22) +update (line 26)		211	23	88	4	0	4
	Total 5 iteration loop (position calculation)		1055	115	440	20	0	20
	Closed loop orientation (orifun)		21	0	9	0	0	0
	Orientation normalized magnitude		3	0	2	1	0	0
	2 Orientation Euler angles		2	2	2	0	2	0
	Shift position coordinate frame and typecasting		0	0	3	0	0	3
	<b>Total for position algorithm</b>		<b>1081</b>	<b>117</b>	<b>456</b>	<b>21</b>	<b>2</b>	<b>23</b>

Table 4.6.3. Computation cost for Kalman filter.

Line	Computation	Multiplication	Division	Addition	Square root	Trigonometric	Conversion, absolute, or negation
	Prediction for X and P						
1	Prediction state vector (5×2)	5	0	5	0	0	0
2	Prediction covariance matrix (2×2)	4	0	6	0	0	0
	Updating X and P						
3	y vector (measurement residual)	0	0	5	0	0	0
4	Kalman gain and S	0	2	1	0	0	0
5	Update state vector (5×2)	10	0	10	0	0	0
6	Update covariance matrix (2×2)	4	0	4	0	0	0
	<b>Total for Kalman filter</b>	<b>23</b>	<b>2</b>	<b>31</b>	<b>0</b>	<b>0</b>	<b>0</b>

Table 4.6.4. Total computation cost in clock cycles for one iteration (position estimation).

Component	Multiplication	Division	Addition	Square root	Trigonometric	Conversion, absolute, or negation
Optimal detection	3693	3	7389	3	3	3694
Mismatch	21	0	18	0	0	12
Position algorithm	1081	117	456	21	2	23
Kalman filter	23	2	31	0	0	0
Convert position/orientation data for transmission	5	0	0	0	0	3
Total number of operations in 1 iteration	4823	122	7894	24	5	3732
Clock cycles per operation	1	14	1	14	48	1
Total clock cycles for each operation	4823	1708	7894	336	240	3732
<b>Total clock cycles of all operations</b>	<b>18733</b>					

Table 4.6.5. Computation time for one position update.

Total clock cycles for all computations (1 iteration)	18733
1 clock cycle time (sec) (clock runs at 168MHz)	5.95E-09
Total time (sec) for 1 iteration of post processing	1.11E-04
Total time (sec) before 1 GUI update rate (8 iterations)	8.92E-04

#### 4.7 Link Budget Analysis

Analysis of communication power gains and losses across the system is important. Such analysis gives insight into the amount of power margin on the receiving end. This indicates if the sensing system is well above the critical SNR so that position algorithm can accurately determine the catheter tip's position. Link budget is a method to calculate the gains and losses in the system. It varies based on the frequency operation, along with powers, such as transmitter driver power, receiver sensitivity, and amplifier gains. Signal losses, such as SMA connector loss, cable losses (twisted pair wire on the transmitter side and SMA coaxial cable on the sensing side), and loss through free air space and human body.

For the proposed system, the link margin ( $L_{margin}$ ) is defined as the sum of all the power gains in the transmitting (Tx) and sensing (Rx) systems and subtracting the losses incurred in the system [97], [98].

$$L_{margin} = P_{driver} + L_{tpw} - L_{mag} - L_{co} + G_{AFE} - S_{rxADC} \quad (4.7.1)$$

where  $P_{driver}$  is the op-amp driver gain;  $G_{AFE}$  is the analog front end gain;  $L_{tpw}$  is the loss incurred through the twisted pair wire for the Tx;  $L_{mag}$  is the magnetic loss incurred through distance and human body;  $L_{co}$  is the coax cable for the Rx; and  $S_{rxADC}$  is the sensitivity of the Rx coil and the ADC which defines the minimum power before the transmitter signal becomes unmeasurable by the sensing coil and ADC.  $P_{txcoil}$  is the B-field transmitting power;  $P_{rxcoil}$  is the measured B-field by the sensing coil;  $P_{min}$  is the power received after all the losses before amplification; and  $P_{ADCin}$  is the input power received by the microcontroller ADC from the amplified sensing coil voltage (Figure 4.7.1).

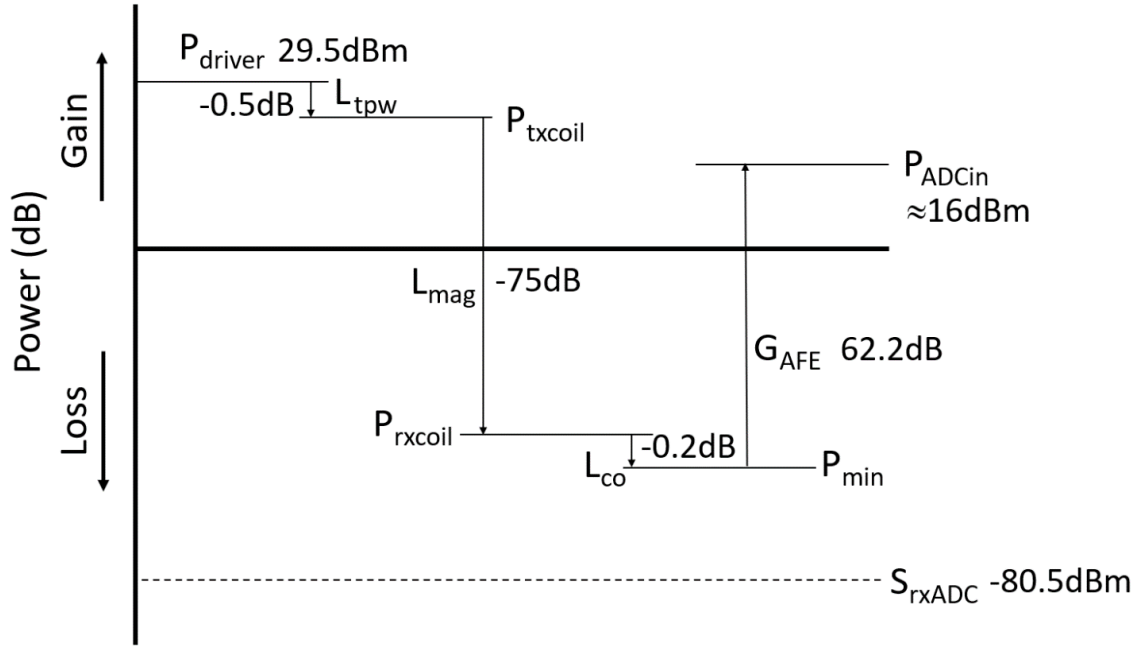


Figure 4.7.1. Forward link budget calculation.

#### 4.8 Algorithm Divergence Correction

The convergence of the positioning algorithm is directly affected by the triaxial coil locations. The optimal receiver coil positions have been described in the sensing coil design section. However, even with the optimal layout identified by Monte Carlo simulations or other methods, there still exist certain transmitter coil positions/orientations at which the algorithm is unable to converge correctly. This is typically because the set of measured B-fields result in a flat objective function in the root-finding algorithm near a correct position. A flat objective function occurs when the Jacobian function has a determinant value of zero (vectors are not linearly independent, and unique roots cannot be found). Even a Jacobian function with determinant close to zero can cause divergence as the system may determine a wrong search direction resulting from an abnormally large search step size (see discussions in Section 2.3.1). This region of flat objective function increases when SNR decreases, because jitter can cause a normally converging position to diverge to a wrong position. Thus, it is necessary to have an additional model step to correct divergence in the position algorithm. Figure 4.8.1 below shows an example of flat object function. Because the

objective function has flat portions, the rooting finding algorithm is unable to determine which direction is the maxima or minima.

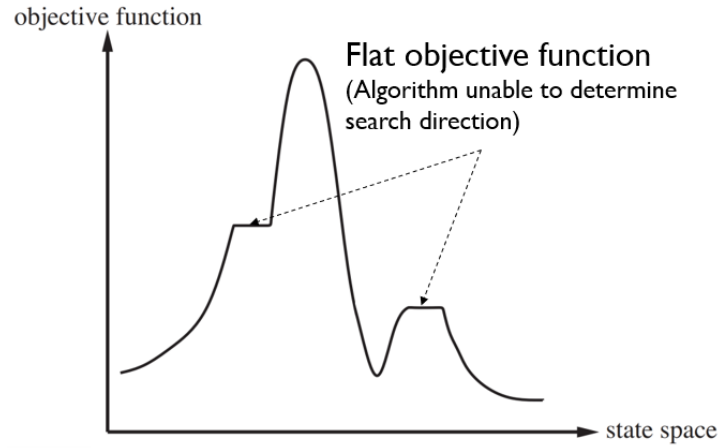


Figure 4.8.1. Flat objective function in search algorithm.

In this case, the distance vector  $\mathbf{r}$  in (4.2.1.16) is a  $3 \times 1$  vector, and there are three search directions in  $x$ ,  $y$ , and  $z$ . The algorithm will not converge if any one of the three step sizes cannot be properly determined. This is especially a problem when the determinant of the Jacobian ( $F'_1$ ) is smaller than the residual function  $F_1$  which leads to an abnormally large step size in the search iteration in the Newton's method. We developed and implemented fixes to navigate around this problem as discussed below.

A solution to the divergence problem is to introduce a second pair of triaxial receivers so that four receivers are used in the system. Figure 4.8.2 illustrates the possible four triaxial receiver layout.

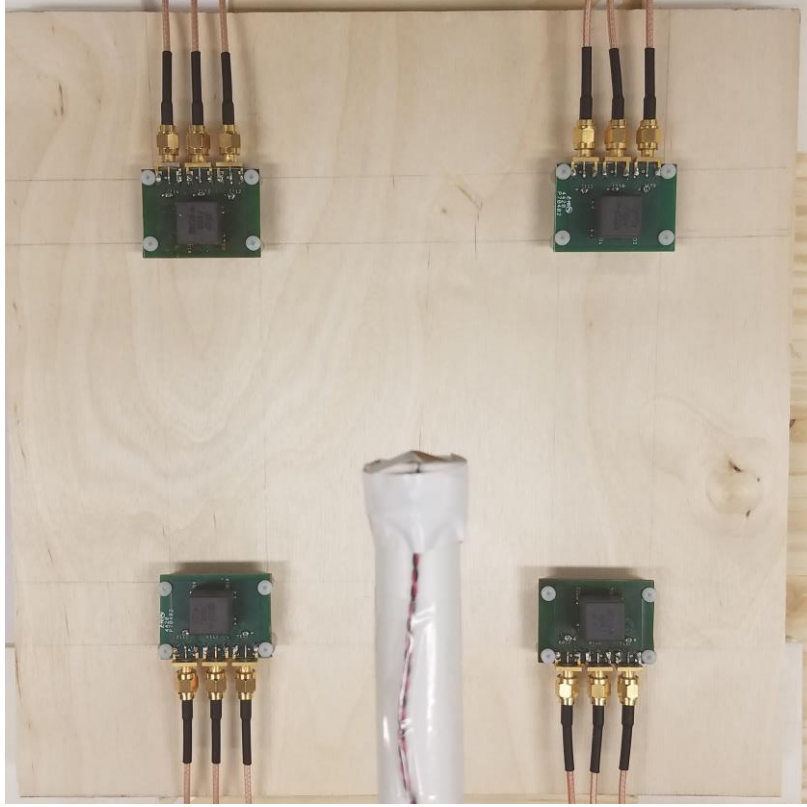


Figure 4.8.2. Four triaxial receiver layout.

Figures 4.8.3 and 4.8.4 show simulation results with two pairs of Rx. We select the pairs of Rx by taking two on main diagonal and the other two in the off diagonal. Thus, the first pair is at the current system locations:  $(0, 0, -0.5)$  cm and  $(23, 23, -0.5)$  cm, and the second pair is at different locations:  $(0, 23, -0.5)$  cm and  $(23, 0, -0.5)$  cm. The results are further illustrated in Figure 4.8.5. It can be seen that small determinant values occur at different sample point positions, which means that the two Rx pairs can be used in alternation to avoid small determinants and to calculate the Tx position.

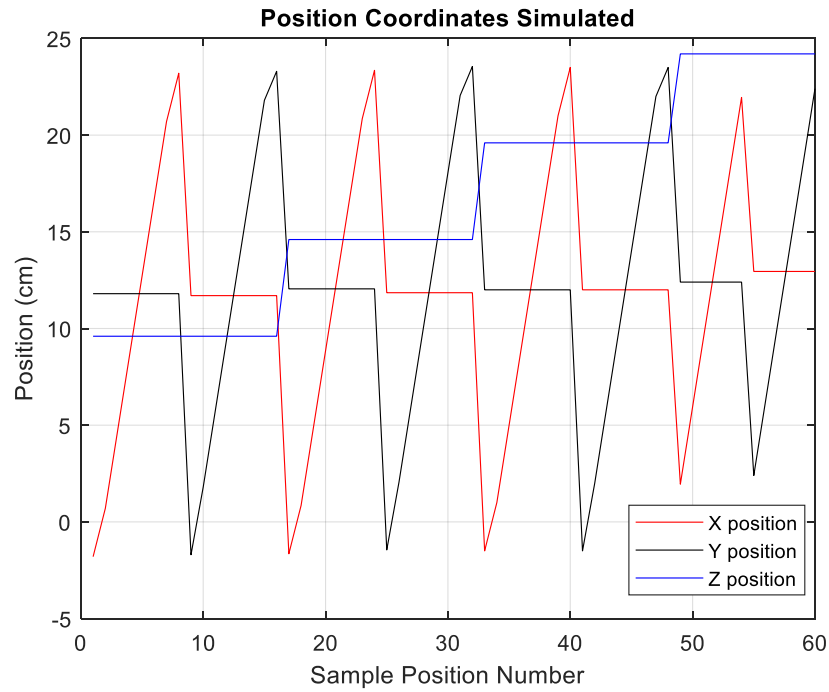


Figure 4.8.3. Location of positions tested.

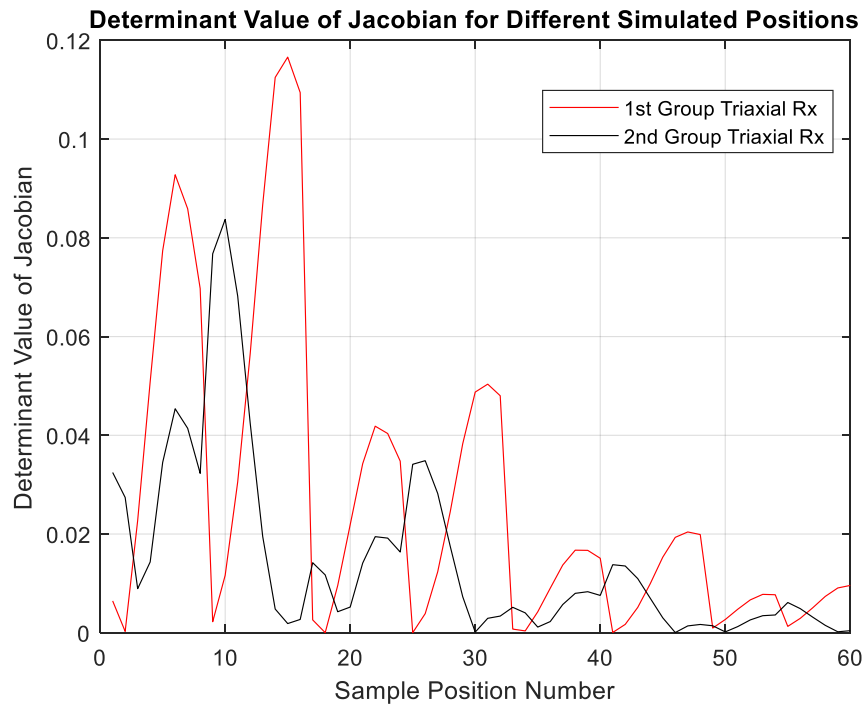


Figure 4.8.4. Simulated determinant for text positions for two different Rx pairs (groups). Rx group 1: (0, 0, -0.5) and (23, 23, -0.5); Rx group 2: (0, 23, -0.5) and (23, 0, -0.5).

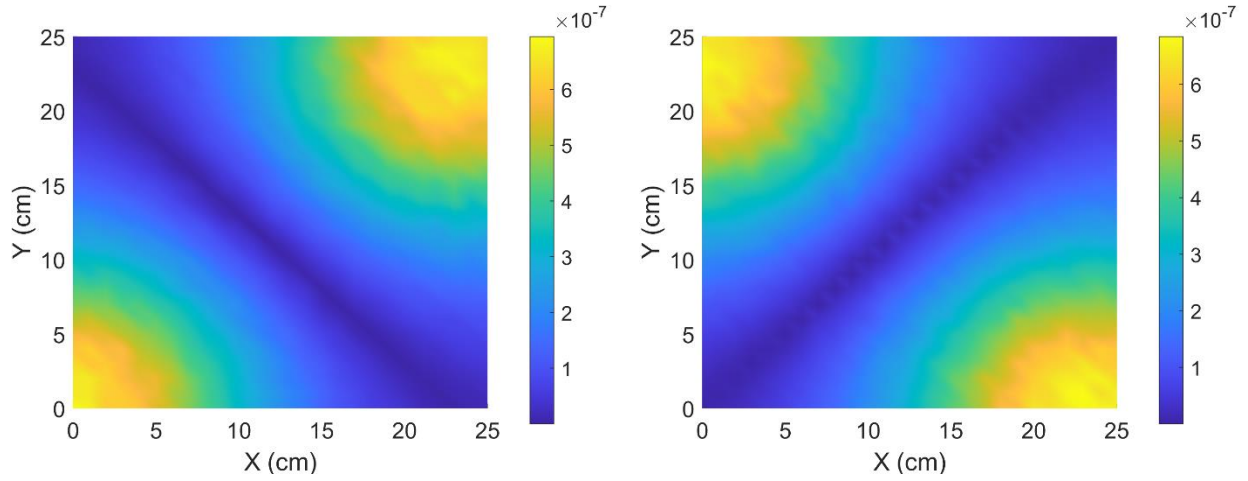


Figure 4.8.5. Simulated determinant for text positions for two different Rx pairs (groups). Rx group 1: (0, 0, -0.5) and (23, 23, -0.5); Rx group 2: (0, 23, -0.5) and (23, 0, -0.5) at  $Z=20\text{cm}$ .

However, in practice such an implementation removes the speed advantage of the system. This is because six additional sensing coils must be measured. The algorithm complexity will increase to accommodate the additional measurement values. Thus, if the same number of ADCs are used, the tracking speed will be cut in half. In addition, even if the tracking speed could be maintained, there are still shared diverging positions between the two Rx groups. Thus, this fix was not implemented.

Another more promising fix to mitigate the problem is by slightly changing the distance vector ( $\mathbf{p}$ ) between  $Rx_1$  and  $Rx_2$  so that the Jacobian determinant is no longer small. Figure 4.8.6 below illustrates such a shift, where the  $\mathbf{p}$  vector in green dashed line is altered slightly when the algorithm detects a divergence.



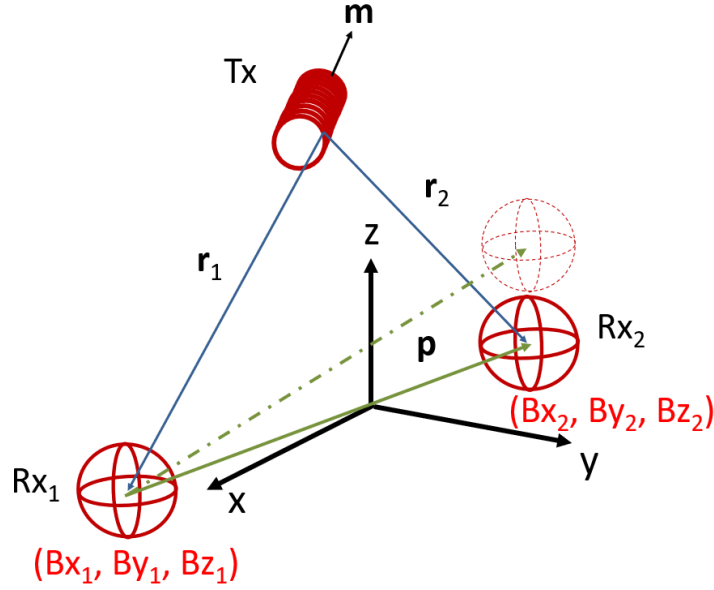


Figure 4.8.6. **p**-vector shift shown by dashed lines.

Note that the small change in **p** in the *z* direction rotates the receiver (Rx<sub>1</sub>-Rx<sub>2</sub>) plane, which effectively alters the Tx orientation from the Rx perspective and changes the Jacobian equation through changing **p** in (3.4.15), which results in a slightly different set of **B**<sub>1</sub> and **B**<sub>2</sub> and a larger determinant.

In most cases, the diverging positions can be easily identified. This is because certain magnetic moments (Tx orientations) cause the Jacobian determinant to approach zero values more easily. In the current Rx layout, this occurs at +*z* and -*z* of the Tx orientation. In these cases, we shift Rx reference position (dashed lines) along the *z* axis up to 5 mm. For the +*z* orientation of Tx positions, we shift Rx in the negative *z* direction, and vice versa.

Because the orientation is incorrect when the system diverges, the algorithm cannot solely detect divergence based on orientation of the Tx coil. In addition, when the algorithm diverges, it may converge to a local minimum, due to the highly nonlinear nature of the B-field equation and the possibility of multiple roots.

To improve the reliability of the divergence check, a new procedure is implemented to check both the orientation and position changes within one position calculation. In this procedure, a position divergence check condition is implemented by taking advantage of the fast update rate of the tracking system. If the orientation angle changes greater than 40° and/or the position changes greater than 3 cm in one axis (5.2 cm in distance), the system considers this position incorrect due

to divergence. Note that the position calculation rate is at 1.6 KHz. With 5.2 cm in distance change, we are assuming that the system's tracking coil does not move faster than 85 m/sec.

When a divergence is detected, the position algorithm is rerun using the same measured B-fields but with a difference in  $\mathbf{p}$  vector. With a new Jacobian determinant, which is larger, the position algorithm will correctly converge. Figures 4.8.7–4.8.9 below depict example positions' X, Y, and Z values with and without the  $\mathbf{p}$ -vector distance correction.

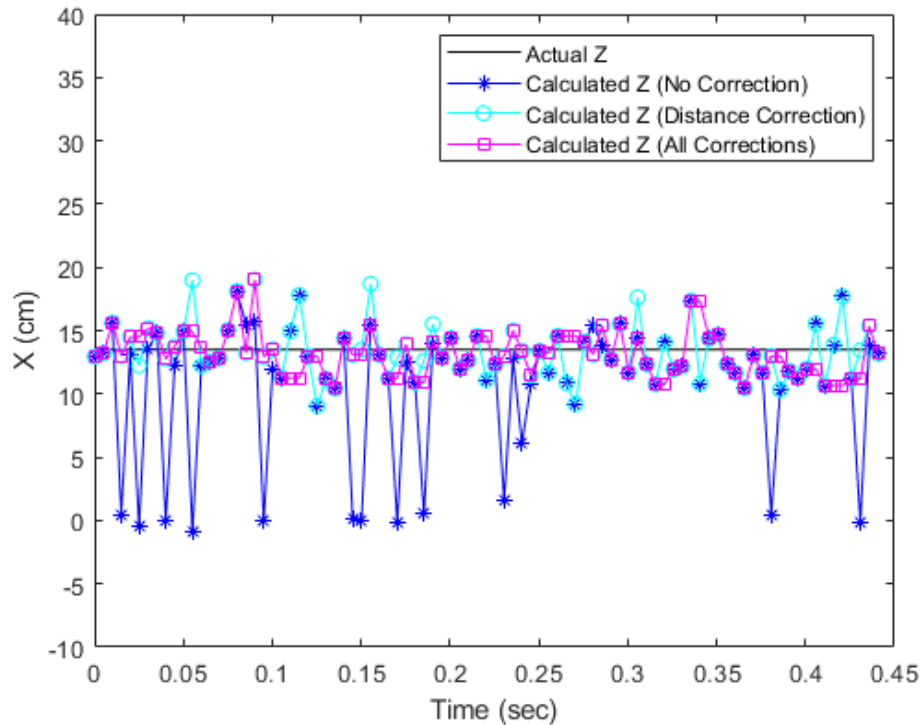


Figure 4.8.7. The effects of  $\mathbf{p}$ -vector correction on X position.

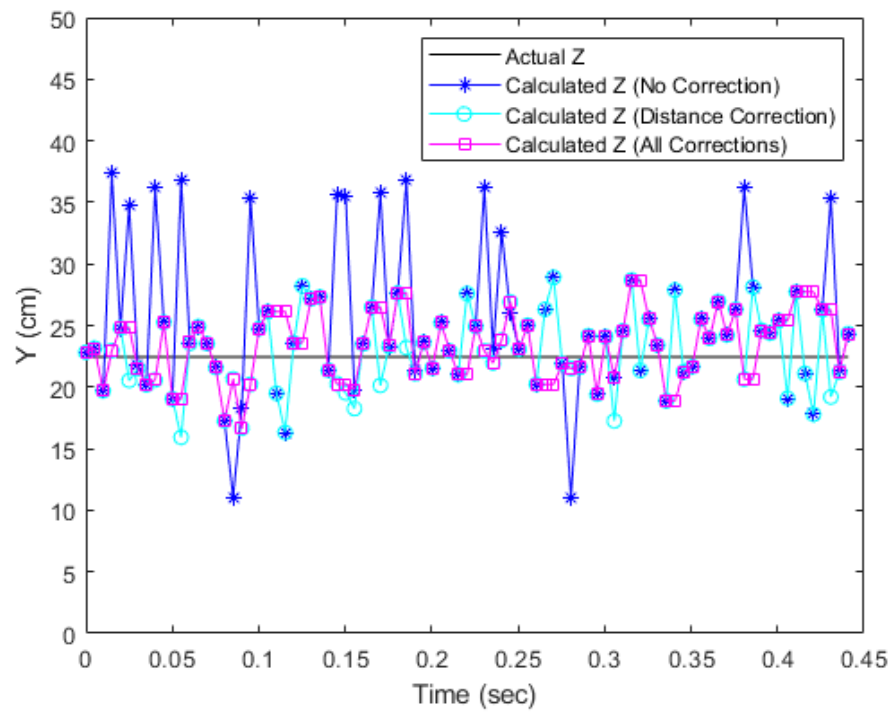


Figure 4.8.8. The effects of  $\mathbf{p}$ -vector correction on Y position.

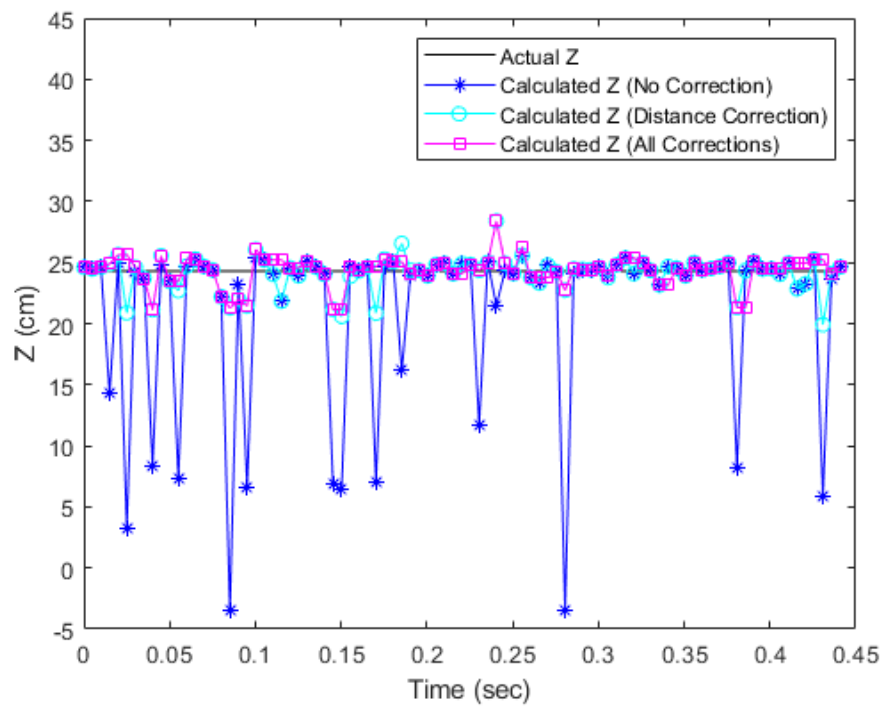


Figure 4.8.9. The effects of  $\mathbf{p}$ -vector correction on Z position.

Note that the limitation of the above fix is that it may lead to increased errors, because of the nonlinear nature of the **B** field. Because the **p** vector is shifted, the calculated position will be shifted as well. To correctly compensate position shift is challenging. The algorithm checks to see if the compensation is correct by doing the same position and orientation check (3 cm per axis and 40° rotation) again. If the system still detects divergence, the previous position point is used. This is shown in the magenta curves where the corrections include both the **p**-vector shift correction and the position orientation final check.

## **5. SYSTEM INTEGRATION AND CALIBRATION**

### **5.1 Hardware Integration**

The complete heart shape mapping system hardware is described in this section. Using the proposed transmitter and sensing system designs, the overall system level diagram is depicted in Figure 5.1.1. The transmitter section consists of a transmitter driver PCB placed at a fixed location and a transmitter coil attached to the catheter tip with a one-meter long twisted pair wire connection to the driver. The sensing section consists of two triaxial sensors with a parallel tuning capacitor on a PCB and analog front end to amplify measured signals from the six coils. Both sections are connected to the STM32 microcontroller, where post-processing is performed all on microcontroller firmware, including measurement using ADC, algorithms for position and orientation, filtering, and calibration. A USB connection allows for the position data to be sent to the user computer to a GUI to display the position results at a rate of 200 Hz.

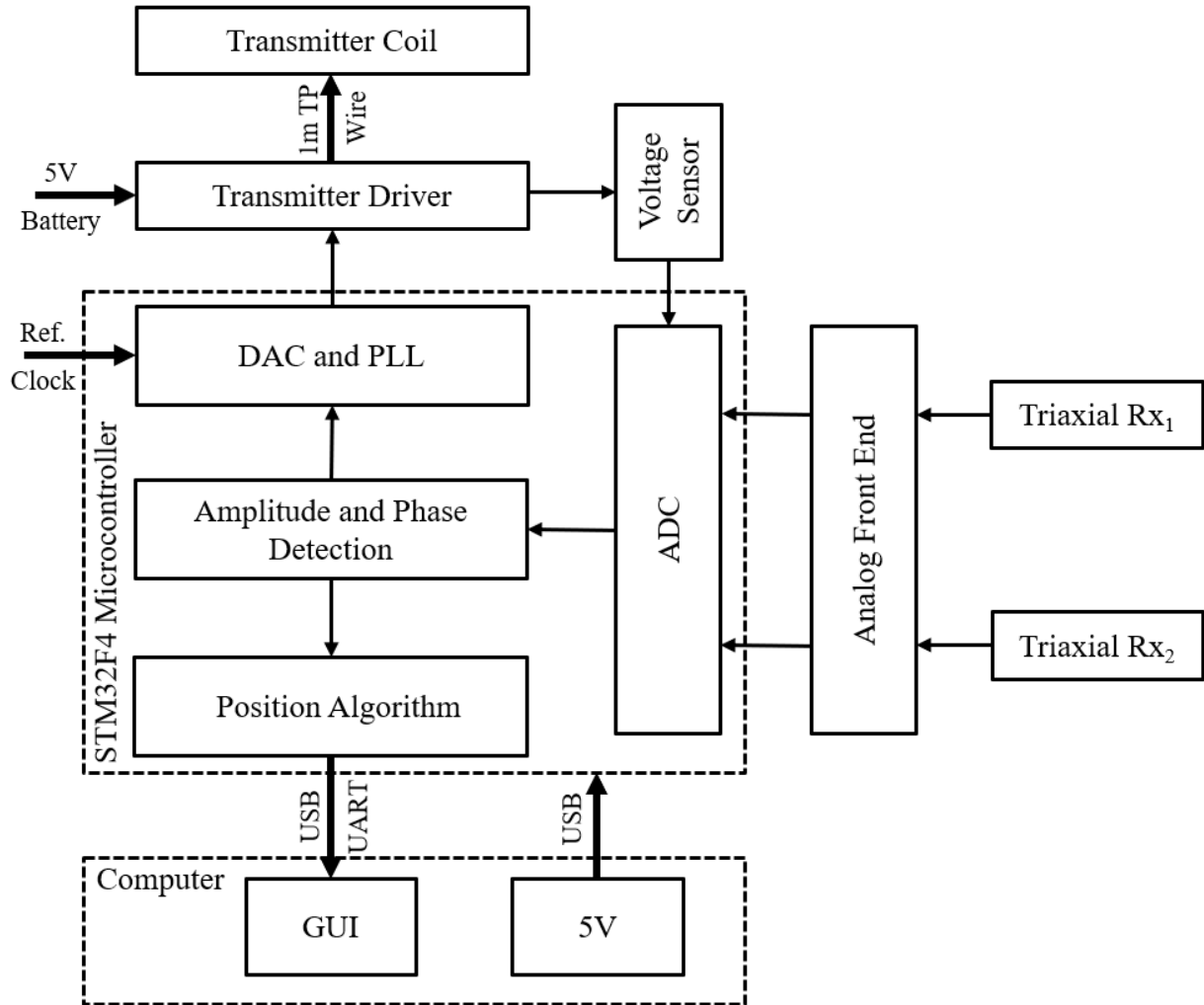


Figure 5.1.1. Tracking system diagram.

## 5.2 Potential Electrical System Integration in Medical Environment

The current system transmits universal asynchronous receiver-transmitter (UART) serial data through USB to the user interface. There are other potential methods for sending the data to the user. A block diagram of the potential electrical system integration is shown in Figure 5.2.1. One method is to communicate with an external Windows computer through USB channel utilizing human interaction device (HID) protocol. A universal HID protocol allows the system to be usable on any computer that supports HID. If the user prefers a wireless communication, Bluetooth data transfer is possible through an HC-05 receiver from the STM32 microcontroller used in the

proposed system. It will use the standard BLE protocol, so any smartphone, tablet, or computer that supports BLE protocol can read the data.

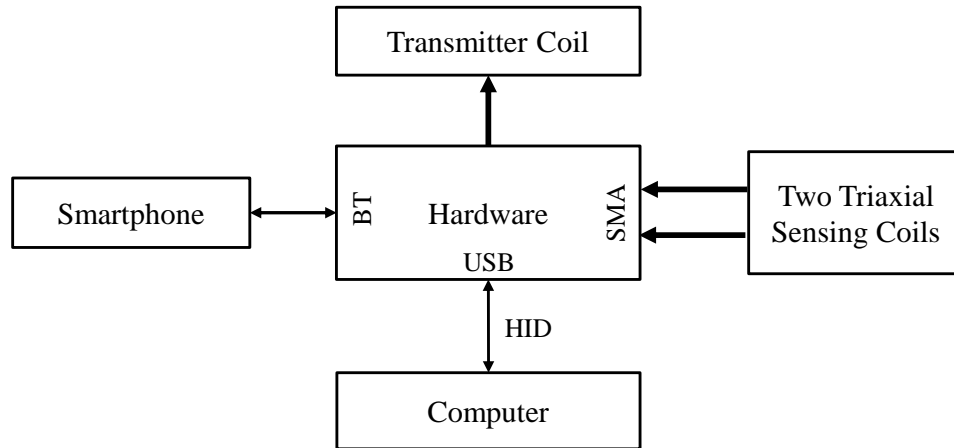


Figure 5.2.1. Electrical system integration (with planned future connection).

### 5.3 Mechanical Integration

Mechanical integration in a medical test environment involved on-site collaboration with the sponsor of the research project reported in this thesis, Nexturn company. The system was tested inside a mock operating room with a patient phantom on top of an operating table. The tiny transmitter coil is attached to the tip of a medical catheter, and the wire is integrated onto the catheter line by winding it around the catheter (Figure 5.3.1).

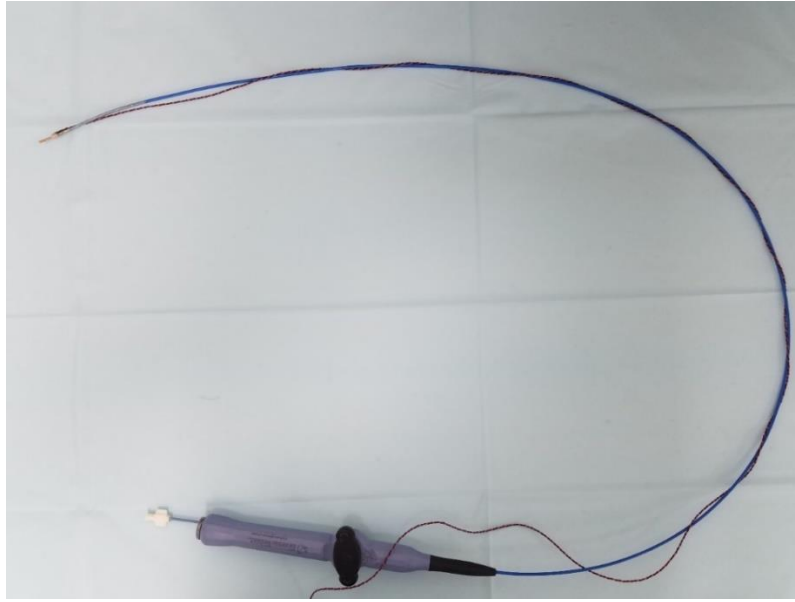


Figure 5.3.1. Transmitter coil with twisted pair wire wrapped on catheter.

The transmitter driver is placed on the side of the patient table. The diagnostic catheter is guided via medical robotic arm. This robot can precisely adjust the catheter handle's and tip's position and orientation (Figure 5.3.2).

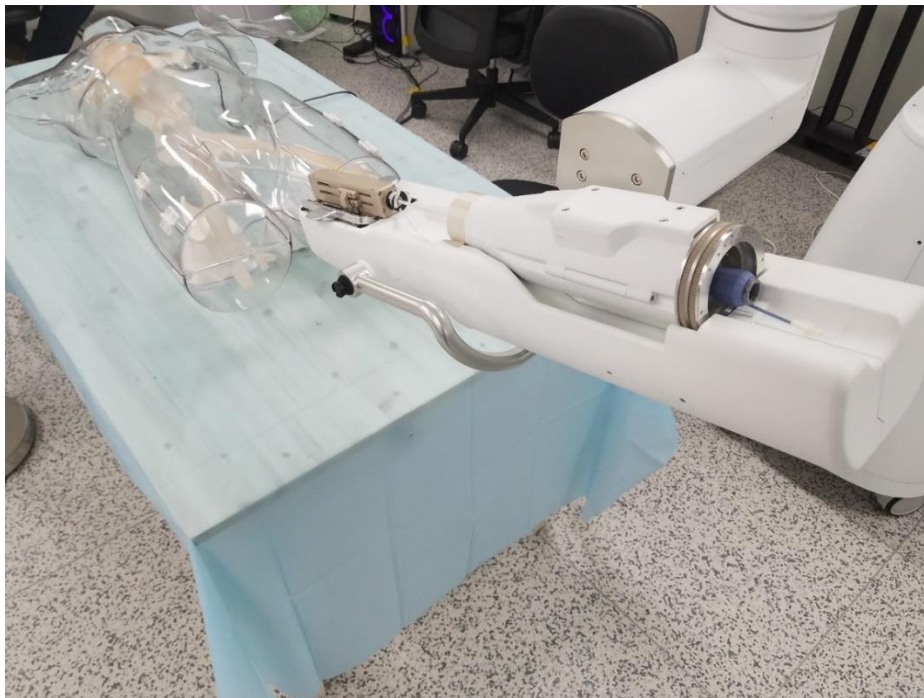


Figure 5.3.2. Catheter installed in medical robot, with patient mannequin.



The patient phantom is lying on the bed with a 3D-printed heart. For the demonstrations, the two triaxial coils are screwed underneath the patient table (Figure 5.3.3). The vertical tracking distance between the receiver and 3D-printed heart is approximately 10–20 cm. Six SMA coaxial cables connect the sensing coils to the microcontroller, where the on-board ADC samples the measurements, and a micro-USB to USB cable connects to the main computer.

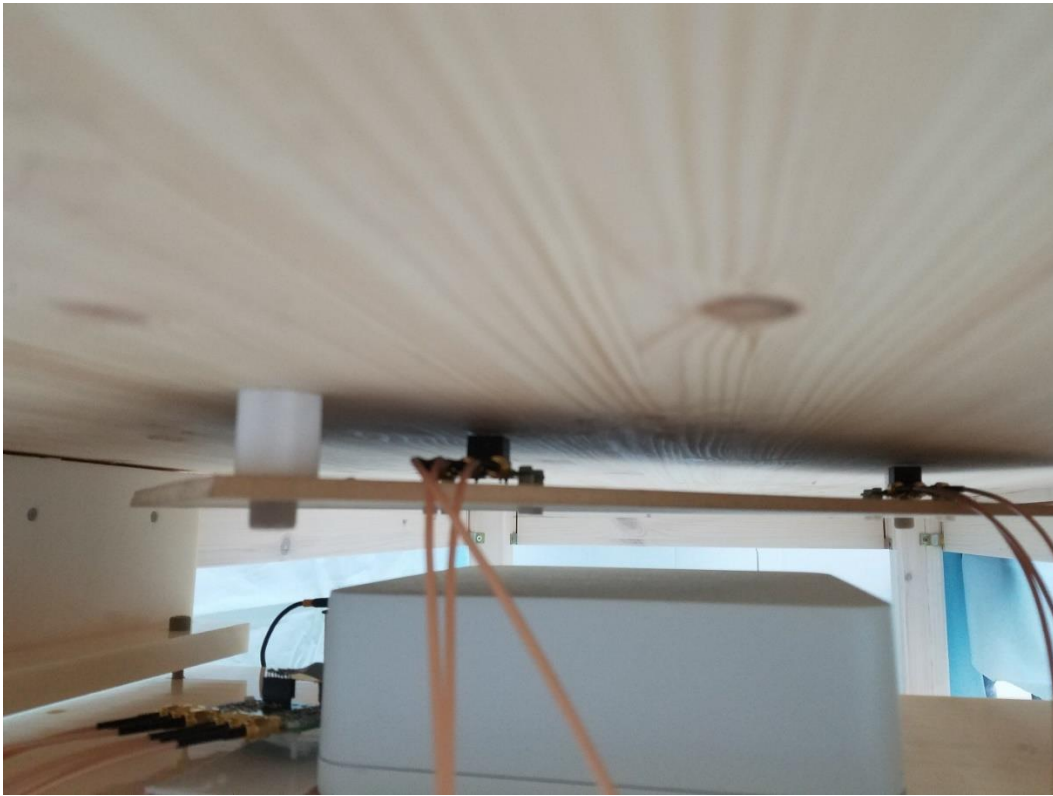


Figure 5.3.3. Reference sensing coils placed underneath patient table.

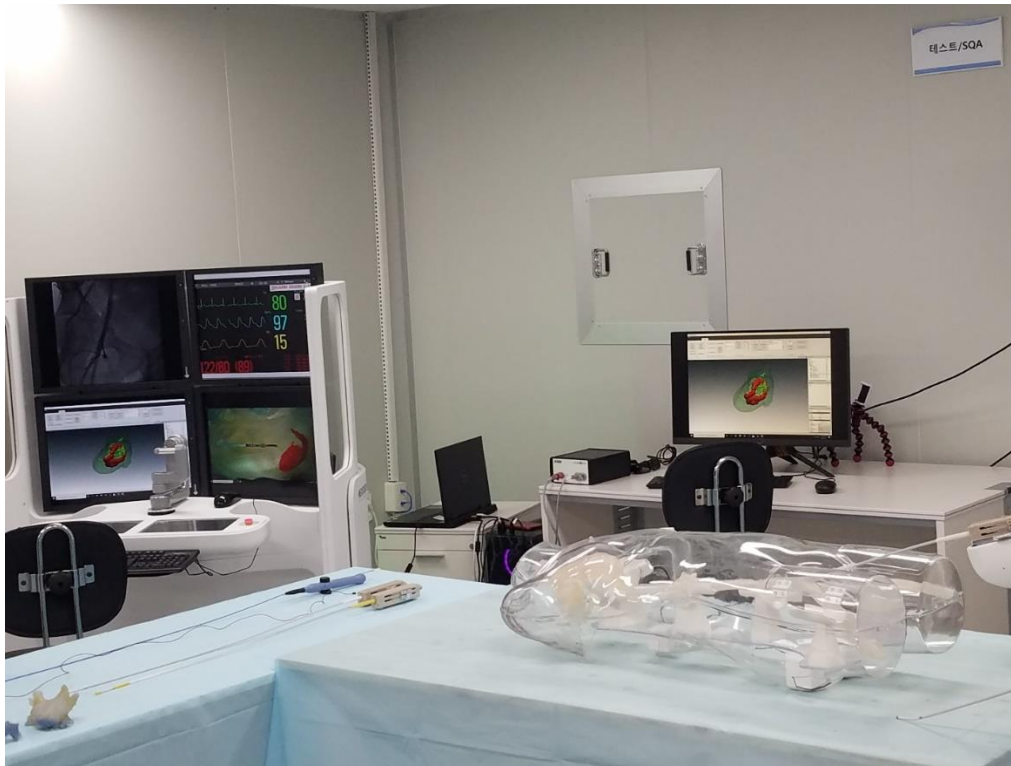


Figure 5.3.4. Real-time tracking of catheter.

The complete test assembly at Nexturn is shown in Figures 5.3.4 and 5.3.5. A 3D point cloud is used to map the locations of the diagnostic catheter tip. A 2D GUI may also be used as seen in the figures for knowledge of the position of catheter tip.

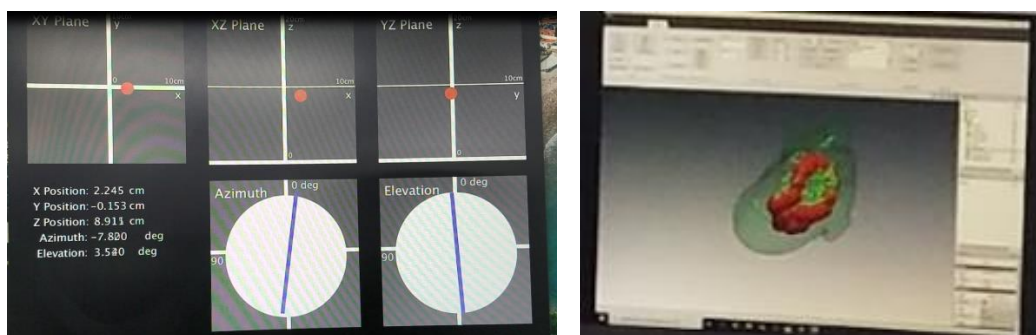


Figure 5.3.5. Graphical user interface for the position/orientation of catheter tip 2D (left) and 3D heart (right).

A semi-translucent 3D heart, which has the exact dimensions of the 3D-printed heart is placed in the point cloud visual display (Figure 5.3.6). The GUI displays the location of the catheter

tip, based on the transmitter coil calculated position using green and red colors. The red regions mark already visited locations, and green regions mark locations visited within the last 10 frames. The goal is to verify that the green and red mapped regions are within the boundaries of the 3D-printed heart. In addition, to verify the catheter tip location, a camera is placed inside the phantom, pointed at the 3D-printed heart to verify the location of the catheter tip with respect to the heart. From this, a 3D mapping of the interior of the heart can be successfully generated.



Figure 5.3.6. Point-cloud GUI representation of catheter tip and camera pointed at the tip.

## 5.4 System Calibration

This section describes the calibration methods used to improve the system accuracy and precision. System calibration will be performed after the exterior system setup is completed, because the knowledge of hardware specifications of this system is necessary. The following calibrations are applied to account for the effects of position, gain, orientation mismatches of the

sensing coils, along with the effect of the coupling among sensing coils' B-fields. Calibration is done using a separate XYZ station (Figure 5.4.1). This XYZ station was used for calibration during Nexturn's mock medical test. The XYZ station used for calibration during tests at Purdue will be shown in the experimental setup section in the next chapter.

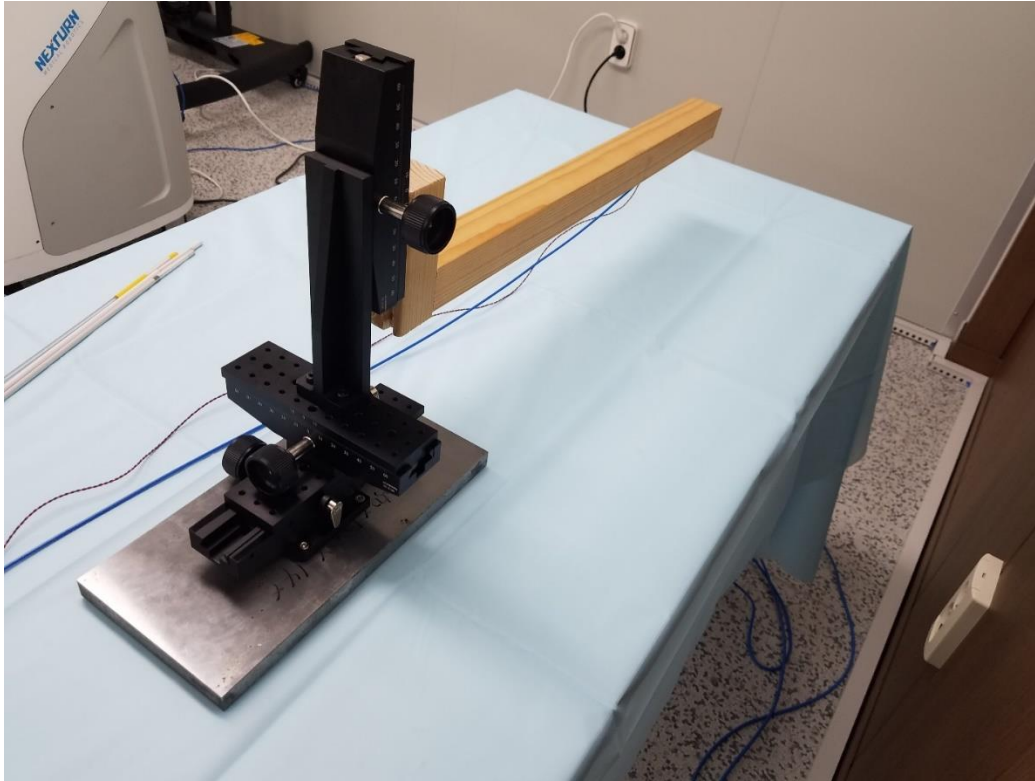


Figure 5.4.1. XYZ test station for calibration.

The calibration procedure is described below. The goal of calibration is to measure and correct mismatches to reduce error. However, in cases where directly measuring the mismatch is not feasible, compensation may be determined empirically. One of the examples is the Rx position mismatch due to minor inconsistencies in drilling holes to secure the receivers. The relative locations of the two receivers can be compensated through trials. Consider the coordinate frame illustrated in Figure 5.4.2,  $Rx_1$  and  $Rx_2$  should ideally have exactly the same  $x$  and  $y$  distances relative to the origin shown, but small errors remain after installation. The position can be compensated through comparison of measured and simulated B-fields and relevant adjustments.

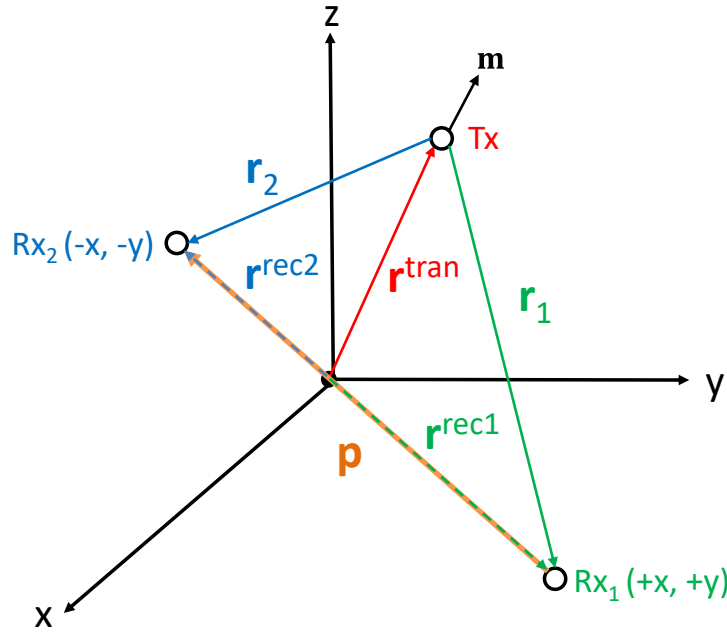


Figure 5.4.2. Tx and two Rx locations with the midpoint of the two Rx as reference.

### 5.4.1 Gain

#### *Analog Front End (AFE) Gain Stage Mismatch*

The dynamic range amplifier minimizes the effect of PVT variations. For the amplifier gain calibration it is assumed that the temperature is constant, and the mismatch is due to the tolerances of resistor and capacitor values, causing different closed loop gains for the six 2-stage amplifiers. Let  $B_{x1}$ ,  $B_{y1}$ ,  $B_{z1}$  be amplitude values measured across each of the triaxial  $Rx_1$  coils and  $B_{x2}$ ,  $B_{y2}$ ,  $B_{z2}$  be amplitude values measured across each of the triaxial  $Rx_2$  coils. Let  $A_1, A_2, \dots, A_6$  be the gain values for the six amplifiers for each individual coil. Then each  $A_i$  has the possibility to be set to either 100 or 1000.

$$B_{out} = B_{in} A_i (1 - m_i) \quad (5.4.1.1)$$

where  $m_i$  with  $i = 1$  to 6 is the % gain mismatch parameter. For example, if ideal  $A = 1000$  and actual  $A = 990$ ,  $m_i = 1\% = 0.01$ .

So for  $B_{x1}$  we have,

$$B_{outx1} = B_{x1} * A_1 * (1 - m_1) \quad (5.4.1.2)$$

By measuring  $B_{in}$  and  $B_{out}$ , we can solve for  $m$

$$m_i = 1 - \frac{B_{out}}{B_{in}A_i} \quad (5.4.1.3)$$

The values of  $m_i$ s are set in the microcontroller firmware and applied to the ADC sampled signals after the amplitude and phase of the B-field are extracted.

### ***Coil Gain Mismatch***

The triaxial coils are geometrically different, which results in different Qs and sensitivities. This will in turn lead to different B-field to sensing voltage conversions. Thus, coil gain mismatch needs to be correctly compensated. Most experiments done so far use an LCR meter to measure inductance and capacitance separately. However, it is impossible to measure inductance using an LCR meter when the triaxial coils are attached to the PCB with a tuned capacitor. Thus, an alternative method is used to measure the actual inductance, resistance, and capacitance of the sensing system.

A test bench is created as shown in Figure 5.4.3 below. A test capacitor with known capacitance (1nF) is connected in series with the sensing LC circuit. The test capacitor is used for capacitive sensing. A function generator ( $V_{AC}$ ) with frequency near the operating frequency of 32 kHz is applied to the circuit, and the magnitude and phase of the signal across the test capacitor (between nodes A and B) and sensing LC circuit are determined. The impedance can also be determined. To solve for all three unknowns, different  $V_{AC}$  frequency values (1–2 kHz away from the previous test frequency) may be applied, and a system of equations is obtained. The minimum number of  $V_{AC}$  required is two because two measurements result in two real and two imaginary impedance values allowing to solve for three unknowns using four equations. This is to determine the actual resistance and inductance of each coil, along with the actual tuning capacitance.

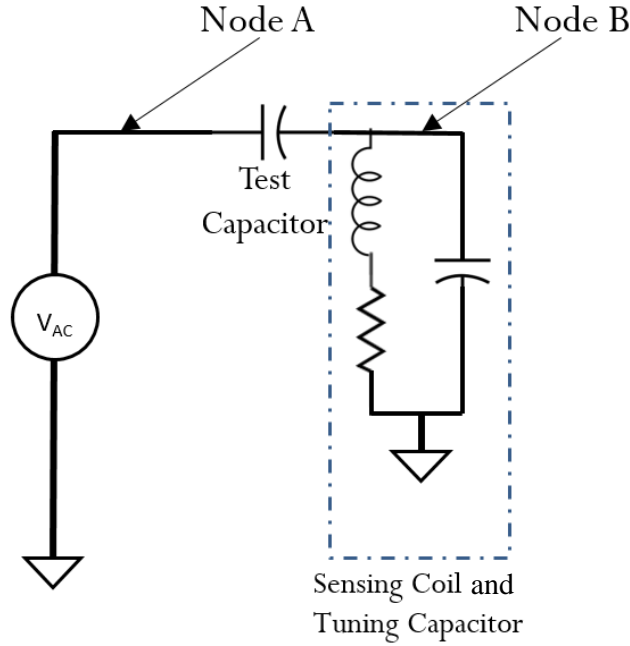


Figure 5.4.3. Mismatch test bench.

The procedure is repeated for each of the six sensing coils. The system of equations used to solve for the inductance and resistance of the sensing coil, tuning capacitor, and parasitic capacitance of the coil, and related circuitry is described below. First, define  $Z1$  (known) as the impedance of the test capacitor:

$$Z1(\omega) = \frac{1}{j\omega C_{test}} \quad (5.4.1.4)$$

Next define  $Z2$  (with  $L$ ,  $R$ , and  $C_{parasitic} + C_{tune}$  as unknowns) as the impedance of the sensing LC circuit taking into account of the coil's resistor.

$$Z2(\omega) = \frac{1}{\frac{1}{j\omega L + R} + j\omega(C_{parasitic} + C_{tune})} \quad (5.4.1.5)$$

Let  $V_{out}$  be the node B's voltage magnitude,  $V_{in}$  the node A's voltage magnitude, and phase difference is between  $V_{in}$  and  $V_{out}$ . Two equations relating to the magnitude and phase can be expressed as follows.

### **Magnitude**

$$\left| \frac{Z_2}{Z_1 + Z_2} * V_{in}(\omega) \right| - V_{out}(\omega) = 0 \quad (5.4.1.6)$$

### **Phase**

$$\tan^{-1} \left( \frac{\text{Im} \left( \frac{Z_2}{Z_1 + Z_2} \right)}{\text{Re} \left( \frac{Z_2}{Z_1 + Z_2} \right)} \right) - \text{phase\_dif} = 0 \quad (5.4.1.7)$$

As stated before, since there are three unknowns:  $R$ ,  $L$ , and  $C_{parasitic} + C_{tune}$ , at least four equations (two magnitudes and two phases being the minimum) must be generated. The number of equations in the system depends on the number of frequencies,  $n$ , tested. Thus, there are possibly  $2n$  equations. After the three unknowns are determined, the gain can be estimated using the quality factor equation with the actual tuned frequency:

$$Q = \frac{\omega L}{R} \quad (5.4.1.8)$$

Once the quality factor is determined for each coil, the effective gains can be obtained for all six sensing coils in the system. These effective gains may be further compensated through empirical tests as well.

## **5.4.2 Orientation**

In this section, the correction is for general orientation mismatch, i.e., we only consider the orientation mismatch of the triaxial coils relative to the  $xyz$  coordinate frame. These mismatches are due to small installation errors (e.g., soldering and drilling imperfections) in the setup of the XYZ test station. Here we assume that the coils in the triaxial receivers are orthogonal to each other. We will consider orthogonality among the three coils for mutual coupling analysis in the next section.

Consider  $\mathbf{Q}$  as the rotation matrix. Gimble lock possibility is minimal because the orientation mismatch rotation angles do not exceed 1–2 degrees. Thus, the Euler angle representation is used here as follows. The angles are rotated intrinsically in the  $(z\text{-}y'\text{-}x'')$  order:

$$\mathbf{Q} = \mathbf{Q}_x \mathbf{Q}_y \mathbf{Q}_z \quad (5.4.1.9)$$



where

$$\mathbf{Q}_x = \begin{bmatrix} 1 & 0 & 0 \\ 0 & \cos \varphi & -\sin \varphi \\ 0 & \sin \varphi & \cos \varphi \end{bmatrix} \quad (5.4.1.10)$$

$$\mathbf{Q}_y = \begin{bmatrix} \cos \theta & 0 & \sin \theta \\ 0 & 1 & 0 \\ -\sin \theta & 0 & \cos \theta \end{bmatrix} \quad (5.4.1.11)$$

$$\mathbf{Q}_z = \begin{bmatrix} \cos \Psi & -\sin \Psi & 0 \\ \sin \Psi & \cos \Psi & 0 \\ 0 & 0 & 1 \end{bmatrix} \quad (5.4.1.12)$$

Thus, we have:

$$\mathbf{Q} = \begin{bmatrix} \cos \theta \cos \Psi & -\cos \varphi \sin \Psi + \sin \varphi \sin \theta \cos \Psi & \sin \varphi \sin \Psi + \cos \varphi \sin \theta \cos \Psi \\ \cos \theta \sin \Psi & \cos \varphi \cos \Psi + \sin \varphi \sin \theta \sin \Psi & -\sin \varphi \cos \Psi + \cos \varphi \sin \theta \sin \Psi \\ -\sin \theta & \sin \varphi \cos \theta & \cos \varphi \cos \theta \end{bmatrix} \quad (5.4.1.13)$$

This rotation matrix can be applied separately to the  $B_x$ ,  $B_y$ , and  $B_z$  fields of each of the sensing coils to get the rotated B-field  $B_{xrot}$ ,  $B_{yrot}$ , and  $B_{zrot}$ . As a result, we have:

$$\begin{bmatrix} B_{xrot} & B_{yrot} & B_{zrot} \end{bmatrix} = \mathbf{Q} \begin{bmatrix} B_x & B_y & B_z \end{bmatrix} \quad (5.4.1.14)$$

To apply this equation, position and B-field amplitude values are measured at various positions with fixed orientation. Afterwards, a Matlab program is run, which sweeps through a set of possible gain, position, and orientation values for each of the six coils. The set of mismatch correction values is identified to minimize the difference between the simulated and measured B-field values. Note that because the sweeping range required is unknown, this process is repeated with a different sweeping range until the optimal orientation angle correction values of each of the triaxial receivers are obtained.

### 5.4.3 Mutual Coupling

Ideally, each of the coils in a triaxial receiver will have a measured B-field value independent from another. However, due to imperfections in winding and internal orientation mismatch among the coils, each of the three coils induces a B-field on others. This causes inductive coupling. Thus, a mutual coupling compensation must be implemented as follows. Letting  $B_u$  be the uncompensated B-field value, we have:

$$B_{cx} = m_{11}B_{ux} + m_{12}B_{uy} + m_{13}B_{uz} \quad (5.4.1.15)$$

$$B_{cy} = m_{21}B_{ux} + m_{22}B_{uy} + m_{23}B_{uz} \quad (5.4.1.16)$$

$$B_{cz} = m_{31}B_{ux} + m_{32}B_{uy} + m_{33}B_{uz} \quad (5.4.1.17)$$

where  $m_{ij}$  is the mutual inductance factor of coil  $j$  that exists with respect to coil  $i$ . Note that this  $m_{ij}$  factor is determined empirically by generating a B-field on one of the 3 coils and measuring the B-field induced on the 2 other coils. Figures 5.4.4–5.4.5 below show the induced field (red curve and black curve) based on the generated field from one of the coils within each of the triaxial Rx coils. From here, we can derive the  $m_{ij}$  factor by calculating the ratio between the generated field and induced field. This ratio is also based on the induced field's phase in relation to the generated field.

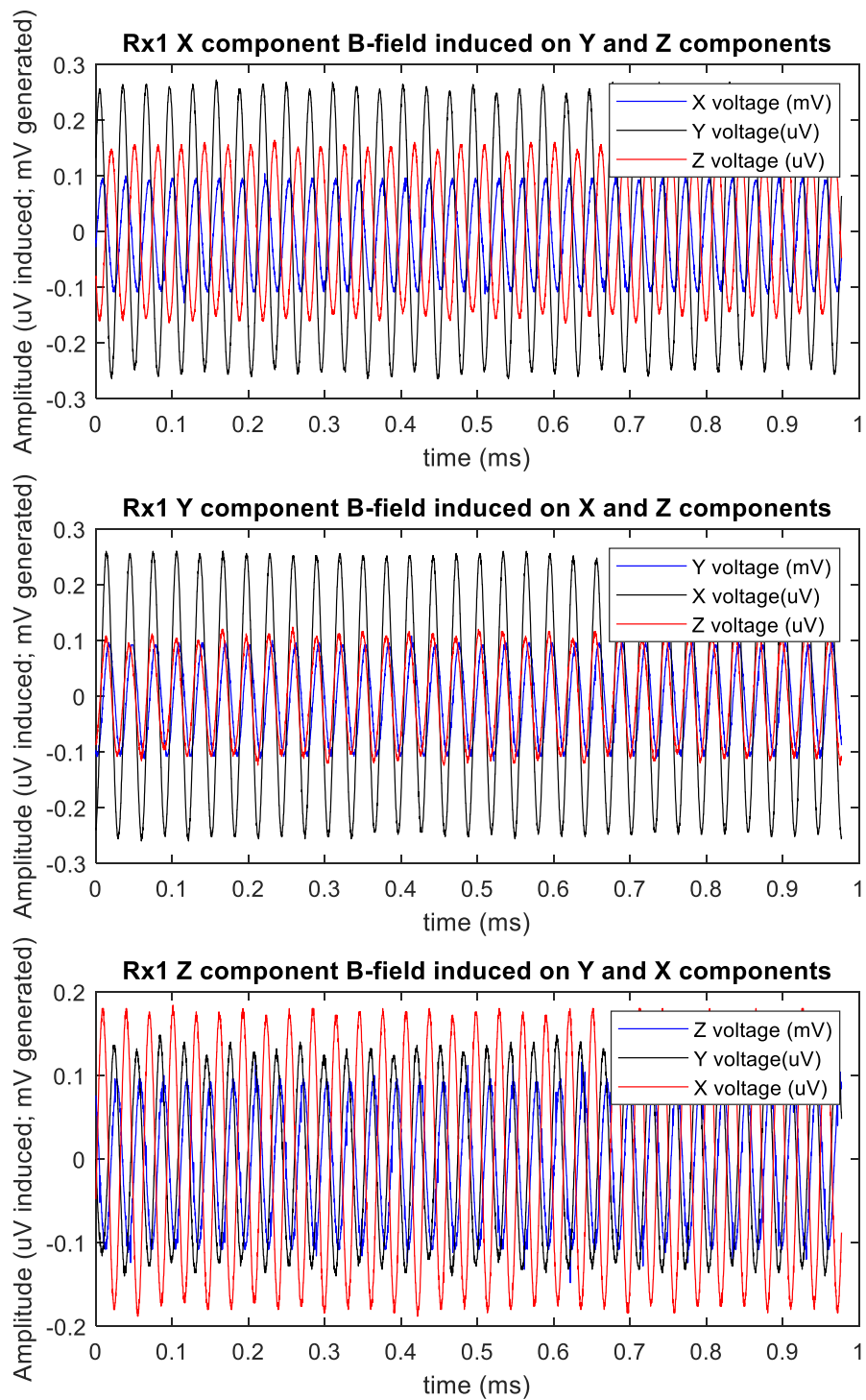


Figure 5.4.4. Rx<sub>1</sub> induced field measurement.

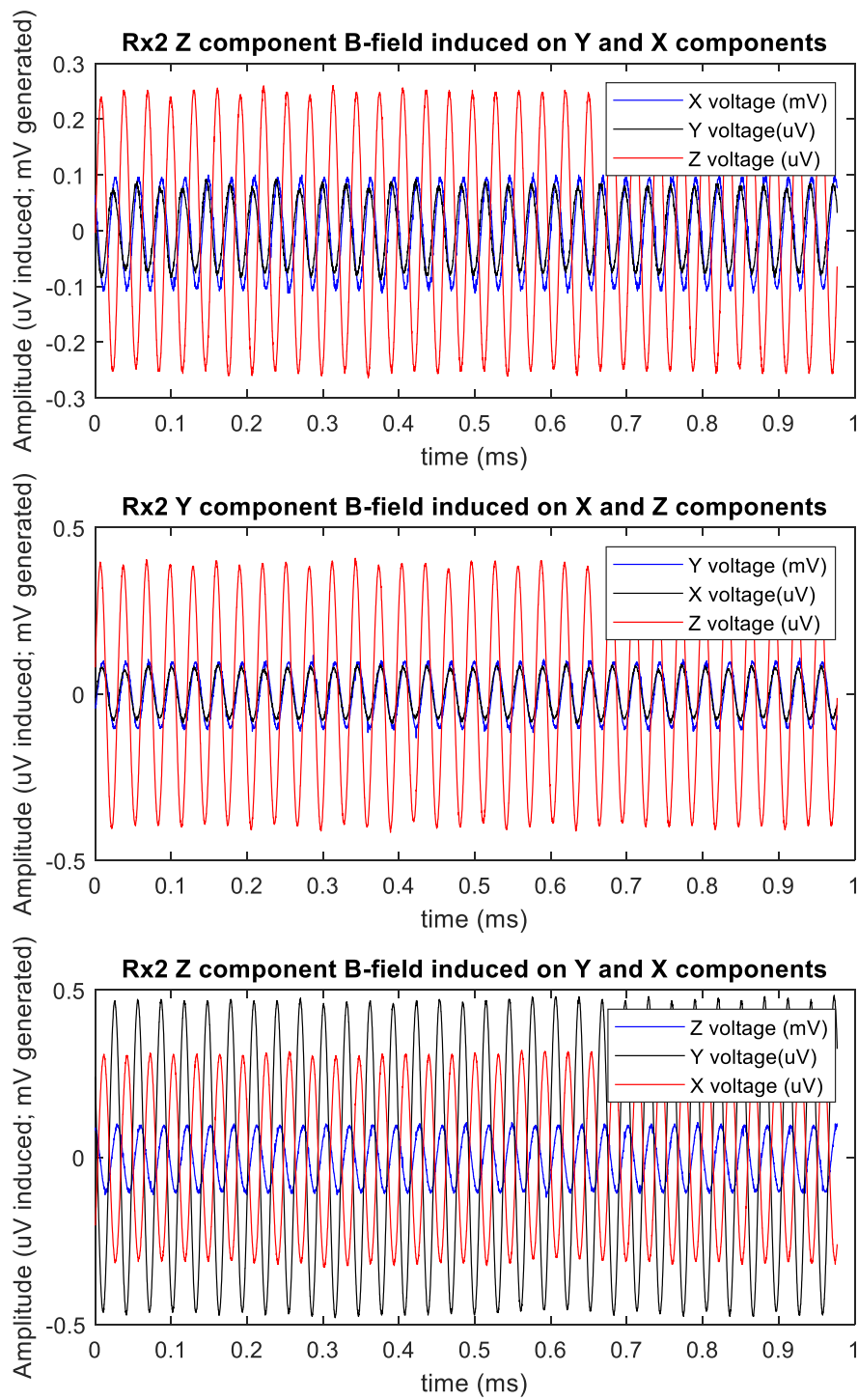


Figure 5.4.5. Rx<sub>2</sub> induced field measurement.

## 6. SYSTEM SETUP AND TESTING

### 6.1 Prototype System Setup

In the test system, the transmitter coil is attached to a 3D-printed structure, where its position can be adjusted precisely using an XYZ test station, and its orientation can be adjusted using a rotation module. The two sensing coils are screwed on a wooden board and placed on a wooden table. The complete test bench is illustrated in Figure 6.1.1.

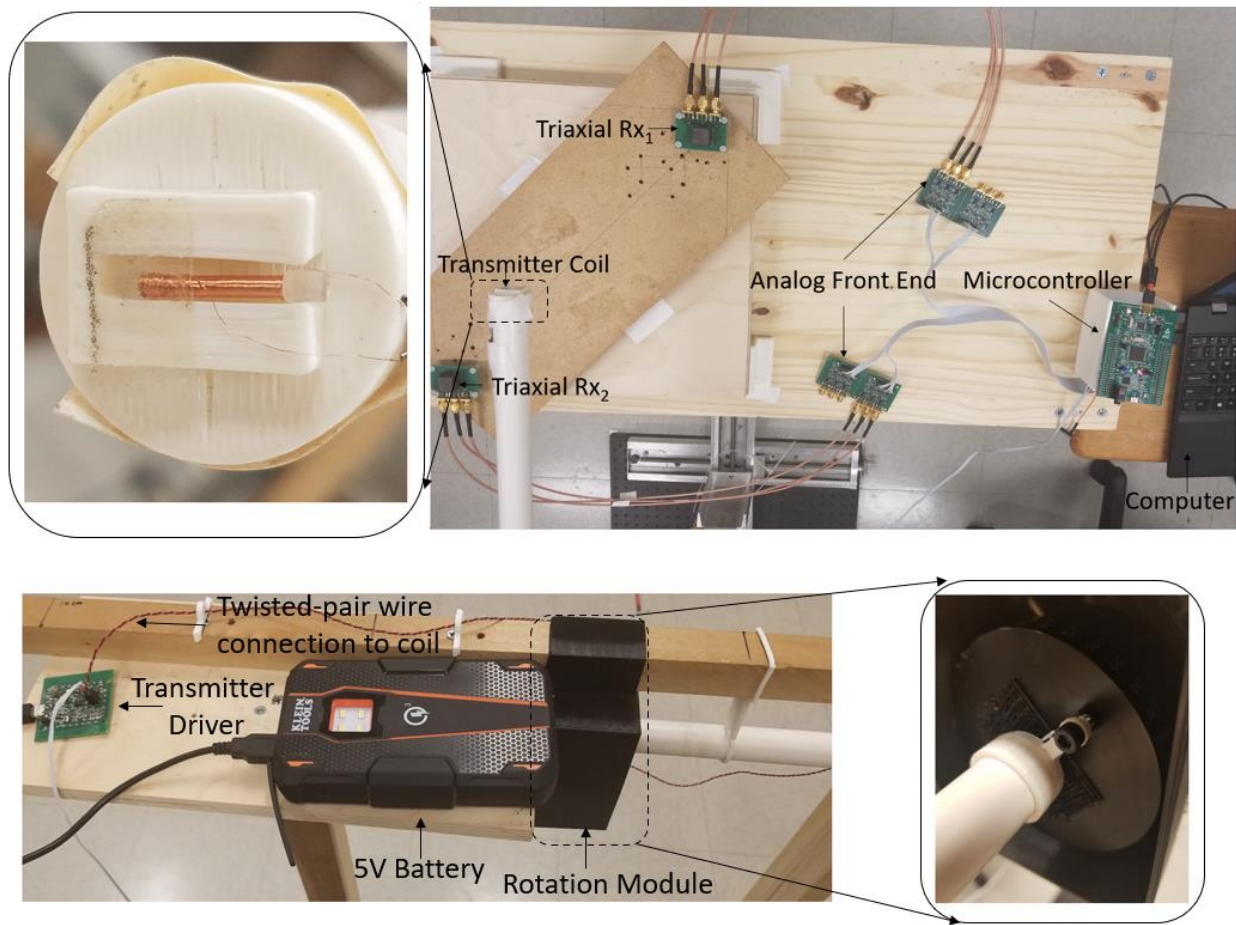


Figure 6.1.1. Test bench.

Figure 6.1.2 below shows the base for the XYZ position test station. The metallic base has three separate knobs, which precisely control the position in the  $x$ ,  $y$ , and  $z$  directions. Each full rotation of a knob adjusts the position in one axis by 2 mm. Because the base for the XYZ station

is a metallic structure that can significantly distort the magnetic field, a wooden platform was built and attached to the base with a height of 1 m, leaving enough distance between the metallic base and the transmitting and sensing coils.

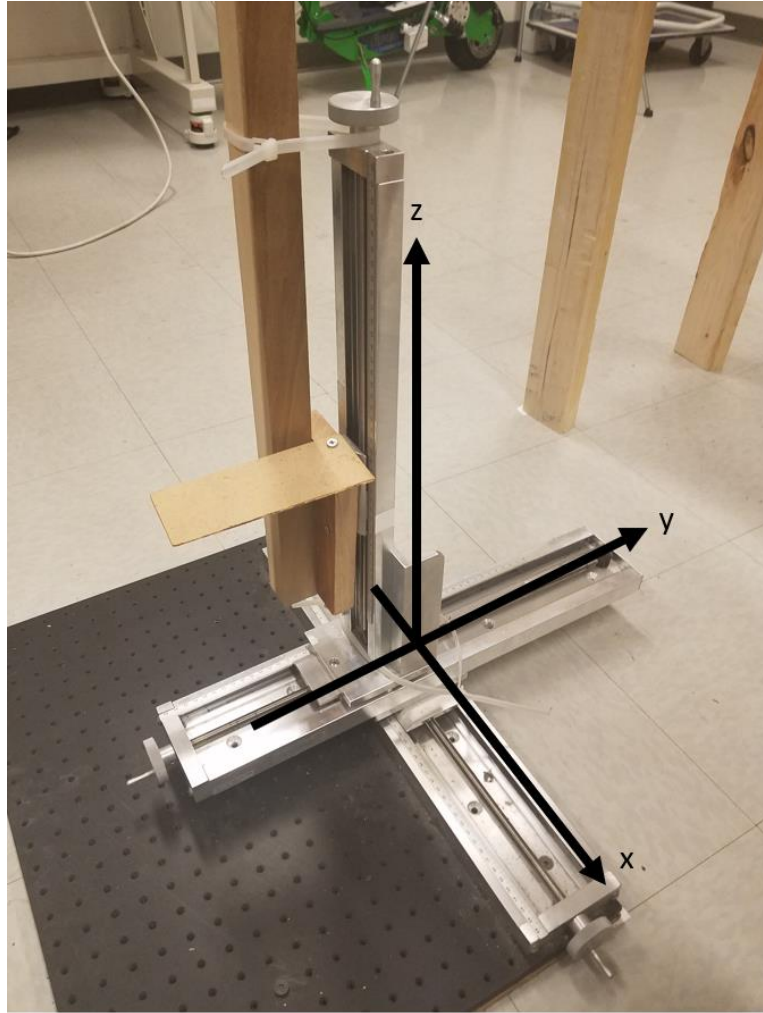


Figure 6.1.2. XYZ test station used for the test.

Data were collected across various positions in increments of 4 cm. The control knobs of the XYZ test station were adjusted to achieve specified positions. Then, the  $x$ ,  $y$ , and  $z$  position values were measured and recorded by the tracking system for each fixed orientation.

The sensing coil position and coordinate frame are shown in Figure 6.1.3. The two triaxial Rx coils are placed in a  $xyz$  coordinate frame at  $(0, 0, -0.5)$  cm and  $(23, 23, -0.5)$  cm. The coil  $z$  position is offset by 0.5 cm because the diameter of the Rx coil is 1 cm, and the top of the Rx coil

is at  $z = 0$  cm. The Tx coil was moved in the tracking area from  $-1.5$  cm to  $23.55$  cm in both the  $x$  and  $y$  directions, and  $10$  cm to  $25$  cm in the  $z$  direction.

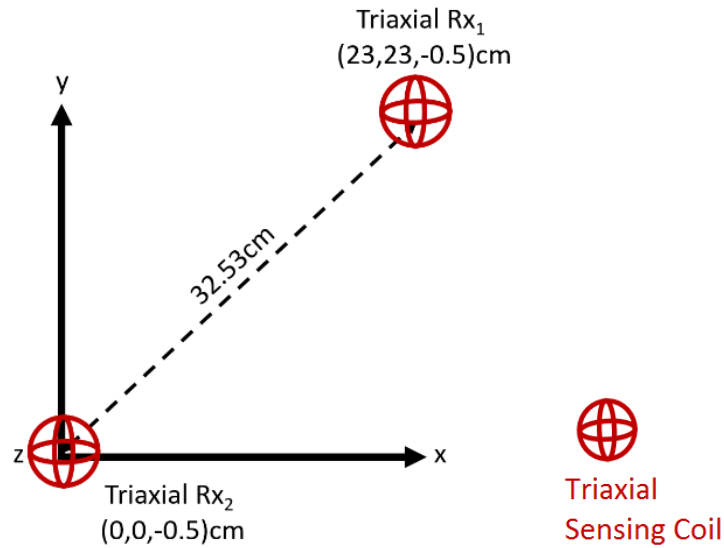


Figure 6.1.3. Coordinate frame.

Figure 6.1.4 shows the test tracking range for the prototype system. The size of a human heart is approximately  $12\text{ cm} \times 8\text{ cm} \times 6\text{ cm}$  [99]. The tracking range needs to cover at least double the heart volume. Thus, the target tracking position range for this system is  $25\text{ cm} \times 25\text{ cm} \times 25\text{ cm}$  depicted by the 3D red box. 60 unique positions, at 7 different orientations, were tested within this range to evaluate the position and orientation accuracy of the system (Table 6.1.1).

Table 6.1.1. Tracking position tests.

	Position Change X	Position Change Y	Position Change Z	Orientation Change Azimuth
Range	$-1.5\text{cm}$ to $23.5\text{cm}$	$-1.5\text{cm}$ to $23.5\text{cm}$	$10$ to $25\text{cm}$	$0$ to $180\text{deg}$
Increment	$4\text{cm}$ ( $1.5\text{cm}$ on edges)	$4\text{cm}$ ( $1.5\text{cm}$ on edges)	$5\text{cm}$	$30\text{deg}$

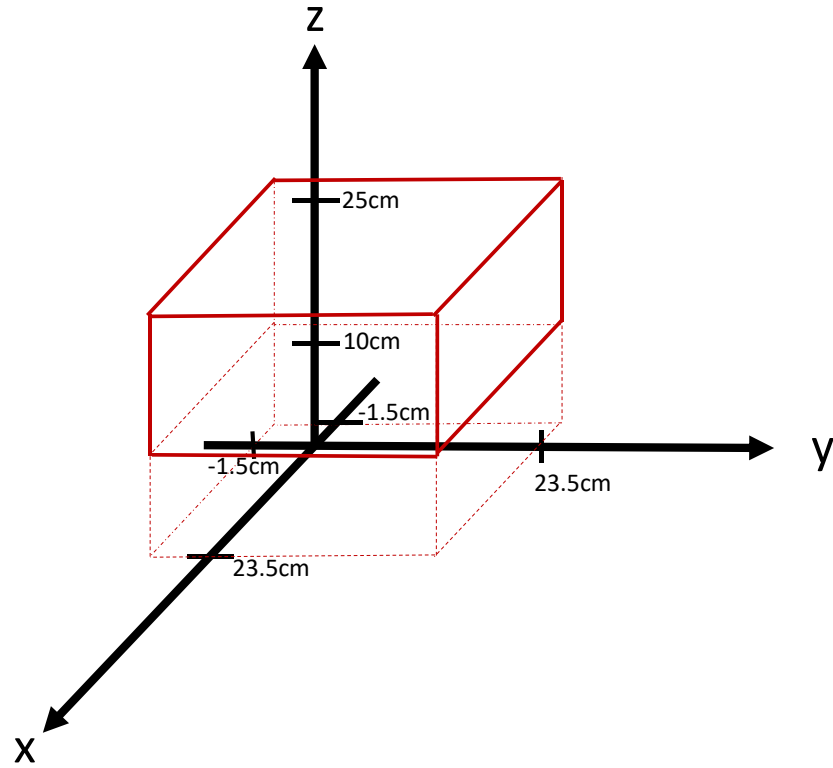


Figure 6.1.4. Position tracking area: test area shown by 3D red box.

## 6.2 Test Results

This section details the position test results for the positions and orientations summarized in Table 6.1.1. Since biological tissues have magnetic permeability that is very close to the magnetic permeability of free space, we assume that the magnetic field generated by the transmitting coil is not altered in a patient's body. However, proving the reliability of this assumption is too challenging as no direct investigation into the effect of biological tissues on EM fields for tracking systems has been published [100]. Hence, our measurements are performed in normal laboratory conditions.

First, the receiver coil B-field magnitude and phase are confirmed through measurement using an oscilloscope. The received voltage shown in Figure 6.2.1 has noise. The only noise that will propagate through to the position calculation is the noise at 32 kHz frequency. The rest of the noise at different frequencies is removed in the amplitude and phase detection algorithm (single tone detection), which isolates the amplitude and phase of only the operating frequency at 32 kHz.



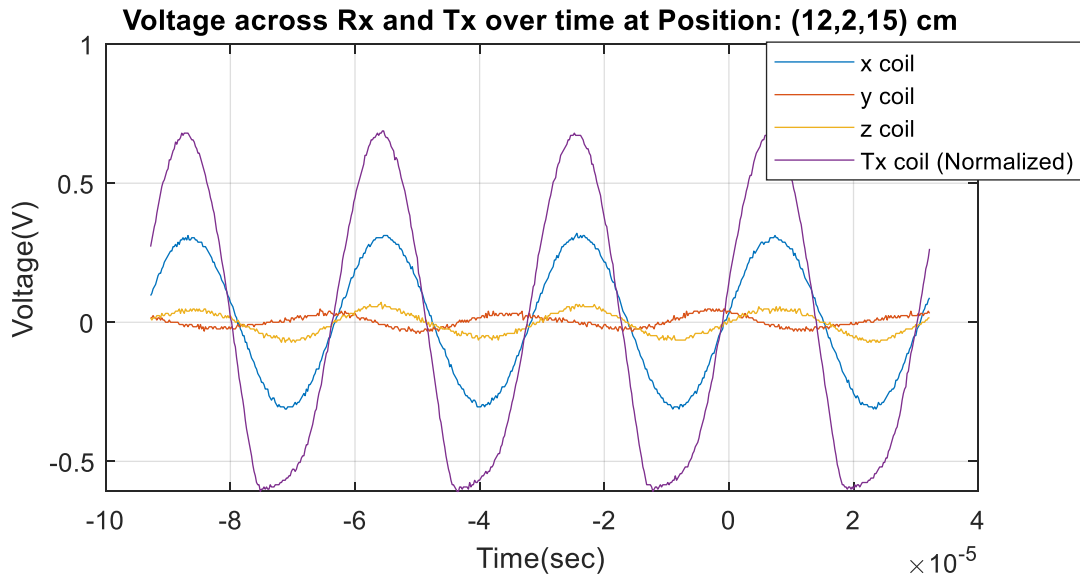
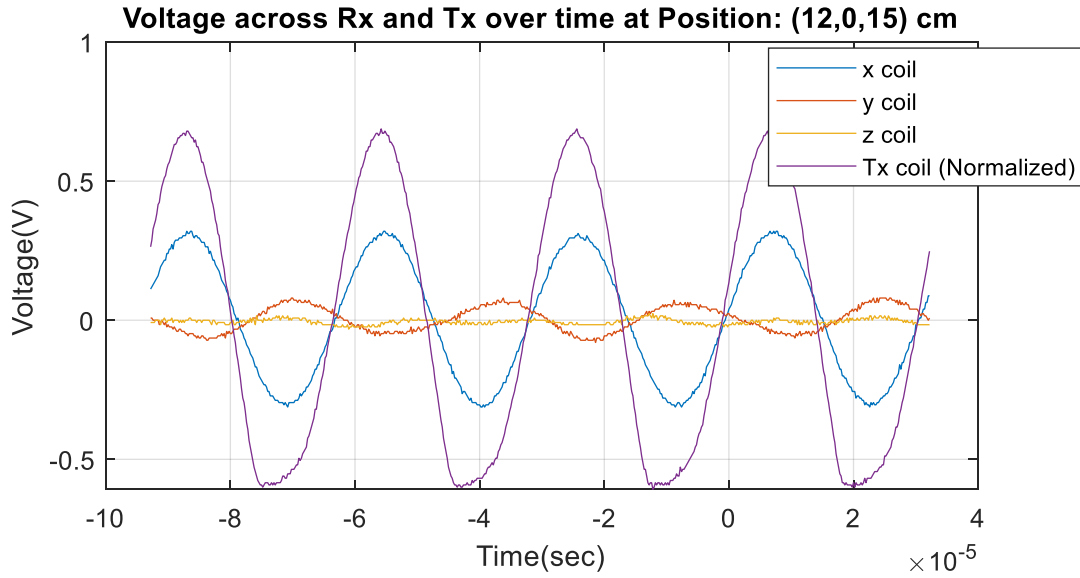


Figure 6.2.1. Voltage measured in receiver and transmitting coils.

Note that the phase is used to determine the sign of the amplitude. For example, a phase of  $-90$  degrees means that the amplitude is positive and a phase of  $+90$  degrees negative. The phase also allows us to check any B-field interference from unwanted sources, because the interfering B-field will cause the phase to incorrectly deviate, which is more pronounced if the interfering B-

field has opposite sign to the transmitting B-field. From our results, we notice that the biggest interference is caused by the twisted pair wire which carries the current to the transmitting coil. Despite most of the B-field being cancelled out by the wire geometry, some of the induced B-field survives and is measurable by the receiving coils. To mitigate this, the wire is shielded, which successfully reduces the interfering B-field and lowers phase deviation.

### 6.2.1 Static Tests

First, static position tests were conducted. Over 60 unique positions were evaluated, and the coil was rotated at each of these positions, with 7 unique orientations described in Table 6.1.1. Figures 6.2.2 through 6.2.8 depict the  $(x, y, z)$  position results within the tested volume at each of the 7 unique orientations. Test results for different angles at different  $z$  positions are shown in Figures 6.2.9 through 6.2.12.

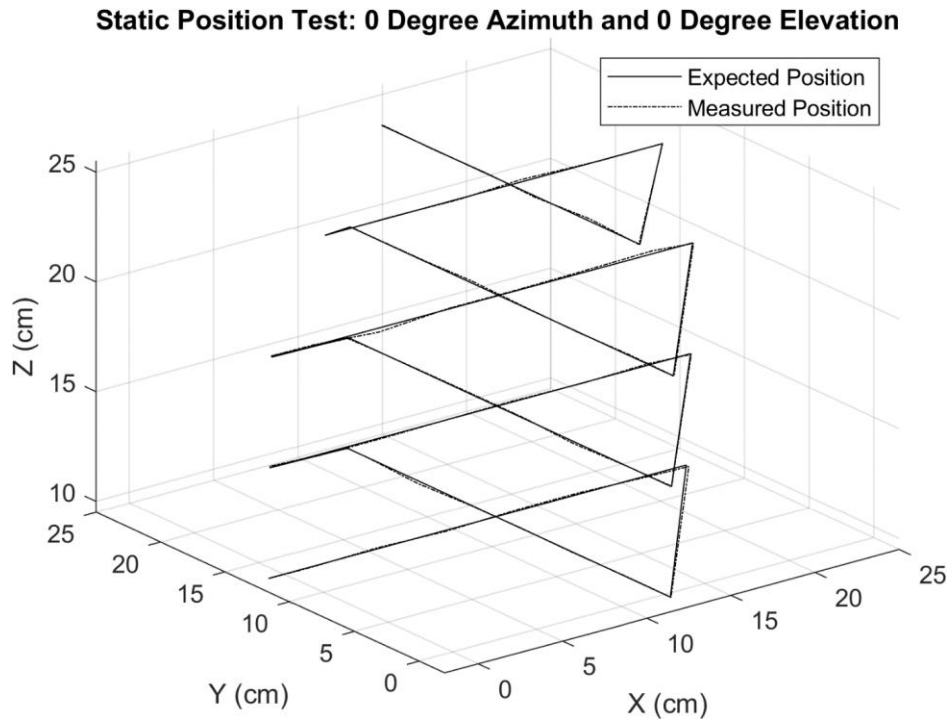


Figure 6.2.2. 0-degree azimuth orientation position result.

**Static Position Test: -30 Degree Azimuth and 0 Degree Elevation**

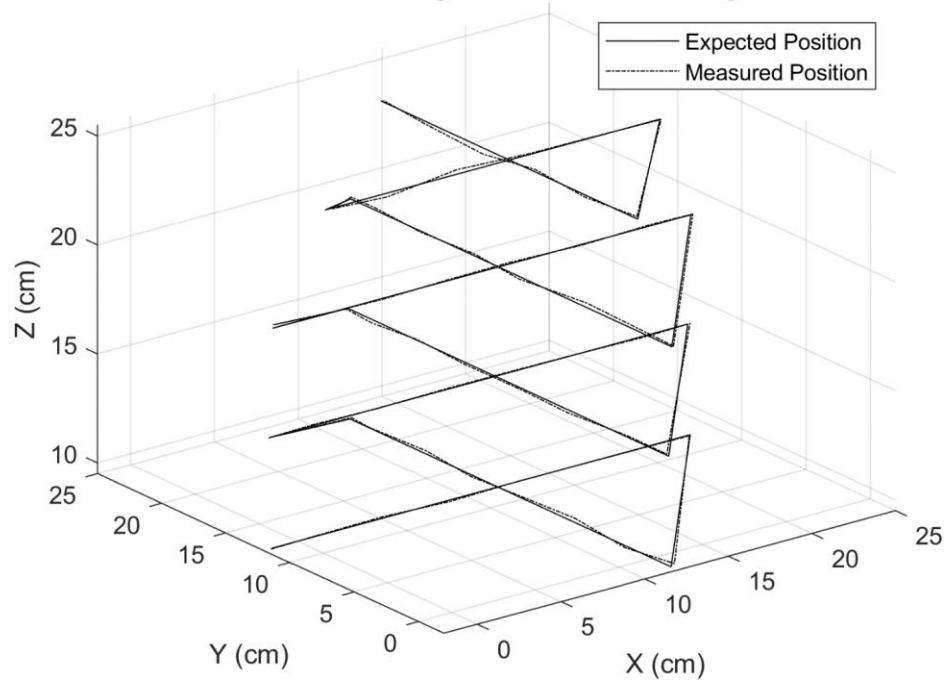


Figure 6.2.3. -30-degree azimuth orientation position result.

**Static Position Test: -60 Degree Azimuth and 0 Degree Elevation**

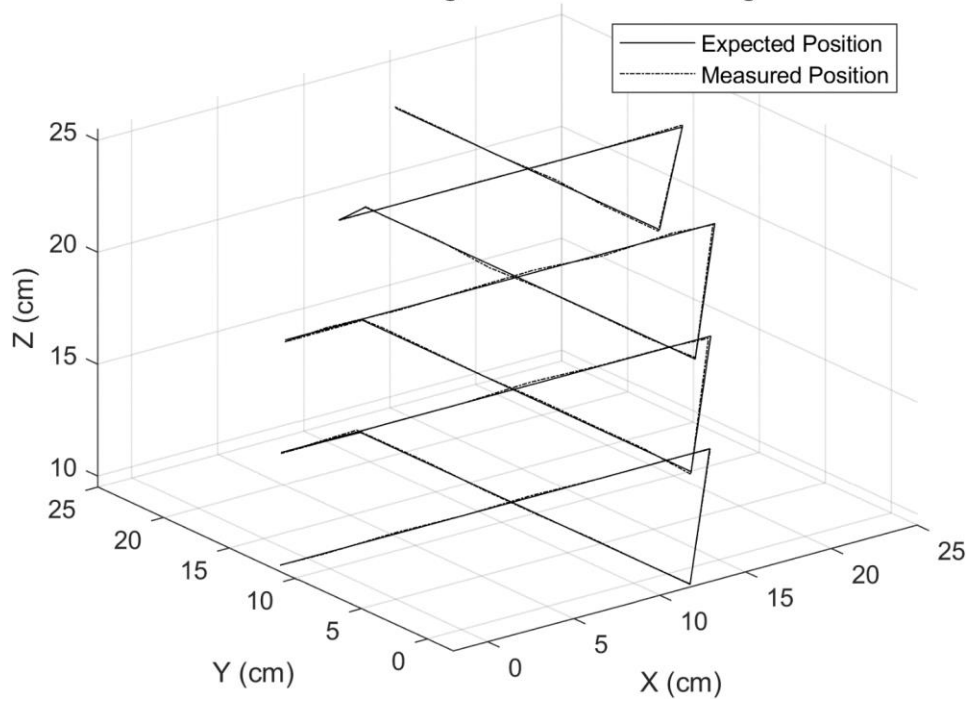


Figure 6.2.4. -60-degree azimuth orientation position result.

**Static Position Test: -90 Degree Azimuth and 0 Degree Elevation**

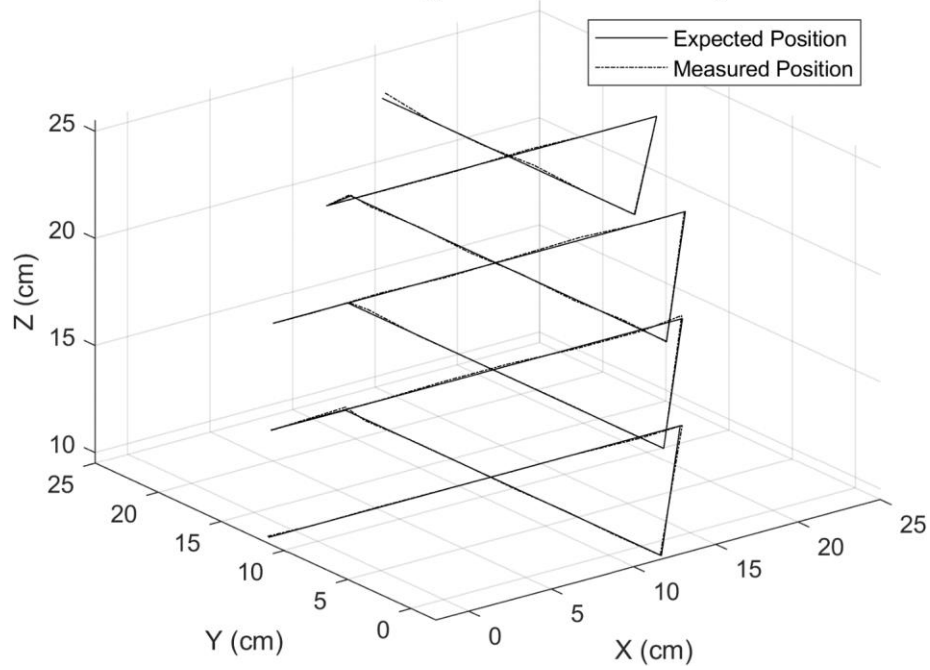


Figure 6.2.5. -90-degree azimuth orientation position result.

**Static Position Test: -120 Degree Azimuth and 0 Degree Elevation**

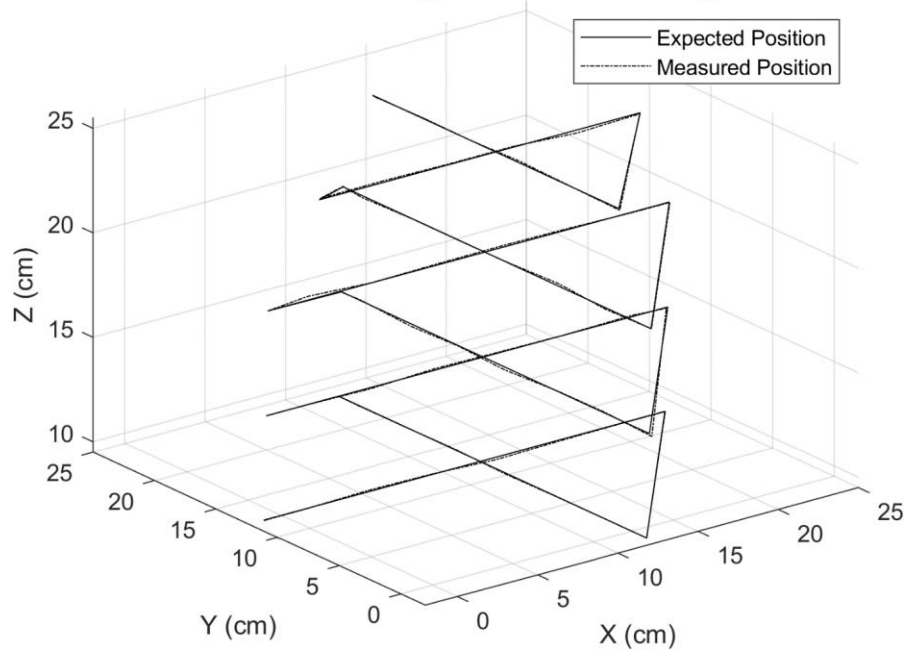


Figure 6.2.6. -120-degree azimuth orientation position result.

### Static Position Test: -150 Degree Azimuth and 0 Degree Elevation

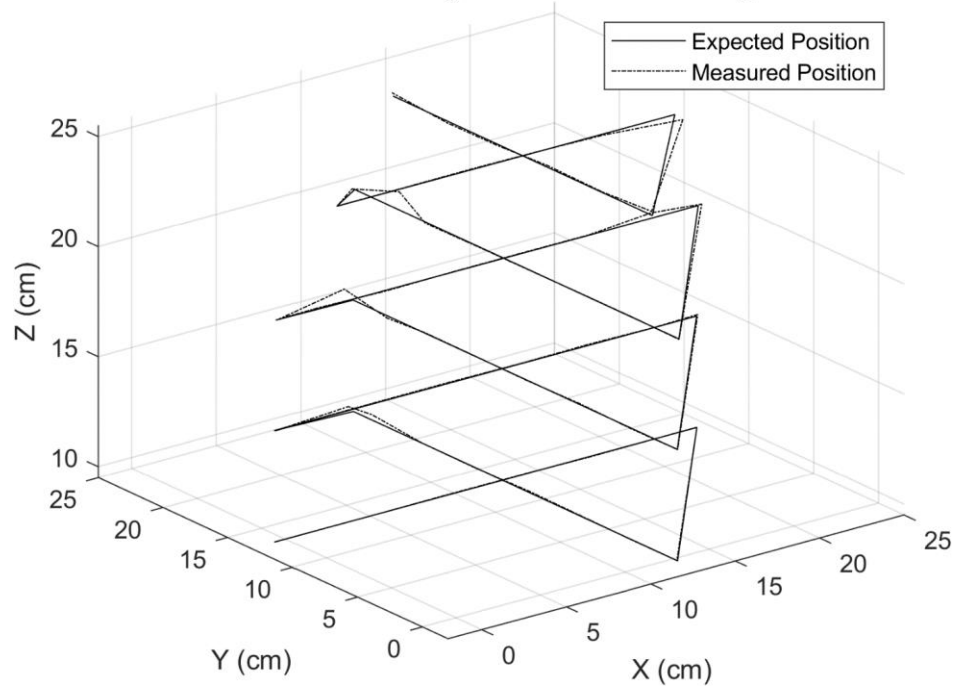


Figure 6.2.7. -150-degree azimuth orientation position result.

### Static Position Test: -180 Degree Azimuth and 0 Degree Elevation

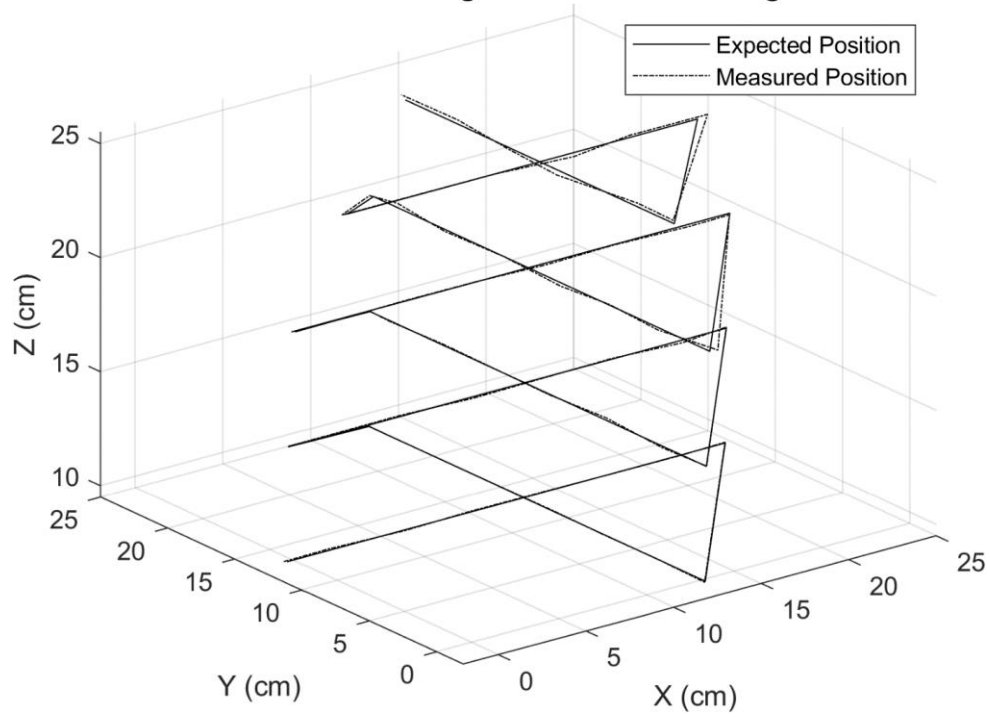


Figure 6.2.8. -180-degree azimuth orientation position result.

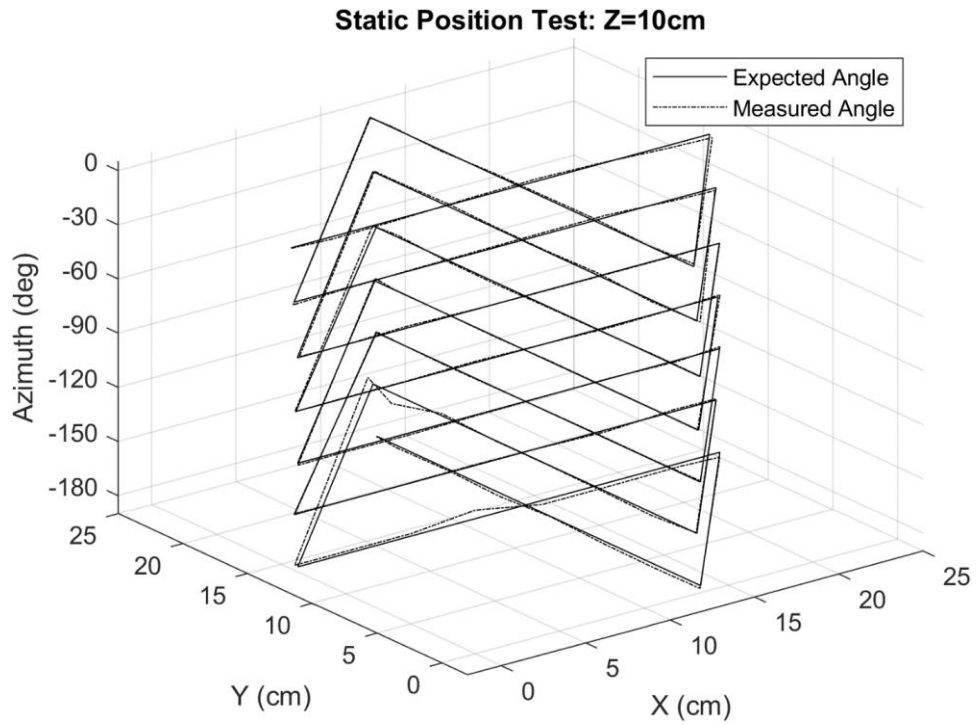


Figure 6.2.9.  $z = 10\text{cm}$  orientation angle varying result.

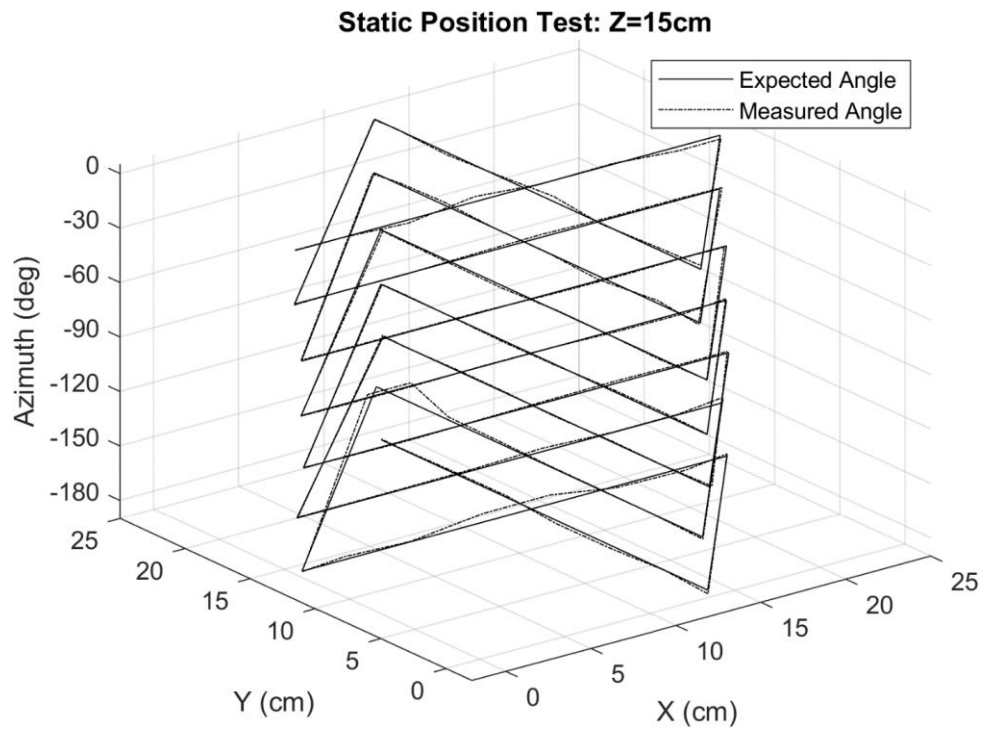


Figure 6.2.10.  $z = 15\text{cm}$  orientation angle varying result.

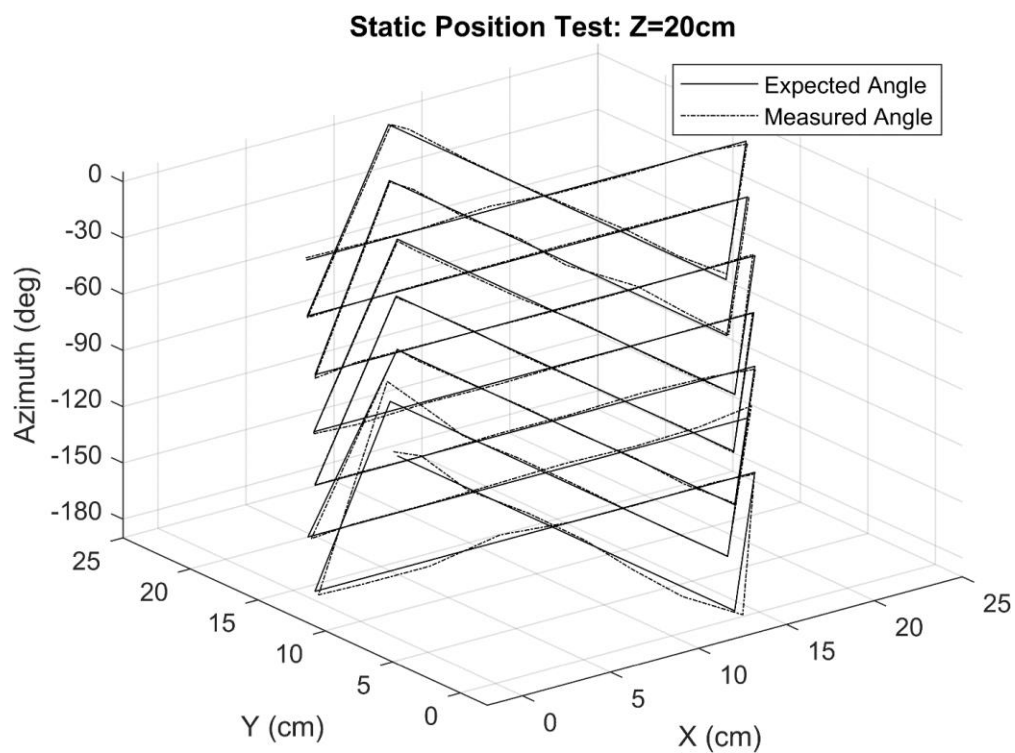


Figure 6.2.11.  $z = 20\text{cm}$  orientation angle varying result.

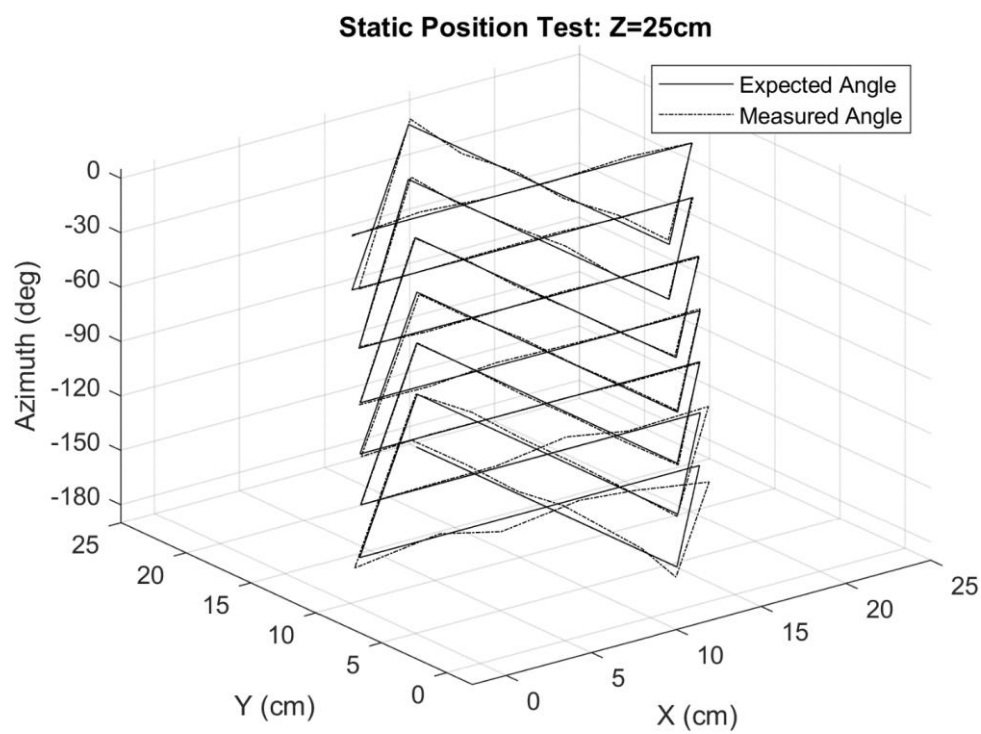


Figure 6.2.12.  $z = 25\text{cm}$  orientation angle varying result.

Each static position is measured 100 times. The resulting position and orientation errors, means, and standard deviations are computed. Tables 6. 2.1 and 6.2.2 summarize the results.

Table 6.2.1. Position error of static position tests.

Azimuth (deg)	Mean position error (mm)				Standard deviation position (mm)			
	$x$	$y$	$z$	$d$	$x$	$y$	$z$	$d$
0	0.83	0.75	0.40	1.37	0.40	0.39	0.18	0.50
–30	1.47	1.41	0.69	2.41	0.72	0.84	0.33	1.00
–60	0.58	0.67	0.48	1.19	0.19	0.28	0.22	0.30
–90	0.56	0.52	0.53	1.10	0.20	0.19	0.26	0.32
–120	0.42	0.59	0.55	1.06	0.18	0.26	0.24	0.33
–150	0.88	1.37	0.72	1.98	0.52	0.76	0.34	0.81
–180	1.32	1.38	0.58	2.26	0.70	0.74	0.26	0.90
Overall	0.86	0.96	0.56	1.62	0.41	0.49	0.26	0.60

Table 6.2.2. Orientation error of static position tests.

Azimuth (deg)	Mean orientation error (deg)			Standard deviation orientation (deg)		
	azimuth	elevation	overall	azimuth	elevation	overall
0	1.24	1.00	2.24	0.30	0.32	0.53
–30	0.97	0.85	1.82	0.40	0.36	0.66
–60	0.54	0.70	1.24	0.11	0.11	0.18
–90	0.54	0.65	1.20	0.11	0.08	0.14
–120	0.57	0.58	1.15	0.12	0.14	0.22
–150	1.92	1.46	3.38	0.63	0.38	0.85
–180	2.12	1.87	3.99	0.53	0.48	0.91
Overall	1.13	1.02	2.15	0.32	0.27	0.50

One observation is that the errors of static position tests at 0 and –180 azimuth angles are larger than test results closer to the –90 azimuth angle. Elevated errors at those two angles are related to the fact that the determinant is very small (closer to 0). This is illustrated in Figures 6.2.13 and 6.2.14 below, where there are significantly more positions with very small determinant at 0 degrees than at –90 degrees. As explained in the above divergence correction section 4.8, when the determinant is close to or equal to 0, the algorithm will fail to find a position. Thus, the



divergence correction is necessary. However, the fix cannot eliminate the errors completely, as seen in Table 6.2.2 in the 1<sup>st</sup> row and 7<sup>th</sup> row (0 and  $-180$  degree azimuth tests).

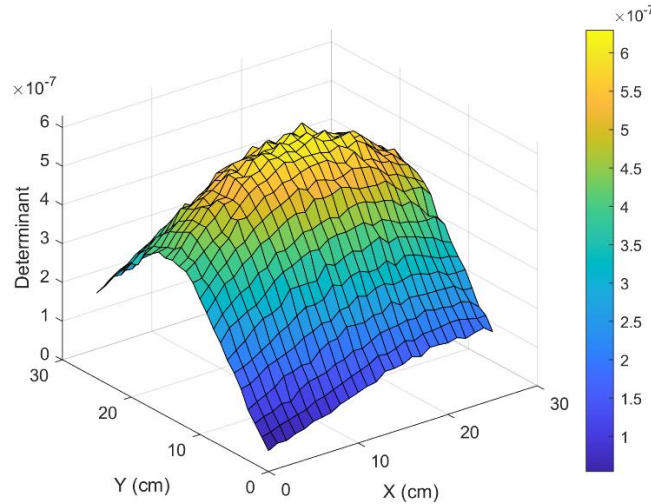


Figure 6.2.13. Determinant for azimuth angle:  $-90$  degrees.

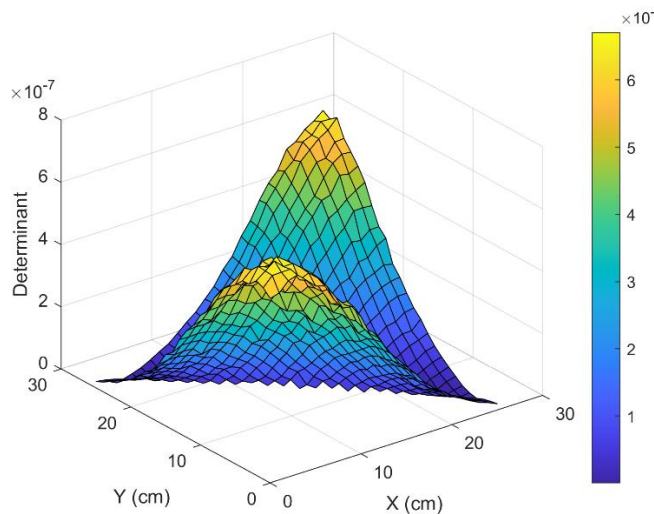


Figure 6.2.14. Determinant for azimuth angle:  $0$  degrees.

## 6.2.2 Dynamic Tests

In addition, dynamic tests were performed on the Tx coil. The position data were calculated at a rate of 1.6 kHz, with a visual update rate of 200 Hz while the system was moving by either adjusting the  $x$ - $y$ - $z$  position or adjusting the azimuth orientation. The slower visual update rate was

used to minimize latency between the unfiltered and filtered results, which is described in the filter design section. Figures 6.2.15–6.2.20 and Figures 6.2.21–6.2.24 depict the unfiltered and filtered results for position and orientation changes, respectively. The filter latency is determined by analyzing the time delay between the unfiltered data and the filtered data. As we can see, the dynamic tests confirm that the system operates with minimal latency (The latency time and settling time are estimated as 15 ms and 62.4 ms, respectively). In addition, the max position variation within the test area is determined from the plots to be 3.44 mm.

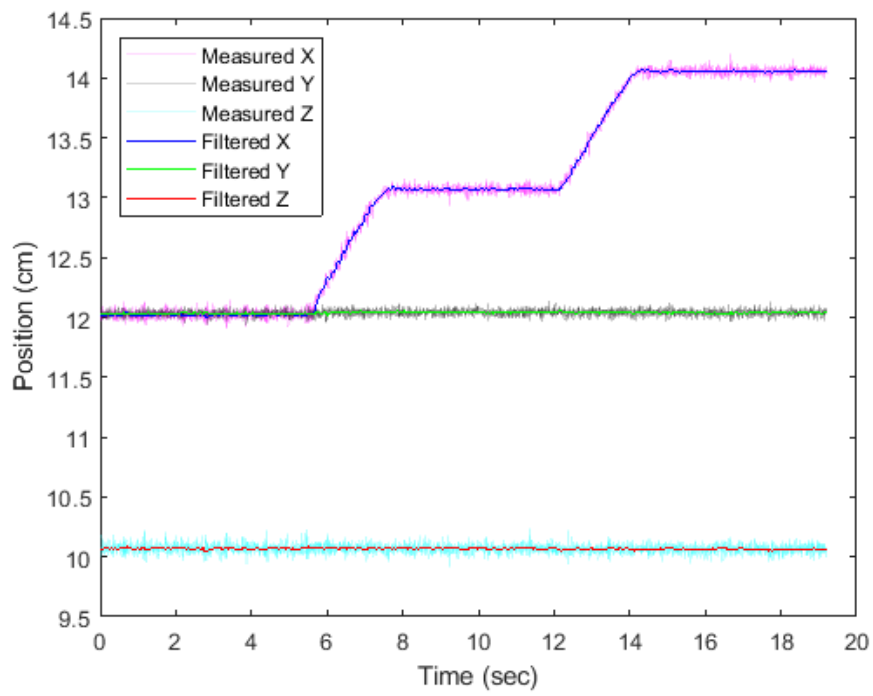


Figure 6.2.15. Dynamic test: position change (a).

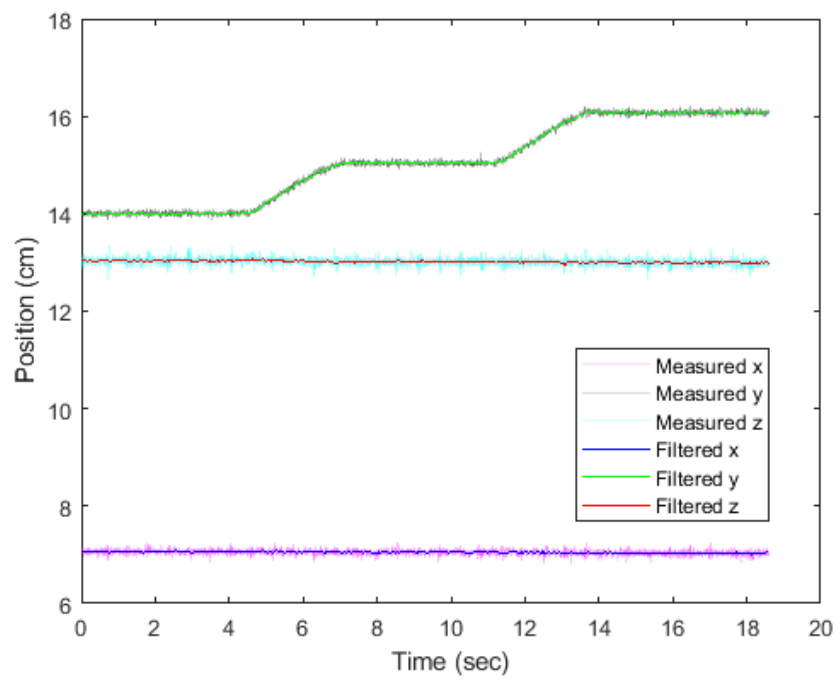


Figure 6.2.16. Dynamic test: position change (b).

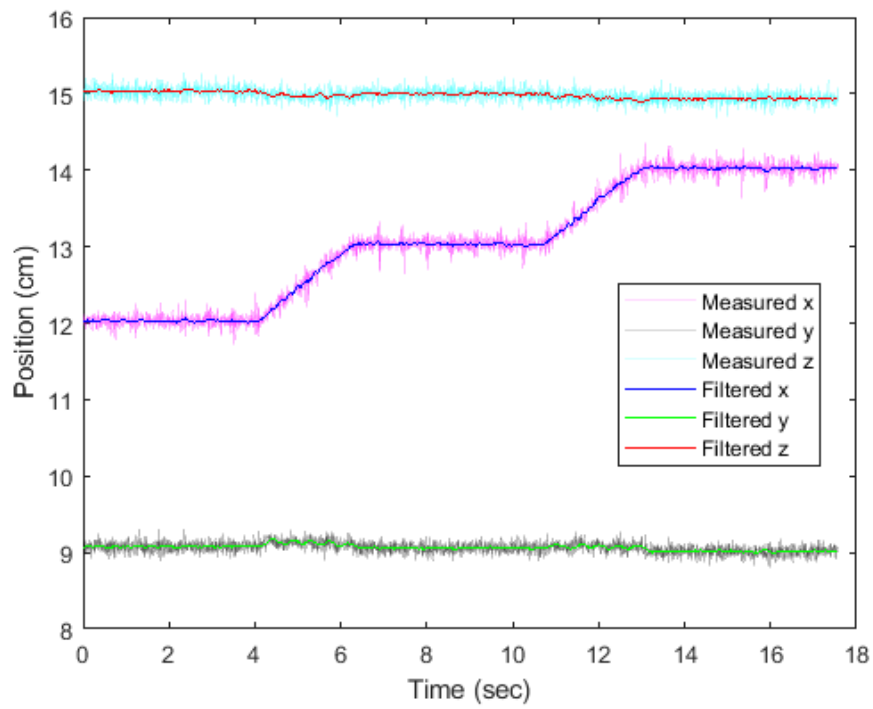


Figure 6.2.17. Dynamic test: position change (c).

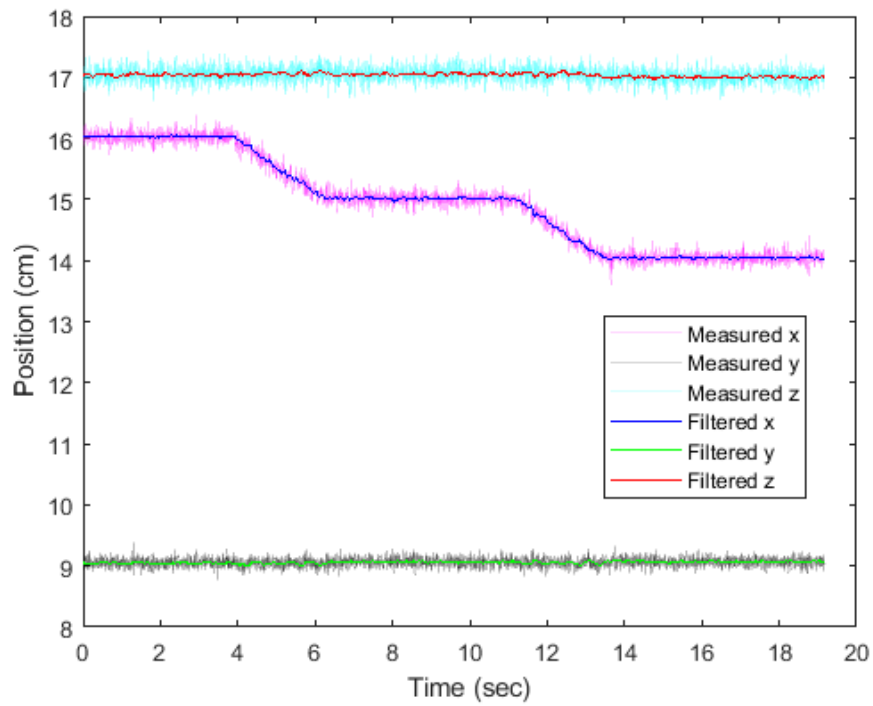


Figure 6.2.18. Dynamic test: position change (d).

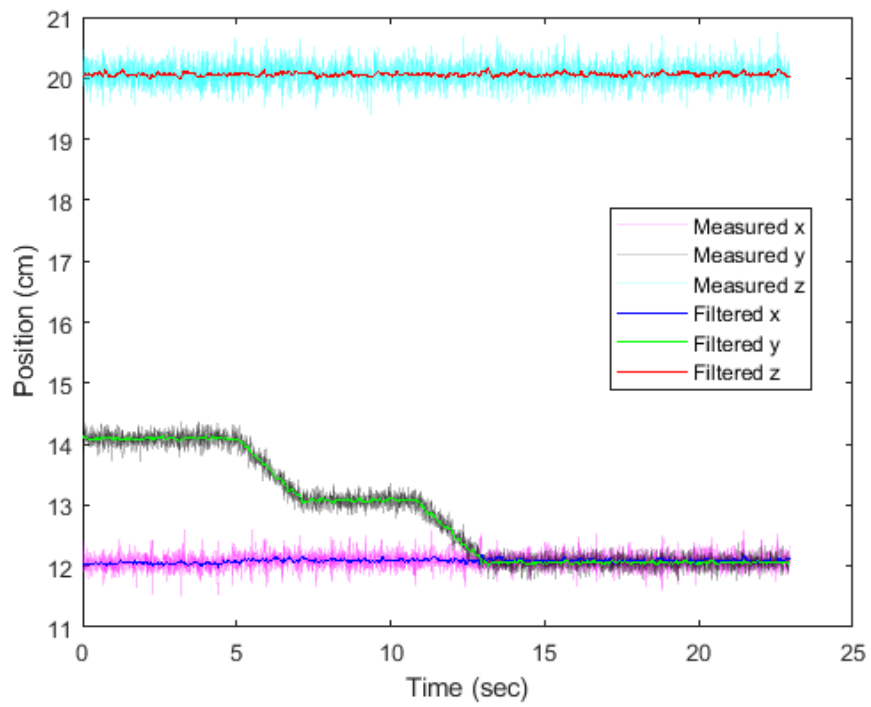


Figure 6.2.19. Dynamic test: position change (e).

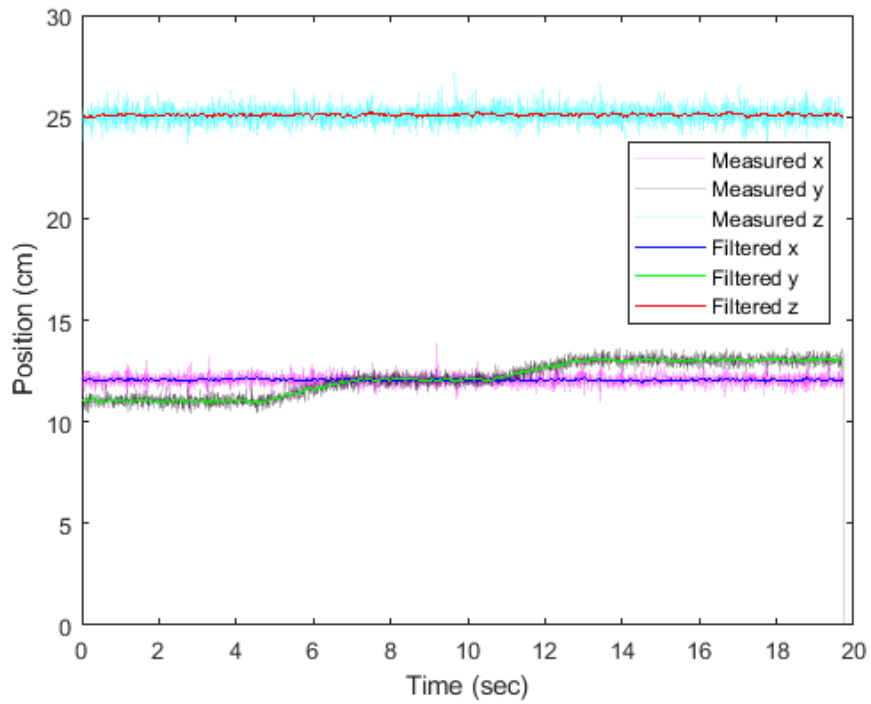


Figure 6.2.20. Dynamic test: position change (f).

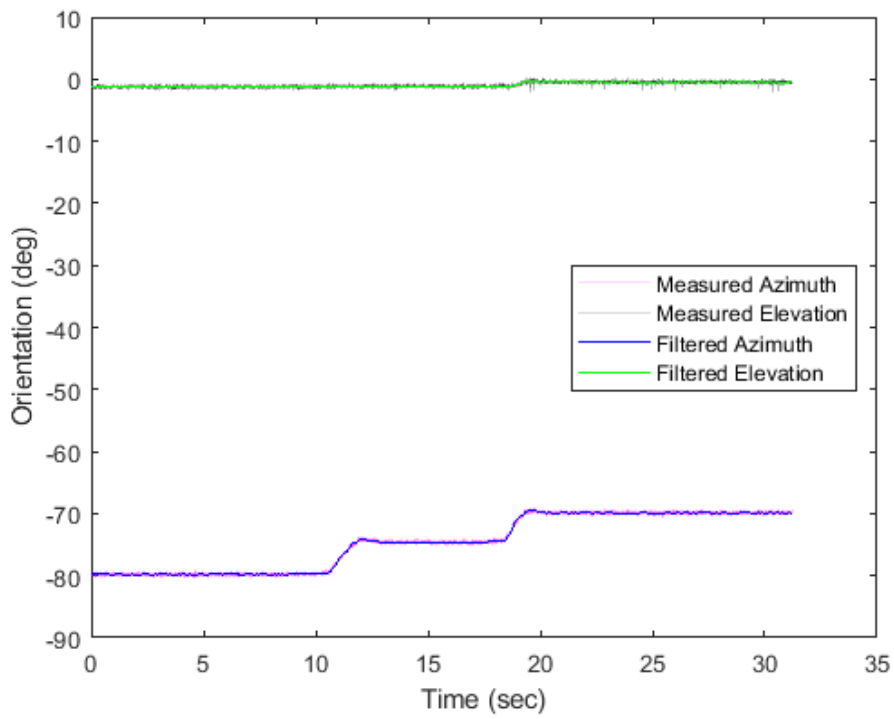
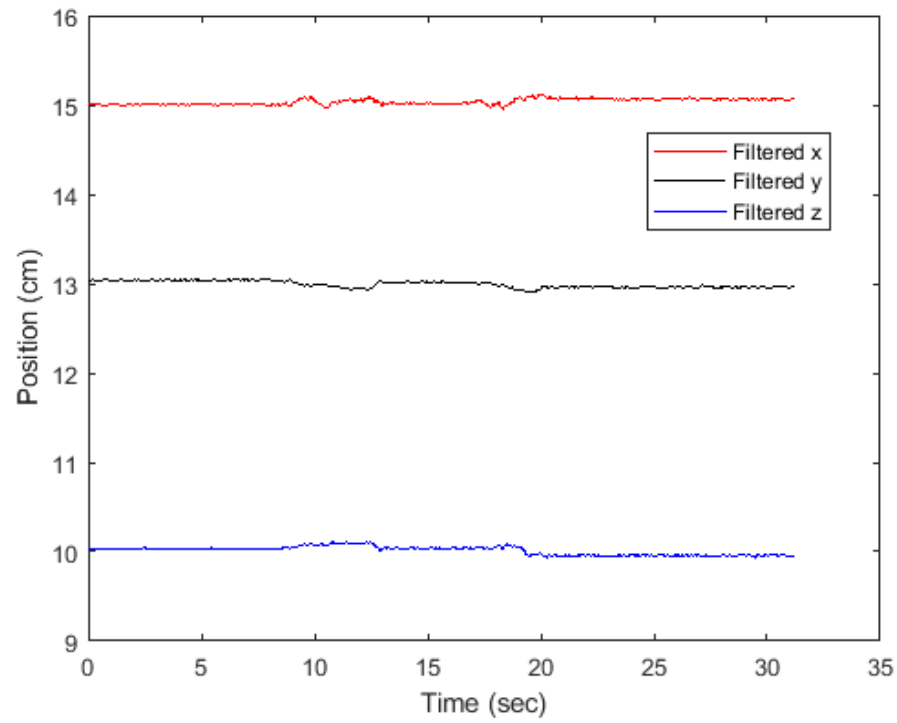


Figure 6.2.21. Dynamic test: orientation change (a).

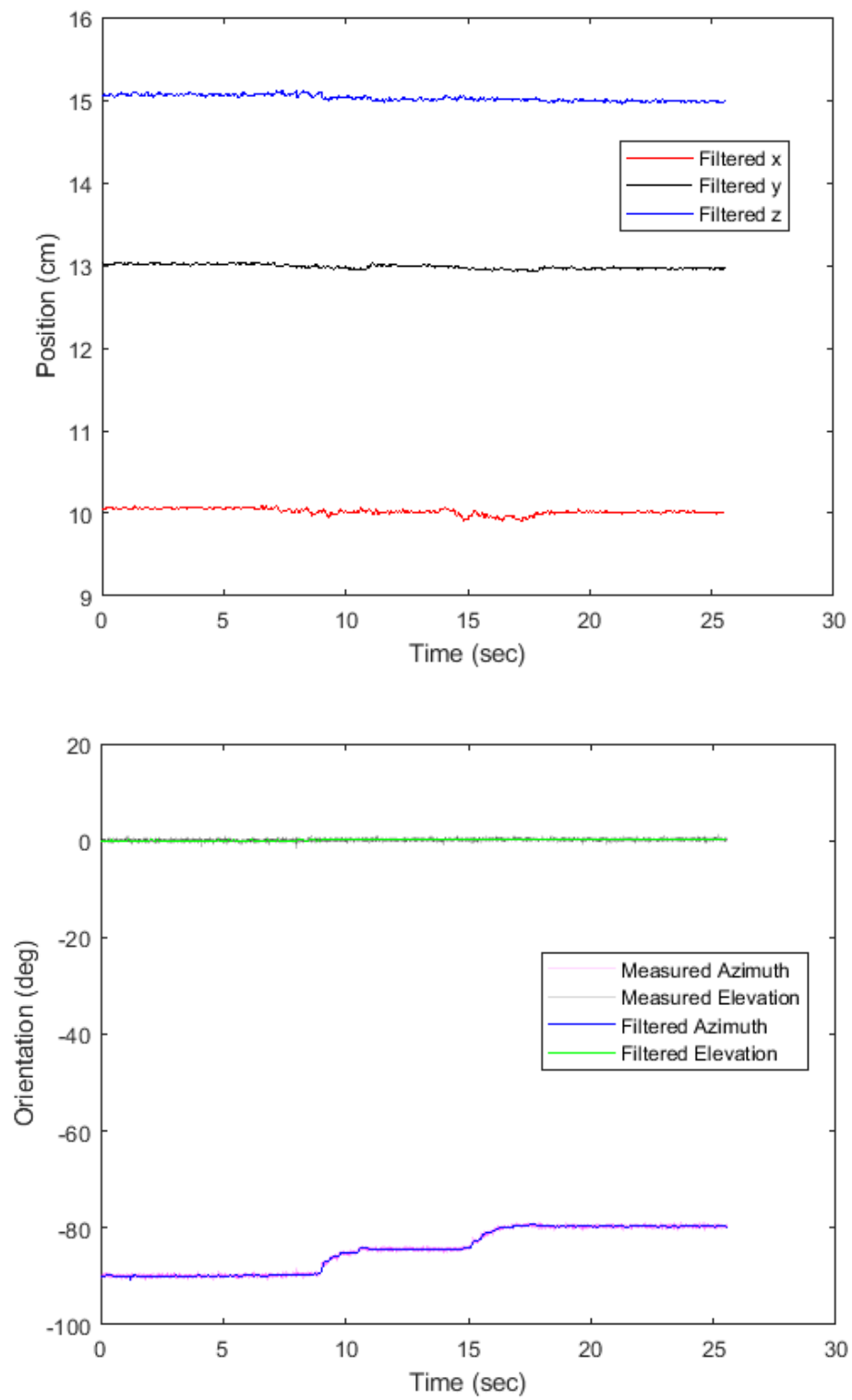


Figure 6.2.22. Dynamic test: orientation change (b).

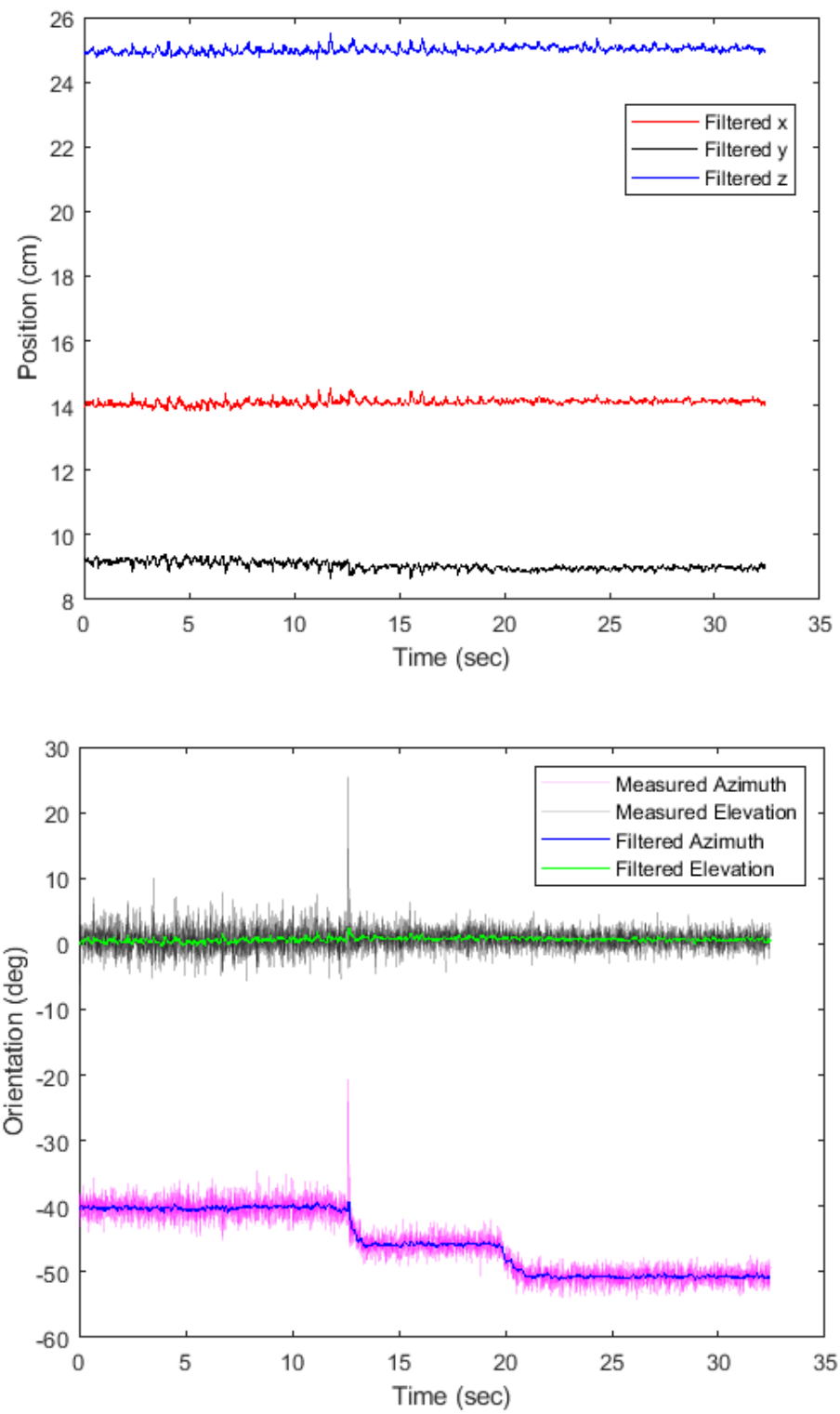


Figure 6.2.23. Dynamic test: orientation change (c).



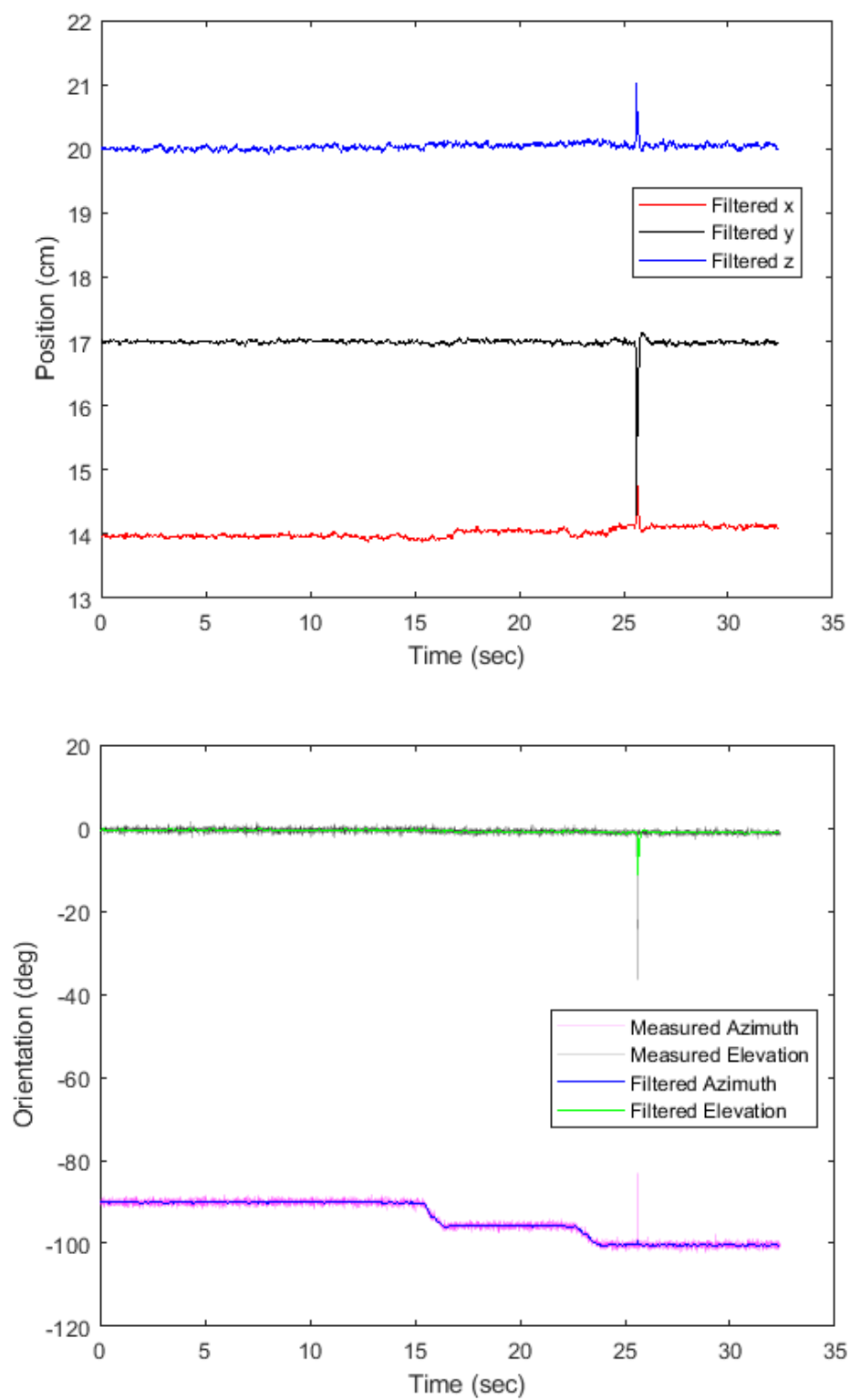


Figure 6.2.24. Dynamic test: orientation change (d).

We also calculate the jitter for all the dynamic test points by taking one standard deviation. Tables 6.2.3 and 6.2.4 show these jitter values for the position and orientation angle.

Table 6.2.3. Dynamic position tests: jitter (mm).

$z$ distance	10cm	15cm	20cm	25cm
$x$ direction	0.05	0.11	0.18	0.03
$y$ direction	0.04	0.08	0.15	0.03
$z$ direction	0.05	0.09	0.25	0.05
Overall distance	0.05	0.10	0.22	0.05

Table 6.2.4. Dynamic orientation tests: jitter (deg).

$z$ distance	10cm	15cm	20cm	25cm
azimuth	0.04	0.07	0.10	0.18
elevation	0.03	0.04	0.07	0.23
Combined	0.06	0.08	0.11	0.18

In summary, the test results indicate that the position determined by the algorithm is very close to the expected position with the mean position error across all static tests being 1.6 mm, which is sufficient for the application of heart shape mapping to catheter ablation.

While the position algorithm works well for most points tested, certain points/orientations have relatively larger error and standard deviations. Some points are outliers, like the one shown in Figure 6.2.23, at around  $t = 12.65$  sec. The orientation data has a spike, despite the position data not having a spike. There are other points with relatively low accuracy, such as those at the orientation of 0 or 180°, where the average error exceeds 2 mm. This is attributed to the divergence problem mentioned in the previous chapter. The divergence fix causes a position offset, which in turn increases mean position and orientation errors. Also, due to SNR variation over distance, positions with weak B-field signals for all 3 coils have increased position jitter.

### 6.3 Repeatability

For this analysis, we examine the static position and orientation test measurements for  $-90^\circ$  azimuth and  $0^\circ$  elevation with same position changes, using results from two different trials. One set of test data was collected on 10/17/2021 and the other on 10/23/2021. In both trials, the transmitting coil was moved along the same position and orientation iterations. The variation observed in the measurements is analyzed using the method described in [101].

For repeatability, the tests results suggest that the  $y$  position values are nearly identical in the two trials. In addition, the orientation values of azimuth and elevation are also identical in the two trials. However, the  $x$  and  $z$  position values have slight offsets, where all the position values are shifted by a constant value. This value changes depending on the  $z$  height of the transmitter coil. Table 6.3.1 below shows the offset values found at different positions.

Table 6.3.1. Offsets in position test results.

$z$ height (cm)	$x$ shift (mm)	$z$ shift (mm)
10	1.3	1.2
15	1.3	1.2
20	0.2	1.6
25	-1.4	0

These shifts occur because of the imperfection of the XYZ test station. The  $z$ -axis control is enabled using a screw at the station's base and zip-tie in the middle. Imperfect flexibility can cause the transmitter coil to slightly tilt along the  $xz$  direction, which may change between different tests, affecting the position results. However, these offsets can be easily compensated in post processing.

The mean error and standard deviation are also compared. The observed  $x$  and  $z$  position shifts (Table 6.3.1) were applied to the trial 2 data. Tables 6.3.2 and 6.3.3 and Figures 6.3.1 and 6.3.2 show the comparison of trial results.

Table 6.3.2. Comparison of mean and standard deviation of position errors.

Trial ID	Azimuth (deg)	Mean position error (mm)				Standard deviation position (mm)			
		$x$	$y$	$z$	$d$	$x$	$y$	$z$	$d$
Trial 1	−90	0.56	0.52	0.53	1.1	0.2	0.19	0.26	0.32
Trial 2	−90	0.64	0.53	0.65	1.25	0.21	0.14	0.27	0.29

Table 6.3.3. Comparison of mean and standard deviation of orientation errors.

Trial ID	Azimuth (deg)	Mean orientation error (deg)			Standard deviation orientation (deg)		
		azimuth	elevation	overall	azimuth	elevation	overall
Trial 1	−90	0.54	0.65	1.2	0.11	0.08	0.14
Trial 2	−90	0.58	0.61	1.2	0.1	0.08	0.13

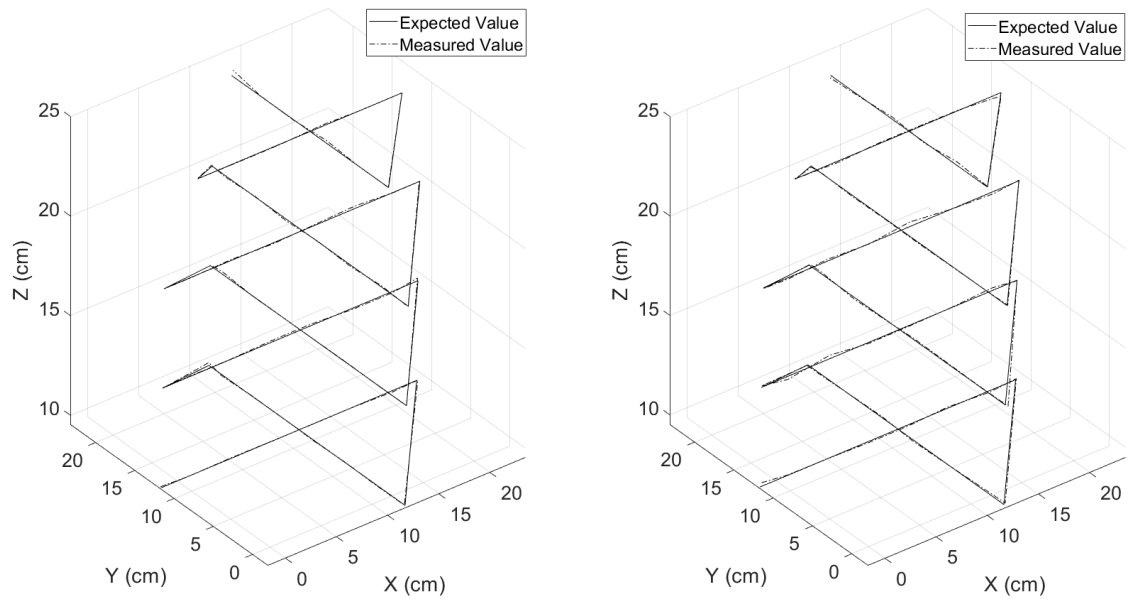


Figure 6.3.1. Trial 1 (left) and Trial 2 (right) position test results.

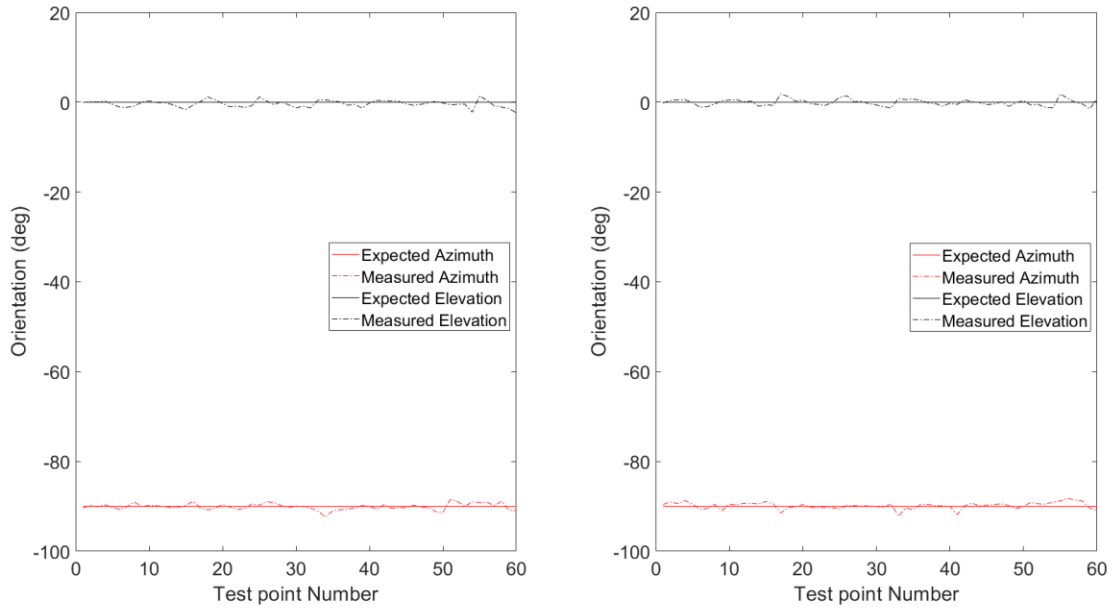


Figure 6.3.2. Trial 1 (left) and Trial 2 (right) orientation test results.

As seen in the position results, the differences in  $x$  and  $z$  position errors are larger (about 0.1 mm) than the  $y$  position errors (about 0.01 mm). There is no significant change in standard deviation of position errors. The orientation error is nearly identical with mean errors only differing in 0.04 degrees and standard deviation differing in 0.01 degrees. This amounts to approximately 1.7 mm variation in position and 0.02 degree variation in orientation.

## 6.4 System Comparison

Through the position and orientation tests, the proposed magnetic tracking system has demonstrated its ability to track the transmitter coil in both static and dynamic environments at an update rate of 200 Hz. The tracking accuracy of newly developed system is comparable to other existing systems. Table 6.4.1 provides a comparison of this system's accuracy and update rate with published experimental results of similar magnetic tracking systems used in the medical environment. Our system is unique in its compactness and its simple algorithm which allow for low latency, while providing high accuracy. In addition, to our knowledge, this is the first operational system which tracks a moving transmitting coil with plastic resin core using two

triaxial sensors. Most commercially available systems (NDI Aurora, Ascension 3D, and Polhemus) employ a ferrite core sensing coil instead, and such tracking systems suffer from slow update rates.

Table 6.4.1. System comparison.

	This Work	NDI Aurora Planar (5DOF) [35]	Ascension 3D Guidance Short [35]	Ascension 3D Guidance Flat [35]	Polhemus Isotrak II [102]	O'Donahuge et al. [100]	Plotkin et al. [33]	Roetenberg et al. [53]	Hu et al. [103]
Test environment	Laboratory	Radiology Suite	Radiology Suite	Radiology Suite	Operating Room	Laboratory	Laboratory	Laboratory	Laboratory
Test volume	25cm×25cm×25cm	18cm×18cm×18cm*	18cm×18cm×18cm*	18cm×18cm×18cm*	18cm×15cm×12cm	25cm×25cm×25cm	28.8cm×28.8cm×20cm**	80cm×80cm×80cm	45cm distance
Test update rate	200Hz	39.86Hz	190Hz	160Hz	n/a	22.6Hz	50Hz	1.7Hz	
Position precision (stdev)	0.60mm	0.67mm	0.18mm	0.48mm	n/a	0.7mm	0.6mm	2.4mm	n/a
Orientation precision (stdev)	0.5deg	n/a	n/a	n/a	n/a	0.8deg	0.4deg	2.6deg	n/a
Mean position error	1.62mm	0.76mm	0.34mm	0.61mm	3.2mm	1.2mm	1mm	7.6mm***	1.8mm
Mean orientation error	2.15deg	n/a	n/a	n/a	2.9deg	1deg	0.6deg	5.9deg***	1.54deg

\* Test area was not provided in the original paper but provided in [28].

\*\* Test was done with 20 cm vertical distance and transmitter array of 28.8 cm × 28.8 cm.

\*\*\* RMS error.

## 6.5 System Cost Estimation

The proposed system is unique in that its cost is significantly lower than most existing magnetic tracking systems on the market with comparable accuracy. Table 6.5.1 shows the estimated hardware costs for the complete system, which totals approximately \$270 (including rechargeable Li-ion battery). This figure includes once off costs involved in low volume production of PCBs, SMA cables, and connectors. Large scale manufacturing would see a significant decrease in the system cost as the majority of system costs are related to PCB, SMA cables, and connectors since each triaxial coil requires 1 SMA cable and 2 connectors which make up approximately \$66 of system cost. These components are commercially available, and the PCBs used are simple and compact. The only cost hard to estimate is the transmitter coil which was wound using a custom motor setup. So, the total cost is more than just the cost to print the 3D resin core and the copper wire.

Table 6.5.1. System cost breakdown.

Module	Cost (\$)
Transmitter coil manufacturing	10
2 Triaxial sensing coils	45
STM32 microcontroller	15
Analog front end	30
Transmitter driver board	40
Battery	50
SMA Cable/Connectors	80
Total	270



## 7. SUMMARY AND FUTURE WORK

### 7.1 Conclusions

Cardiac ablation is a minimally invasive, low risk procedure that can correct heart rhythm problems. Current techniques which determine catheter positioning while a patient is undergoing heart surgery are usually invasive, often inaccurate, and require some forms of imaging. In this study, we develop a unique real-time tracking system which can track the position and orientation of a medical catheter inside a human heart with fast update rate of 200 Hz and high precision. This thesis details the analysis, design consideration, and implementation of the system for a diagnostic catheter to map the shape of the heart.

The system utilizes a magnetic positioning method involving a new solution algorithm and innovative designs of magnetic field detection hardware and software. The successful implementation of the EM tracking system demonstrates that this type of positioning has the benefits of not needing a line-of-sight between emitter and sensor. The proposed system can be applied to other medical applications in need of real-time positioning.

Specific contributions of the study include a novel design of an air core single uniaxial transmitter (1.5 mm in diameter) placed on a medical catheter tip and two triaxial receivers placed in reference locations. Such a design employs a minimal number of coils, allowing for simple implementation of EM tracking. Magnetic field magnitude measurements from the six sensing coils are sampled by a microcontroller ADC, and the firmware executes an efficient positioning algorithm to determine the position and orientation of the catheter.

The system has been successfully evaluated through simulation and laboratory tests. The results of both static and dynamic tests performed on the system show that the average tracking accuracy is 1.6 mm, which is well suited for catheter-based tracking.

In summary, this system has several advantages over existing systems reported in the literature. Specifically,

- (1) The tracking system concept is based on an efficient theoretical model developed by McGary [42], which needs only two fixed triaxial receivers. In contrast, other systems typically require additional sensors or transmitters [33], or rotating sensors [104], [105].

- (2) The hardware of the system is simpler and easier to manufacture than other systems [32], [58], [106].
- (3) The system has a low-cost advantage over other systems on the market.

The uniaxial transmitter in this system has the following advantages:

- Simple and compact circuitry,
- Op-amp driver minimizing noise and distortion of output current to the transmitter,
- PLL feedback design to minimize phase and other sideband noise, and
- Active feedback power regulation for high SNR inductor current under heat constraints.

The sensing circuit has the following advantages:

- Two stage amplification, with automated adaptive gain control for a wide dynamic range and resistance to PVT variations,
- Compact two triaxial coil design for 5DoF tracking, allowing for simple and low cost implementation for large scale manufacturing, and
- Tracking algorithm in the form of microcontroller firmware for fast, low-latency tracking, instead of a separate offline software used in many other tracking systems with slow update rates.

Finally, the proposed system has been shown to have comparable accuracy with existing products on the market. Through the system's unique and novel hardware and firmware, the study contributes to the advancement in EM tracking applications in the medical and other fields.

## **7.2 Future Work**

### **7.2.1 Additional Sensing Coils and Layout Optimization**

The optimization of sensing coil locations may further improve tracking system accuracy and reduce position algorithm divergence. A relevant optimization procedure is proposed in [50]. The procedure is based on the characterization of the Fisher information matrix [107] of an EM tracking system. The sensing errors can be minimized by maximizing the FIM. However, the complexity involved in constructing the FIM and the independent assumption of sensing error distribution make the procedure less effective for the proposed system. As noted in the divergence correction section, although adding more sensing coils allows for more information to be available

for position calculation, it also increases the system complexity which affects the update rate as well as other system performance. Thus, improvements and simplifications in the procedure to optimize sensing coil layout should be investigated in future studies for this type of EM tracking systems.

### **7.2.2 Commercialization and Medical Device Classification**

The proposed system is intended for catheter ablation treatment of arrhythmia. However, for this system to be commercialized and sold for medical applications, it must adhere to all the guidelines specified in relevant documents. For certification in the United States, an EM tracking system for application would be a Class II device. Few devices currently fall under the one Tx and multiple Rx system in the medical environment. The certification of this device may involve additional efforts compared to other systems with conventional architectures.

### **7.2.3 6DOF Tracking**

A drawback of the proposed EM tracking system is limited to 5DOF. As of now, certain EM tracking systems on the market have 6DOF sensors. However, the implementation of tiny 6DOF coils is difficult due to size limitation. One method is to have a two-coil combined Tx, with slight angle tilt between the two coils (Figure 2.4.3). The non-symmetric core design allows for all three Euler angles to be tracked. Another method is to have two slanted winding coils on the same core axis, where the slants are orthogonal to each other. Initial COMSOL simulations using a staircase geometric setup to mimic such coil windings have shown that it is possible to generate two different B-fields using the two coils with the same core. However, winding a slanted coil has its own challenges.

### **7.2.4 Multi-Catheter Support**

The proposed system supports one frequency. However, the hardware can be easily adjusted to support multiple frequencies. This will allow for different transmitter coils operating at different frequencies on different catheter tips. For the sensing system, the amplifier is wideband, so there is no need for a new amplification system. The amplitude and phase algorithms only need

to be adjusted to accommodate the new frequencies. However, frequency mixing among different transmitter frequencies will require corrective compensation for a successful implementation.

## REFERENCES

- [1] H. Wang *et al.*, “Global, regional, and national life expectancy, all-cause mortality, and cause-specific mortality for 249 causes of death, 1980–2015: A systematic analysis for the global burden of disease study 2015,” *The Lancet*, vol. 388, no. 10053, pp. 1459–1544, Oct. 2016, doi: 10.1016/S0140-6736(16)31012-1.
- [2] “Arrhythmia,” Carolina Heart and Leg Center, Apr. 23, 2018. <https://www.carolinaheartandleg.com/arrhythmia/> (accessed Dec. 17, 2021).
- [3] “Heart pacemaker: MedlinePlus medical encyclopedia,” <https://medlineplus.gov/ency/article/007369.htm> (accessed Dec. 14, 2021).
- [4] R. N. Fogoros and J. M. Mandrola, *Fogoros’ Electrophysiologic Testing*, 6th edition, Hoboken, NJ: Wiley-Blackwell, 2017.
- [5] M. T. Liaquat, I. Ahmed, and T. Alzahrani, “Pacemaker malfunction,” *StatPearls*, Treasure Island (FL): StatPearls Publishing, 2021 (accessed Dec. 14, 2021). [Online] Available: <http://www.ncbi.nlm.nih.gov/books/NBK553149/>.
- [6] “Tachycardia - Symptoms and causes,” Mayo Clinic, <https://www.mayoclinic.org/diseases-conditions/tachycardia/symptoms-causes/syc-20355127> (accessed Dec. 14, 2021).
- [7] “Cardiac ablation,” Mayo Clinic, <https://www.mayoclinic.org/tests-procedures/cardiac-ablation/about/pac-20384993> (accessed Dec. 14, 2021).
- [8] R. K. Thakur, G. J. Klein, and R. Yee, “Radiofrequency catheter ablation in patients with Wolff-Parkinson-White syndrome,” *CMAJ Can. Med. Assoc. J.*, vol. 151, no. 6, pp. 771–776, Sep. 1994.
- [9] A. Speicher, “Having an exam that uses contrast dye? Here’s what you need to know,” *UVA Radiology and Medical Imaging Blog for Patients*, Jul. 03, 2017. <https://blog.radiology.virginia.edu/medical-contrast/> (accessed Nov. 21, 2021).
- [10] P. A. McCullough *et al.*, “Contrast-induced acute kidney injury,” *J. Am. Coll. Cardiol.*, vol. 68, no. 13, pp. 1465–1473, Sep. 2016, doi: 10.1016/j.jacc.2016.05.099.
- [11] R. S. of N. A. (RSNA) and A. C. of Radiology (ACR), “Contrast materials,” *Radiologyinfo.org*, <https://www.radiologyinfo.org/en/info/safety-contrast> (accessed Nov. 21, 2021).

- [12] E. J. Schmidt *et al.*, “Electro-anatomic mapping and radio-frequency ablation of porcine left atria and atrio-ventricular nodes using magnetic resonance catheter tracking,” *Circulation Arrhythmia and Electrophysiology*, p. CIRCEP.109.882472, Jan. 2009, doi: 10.1161/CIRCEP.109.882472.
- [13] “French catheter scale,” *Wikipedia*, Dec. 11, 2021 (accessed Dec. 14, 2021). [Online] Available: [https://en.wikipedia.org/w/index.php?title=French\\_catheter\\_scale&oldid=1059721665](https://en.wikipedia.org/w/index.php?title=French_catheter_scale&oldid=1059721665).
- [14] “The heart, Part 6: Blood vessel basics,” <https://www.crossfit.com/essentials/the-heart-part-6-blood-vessel-basics> (accessed Dec. 14, 2021).
- [15] R. A. Lange and L. D. Hillis, “Diagnostic cardiac catheterization,” *Circulation*, vol. 107, no. 17, pp. e111–e113, May 2003, doi: 10.1161/01.CIR.0000070982.94049.A2.
- [16] “CARTO® NAVISTAR® DS - Mapping catheter by Biosense Webster | MedicalExpo,” <https://www.medicaexpo.com/prod/biosense-webster/product-71118-716582.html> (accessed Dec. 17, 2021).
- [17] Northwestern Medicine, “Heart catheterization,” *Northwestern Medicine*, <https://www.nm.org/conditions-and-care-areas/tests/heart-catheterization> (accessed Dec. 17, 2021).
- [18] R. S. of N. A. (RSNA) and A. C. of Radiology (ACR), “Catheter angiography,” *Radiologyinfo.org*, <https://www.radiologyinfo.org/en/info/angiocath> (accessed Dec. 17, 2021).
- [19] “cag.jpg (1500×1414),” <https://www.londoncardiovascularclinic.co.uk/wp-content/uploads/2012/06/cag.jpg> (accessed Feb. 25, 2022).
- [20] “Magnetic tracking - An overview | ScienceDirect Topics,” <https://www.sciencedirect.com/topics/computer-science/magnetic-tracking> (accessed Dec. 14, 2021).
- [21] “Magnetic tracker - An overview | ScienceDirect Topics,” <https://www.sciencedirect.com/topics/computer-science/magnetic-tracker> (accessed Dec. 14, 2021).
- [22] L. Farhi, L. Zhao, and Z. Liao, “Constrained weighted least square optimization for vehicle position tracking,” *GLOBECOM 2009 - 2009 IEEE Global Telecommunications Conference*, Nov. 2009, pp. 1–6. doi: 10.1109/GLOCOM.2009.5425650.
- [23] A. S. Paul and E. A. Wan, “Wi-Fi based indoor localization and tracking using sigma-point Kalman filtering methods,” *2008 IEEE/ION Position, Location and Navigation Symposium*, pp. 646–659, May 2008, doi: 10.1109/PLANS.2008.4569985.

- [24] X. Yuan, S. Yu, S. Zhang, G. Wang, and S. Liu, "Quaternion-based unscented Kalman filter for accurate indoor heading estimation using wearable multi-sensor system," *Sensors*, vol. 15, no. 5, pp. 10872–10890, May 2015, doi: 10.3390/s150510872.
- [25] I. Guvenc, "Enhancements to RSS based indoor tracking systems using Kalman filters," 2003.
- [26] E. Pietka, J. Kawa, and W. Wieclawek, *Information Technologies in Biomedicine, Volume 4*, Springer Science & Business, 2014.
- [27] A. Sorriento *et al.*, "Optical and electromagnetic tracking systems for biomedical applications: A critical review on potentialities and limitations," *IEEE Rev. Biomed. Eng.*, vol. 13, pp. 212–232, 2020, doi: 10.1109/RBME.2019.2939091.
- [28] A. M. Franz, T. Haidegger, W. Birkfellner, K. Cleary, T. M. Peters, and L. Maier-Hein, "Electromagnetic tracking in medicine #x2014; A review of technology, validation, and applications," *IEEE Trans. Med. Imaging*, vol. 33, no. 8, pp. 1702–1725, Aug. 2014, doi: 10.1109/TMI.2014.2321777.
- [29] D. D. Frantz, A. D. Wiles, S. E. Leis, and S. R. Kirsch, "Accuracy assessment protocols for electromagnetic tracking systems," *Phys. Med. Biol.*, vol. 48, no. 14, p. 2241, 2003, doi: 10.1088/0031-9155/48/14/314.
- [30] G. Placidi, D. Franchi, A. Maurizi, and A. Sotgiu, "Review on patents about magnetic localisation systems for in vivo catheterizations," *Recent Pat. Biomed. Eng.*, vol. 2, no. 1, pp. 58–64, Jan. 2009.
- [31] P. T. Anderson, "Electromagnetic tracking system and method using a single-coil transmitter," January 02, 2007. [Online] Available: <http://www.google.com/patents/US7158754>.
- [32] J. S. Bladen and A. P. Anderson, "Position location system," US5913820A, June 22, 1999 (accessed December 28, 2020). [Online] Available: <https://patents.google.com/patent/US5913820A/en>.
- [33] A. Plotkin and E. Paperno, "3-D magnetic tracking of a single subminiature coil with a large 2-D array of uniaxial transmitters," *IEEE Trans. Magn.*, vol. 39, no. 5, pp. 3295–3297, Sep. 2003, doi: 10.1109/TMAG.2003.816750.

- [34] K. O'Donoghue *et al.*, "Catheter position tracking system using planar magnetics and closed loop current control," *IEEE Trans. Magn.*, vol. 50, no. 7, pp. 1–9, Jul. 2014, doi: 10.1109/TMAG.2014.2304271.
- [35] E. Wilson, Z. Yaniv, D. Lindisch, and K. Cleary, "A buyer's guide to electromagnetic tracking systems for clinical applications," *Medical Imaging 2008: Visualization, Image-Guided Procedures, and Modeling*, Mar. 2008, vol. 6918, pp. 777–788. doi: 10.1117/12.770509.
- [36] Z. Yaniv, E. Wilson, D. Lindisch, and K. Cleary, "Electromagnetic tracking in the clinical environment," *Med. Phys.*, vol. 36, no. 3, pp. 876–892, Mar. 2009, doi: 10.1118/1.3075829.
- [37] Li, M., C. Hansen, and G. Rose, "A robust electromagnetic tracking system for clinical applications," *CURAC*, pp. 31–36, 2015. [Online] Available: [http://www.var.ovgu.de/pub/Li\\_2015\\_CURAC.pdf](http://www.var.ovgu.de/pub/Li_2015_CURAC.pdf).
- [38] Y. Zhang, K. Wang, J. Jiang, and Q. Tan, "Research on intraoperative organ motion tracking method based on fusion of inertial and electromagnetic navigation," *IEEE Access*, vol. 9, pp. 49069–49081, 2021, doi: 10.1109/ACCESS.2021.3068741.
- [39] N. Faddis Mitchell *et al.*, "Novel, magnetically guided catheter for endocardial mapping and radiofrequency catheter ablation," *Circulation*, vol. 106, no. 23, pp. 2980–2985, Dec. 2002, doi: 10.1161/01.CIR.0000038704.84304.6F.
- [40] J. Liu *et al.*, "Design and fabrication of a catheter magnetic navigation system for cardiac arrhythmias," *IEEE Trans. Appl. Supercond.*, vol. 26, no. 4, pp. 1–4, Jun. 2016, doi: 10.1109/TASC.2016.2514265.
- [41] J. Nam, W. Lee, E. Jung, and G. Jang, "Magnetic navigation system utilizing a closed magnetic circuit to maximize magnetic field and a mapping method to precisely control magnetic field in real time," *IEEE Trans. Ind. Electron.*, vol. 65, no. 7, pp. 5673–5681, Jul. 2018, doi: 10.1109/TIE.2017.2782220.
- [42] J. E. McGary, "Real-time tumor tracking for four-dimensional computed tomography using SQUID magnetometers," *IEEE Trans. Magn.*, vol. 45, no. 9, pp. 3351–3361, Sep. 2009, doi: 10.1109/TMAG.2009.2020430.



- [43] ITU, “Rec. ITU-R V.431-7, Nomenclature of the frequency and wavelength bands used in telecommunications,” Oct. 31, 2013. [https://web.archive.org/web/20131031020427/http://www.itu.int/dms\\_pubrec/itu-r/rec/v/R-REC-V.431-7-200005-I%21%21PDF-E.pdf](https://web.archive.org/web/20131031020427/http://www.itu.int/dms_pubrec/itu-r/rec/v/R-REC-V.431-7-200005-I%21%21PDF-E.pdf) (accessed Jan. 05, 2022).
- [44] A. Barbault *et al.*, “Amplitude-modulated electromagnetic fields for the treatment of cancer: Discovery of tumor-specific frequencies and assessment of a novel therapeutic approach,” *J. Exp. Clin. Cancer Res.*, vol. 28, no. 1, p. 51, Apr. 2009, doi: 10.1186/1756-9966-28-51.
- [45] D. Formica and S. Silvestri, “Biological effects of exposure to magnetic resonance imaging: An overview,” *Biomed. Eng. OnLine*, vol. 3, p. 11, Apr. 2004, doi: 10.1186/1475-925X-3-11.
- [46] W. T. Kaune, J. L. Guttman, and R. Kavet, “Comparison of coupling of humans to electric and magnetic fields with frequencies between 100 Hz and 100 kHz,” *Bioelectromagnetics*, vol. 18, no. 1, pp. 67–76, 1997.
- [47] E. K. P. Chong and S. H. Zak, *An Introduction to Optimization*, John Wiley & Sons, 2004.
- [48] C. Cheng, X. Huo, and M. Ghovanloo, “Towards a magnetic localization system for 3-D tracking of tongue movements in speech-language therapy,” *Conf. Proc. Annu. Int. Conf. IEEE Eng. Med. Biol. Soc. IEEE Eng. Med. Biol. Soc. Annu. Conf.*, vol. 2009, pp. 563–566, 2009, doi: 10.1109/IEMBS.2009.5334058.
- [49] B. A. Riwanto, T. Tikka, A. Kestilä, and J. Praks, “Particle swarm optimization with rotation axis fitting for magnetometer calibration,” *IEEE Trans. Aerosp. Electron. Syst.*, vol. 53, no. 2, pp. 1009–1022, Apr. 2017, doi: 10.1109/TAES.2017.2667458.
- [50] O. Talcoth and T. Rylander, “Optimization of sensor positions in magnetic tracking,” Chalmers University of Technology, Report, 2011 (accessed: Jul. 11, 2017). [Online] Available: <http://publications.lib.chalmers.se/publication/149466-optimization-of-sensor-positions-in-magnetic-tracking>.
- [51] J. P. Morgan and X. Deng, “Experimental design,” *Wiley Interdiscip. Rev. Data Min. Knowl. Discov.*, vol. 2, no. 2, pp. 164–172, Mar. 2012, doi: 10.1002/widm.1046.
- [52] S. Joshi and S. Boyd, “Sensor selection via convex optimization,” *IEEE Trans. Signal Process.*, vol. 57, no. 2, pp. 451–462, Feb. 2009, doi: 10.1109/TSP.2008.2007095.

- [53] D. Roetenberg, P. Slycke, A. Ventevogel, and P. H. Veltink, "A portable magnetic position and orientation tracker," *Sens. Actuators Phys.*, vol. 135, no. 2, pp. 426–432, Apr. 2007, doi: 10.1016/j.sna.2006.08.020.
- [54] W. Fang and H. Son, "Optimization of measuring magnetic fields for position and orientation tracking," *IEEEASME Trans. Mechatron.*, vol. 16, no. 3, pp. 440–448, Jun. 2011, doi: 10.1109/TMECH.2011.2125979.
- [55] E. Foxlin, "Inertial head-tracker sensor fusion by a complementary separate-bias Kalman filter," *Proceedings of the IEEE 1996 Virtual Reality Annual International Symposium*, pp. 185–194, Mar. 1996, doi: 10.1109/VRAIS.1996.490527.
- [56] A. M. Sabatini, "Quaternion-based extended Kalman filter for determining orientation by inertial and magnetic sensing," *IEEE Trans. Biomed. Eng.*, vol. 53, no. 7, pp. 1346–1356, Jul. 2006, doi: 10.1109/TBME.2006.875664.
- [57] R. Faragher, "Understanding the basis of the Kalman filter via a simple and intuitive derivation [Lecture notes]," *IEEE Signal Process. Mag.*, vol. 29, no. 5, pp. 128–132, Sep. 2012, doi: 10.1109/MSP.2012.2203621.
- [58] W. S. Ashe, "Magnetic sensors," US9360294B2, Jun. 07, 2016.
- [59] W. S. Ashe, "Magnetically tracked surgical needle assembly," US2013/0296691, Nov. 07, 2013.
- [60] W. S. Ashe, "Magnetically tracked sensor," US8994366B2, Mar. 31, 2015 (accessed Nov. 26, 2021). [Online] Available: <https://patents.google.com/patent/US8994366/en>.
- [61] J. C. Simpson, J. E. Lane, C. D. Immer, and R. C. Youngquist, "Simple analytic expressions for the magnetic field of a circular current loop," Feb. 2001. [Online] Available: <https://ntrs.nasa.gov/search.jsp?R=20140002333>.
- [62] J. Dunn, "Core saturation," *EDN*, May 07, 2013. <https://www.edn.com/core-saturation/> (accessed Dec. 22, 2021).
- [63] P. N. Stroski, "Skin effect: What is it?" *Electrical e-Library.com*, Nov. 17, 2021. <https://www.electricalibrary.com/en/2021/11/17/skin-effect-what-is-it/> (accessed Dec. 22, 2021).
- [64] S. Zurek, "Qualitative FEM study of proximity loss reduction by various winding configurations, Part 2," *Transform. Mag.*, vol. 3, p. 72, Jan. 2016.
- [65] "AWG - HwB," <http://www.hardwarebook.info/AWG> (accessed Dec. 22, 2021).

- [66] R. Ridley, "Proximity loss in magnetics windings," *Switching Power Magazine*, Designers Series XIII, p. 9, 2005.
- [67] M. Popescu and D. Dorrell, "Skin effect and proximity losses in high speed brushless permanent magnet motors," *2013 IEEE Energy Conversion Congress and Exposition*, p. 3527. doi: 10.1109/ECCE.2013.6647164.
- [68] "Calculation of the multilayer inductor," *Coil32*, <https://coil32.net/multi-layer-coil.html> (accessed Jan. 08, 2022).
- [69] A. Rikhter and M. M. Fogler, "Inductor coil of the highest possible Q," *Sci. Rep.*, vol. 10, no. 1, p. 15380, Sep. 2020, doi: 10.1038/s41598-020-72308-9.
- [70] M. Basharat, M. Ding, H. Cai, Y. Li, and J. Fang, "Design and analysis of multilayer solenoid coil for Faraday modulator," *MATEC Web Conf.*, vol. 114, p. 04004, 2017, doi: 10.1051/mateconf/201711404004.
- [71] R. Ridley, "The power of Dowell's equations and curves - Technical articles," <https://eepower.com/technical-articles/the-power-of-dowells-equations-and-curves/> (accessed Jan. 07, 2022).
- [72] Z. Shen, Z. Li, L. Jin, and H. Wang, "An AC resistance optimization method applicable for inductor and transformer windings with full layers and partial layers," *2017 IEEE Applied Power Electronics Conference and Exposition (APEC)*, pp. 2542–2548, Tampa, FL, USA, Mar. 2017, doi: 10.1109/APEC.2017.7931055.
- [73] P. L. Dowell, "Effects of eddy currents in transformer windings," *Proc. Inst. Electr. Eng.*, vol. 113, no. 8, p. 1387, 1966, doi: 10.1049/piee.1966.0236.
- [74] C. Gillespie, "How to calculate the amount of heat released," *Sciencing*, <https://sciencing.com/calculate-amount-heat-released-8219426.html> (accessed Jan. 07, 2022).
- [75] G. Carluccio, M. Bruno, and C. M. Collins, "Predicting long-term temperature increase for time-dependent SAR levels with a single short-term temperature response," *Magn. Reson. Med.*, vol. 75, no. 5, pp. 2195–2203, May 2016, doi: 10.1002/mrm.25805.
- [76] T.-C. Shih, P. Yuan, W.-L. Lin, and H.-S. Kou, "Analytical analysis of the Pennes bioheat transfer equation with sinusoidal heat flux condition on skin surface," *Med. Eng. Phys.*, vol. 29, no. 9, pp. 946–953, Nov. 2007, doi: 10.1016/j.medengphy.2006.10.008.

- [77] “Specific absorption rate,” *Wikipedia*, Jun. 09, 2021 (accessed Jan. 08, 2022). [Online] Available: [https://en.wikipedia.org/w/index.php?title=Specific\\_absorption\\_rate&oldid=1027652863](https://en.wikipedia.org/w/index.php?title=Specific_absorption_rate&oldid=1027652863).
- [78] T. R. Kuphaldt, *Lessons In Electric Circuits, Volume II -- AC*, p. 566, 2007.
- [79] “H-bridges,” *Practical EE*, <https://practicalee.com/h-bridges/> (accessed Dec. 25, 2021).
- [80] “Glossary definition for break-before-make,” <https://www.maximintegrated.com/en/glossary/definitions.mvp/term/Break-Before-Make/gpk/369> (accessed Dec. 25, 2021).
- [81] “Series 1 | NKK SWITCHES,” [https://www.nkkswitches.eu/learning/fundamentals/series\\_01.html](https://www.nkkswitches.eu/learning/fundamentals/series_01.html) (accessed Dec. 25, 2021).
- [82] “LC circuit: Parallel and series circuits, equations & transfer function | Electrical4U,” <https://www.electrical4u.com/>. <https://www.electrical4u.com/lc-circuit-analysis/> (accessed Dec. 25, 2021).
- [83] “Non-inverting and inverting amplifiers basic analysis,” <https://www.apogeeweb.net/electron/non-inverting-op-amp.html> (accessed Dec. 27, 2021).
- [84] “H-bridges vs. op-amps,” *All About Circuits*, <https://forum.allaboutcircuits.com/threads/h-bridges-vs-op-amps.85009/> (accessed Jan. 05, 2022).
- [85] M. McElfresh, *Effects of Magnetic Field Uniformity on the Measurement of Superconducting Samples*, p. 39.
- [86] W. F. Loke, T. Y. Choi, T. Maleki, L. Papiez, B. Ziaie, and B. Jung, “Magnetic tracking system for radiation therapy,” *IEEE Trans. Biomed. Circuits Syst.*, vol. 4, no. 4, pp. 223–231, Aug. 2010, doi: 10.1109/TBCAS.2010.2046737.
- [87] J. Karki, “Calculating noise figure in op amps,” *Op Amps*, p. 8, 2003.
- [88] M. Singh, “Wireless personal area tracking,” Ph.D. dissertation, Purdue University, West Lafayette, Indiana, 2019.
- [89] Advanced Solutions Nederland (ASN), “Difference between IIR and FIR filters: A practical design guide,” *ASN Home*, Apr. 28, 2020. <https://www.advsolned.com/difference-between-iir-and-fir-filters-a-practical-design-guide/> (accessed Nov. 21, 2021).
- [90] C. W. Kang and C. G. Park, “Attitude estimation with accelerometers and gyros using fuzzy tuned Kalman filter,” *2009 European Control Conference (ECC)*, pp. 3713–3718, Aug. 2009, doi: 10.23919/ECC.2009.7074977.

- [91] Y. Kim and H. Bang, *Introduction to Kalman Filter and Its Applications*, IntechOpen, 2018, doi: 10.5772/intechopen.80600.
- [92] MATLAB & Simulink, “Estimate computation costs,” <https://www.mathworks.com/help/physmod/simscape/ug/estimate-computation-costs.html> (accessed Jan. 13, 2022).
- [93] “Analysis of algorithms | Set 3 (Asymptotic notations),” *GeeksforGeeks*, Oct. 26, 2013. <https://www.geeksforgeeks.org/analysis-of-algorithms-set-3asymptotic-notations/> (accessed Jan. 15, 2022).
- [94] “W. D. Leahy Jr. Lecture Slides - CS 1311 Fall 2000,” 2000. <https://faculty.cc.gatech.edu/~bleahy/> (accessed Jan. 15, 2022).
- [95] M. H. Croy, “How to calculate time complexity with big O notation,” *DataSeries*, Jul. 28, 2020. <https://medium.com/dataseries/how-to-calculate-time-complexity-with-big-o-notation-9afe33aa4c46> (accessed Jan. 15, 2022).
- [96] STMicroelectronics, “Floating point unit demonstration on STM32 microcontrollers,” 2016. [Online] Available: [https://www.st.com/resource/en/application\\_note/dm00047230-floating-point-unit-demonstration-on-stm32-microcontrollers-stmicroelectronics.pdf](https://www.st.com/resource/en/application_note/dm00047230-floating-point-unit-demonstration-on-stm32-microcontrollers-stmicroelectronics.pdf).
- [97] “Advanced tutorial on wireless communication and electronic tracking: Appendix B,” <https://www.cdc.gov/niosh/mining/content/emergencymanagementandresponse/commtracking/advcommtrackingtutorialb.html#B5LinkBudgetAnalysis> (accessed Jan. 30, 2022).
- [98] H. Yoon and B.-J. Jang, “Link budget calculation for UHF RFID systems,” 2008. <https://www.microwavejournal.com/articles/7295-link-budget-calculation-for-uhf-rfid-systems> (accessed Jan. 31, 2022).
- [99] J. G. Betts, K. A. Young, and J. A. Wise, “19.1 Heart anatomy,” *Anatomy and Physiology | OpenStax, Anatomy and Physiology*, 2021. <https://openstax.org/books/anatomy-and-physiology/pages/19-1-heart-anatomy> (accessed Jan. 03, 2022).
- [100] K. O’Donoghue, “Electromagnetic tracking and steering for catheter navigation,” Doctoral thesis, University College Cork, 2014 (accessed Nov. 19, 2021). [Online] Available: <https://cora.ucc.ie/handle/10468/2025>.
- [101] B. Pandiripalli, “Repeatability and reproducibility studies: A comparison of techniques,” Master of Science, Wichita State University, 2010. [Online] Available: [https://soar.wichita.edu/bitstream/handle/10057/3736/t10107\\_Pandiripalli.pdf?sequence=3](https://soar.wichita.edu/bitstream/handle/10057/3736/t10107_Pandiripalli.pdf?sequence=3).

- [102] W. Birkfellner *et al.*, “Systematic distortions in magnetic position digitizers,” *Med. Phys.*, vol. 25, no. 11, pp. 2242–2248, 1998, doi: 10.1118/1.598425.
- [103] C. Hu, M. Li, S. Song, W. Yang, R. Zhang, and M. Q.-H. Meng, “A cubic 3-axis magnetic sensor array for wirelessly tracking magnet position and orientation,” *IEEE Sens. J.*, vol. 10, no. 5, pp. 903–913, May 2010, doi: 10.1109/JSEN.2009.2035711.
- [104] X. Ge, Y. Wang, N. Ding, X. Wu, Y. Wang, and Z. Fang, “An electromagnetic tracking method using rotating orthogonal coils,” *IEEE Trans. Magn.*, vol. 48, no. 12, pp. 4802–4810, Dec. 2012, doi: 10.1109/TMAG.2012.2203917.
- [105] S. Song, W. Qiao, B. Li, C. Hu, H. Ren, and M. Q. H. Meng, “An efficient magnetic tracking method using uniaxial sensing coil,” *IEEE Trans. Magn.*, vol. 50, no. 1, pp. 1–7, Jan. 2014, doi: 10.1109/TMAG.2013.2273061.
- [106] I. Khalfin and H. R. J. Jr, “Methods and apparatus for electromagnetic position and orientation tracking with distortion compensation,” Jun. 04, 2002 (accessed Jul. 18, 2017). [Online] Available: <http://www.google.com/patents/US6400139>.
- [107] P. J. Bickel and K. A. Doksum, *Mathematical Statistics: Basic Ideas and Selected Topics, Volumes I-II Package*, CRC Press, 2015.

## **VITA**

### **EDUCATION**

Purdue University, West Lafayette, IN.

Ph.D. Candidate in School of Electrical and Computer Engineering, Aug. 2015–Present.

Boston University, Boston, MA.

Bachelor of Science in Electrical Engineering (Cum Laude), May 2014.

### **PROFESSIONAL EXPERIENCE**

Purdue University, Graduate Teaching Assistant, Aug. 2015–May 2017; Jan. 2021–Present.

Purdue University, Graduate Research Assistant, May. 2017–Present.

NASA Marshall Space Flight Center, Intern, Sept.–Dec. 2014.

NASA Goddard Space Flight Center, Intern, Jun.–Aug. 2014.

Boston University (BU), Laboratory Assistant, Jan.–May 2014.

BU Space Physics (ANDESITE division), Intern/Research Assistant, May 2013–Mar. 2014.

BU Information Services & Technology, Media Assistant, Sept. 2012–May 2013; Sept. 2013–May 2014.

## **PUBLICATION**

Jin, R. and Jung, B. 2022. Magnetic tracking system for heart surgery. *IEEE Transactions on Biomedical Circuits and Systems*. Accepted.